CFD simulations on the effect of the diameter of an interatrial shunt for the treatment of heart failure

A Master Thesis

AE5110: Thesis Aerodynamics & Wind Energy

G. R. Meindertsma

Delft University of Technology

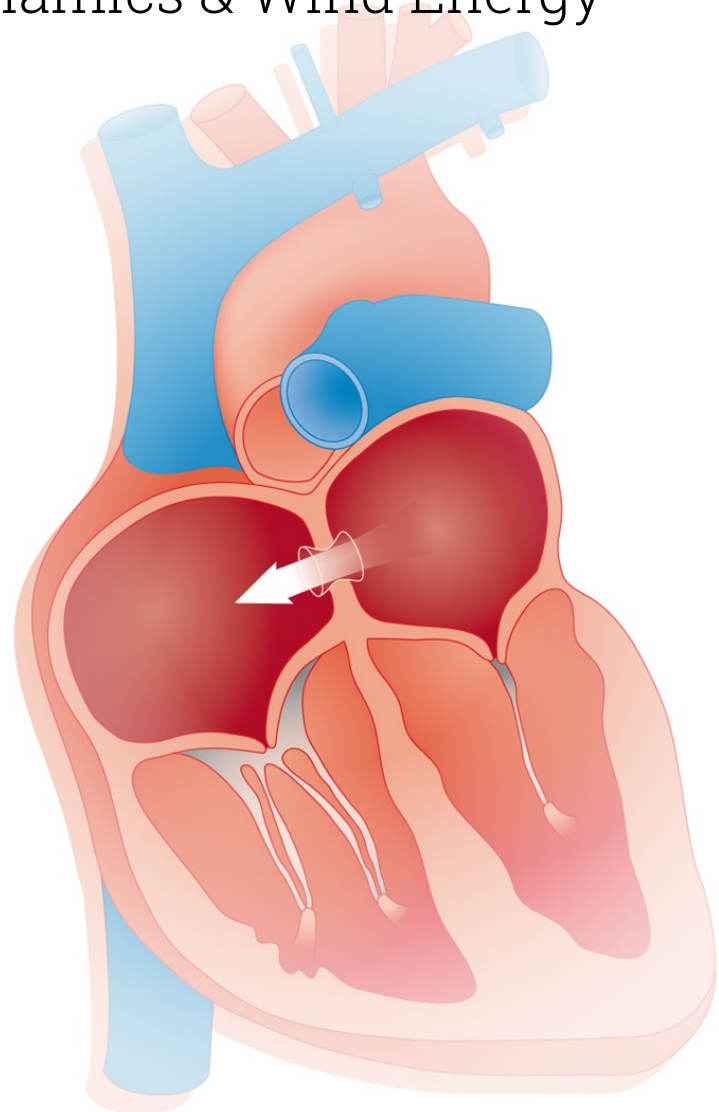

TU Delft

CFD simulations on the effect of the diameter of an interatrial shunt for the treatment of heart failure

A Master Thesis

by

G. R. Meindertsma

to obtain the degree of Master of Science
at the Delft University of Technology,
to be defended publicly on Thursday December 21, 2023 at 9:00 AM.

Student number:	5400325	
Project duration:	March 6, 2023 – December 21, 2023	
Thesis committee:	Dr. ir. A. H. van Zuijlen,	TU Delft, chair
	Dr. ir. M. I. Gerritsma,	TU Delft, responsible thesis supervisor
	Dr. ir. P. Breedveld,	TU Delft, examiner
	Ir. B. Verveld,	DEMCON Multiphysics, daily supervisor

Cover: I. Fernández-Ruiz. ”Interatrial shunting for the treatment of heart failure”. In: *Nature Reviews Cardiology* 13 (2016), pp. 312-313. DOI: https://doi.org/10.1038/nrcardio.2016.56. [21]

TU Delft

Preface

Thank you, Marc Gerritsma, Michiel van Limbeek and Bryan Verveld, for supervising me during this project. Thank you, Sander van Zuijlen and Paul Breedveld, for your contributions to the thesis committee.

Thank you, Joost Mulder, for giving me the opportunity to perform this research at DEMCON Multiphysics, and thank you to all my Multiphysics colleagues for making me feel very welcome.

Thank you, Jozef Bartunek and Esteban Montenegro, for the helpful meetings that have given me direct insight into the medical world.

Finally, thank you to my family and friends for your support, with my girlfriend in particular.

Dedicated to oma Truus.

Guido
Hengelo, December 2023

Abstract

Interatrial shunting is a proposed technique to reduce elevated left heart and pulmonary pressures in heart failure patients. Clinical trials show promising results in relief of symptoms and improvements in quality of life, but little is still known about the working principles of interatrial shunting and important questions remain regarding the optimal diameter. The current research investigates the patient-specific optimal diameter of an interatrial shunt through computational fluid dynamics simulations. An idealized two-dimensional model of the left and right atria, four pulmonary veins, the two vena cavae and the two atrioventricular valves is used to study the intra- and interatrial flow fields in absence and presence of an interatrial shunt through steady-state and transient simulations. For the transient simulations, the inlets and outlets are coupled through a Windkessel including four reservoirs, representing the two ventricles and the pulmonary and systemic circulations. This coupling represents the closed-loop behavior of the circulatory system and ensures realistic inlet and outlet pressures throughout the cardiac cycle. Furthermore, wall movement is applied in the transient simulation to model the atrial deformation during the systolic and diastolic phases of the heart cycle. The introduction of an interatrial shunt significantly influences the atrial flow field and a shunt flow from the left atrium to the right atrium is observed in all the simulations throughout the cardiac cycle, increasing the ratio of pulmonary to systemic blood flow (Qp:Qs). This reduces pulmonary, left atrial and left ventricular pressures while slightly increasing systemic, right atrial and right ventricular pressures. The patient-specific optimal shunt diameter is studied by applying shunts with diameters ranging between 0 and 20 mm to three patients of varying left ventricular stiffness. From this, it is found that the pressure reductions of the smallest (< 6 mm) as well as the largest shunts (> 12 mm) are little sensitive to shunt diameter, whereas medium-sized shunts are the most sensitive to the diameter. It is concluded that the optimal shunt diameter is patient-specific and is defined as the smallest diameter that manages to reduce a patient's peak pulmonary pressure to below 15 mmHg, as long as its Qp:Qs ratio does not exceed 1.5. Otherwise, the optimal shunt is the one with the largest diameter that does not exceed Qp:Qs = 1.5.

Contents

Nomenclature

Abbreviations

Abbreviation	Definition
0D	Zero-dimensional
2D	Two-dimensional
3D	Three-dimensional
6MWD	Six-Minute Walk Distance
AFR	Atrial Flow Regulator
AoV	Aortic Valve
ASD	Atrial Septal Defect
AV	Atrio-Ventricular
BAS	Balloon Atrial Septostomy
BDF	Backward Differentiation Formula
CAD	Computer-Aided Design
CFD	Computational Fluid Dynamics
CO	Cardiac Output
CVP	Central Venous Pressure
DNS	Direct Numerical Simulation
ED	End of Diastole
EDPVR	End-Diastolic Pressure-Volume Relationship
EF	Ejection Fraction
ES	End of Systole
ESPVR	End-Systolic Pressure-Volume Relationship
FSI	Fluid-Structure Interaction
HF	Heart Failure
HFmrEF	Heart Failure with mildly reduced Ejection Fraction
HFpEF	Heart Failure with preserved Ejection Fraction
HFrEF	Heart Failure with reduced Ejection Fraction
HRQoL	Health-Related Quality of Life
IASD	Inter-Atrial Shunt Device
IVC	Inferior Vena Cava
KCCQ	Kansas City Cardiomyopathy Questionnaire
LA	Left Atrium
LAA	Left Atrial Appendage
LEM	Lumped Element Model
LES	Large Eddy Simulation
LPVD	Latent Pulmonary Vascular Disease
LV	Left Ventricle
LVEDV	Left Ventricular End-Diastolic Volume
LVEF	Left Ventricular Ejection Fraction
MAGGIC	Meta-Analysis Global Group in Chronic Heart Failure
MLHFQ	Minnesota Living with Heart Failure Questionnaire
MV	Mitral Valve
NYHA	New York Heart Association
ODE	Ordinary Differential Equation
PAP	Pulmonary Arterial Pressure
PCWP	Pulmonary Capillary Wedge Pressure

Abbreviation	Definition
PH	Pulmonary Hypertension
PV	Pulmonary Vein
PVa	Pulmonary Valve
PVD	Pulmonary Vascular Disease
PVR	Pulmonary Vascular Resistance
QoL	Quality of Life
Qp:Qs	Ratio of pulmonary to systemic blood flow
RA	Right Atrium
RANS	Reynolds-Averaged Navier-Stokes
RV	Right Ventricle
RVCO	Right Ventricular Cardiac Output
RVEDV	Right Ventricular End-Diastolic Volume
RVEF	Right Ventricular Ejection Fraction
SI	Système International
SST	Shear Stress Transport
SV	Stroke Volume
SVC	Superior Vena Cava
TV	Tricuspid Valve

Symbols

Symbol	Definition	Unit
A	Area	[m^2]
C	Compliance	[m^3/mmHg]
d	Diameter	[mm]
E	Elastance	[mmHg/m^3]
f	Frequency	[Hz]
K	Proportionality constant	[cm/(mmHg·s)]
L	Inertance	[kg/m^4]
n	Power law index	[-]
P	Pressure	[mmHg]
Q	Flow rate	[m^3/s]
r	Radius	[mm]
R	Resistance	[mmHg·s/m^3]
T	Time	[s]
U	Velocity	[m/s]
V	Volume	[m^3]
Z	Impedance	[mmHg·s/m^3]
α	Exponent for EDPVR	[m^{-3}]
β	Scaling factor for EDPVR	[mmHg]
$\dot{\gamma}$	Shear rate	[s^{-1}]
λ	Time constant	[s]
μ	Dynamic Viscosity	[Pa·s]
ν	Kinematic Viscosity	[m^2/s]
ρ	Density	[kg/m^3]
τ	Time constant of relaxation	[s]

1 Introduction

The human body needs oxygen to function, which is transported through the body by the blood circulation, see Figure 1.1. Through arteries, arterioles and eventually capillaries, oxygenated blood reaches every part of the human body. In the capillaries, the oxygen moves from the blood vessels to the cells of organs in exchange for waste products like carbon dioxide [2]. Now that the oxygen has been delivered, the waste products are transported away by the deoxygenated blood. Through the capillaries, the venules and eventually veins, the blood is returned to its starting point: the heart. Via the heart, the blood moves through the pulmonary artery into the lungs, where again an exchange is made. This time, carbon dioxide leaves the blood vessels to the alveoli of the lungs in exchange for oxygen. The reoxygenated blood flows back towards the heart to start this cycle again.

Naturally, this movement of blood through the body costs energy, and this energy is provided by the heart. For proper functioning of the human body, it is therefore essential that the heart functions optimally. In the case of Heart Failure (HF), however, this is not the case. Heart failure can be described by the inability of the heart to pump an adequate supply of blood to the body [33]. In other words, the heart is not pumping efficiently enough to keep a person healthy [24]. A patient's symptoms include shortness of breath (dyspnea), reduced exercise tolerance, fatigue and pulmonary or peripheral edema, which is water accumulation in the lungs or in the legs and feet, respectively. As a result, heart failure causes a poor Quality of Life (QoL).

Heart failure can be split into three categories, depending on the fraction of blood volume that is ejected from the heart's left ventricle. This is called the Left Ventricular Ejection Fraction (LVEF) and is defined as the ratio between the Stroke Volume (SV) and the volume at the start of contraction, the Left Ventricular End-Diastolic Volume (LVEDV) [33]. The heart failure phenotype where this Ejection Fraction (EF) is lower than 40%, is referred to as Heart Failure with reduced Ejection Fraction, or HFrEF. When a patient's EF is in the normal range (>50%), this person has Heart Failure with preserved Ejection Fraction, or HFpEF. Preserved EF might sound healthy, but the EF is only in the normal range because the volume at the start of contraction is lower than normal. Finally, in the range where a person's EF lies between 40% and 50%, this is called Heart Failure with mid-range or mildly reduced Ejection Fraction (HFmrEF).

Whereas studies to treat HFrEF have been successful and have made rapid progress with effective treatments as a result, studies researching HFmrEF and HFpEF treatment have mostly failed and few effective treatments exist to date [6]. This is possibly due to different causes leading to this heart failure phenotype or due to a large variety in comorbid conditions in these patients [30]. Something all the heart failure phenotypes have in common, however, is elevated pressure in the pulmonary capillaries, referred to as Pulmonary Capillary Wedge Pressure (PCWP). Its cause lies downstream of the lungs, where the Cardiac Output (CO) from the left ventricle is too small, resulting in elevated pressures in the left heart and upstream.

Although these symptoms of elevated pressure result in an adverse effect on a patient's quality of life, they open the door for a treatment option for heart failure, irrespective of phenotype. With the goal of relieving elevated pressures, it has been proposed to create a small permanent opening between the left and right atria in the heart [30]. This procedure allows blood to flow from the left atrium into the right atrium, creating a so-called shunt, decompressing the left atrium and regions up- and downstream of it.

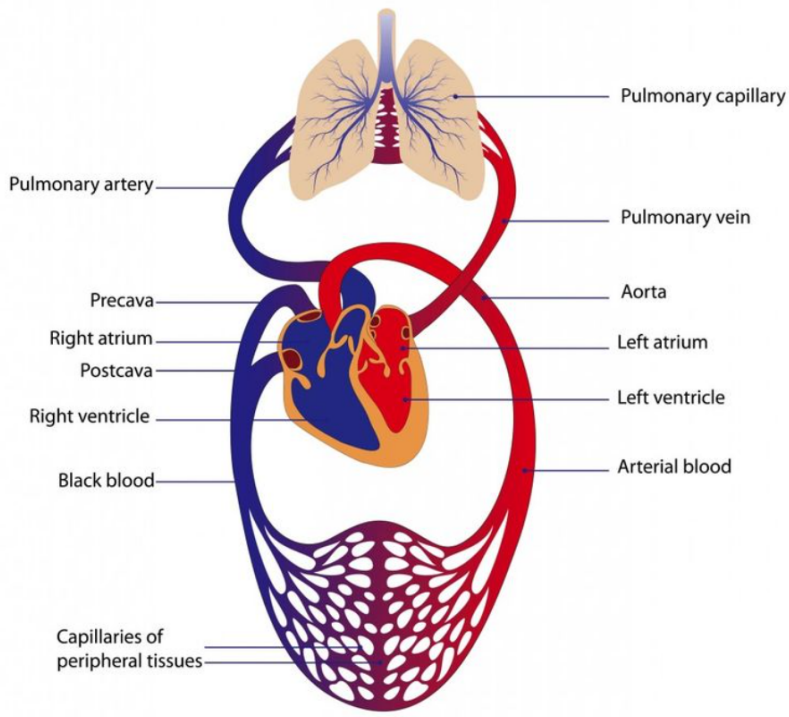

Figure 1.1: Schematic representation of the human circulatory system [19]

This idea is based on the Lutembacher syndrome, in which patients with elevated left heart pressures due to mitral stenosis experience fewer symptoms in combination with an Atrial Septal Defect (ASD) [30]. An ASD is a congenital heart defect where an opening is present in the interatrial septum, resulting in a permanent interatrial shunt.

One of the procedures to create an opening in the interatrial septum is Balloon Atrial Septostomy (BAS) [33], where a catheter punctures the septum and a balloon is inflated. This widens the puncture and creates an opening of controlled size. However, BAS only stretches the muscles, which causes the opening to close itself over time, resulting in a variable shunt size. Therefore, cardiac implants have been designed to keep a consistent size of the interatrial shunt, termed Inter-Atrial Shunt Devices (IASDs) [34].

Clinical trials are currently ongoing, showing promising results in relief of symptoms and improvements in quality of life (see chapter 2). Meanwhile, little is known about the working principles of interatrial shunting and important questions remain regarding the optimal diameter and possible long-term (health) effects [22, 34]. This study focuses on the former of the two, investigating the optimal diameter of an interatrial shunt through the following research question:

> *What is the optimal diameter of an interatrial shunt for different patients with heart failure with preserved ejection fraction?*

In this report, this question will be answered by studying various methods into interatrial shunting. In the following chapter, the state of the art regarding clinical trials will be described. After this, computational research into interatrial shunting is considered. Chapter 3 will treat the use of Lumped Element Modeling (LEM) to model the human body's circulatory system, whereas chapter 4 will employ Computational Fluid Dynamics (CFD) simulations to investigate the effect of an interatrial shunt. In CFD, a two-dimensional double-atrium model is created to simulate inter- and intra-atrial blood flow in steady-state and transient simulations. The transient simulations are performed with a static domain as well as with a moving mesh and the differences between the simulations are analyzed. Furthermore, for the transient simulation including a moving mesh, the boundary conditions as well as the shunt size are varied to study the patient-specific optimal shunt diameter. Finally, the report is concluded by a discussion of the results in chapter 5 and a conclusion including recommendations for future research in chapter 6.

2

Clinical Trials

This chapter of the report presents an overview of interatrial shunt research performed *in vivo*. Such research happens in clinical trials, which are biomedical research studies on human participants. In clinical trials, new treatment options are tested before they are approved. In this case, the clinical trials will consider research on various methods to create and maintain an interatrial shunt.

To date, six methods to create and preserve a permanent interatrial communication have been developed [1, 3, 14, 26, 41, 61]. Three of these are implantable devices, whereas the other three are no-implant procedures [34]. The three implants are the Corvia Atrial Shunt System by Corvia Medical [14], the V-Wave Ventura Interatrial Shunt System by V-Wave Medical [61] and the Atrial Flow Regulator by Occlutech [3], see Figure 2.1. The three no-implant procedures are the ALV1 System by Alleviant Medical [1], the NoYA Radiofrequency Interatrial Shunt System by NoYA MedTech [41] and the InterShunt Percutaneous Atrial Shunt Catheter System (PAS-C System) by InterShunt Technologies [26]. These no-implant interatrial shunts are believed to be more beneficial as nothing is left behind in the body. This takes away the risk of device thrombosis, infection or dislodgement [34]. Furthermore, access to the interatrial septum is also easier, should this ever be necessary in the future.

Another method for the treatment of heart failure is the Transcatheter Atrial Shunt System by Edwards Lifesciences [20]. However, this considers an implant that creates a shunt from the left atrium to the coronary sinus [28]. As this is not an interatrial shunt, it is outside the scope of the current study.

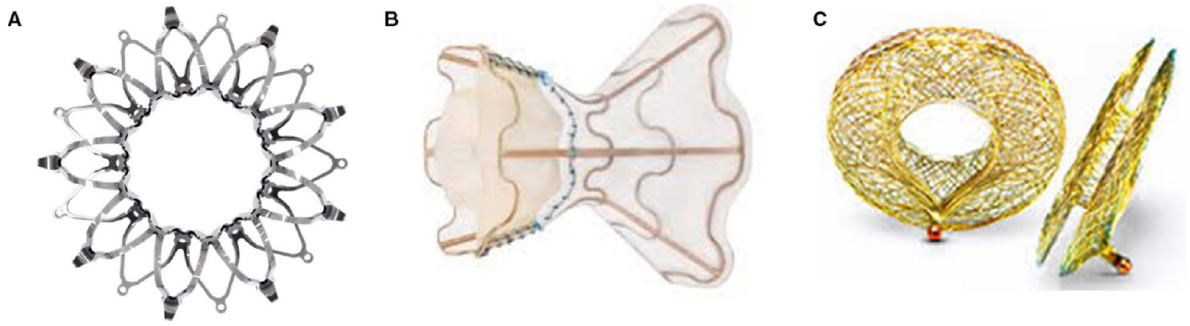

Figure 2.1: IASDs by Corvia Medical (A), V-Wave Medical (B) and Occlutech (C) [22]

In *Update on Atrial Shunt Therapy for Treatment of Heart Failure*, Litwin, Borlaug, and Komtebedde [34] summarize the results of the published data and the current interatrial shunting therapies under investigation. The Corvia Atrial Shunt System was the first device to be studied with a feasibility study in 2014. This considered 11 patients over a 30-day period, which showed that mean PCWP at rest decreased from 19 mmHg to 14 mmHg in 10 of the 11 patients. Another important measure of improvement is the 6-Minute Walk Distance (6MWD), where the distance is measured that a patient is able to traverse in six minutes. In Corvia's first feasibility study, this improved by 32 meters on average. More subjective measures of improvement are the change in a patient's New York Heart Association (NYHA) functional class or Health-Related Quality of Life (HRQoL). The latter is assessed either by the Kansas

City Cardiomyopathy Questionnaire (KCCQ) or the Minnesota Living with Heart Failure Questionnaire (MLHFQ). As these measures are derived by a physician, they are however amenable to bias [32]. Corvia's Atrial Shunt System showed a significant improvement of 29 points (on a scale of 0 to 105 [4]) on the MLHFQ in this feasibility study [34]. Furthermore, Biscopink, Mostertz, and Grewal [5] report that, importantly, no thrombo-embolic events were observed. Therefore, it was concluded from this pilot study that interatrial shunting is a feasible treatment option suggesting positive safety signals and hemodynamic efficacy.

In 2016, testing of Corvia's device continued in the Reduce Elevated Left Atrial Pressure in Patients with Heart Failure (REDUCE LAP-HF) trial. This study was an open-label, single-arm, phase 1 study including 68 patients with HFmrEF or HFpEF [5]. Further inclusion criteria consisted of elevated left atrial pressure, with PCWP exceeding 15 mmHg at rest or 25 mmHg during exercise. Six months into the trial, it showed an average reduction in PCWP from 34 mmHg to 32 mmHg at peak exercise [34]. There was, however, an average increase in right atrial pressure from 9 mmHg to 11 mmHg. The study also showed that Cardiac Output (CO) had not decreased, which is an important result as this is one of the concerns of interatrial shunting. These positive outcomes meant that Corvia's IASD received the CE mark in May 2016 [23]. According to Biscopink, Mostertz, and Grewal [5], these hemodynamic changes were associated with improvements in MLHFQ score, 6MWD, exercise time and NYHA functional class. The results after one year did not change compared to the results at six months, but changes in heart chamber properties were reported. This included a small reduction in left ventricular volume at the end of diastole (Left Ventricular End-Diastolic Volume, LVEDV), a small increase in right ventricular volume at the end of diastole (RVEDV) and an increase in Right Ventricular Ejection Fraction (RVEF). Moreover, a separate study of the same cohort with a follow-up after two years (729 days on average) concluded a lower mortality rate than predicted by the Meta-Analysis Global Group in Chronic Heart Failure (MAGGIC) score.

The REDUCE LAP-HF trial was followed by REDUCE LAP-HF I, a phase 2, randomized, parallel-group, blinded, multi-center study [5]. This was the first sham-controlled study of this device, in which 44 patients were randomized 1:1 to the interatrial shunt device or a placebo [34]. At one month, the results showed on average improvements in PCWP (3.2 mmHg reduction), exercise duration (1.2 minute increase), achieved work (1.5 W increase), workload-corrected PCWP (5.7 mmHg/W reduction) and Pulmonary Vascular Resistance (PVR) (0.29 WU reduction). Pulmonary vascular resistance describes the resistance that the blood must overcome to pass through the pulmonary vasculature. This is defined by the ratio of the pressure drop between the pulmonary artery (PAP) and the pulmonary capillaries (PCWP) to the cardiac output of the right ventricle (RVCO) as:

$$\text{PVR} = \frac{\text{PAP} - \text{PCWP}}{\text{RVCO}}. \tag{2.1}$$

With the pressures in mmHg and cardiac output in liters per minute, the unit of PVR is mmHg·min/L, also known as Wood Units (WU) [29]. In *Effects of Interatrial Shunt on Pulmonary Vascular Function in Heart Failure With Preserved Ejection Fraction*, Obokata, Reddy, and Shah [43] showed that this reduction in PVR is likely a result from the increase in pulmonary blood flow and oxygen content due to the interatrial shunt.

After the accomplishments of REDUCE LAP-HF and its successor, logically REDUCE LAP-HF II followed. In this international, blinded, phase 3 study, 626 patients with either HFmrEF or HFpEF were once again 1:1 randomized between the shunt device or a placebo [34]. At two years of follow-up, the results showed no significant difference between the IASD group and the sham group over the entire population. Prespecified and post-hoc subgroup analyses however showed that patients with peak exercise PVR < 1.74 WU were 31% more likely to gain clinical benefit from the shunt than patients above this value [6]. Patients below this value scored significantly lower on the Kansas City Cardiomyopathy Questionnaire and showed an increased risk for heart failure events [5]. Pulmonary Vascular Disease (PVD) is defined as resting PVR > 3.5 WU and patients with PVD were excluded from the trial. This is because it was deemed that these patients could not cope with the increased hemodynamic demands that interatrial shunting puts on the pulmonary vasculature. The newly-defined 'Latent' Pulmonary Vascular Disease (LPVD) however only becomes apparent at peak exercise and was defined by Borlaug, Blair, and Bergmann [6] as peak exercise PVR ≥ 1.74 WU, reflecting the highest tertile of peak exercise PVR. This implies that not only resting PVR, but also PVR on exertion should be considered at enrollment [34]. Other subgroups found to be at increased clinical risk are

men, patients with a dilated right atrium and patients with a pacemaker. In short, REDUCE LAP-HF II has been a valuable trial in the research of interatrial shunting, showing clear improvement in a specific subgroup.

The interesting result from Corvia Medical's REDUCE LAP-HF II trial has laid the foundation for their next trial: Re-Evaluation of the Corvia Atrial Shunt Device in a Precision Medicine Trial to Determine Efficacy in Mildly Reduced or Preserved Ejection Fraction (EF) Heart Failure (RESPONDER-HF) [51]. This multicenter, prospective, randomized, sham-controlled, double-blinded clinical trial with 1:1 randomization has started in November 2022 and is currently recruiting. The estimated enrollment includes 750 patients that will be followed for five years and will be evaluated at pre-specified time intervals. This study introduces a new exclusion criterion as patients with PVR ≥ 1.75 WU are excluded from the study, unlike previously [5]. However, this brings the challenge of performing, measuring and interpreting hemodynamics at peak exercise. As previously mentioned (see Equation 2.1), this requires measurements of pulmonary arterial pressure, pulmonary capillary wedge pressure and cardiac output. From these, especially PAP and CO are particularly challenging during peak exercise. Furthermore, according to Biscopink, Mostertz, and Grewal [5], also their assessment lacks uniform agreement, even among experts. Therefore, this study will also prove to show if measurements at peak exercise will be able to show a distinction between responders and non-responders.

In this brief description of the trial results, only Corvia's Atrial Shunt System has been mentioned as it is the most developed device to date. Other trials studying the V-Wave Ventura, Atrial Flow Regulator and the nonimplant procedures have shown similar improvements of interatrial shunts in heart failure patients [5, 34]. Still, some researchers keep concerns over the long-term effects of interatrial shunting, as Saunders and Michelakis [53] argue that shunts could cause PVD, even in patients without LPVD. This is based on the observation that shunt-treated patients showed enlargement of the right heart chambers [5], which could be indicative of Pulmonary Hypertension (PH). This is backed by Shah, Borlaug, and Chung [54] as well as by Kapur, Upshaw, and Wessler [29], who propose to measure right heart dilation in follow-up to check right heart function. Moreover, Obokata, Reddy, and Shah [43] mentioned the concern that interatrial shunting could lead to Eisenmenger syndrome, which takes years to develop. These concerns stress the essence of performing further trials to study the long-term effects of interatrial shunting.

In conclusion, clinical trials have shown that interatrial shunting is a feasible treatment option for patients with heart failure with preserved or mildly reduced ejection fraction. However, little is still understood about the working principles of interatrial shunts in heart failure, which is essential for the development and optimization of this technique. Methods that can give insight into these working principles and that can be used to optimize interatrial shunts will be introduced in the following chapters.

3

Lumped Element Modeling

In contrast to the previous chapter, this chapter as well as the next consider interatrial shunt research through computer simulations. This chapter discusses zero-dimensional lumped element modeling, whereas the next chapter treats a computational method of a higher dimension.

3.1. Theory

Lumped element modeling is a technique that can be used to computationally model the human body's vasculature. The technique applied in the current research is based on the hydraulic analogy, which is the analogy between fluid flow through pipes and electrical current through wires [8]. Where the body's hemodynamics considers pressure, volume and flow rate, this is analogous to voltage, charge and current in an electronic circuit, respectively [11]. As such, the resistance of a blood vessel (pressure drop over flow rate) can be modeled by an electrical resistance (voltage drop over current). Similarly, an electrical capacitor is able to model the elasticity of arteries. This elasticity allows the arteries to distend when blood pressure rises during the systole and recoil when the pressure drops during diastole. This damps the fluctuation in blood pressure over the cardiac cycle and results in a continuous transport of blood, similar to a Windkessel (German for 'air chamber') present in fire engines [62]. Therefore, a lumped element model is also called a Windkessel model. Figure 3.1 schematically shows this concept in two ways: for a fire engine and for a part of the human body's vasculature, with the veins acting as a reservoir, the heart acting as as pump, the arteries acting as the Windkessel and a resistance acting as the spout.

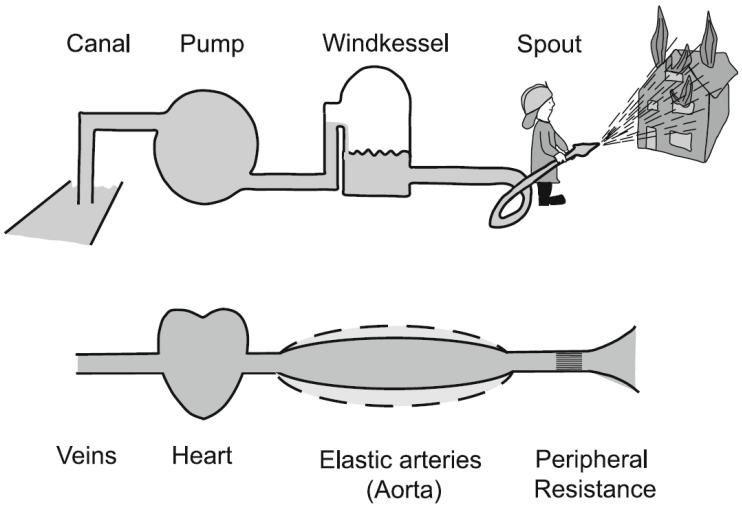

Figure 3.1: The concept of the Windkessel effect and the hydraulic analogy [62]

3.1.1. Two-element Windkessel model

Summing this up, the human body's vascular system can be modeled by a series of resistances and capacitances in a two-element Windkessel model [62]. To determine the resistance of the circulatory system, one needs to sum the resistances of all the blood vessels in the body. These include the arteries, arterioles, capillaries, venules and veins. However, not all blood vessels have the same resistance. Rather, the resistance of a blood vessel is inversely proportional to blood vessel radius to the fourth power according to Poiseuille's law. Therefore, the smallest arteries and veins are responsible for most of the resistance in the arterial system, whereas the resistance of the biggest arteries and veins can be neglected. Accordingly, these smallest vessels are also termed the resistance vessels. Adding the resistances of all these microvessels results in the total resistances of the pulmonary and systemic circulations. This total resistance is called the peripheral resistance R and can simply be calculated by measuring mean aortic blood pressure $P_{ao_{mean}}$, mean venous blood pressure $P_{ven_{mean}}$ and cardiac output CO:

$$R = \frac{P_{ao_{mean}} - P_{ven_{mean}}}{CO}. \tag{3.1}$$

Furthermore, since $P_{ven_{mean}}$ is negligible compared to $P_{ao_{mean}}$, Equation 3.1 can be simplified to:

$$R = \frac{P_{ao_{mean}}}{CO}. \tag{3.2}$$

In a lumped element model, R is now the total resistance of the circulatory system 'lumped' into a single element.

Similar to the total resistance of the pulmonary and systemic circulations, the total compliance of the circulations is the sum of the individual compliances of all arteries, arterioles, capillaries, venules and veins. In contrast to the resistance, however, the total compliance is dominated by the largest arteries and veins. Therefore, the total compliance is also termed the (total) arterial compliance, C. It is the opposite of arterial elastance and is defined as a volume change ΔV divided by a resulting change in pressure ΔP:

$$C = \frac{\Delta V}{\Delta P}. \tag{3.3}$$

This value can be determined by considering ΔV as the stroke volume and measuring the difference in blood pressure between the start of systole and the end of systole, hence obtaining ΔP.

3.1.2. Three-element Windkessel model

The two-element Windkessel model is found to poorly predict the pressure-flow relation during the systolic phase of the cardiac cycle at frequencies higher than 1 Hz [62]. To resolve this shortcoming, a third element is added to the model, resulting in a three-element Windkessel model. This third element is an impedance and represents the characteristic impedance Z_c of the proximal artery, which is the pulmonary artery for the pulmonary circulation and the aorta for the systemic circulation. The addition of this third element results in a much more accurate lumped element model compared to the two-element Windkessel model [62]. However, the drawback of adding a characteristic impedance is that the total resistance of the mean flow, i.e. at 0 Hz, is now overestimated by the absolute value of Z_c. Also, it is found that the three-element Windkessel model is able to produce realistic results, but it can only do so with parameter values that quantitatively differ from the vascular properties [58]. It is concluded that the three-element Windkessel model overestimates the total arterial compliance C and underestimates the characteristic impedance Z_c.

3.1.3. Four-element Windkessel model

To resolve the limitations of the three-element Windkessel model, another model improvement is proposed. Since the errors of the three-element Windkessel are present at low frequencies, an element is added that tackles mainly this frequency range. In the four-element Windkessel model, an inertial term L is added, which is analogous to an inductance in electrical circuits. By placing the element in parallel with the characteristic impedance Z_c, it resolves the error in the total resistance of the mean flow and it accounts for the inertia of the whole arterial system [59]. Through the addition of this fourth element, this Windkessel model contains the beneficial characteristics of both the two- and three-element

Windkessel models over the frequency range. At low frequencies, it follows the two-element Windkessel model, whereas the characteristics of the three-element Windkessel model become apparent at higher frequencies. Although the four-element Windkessel model is a useful improvement on the three-element Windkessel model, Westerhof, Lankhaar, and Westerhof [62] argue that the inertance L is very difficult to estimate in practice. Therefore, the authors conclude that the three-element Windkessel model is actually often preferred over the four-element Windkessel model.

An overview of the different Windkessel models and their hydraulic analogy is presented in Figure 3.2.

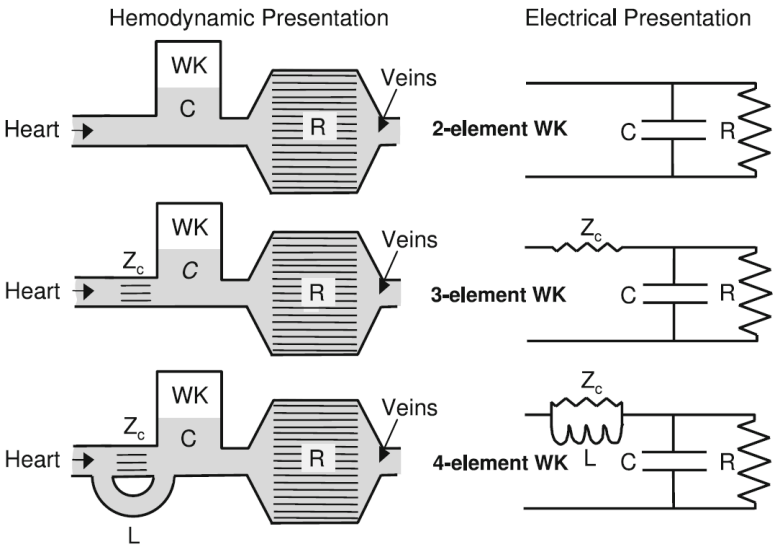

Figure 3.2: Hemodynamic and electrical representations of two-, three- and four-element Windkessel models [62]. WK, Windkessel; Z_c, characteristic impedance; C, total arterial compliance; R, total peripheral resistance; L, total arterial inertance.

3.2. Implementation

The previous section has treated the theory behind lumped element modeling, which has established the foundation for this section. Here, the implementation of the theory into a custom built lumped element model is discussed.

To study interatrial shunting using a lumped element model, a three-element Windkessel model previously introduced by Kaye et al. [30] (see Figure 3.3) is reproduced in system simulation software SimulationX 4.2 [55] to represent the human body's circulatory system. As discussed in the previous section, lumped resistance elements represent the resistances of the arteries and veins in the human body. Furthermore, every resistor is accompanied by a lumped capacitance which models the Windkessel effect of these blood vessels. Moreover, the Rc elements in Figure 3.3 are the impedance elements modeling the characteristic impedance of the proximal arteries. Elements that have not been discussed previously include the resistance elements for the atrioventricular valves (R_{MV} and R_{TV}), the resistance element modeling the interatrial shunt (R_{ASD}), the diodes representing the unidirectional flow through the four heart valves and finally the time-varying capacitance elements representing the contraction of the heart chambers.

For each heart chamber, instantaneous ventricular pressure $P(t)$ is related to instantaneous ventricular volume $V(t)$ through the time-varying elastance $e(t)$ in an equation proposed by Suga and Sagawa [60] and adjusted by Kaye et al. [30] into its current form:

$$P(t) = P_{ed}(V) + e(t)\left[P_{es}(V) - P_{ed}(V)\right], \tag{3.4}$$

where

$$P_{ed}(V) = \beta\left(e^{\alpha(V-V_0)} - 1\right), \tag{3.5}$$

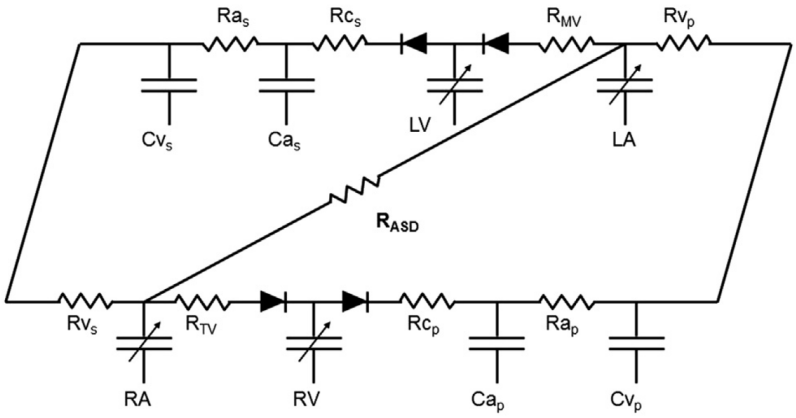

Figure 3.3: Electrical representation of the three-element Windkessel model employed by Kaye et al. [30] to simulate an interatrial shunt. C, Capacitance; R, Resistance; v, venous; a, arterial; s, systemic; p, pulmonary; LV, Left Ventricle; LA, Left Atrium; RA, Right Atrium; RV, Right Ventricle; MV, Mitral Valve; TV, Tricuspid Valve; ASD, Atrial Septal Defect.

$$P_{es}(V) = E_{es}(V - V_0), \tag{3.6}$$

and

$$e(t) = \begin{cases} \frac{1}{2}\left(\sin\left[\frac{\pi}{T_{max}}t - \frac{\pi}{2}\right] + 1\right), & \text{for } 0 < t \leq \frac{3}{2}T_{max} \\ \frac{1}{2}e^{-(t-\frac{3}{2}T_{max})/\tau}, & \text{for } t > \frac{3}{2}T_{max}. \end{cases} \tag{3.7}$$

In these equations, P_{ed} is the end-diastolic pressure describing its relationship with the end-diastolic volume V. This is also known as the End-Diastolic Pressure-Volume Relationship (EDPVR) and is a nonlinear equation [9]. The EDPVR along with other variables from the presented equations are graphically presented in a pressure-volume loop[1] in Figure 3.4. As shown in Equation 3.5, apart from the volume V, P_{ed} also depends on constants α and β and the volume V_0. V_0 is the volume-axis intercept of the EDPVR and the volume at which end-systolic pressure is 0 mmHg [52], see Figure 3.4. P_{es} on the other hand is the End-Systolic Pressure-Volume Relationship (ESPVR) which is linear and only depends on V, V_0 and E_{es}. The latter is the maximum value of the time-function $e(t)$, which describes the elastance as a function of time over the cardiac cycle. The first part of Equation 3.7 describes the systolic part of the cardiac cycle, where the heart's elastance rapidly rises as it contracts. T_{max} is the point of maximal chamber elastance and diastole starts shortly after [30]. In the diastolic part of the cardiac cycle, the heart muscle fully relaxes and its elastance is described by an exponential decay.

For all the mentioned parameters, the values are used from the research paper by Kaye et al. [30]. These values represent hemodynamic data from two independent studies by Maeder et al. [36] and Borlaug et al. [7] with a total of 46 HFpEF patients [30]. The parameter values are presented in Tables 3.1 and 3.2. Only the systemic arterial resistance Ra_s is not provided by Kaye et al. [30]. This value of 1 mmHg·s/mL is however provided by a research paper by Morley et al. [39]. Note that Table 3.2 shows that the values between the two atria are equal, as well as those between the two ventricles. Furthermore, note that all parameters in the tables are given in hydraulic units, whereas the lumped element model uses an electrical description. Therefore, it has been assumed that the units in Tables 3.1 and 3.2 correspond to their SI electrical units. For instance, the pulmonary and systemic characteristic impedances of 0.045 mmHg·s/mL have been prescribed in the lumped element model as 0.045 Ω. Moreover, the Atrio-Ventricular (AV) Delay in Table 3.2 has not been presented previously in any of the equations. The AV delay is the time delay between the atrial and ventricular contractions.

Also note that time-varying capacitors are used in the lumped element model, whereas a function for the elastance $e(t)$ is given by Equation 3.7. Since capacitance or compliance is the inverse of elastance, $1/e(t)$ is prescribed at the time-varying capacitance elements. However, $e(t)$ is a function

[1] A pressure-volume loop is a graph of the pressure of a heart chamber as a function of its volume. Since this is a periodic function, the pressure-volume relationship forms a loop, hence its name.

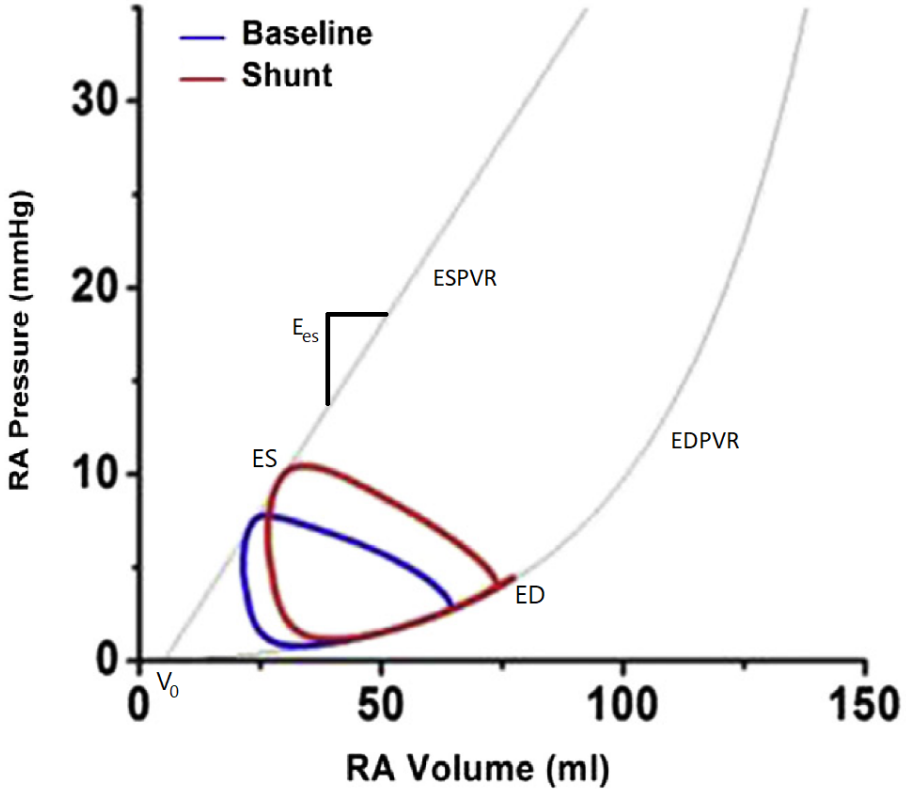

Figure 3.4: Example of two pressure-volume loops of the Right Atrium (RA): one in absence and one in presence of an interatrial shunt, from Kaye et al. [30]. Indicated in the figure are the End of Diastole (ED), End of Systole (ES), End-Diastolic (EDPVR) and End-Systolic (ESPVR) Pressure-Volume Relationships, End-Systolic Elastance (E_{es}) and the volume-axis intercept V_0.

from 0 to 1. Firstly, this means that $e(t)$ needs to be multiplied by the heart chamber's end-systolic elastance E_{es}, since this is its maximum value. The research paper by Kaye et al. [30] only provides these values for the two ventricles, so the values for the two atria were derived from pressure-volume loops in the research paper. The end-systolic elastances of the four heart chambers are presented in Table 3.3.

Secondly, the time-varying elastance $e(t)$ nearing zero causes an issue for the capacitance $c(t)$, since $1/e(t)$ blows up for small values of $e(t)$. Therefore, a value has to be added to the time-varying elastance such that it does not reach zero. A logical value for this would be a minimum value of the elastance, which is found at the end of the diastolic phase of the cardiac cycle, termed E_{ed}. These values are not provided by Kaye et al. [30] and are not straight-forward to determine either. This is because they are a function of volume, unlike E_{es}, as the end-diastolic pressure-volume relationship is a nonlinear equation (see Equation 3.5 and Figure 3.4). At first, values of E_{ed} were determined by following the logic behind E_{es} being the derivative of the ESPVR:

Circulation	Symbol	Units	Pulmonary	Systemic
Characteristic impedance	Rc	mmHg·s/mL	0.045	0.045
Arterial resistance	Ra	mmHg·s/mL	0.052	1
Venous resistance	Rv	mmHg·s/mL	0.025	0.025
Arterial compliance	Ca	mL/mmHg	7	1
Venous compliance	Cv	mL/mmHg	4	70

Table 3.1: Circulation-dependent parameter values [30]

Parameter	Symbol	Units	Value			
AV Delay	AVD	ms	160			
			RA	**RV**	**LA**	**LV**
Volume axis intercept	V_0	mL	5	0	5	0
Scaling factor for EDPVR	β	mmHg	0.44	0.34	0.44	0.34
Exponent for EDPVR	α	mL^{-1}	0.044	0.034	0.044	0.034
Time to end-systole	T_{max}	ms	125	200	125	200
Time constant of relaxation	τ	ms	25	50	25	50
AV valve resistance	R_{av}	mmHg·s/mL	0.0025		0.0025	

Table 3.2: Other parameter values [30]

$$E_{max} = \frac{dP_{es}}{dV} = \frac{d}{dV}\left[E_{es}(V - V_0)\right] = E_{es}. \tag{3.8}$$

Therefore:

$$E_{min} = \frac{dP_{ed}}{dV} = \frac{d}{dV}\left[\beta\left(e^{\alpha(V-V_0)} - 1\right)\right] = \alpha\beta e^{\alpha(V-V_0)} = E_{ed}. \tag{3.9}$$

From Equation 3.9, it is clear that the end-diastolic elastance E_{ed} is indeed a function of volume. To calculate E_{ed} for the pressure-volume loops in the research paper by Kaye et al. [30], the volume at the end of diastole was taken. This results in the values presented in the third column of Table 3.3. However, the atrial values of the minimum elastance E_{ed} can be seen to exceed the maximum elastance E_{es}. From this, it became apparent that Equations 3.4 to 3.7 with the values given in the research paper by Kaye et al. [30] do not correspond to the pressure-volume loops presented in the same paper. Therefore, the decision was made to determine E_{ed} through an estimation of the EDPVR slope at the end of diastole, rather than through Equation 3.9. These values are presented in the fourth column of Table 3.3 and are indeed smaller than the maximum values of the elastance in the second column.

Combining the minimum and maximum values of the elastance with the time-varying elastance function $e(t)$ between 0 and 1, the time-varying elastance function $E(t)$ is proposed that gives values between E_{ed} and E_{es}:

$$E(t) = E_{ed} + e(t)\left[E_{es} - E_{ed}\right]. \tag{3.10}$$

Therefore, the time-varying capacitance $C(t)$ is:

$$C(t) = \frac{1}{E(t)} = \frac{1}{E_{ed} + e(t)\left[E_{es} - E_{ed}\right]}. \tag{3.11}$$

Heart chamber	E_{es} (mmHg/mL)	E_{ed} (mmHg/mL)	
		Equation 3.9	Estimation
RA	0.4	0.46	0.15
RV	0.97	0.68	0.36
LA	0.4	1.27	0.32
LV	2.54	1.26	0.56

Table 3.3: End-systolic and end-diastolic values for the elastance of the four heart chambers [30]

Finally, the resistance of the interatrial shunt was determined through an equation provided by Kaye et al. [30]:

$$\text{Flow} = K \cdot \text{Area} \cdot \Delta P, \tag{3.12}$$

where Flow is the shunt flow rate, Area is the surface area of the shunt in cm^2, ΔP is the pressure gradient across the shunt in mmHg and $K = 2.66$. Since the research paper does not provide units for K, the units of the shunt flow rate are unclear. K cannot be unitless, because mmHg·cm^2 is not a unit

of flow rate. Since the shunt resistance is defined as the pressure difference ΔP divided by the flow rate:

$$R = \frac{1}{K \cdot \text{Area}}. \tag{3.13}$$

Assuming that the shunt resistance uses similar units as the rest of the research paper (mmHg·s/mL), by considering that 1 $cm^3 = 1$ mL and by knowing that Area is in cm^2, the units of K are cm/(mmHg·s) and the flow rate is in mL/s. Using the expression for Area as a function of diameter, the shunt resistance is determined as follows:

$$R = \frac{1}{K \cdot 0.25\pi d^2}. \tag{3.14}$$

In short, the model in Figure 3.3 is implemented in SimulationX 4.2 and the parameter values from Table 3.1 are applied to the resistance, impedance and capacitance elements in the circuit. Equation 3.11 is applied to the time-varying capacitance elements representing the heart chambers, with the values from Table 3.2 used for $e(t)$ and the values from Table 3.3 used for E_{ed} and E_{es}. A heart rate of 60 bpm (1 Hz) is considered and initial voltages of the time-varying capacitors are adjusted to obtain as physically realistic results as possible. These are set to 0 volt for the two atria and 200 volt for the two ventricles.

3.2.1. Results

In Figure 3.5, the pressure-volume loops from the reproduced lumped element model as described above are compared to those from the research paper by Kaye et al. [30]. The upper left corners of both figures show the right atrium (as previously presented in Figure 3.4), the upper right corners show the left atrium, the bottom left corners show the right ventricle and the bottom right corners show the left ventricle. Note that Figure 3.5b shows results in absence and presence of a shunt, whereas Figure 3.5a only shows results in absence of a shunt. Therefore, the comparison between the two figures only considers the 'Baseline' results in Figure 3.5b.

Since the reproduced lumped element model uses an electrical description, Figure 3.5a shows the voltage in Volt (V) on the y-axis and the charge in Coulomb (C) on the x-axis. According to the hydraulic analogy, these correspond to pressure and volume, respectively. Therefore, Figure 3.5a can be compared to Figure 3.5b and the same values on the axes have been chosen. Also note that the results from SimulationX show the convergence of the results from the initial condition to a stable orbit. For clarity, the converged pressure-volume loops have been indicated in red.

Comparing Figure 3.5a to Figure 3.5b for each of the heart chambers, it can be seen that the characteristic shapes of the pressure-volume loops show good resemblance. The actual values of voltage (pressure) and charge (volume), however, are very different in the reproduced LEM compared to the results from Kaye et al. [30] that show a good match with measured data. Adjusting the initial conditions of the time-varying capacitors did not result in a suitable fit for all chambers. From the four chambers, the right atrium shows the closest match, as it is approximately in the correct pressure and volume range. The left atrium and both ventricles, however, show pressure-volume loops with pressure and volume fluctuations that are significantly different from the results in Figure 3.5b.

Due to these results and the limited time for the research project, it was decided to discontinue the interatrial shunt research through lumped element modeling, since a good baseline match between the reproduced model and literature could not be established. Still, these results serve as a proof of principle of using a lumped element model to simulate the body's circulatory system, as the shapes between the two results are clearly similar. However, for the lumped element model to be of any use to this research, also the values between the reproduced model and the model from Kaye et al. [30] should show a good match.

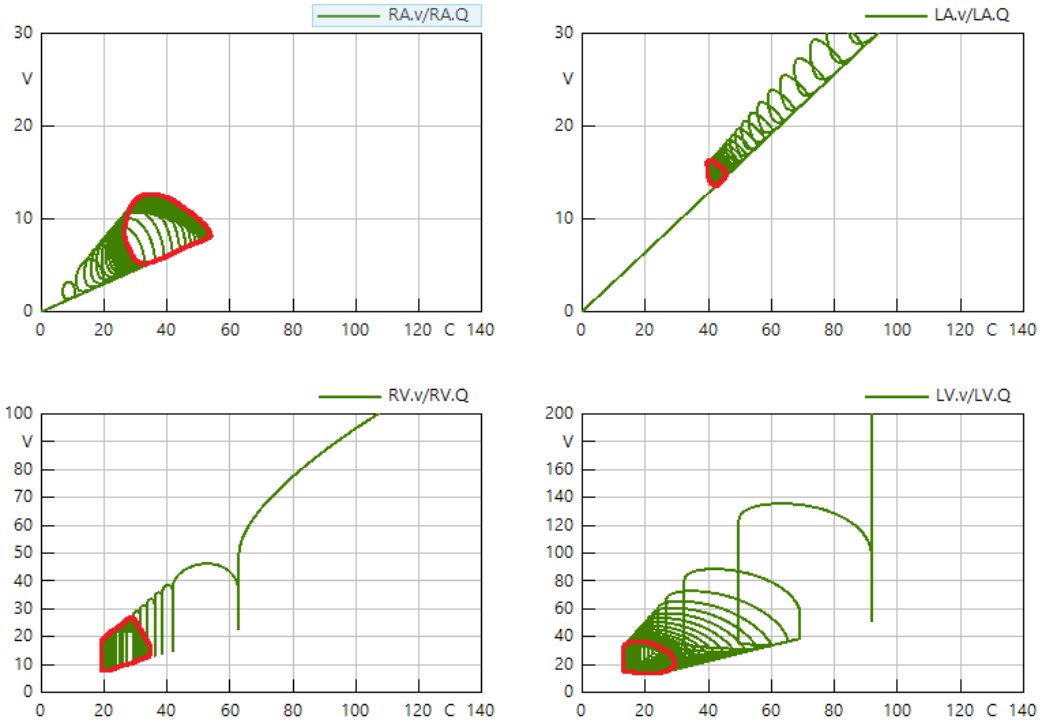

(a) Reproduced LEM

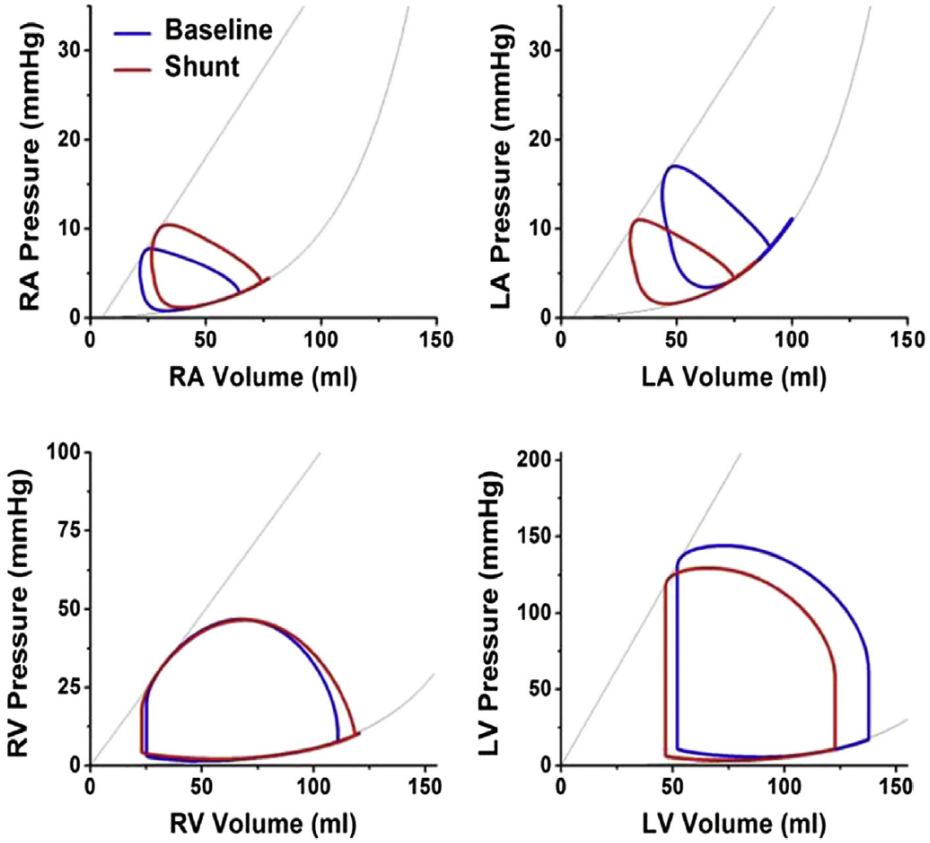

(b) Results from Kaye et al. [30]

Figure 3.5: Pressure-volume loops from the reproduced Lumped Element Model (LEM) in SimulationX (a) and from the research paper by Kaye et al. [30] for the four heart chambers

4

Computational Fluid Dynamics

As in chapter 3, the current chapter discusses *in silico* research into interatrial shunting. However, where the previous chapter considered 0D lumped element modeling, this chapter considers a two-dimensional modeling technique employing Computational Fluid Dynamics (CFD). For the theory behind CFD simulations and their application in cardiovascular research, the reader is referred to the literature report [37]. In this chapter, the setup of the model and its results are described for two-dimensional CFD simulations that are performed steady-state as well as transient, with a static as well as with a moving domain.

4.1. Geometry and conditions

The CFD simulations are performed using a two-dimensional Computer-Aided Design (CAD) model of the two atria of the human heart, see Figure 4.1. Though this geometry is clearly three-dimensional in reality, the choice is made for a two-dimensional computational domain to simplify the simulations. As will be shown in section 4.3, a complex system of equations is built around the computational domain to couple the inlet and outlet boundary conditions for the transient simulations. This system is much easier to implement and tune in a 2D model than in a 3D model, which drove the decision for a two-dimensional model. With the coupling system implemented in the 2D model, the extension to a 3D model can more easily be made in future work. This '2D assumption' affects the results in various ways, as will be discussed in chapter 5.

In three dimensions, the two atria combined are considered a sphere, separated by a wall of 1 mm thickness which represents the interatrial septum [17]. The volume of the sphere is based on the combined average volumes of the left and right atria of HFpEF patients according to Kaye et al. [30], which is 125 mL. This corresponds to a radius of 0.03 m. For the 2D simulations, a plane is defined perpendicular to the interatrial septum and passing through the center of the sphere. The 2D CAD model is the intersection of this plane with the sphere. The simulations are performed in the multiphysics simulation software COMSOL Multiphysics 6.1 [12], in which this intersection is extruded by 1 m for the simulations.

Two inlets are connected to the right atrium which represent the vena cavae, with the upper inlet representing the Superior Vena Cava (SVC) and the lower inlet representing the Inferior Vena Cava (IVC). The right atrium has an outlet at the bottom, which represents the Tricuspid Valve (TV). Four inlets are connected to the left atrium, representing the Pulmonary Veins (PVs). The left atrium also has an outlet at the bottom, which represents the Mitral Valve (MV). Note that the left atrium along with its inlets and outlets are shown on the right side in Figure 4.1 and vice versa. This convention is used throughout this report.

Inlet and outlet diameters are taken from a research paper by Kemmerling [31] and inlets/outlets connected to the right and left atria are spaced evenly over the right and left atrial walls, respectively. The inlet and outlet diameters as they are in 3D are scaled for the 2D CAD model. This is done by considering the ratio of inlet/outlet surface area to sphere surface area in the 3D model. The same ratio is applied in the 2D model to the inlet/outlet arc length to circle circumference. The real and scaled values of the inlet and outlet diameters are presented in Table 4.1. Finally, all inlets are extended by 10

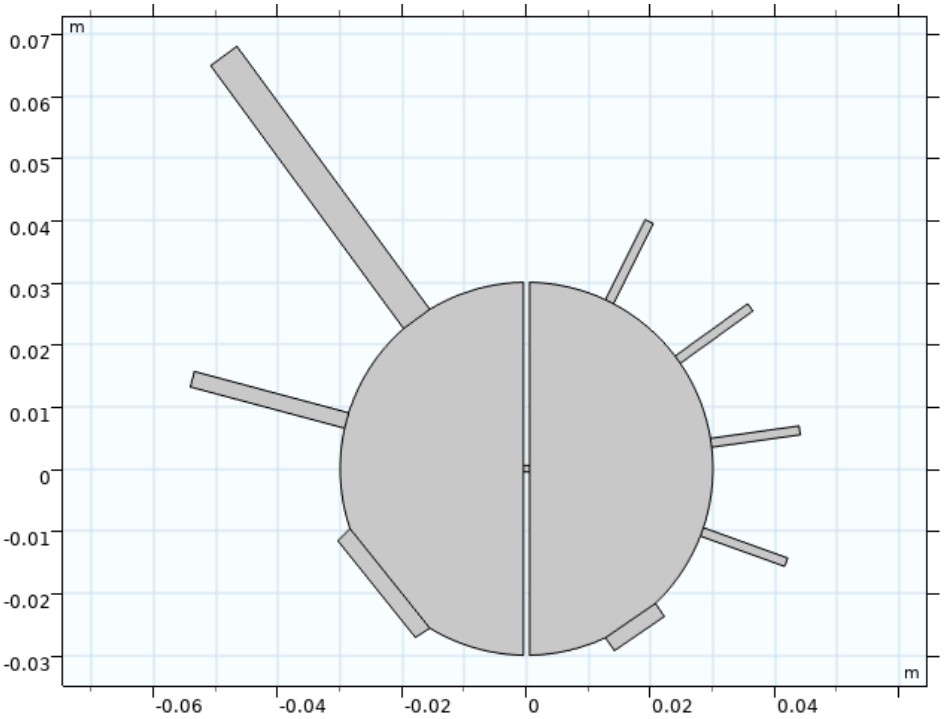

Figure 4.1: 2D double atrium geometry, featuring the right atrium on the left side of the image and the left atrium on the right side. The right atrium is connected to the Vena Cavae (VCe) and the Tricuspid Valve (TV). The left atrium is connected to the Pulmonary Veins (PVs) and the Mitral Valve (MV). The geometry also features an 8 mm interatrial shunt.

inlet diameters and all outlets are extended by a length of 2.5 mm, which represents the valve thickness [13, 27].

Domain	Opening	Real diameter (mm)	Scaled diameter (mm)
RA	SVC	20	5.24
	IVC	14	2.57
	TV	40	20.94
LA	MV	27.4	9.83
	PV	10.5	1.44
N/A	Shunt	8	1.07

Table 4.1: Real and scaled inlet, outlet and shunt diameters

For the simulations including an interatrial communication, an opening is introduced in the center of the interatrial septum. Similar to the scaling of the inlet and outlet diameters, also the shunt size is scaled for the 2D geometry. Here, the ratio of shunt surface area to interatrial septum surface area in 3D is considered. This ratio is then applied to the shunt length to septum length in 2D. Throughout this report, the shunt sizes refer to the three-dimensional sizes, i.e. as they would be in reality, unless mentioned otherwise. The default shunt size of 8 mm with its scaled size is included in Table 4.1.

The two-dimensional CFD simulations are performed in COMSOL Multiphysics 6.1 by solving the Reynolds-Averaged Navier-Stokes (RANS) equations, while turbulence is modeled by the k-ω turbulence model with wall functions. P1 + P1 fluid discretization is applied with consistent stabilization in the streamline and crosswind directions. Blood is assumed an incompressible, Newtonian fluid (see Appendix A) of density $\rho = 1050$ kg/m^3 and dynamic viscosity $\mu = 3.5$ mPa·s. A reference pressure of 1 atm ($1.01325 \cdot 10^5$ Pa) is used in all simulations.

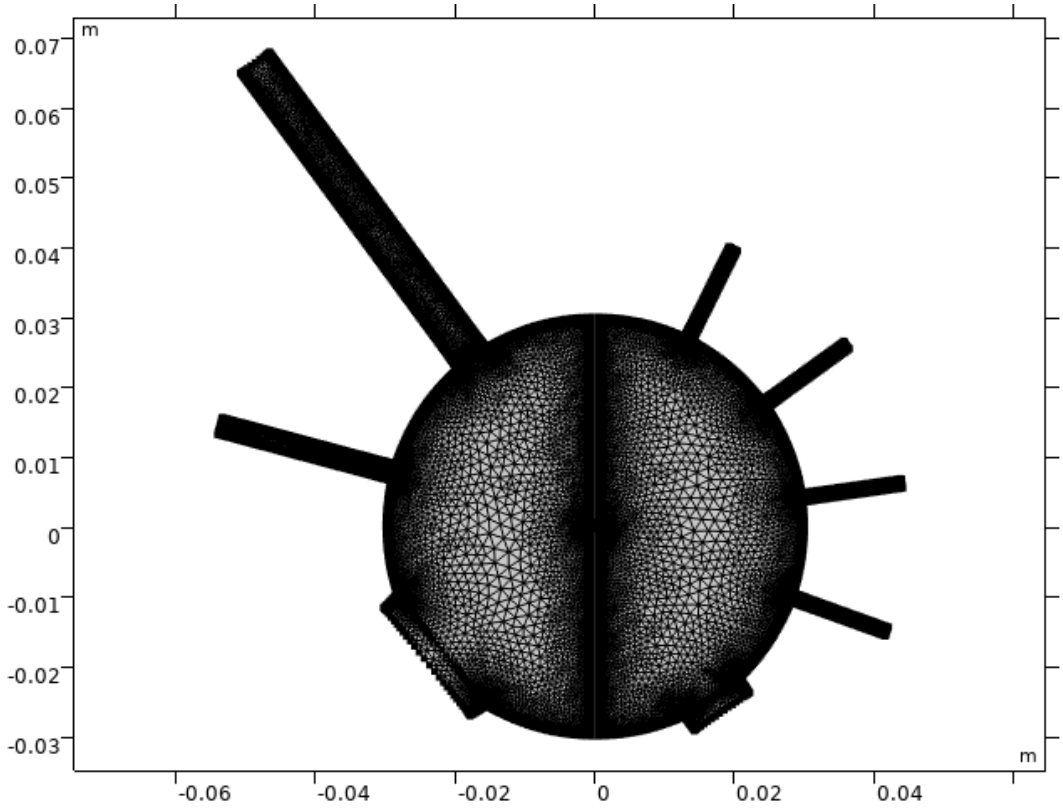

Figure 4.2: Mesh of the 2D double atrium geometry in presence of an 8 mm shunt

4.1.1. Discretization

Spatial

For the 2D double atrium geometry presented in Figure 4.1, a free triangular mesh is built. The core mesh has a maximum element size of 4.41 mm and a minimum element size of 0.196 mm with a maximum element growth rate of 1.15. Near the walls, the mesh is refined to obtain sufficient resolution of the boundary layer such that $y^+ = 1$. For the velocities encountered in the simulations, this is obtained with 5 cell layers with a maximum element size of 0.343 mm and a maximum element growth rate of 1.1, while the minimum element size is set to 0.0392 mm. The resulting mesh in presence of an 8 mm interatrial shunt is shown in Figure 4.2. Two close-ups of interesting mesh regions are shown in Figure 4.3, which show the mesh around the corner of the upper PV inlet (Figure 4.3a) and the 8 mm interatrial shunt (Figure 4.3b). In Appendix B, a mesh convergence and sensitivity study discusses the choice for the mesh that is used and presents an analysis of the error that is introduced in the results by the mesh.

Temporal

For the transient simulations that will be discussed in sections 4.3 and 4.4, the simulations also consider a temporal discretization. Adaptive time stepping is used through an implicit Backward Differentiation Formula (BDF) time-stepping method of first or second order. Therefore, the time step throughout a simulation is not constant. Rather, it is determined based on the convergence criteria during the simulation through a set relative tolerance. In COMSOL Multiphysics, the relative tolerance for all transient simulations is set to 0.005. This means that each time step is solved until the relative error is smaller than this value. In Appendix C, a study on the temporal discretization is presented.

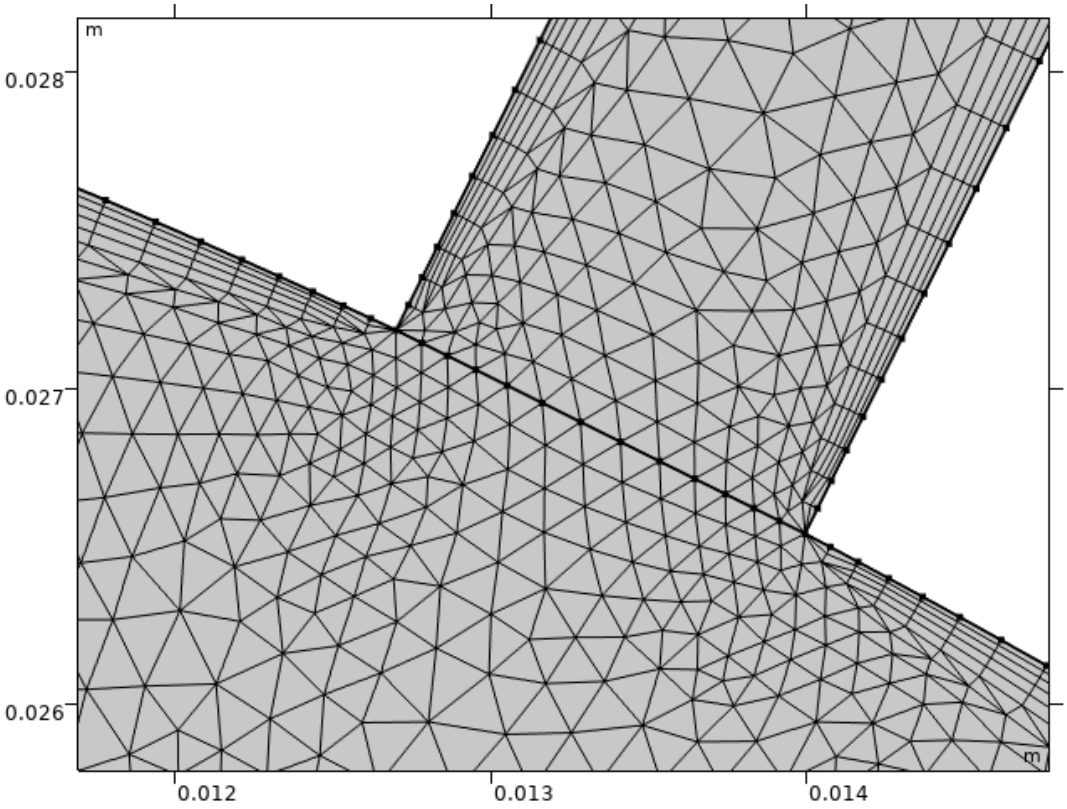

(a) Corner of upper PV inlet

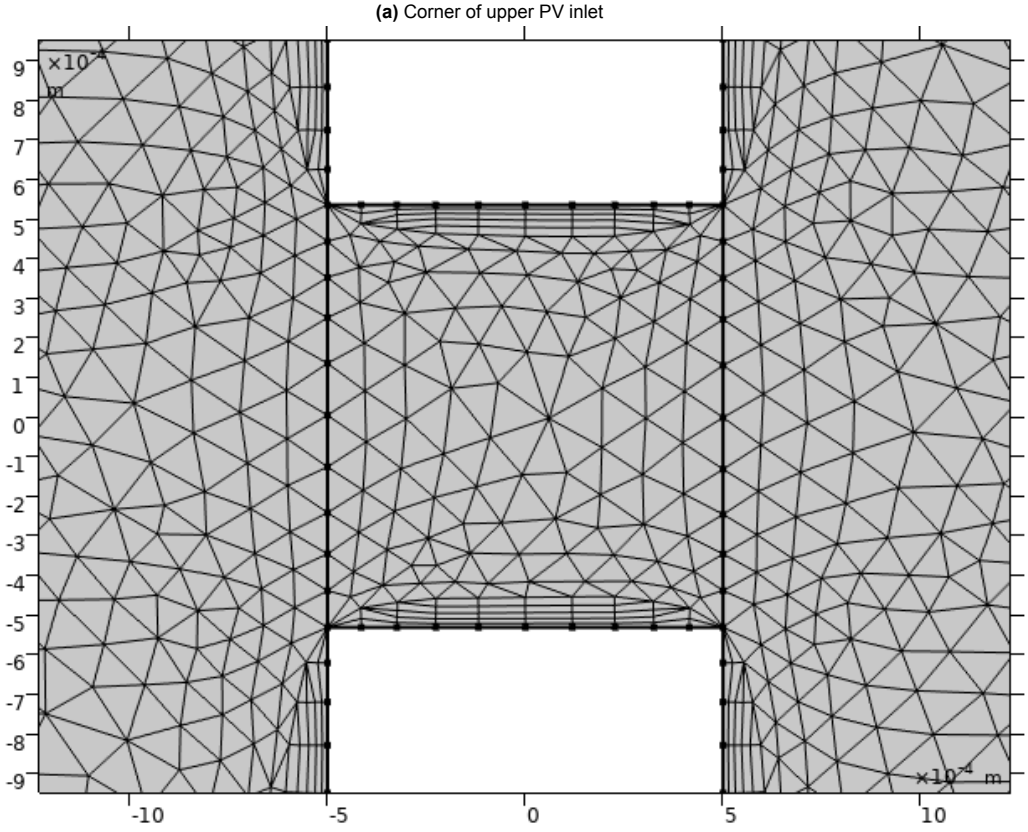

(b) 8 mm shunt

Figure 4.3: Close-up of two regions of the 2D double atrium mesh, showing the corner of the upper PV inlet (a) and the mesh around the interatrial shunt (b)

4.2. Steady-state

The steady-state CFD simulation considers the average situation during the phase of the heart cycle in which the atrioventricular valves are opened: the diastole. This phase is considered to quantitatively and qualitatively study the atrial flow field in which the largest velocity and pressure gradients are present, creating the most pronounced flow features. The inlets are described by velocities normal to the inlet with a fully developed flow profile and the outlets are described by average static pressures in the right and left ventricles for the TV and MV, respectively, as taken from Kaye et al. [30]. As the inlet diameters are scaled for the 2D geometry, the inlet velocities are scaled to equal the Reynolds numbers as provided by Kemmerling [31]. The boundary conditions of the steady-state simulation are presented in Table 4.2. Furthermore, the left atrium is assigned a pressure of 17 mmHg and the right atrium a pressure of 8 mmHg, as also taken from Kaye et al. [30]. Finally, the no-slip condition is applied to all the walls in the domain.

Domain	Inlet	Re_d	Real (m/s)	Scaled (m/s)	Outlet	Pressure (mmHg)
RA	SVC	674	0.13	0.43	TV	6
	IVC	1750	0.47	2.27		
LA	PV	904	0.33	2.09	MV	11

Table 4.2: Boundary conditions of the steady-state simulation

4.2.1. Results

Velocity field

In Figure 4.4, the velocity magnitude and streamlines of the steady-state simulation are presented. Figure 4.4a shows the results in absence of an interatrial shunt. In the right atrium, it can be seen that the two jets from the vena cavae merge as they flow towards the outlet, the tricuspid valve. Close to the interatrial septum, a big recirculation zone of low velocity is visible. Also between the two vena cavae and below the inferior vena cava, recirculation zones are present. In the left atrium, the jets from the four pulmonary veins achieve a more equal spread of the velocity magnitude compared to the right atrium, as less of a recirculation zone near the interatrial septum is present. As in the right atrium, the inlet jets merge as they flow towards the outlet valve. In between each of the PVs, two counter-rotating recirculation zones are found, whereas this is not seen in the right atrium.

When a shunt of 8 mm is introduced, the flow field is significantly altered, as shown in Figure 4.4b. The interatrial communication allows blood to flow from the left atrium through the interatrial septum into the right atrium. The flow from the upper two pulmonary veins seems to be mostly responsible for this shunt flow, as these merge and flow past the interatrial septum. The jets from the two lower PVs cause a recirculation zone in the bottom half of the left atrium and flow into the mitral valve outlet. Compared to the situation without the shunt, the two counter-rotating recirculation zones between each of the PVs are still present in the left atrium. It can also be seen that the recirculation zones between the two middle pulmonary veins have moved inwards. This happens as the jets from the upper two pulmonary veins are now directed towards the shunt, making room for a larger recirculation zone between the middle two pulmonary veins. In turn, the recirculation zone in the upper corner of the left atrium near the interatrial septum has vastly reduced its size, as have the two counter-rotating zones between the lower two PVs. In the right atrium, the flow field in the upper half has vastly remained the same, whereas the shunt flow has had a profound effect on the bottom half of the domain. The large recirculation zone near the interatrial septum has been divided in two by the jet through the interatrial communication. A new, smaller, recirculation zone is now present between the shunt jet and the interatrial septum. Furthermore, the shunt flow has slightly moved the jet emanating from the IVC to make room for the shunt flow entering the TV. This has also reduced the size of the recirculation zone between the IVC and the tricuspid valve.

Flow rates

In absence of a shunt, the flow rate through the heart valve is equal to the flow rates through the inlets of the atrium in question. This is because the current model assumes incompressible flow and rigid walls without movement. Therefore, the flow rate through the TV equals the flow rates through the SVC and IVC, and the flow rate through the MV equals the flow rates through the PVs. In this

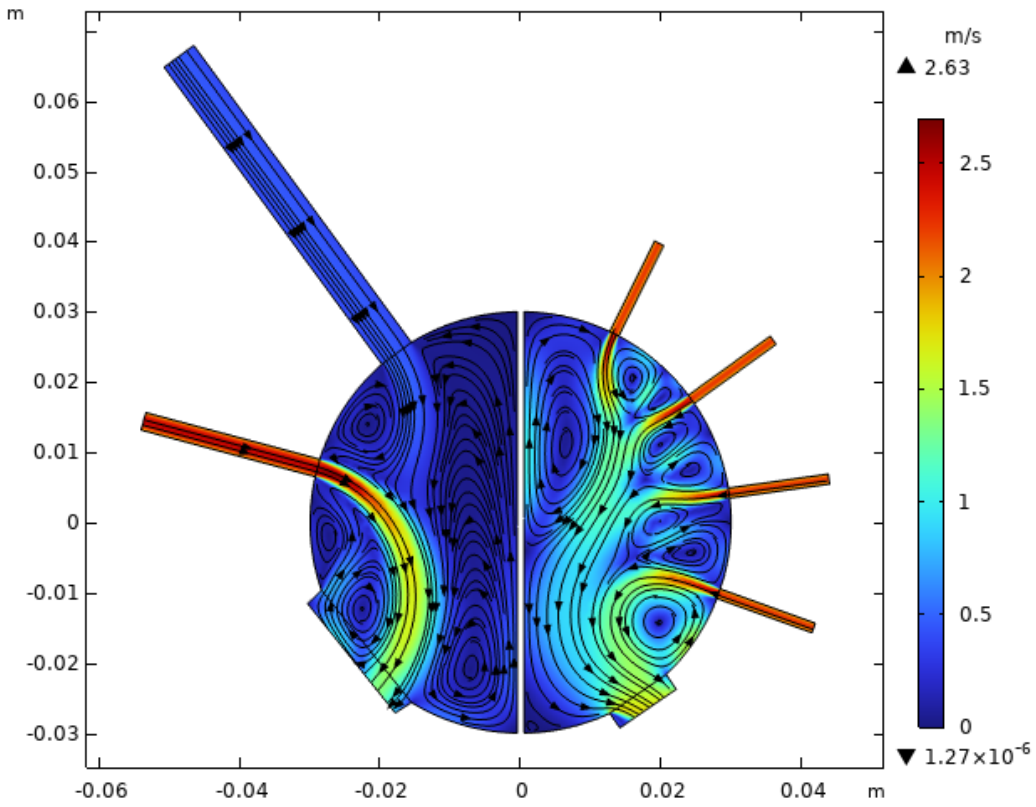

(a) Without shunt

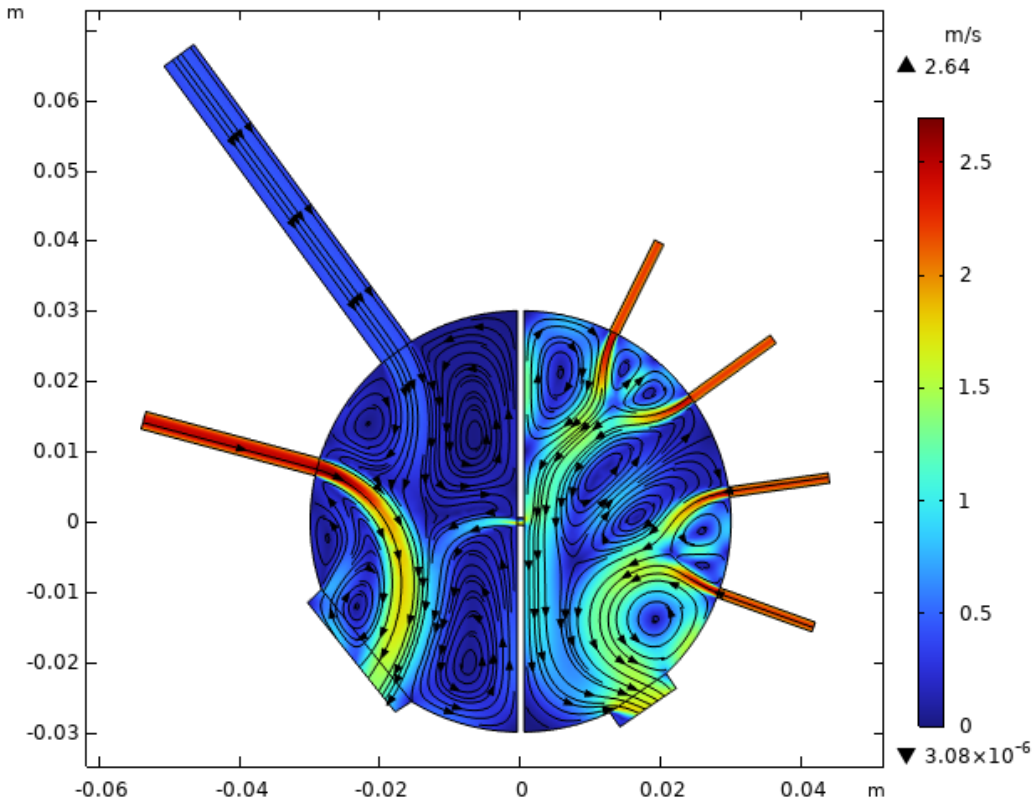

(b) 8 mm shunt

Figure 4.4: Velocity field of the steady-state CFD simulation in absence (a) and presence (b) of an 8 mm shunt

				No shunt		8 mm shunt	
Domain	**Inlet**	**Flow rate (10^{-3} m^3/s)**	**Outlet**	**Flow rate (10^{-3} m^3/s)**	Qp:Qs	**Flow rate (10^{-3} m^3/s)**	**Qp:Qs**
RA	SVC	2.25	TV	8.08	0.67	9.10	0.83
	IVC	5.83					
LA	PVs	3.01	MV	12.04		11.02	

Table 4.3: Flow rates and Qp:Qs ratios of the steady-state CFD simulation in absence and presence of an 8 mm shunt

simulation, the flow rate through the SVC equals $U \cdot d \cdot 1$ [m] $= 0.43 \cdot 5.24 \cdot 10^{-3} \cdot 1 = 2.25 \cdot 10^{-3}$ m^3/s, where the values for U and d are taken from Table 4.2 and Table 4.1, respectively. Similarly, the flow rate through the IVC is $5.83 \cdot 10^{-3}$ m^3/s, which means that the flow rate through the TV equals $2.25 \cdot 10^{-3} + 5.83 \cdot 10^{-3} = 8.08 \cdot 10^{-3}$ m^3/s. Note that these values should not directly be compared to realistic values, as the values from the CFD simulations significantly differ from reality due to the 1 meter extrusion of the computational domain. In the left side of the heart, the flow rate through one pulmonary vein is $2.09 \cdot 1.44 \cdot 10^{-3} \cdot 1 = 3.01 \cdot 10^{-3}$ m^3/s, so the flow rate through all four pulmonary veins and therefore through the mitral valve is $4 \cdot 3.01 \cdot 10^{-3} = 12.04 \cdot 10^{-3}$ m^3/s. In reality, the flow rates through the two heart valves are equal, as the blood circulation is a closed system. In other words, what flows through the tricuspid valve at one point, will flow through the mitral valve later. This means that the ratio of pulmonary to systemic blood flow, the Qp:Qs ratio, is equal to unity. In this simulation, however, the flow rates do not match and Qp:Qs = 0.67. This is because the inlet diameters have been scaled for the 2D geometry and the inflow velocities have been scaled to equal the inflow Reynolds numbers. As the scaling of the inlets considers a quadratic relationship, whereas the Reynolds scaling considers a linear relationship, a mismatch occurs in the flow rates.

When a shunt is introduced between the two atria, part of the flow rate into one of the atria is shunted to the other atrium. This increases the flow rate through one of the heart valves, whereas the flow rate through the other valve decreases by the same amount. As this simulation shows a shunt from the left atrium to the right atrium, the flow rate through the tricuspid valve increases and the mitral valve flow rate decreases. From the simulation, a flow rate of $11.02 \cdot 10^{-3}$ m^3/s is found through the mitral valve and a flow rate of $9.10 \cdot 10^{-3}$ m^3/s is found through the tricuspid valve. This makes the ratio of pulmonary to systemic blood flow (Qp:Qs) equal to 0.83, which is 24% higher than in absence of the shunt. Considering Qp:Qs = 1 in absence of a shunt in reality, this simulation would indicate that Qp:Qs = 1.24 in presence of an 8 mm interatrial shunt. Also note that $11.02 \cdot 10^{-3} + 9.10 \cdot 10^{-3} = 20.12 \cdot 10^{-3}$ m^3/s, which is equal to $8.08 \cdot 10^{-3} + 12.04 = 20.12 \cdot 10^{-3}$ m^3/s found in the absence of a shunt, such that the flow rate exiting the domain is conserved.

The presented results are summarized in Table 4.3.

Pressure field

Figure 4.5 presents the pressures throughout the two atria, again in absence (Figure 4.5a) and presence (Figure 4.5b) of an 8 mm interatrial shunt. In Figure 4.5a, it can be seen that the highest pressures are found in the PV inlets. In the left atrium, the highest pressure is found near the interatrial septum, whereas the region closer to the wall shows a lower pressure. This is in accordance with the observations made on the velocity field, as the recirculation zones are expected to be of lower pressure. In contrast to the pulmonary veins, the vena cavae connected to the right atrium show a significant pressure difference, with the inferior vena cava having a higher pressure than the superior vena cava. The pressure in the right atrium itself is fairly constant and seemingly equal to the SVC pressure. One thing to point out, however, is the region of low pressure between the IVC and the TV, which corresponds to the recirculation zone seen in Figure 4.4a. In absence of a shunt, the average left atrial pressure is 16.0 mmHg, whereas the average right atrial pressure is 5.66 mmHg.

The introduction of the 8 mm shunt alters the pressure field in the atria, as can be seen in Figure 4.5b. The most noteworthy difference compared to the case without shunt are the shifts in high and low pressure zones in the left atrium. These correspond to the zones of recirculation pointed out in the velocity field, with the regions between the pulmonary veins showing structures of relatively low pressure. Also the region near the mitral valve and a smaller region near the upper pulmonary vein stand out in the pressure field of the left atrium. In the right atrium, the upper half has remained approximately unchanged, as was also noted in the velocity field. The bottom half, however, shows two small differences compared to the situation without the interatrial communication. As discussed previously, the shunt flow through the interatrial septum creates a new region of recirculation in the lower part

of the right atrium. This region is a darker shade of blue as it has a slightly lower pressure pressure than the rest of the atrium. Another effect that the shunt has on the pressure field in the right atrium was also noted previously, as the jet from the IVC has had to make some room for the jet through the interatrial septum. This has slightly limited the space for the recirculation zone between the IVC and the TV, which can also be seen in the pressure field. The 8 mm interatrial shunt has slightly lowered the average left atrial pressure, which is now 15.8 mmHg. On the other hand, it has even more slightly increased the right atrial pressure to 5.70 mmHg.

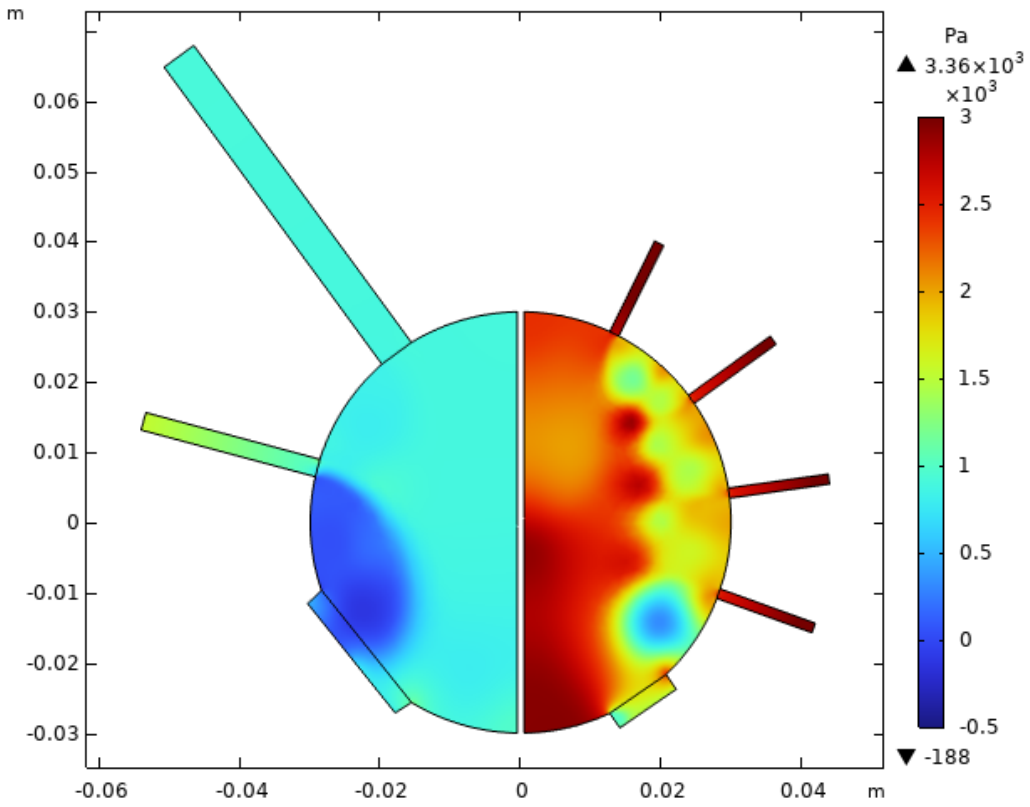

(a) Without shunt

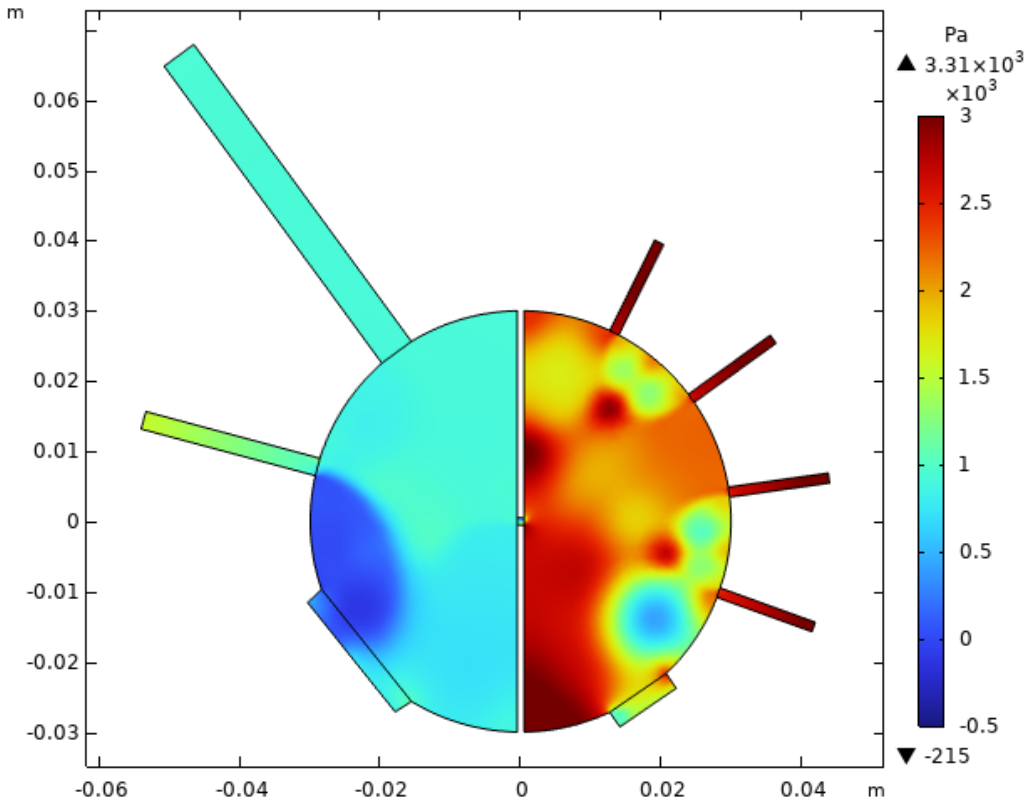

(b) 8 mm shunt

Figure 4.5: Pressure field of the steady-state CFD simulation in absence (a) and presence (b) of an 8 mm shunt

4.3. Transient

The transient CFD simulation uses the same geometry as the steady-state simulation (see Figure 4.1), but applies time-dependent boundary conditions, resulting in a transient flow field. A heart rate of 60 beats per minute is considered, so one heart cycle takes one second. The diastole is assumed to last for 2/3 of the cardiac cycle, with the systole completing the other 1/3 [31]. During the systole, the heart valves are closed, which is modeled by locally and temporarily increasing the viscosity to 10^8 Pa·s in the small domains in front of the outlets. This prevents fluid from passing through the outlet valves during the systolic phase of the heart cycle. The changes in viscosity take 60 ms, representing the time it takes for the atrioventricular valves to open and close [13, 42].

Furthermore, the inlets and outlets are all described by static pressures, which are coupled through a Windkessel (see Figure 4.6). The blood flow through each outlet valve is stored in a virtual reservoir, representing the ventricle (RV or LV). This increase in volume linearly raises the pressure in this reservoir through the definition of an elastance (units mmHg/m^3) and this pressure is prescribed at the outlet of the domain. During the systole, when the atrioventricular valves are closed, the volume from the ventricle is released into another virtual reservoir, representing the systemic (S) or pulmonary (P) blood circulation. This reduces the pressure in the ventricle while increasing it in the blood circulation. The pressure of the latter is prescribed at the inlets on the respective side of the heart, which drives the blood into the atria and in turn decreases the pressure in the reservoir. The blood has now returned to the atria, which is where it started. Hence, this Windkessel coupling between the inlets and outlets represents the closed-loop behavior of the circulatory system.

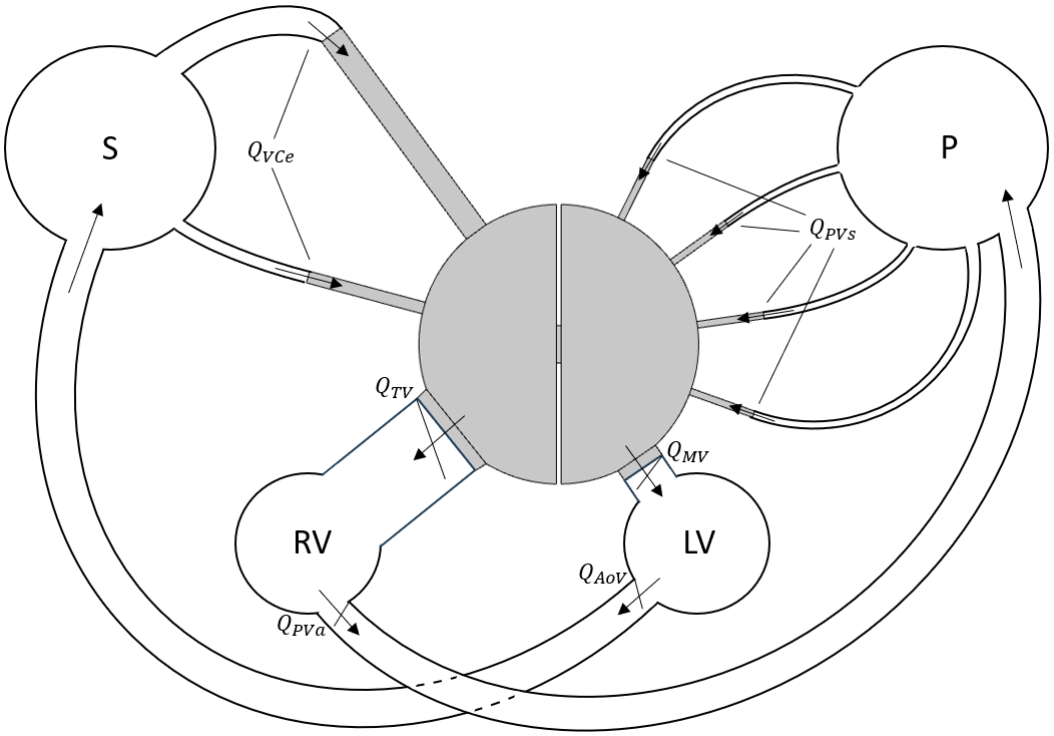

Figure 4.6: Graphical representation of the Windkessel coupling between the inlets and outlets of the double-atrium geometry. AoV, Aortic Valve; LV, Left Ventricle; MV, Mitral Valve; P, Pulmonary circulation; PVa, Pulmonary Valve; PVs, Pulmonary Veins; RV, Right Ventricle; S, Systemic circulation; TV, Tricuspid Valve; VCe, Vena Cavae.

In a mathematical formulation, the Windkessel coupling is described by four Ordinary Differential Equations (ODEs) and four linear equations. Two ODEs are used to determine the volumes of the two ventricles as follows:

$$\frac{dV_{LV}}{dt} = Q_{MV} - Q_{AoV}, \tag{4.1a}$$

$$\frac{dV_{RV}}{dt} = Q_{TV} - Q_{PVa}, \tag{4.1b}$$

where V_{LV} and V_{RV} are the volumes in m^3 of the left and right ventricles, respectively. Q_{MV}, Q_{AoV}, Q_{TV} and Q_{PVa} are the flow rates entering and leaving the ventricles in m^3/s through the mitral, aortic, tricuspid and pulmonary valve, respectively. Note that the Pulmonary Valve (PVa) is not to be confused with the Pulmonary Vein (PV) or its plural (PVs) mostly used in this report. Also, whereas Q_{MV} and Q_{TV} follow from the simulation, Q_{AoV} and Q_{PVa} are set functions of time. All the volume in the ventricle is namely released during the systolic phase of the heart cycle. The equations for Q_{AoV} and Q_{PVa} are:

$$Q_{AoV} = C(t) \cdot V_{LV_{ED}}, \tag{4.2a}$$

$$Q_{PVa} = C(t) \cdot V_{RV_{ED}}, \tag{4.2b}$$

where the subscript ED indicates the volume at the end of diastole. This is the moment when the volume of the ventricle is at its maximum, the atrioventricular valves close and the systole commences. $C(t)$ is a time-dependent coefficient in 1/s that determines the amount of flow rate through the valves towards the systemic and pulmonary circulations. During the first 2/3 of the heart cycle, the diastole, $C(t) = 0$ and blood only enters the ventricle, but does not leave. Only during the last 1/3 of the heart cycle, the systole, $C(t)$ is nonzero and the volume from the ventricle is released into the blood circulation. The function for $C(t)$ was derived from Lumens et al. [35] and looks as follows:

$$C(t) = \begin{cases} 0, & \text{if } 0 < t < 2/3 \\ 3 \cdot \cos(6\pi t - \pi) + 3, & \text{if } 2/3 \leq t \leq 1. \end{cases} \tag{4.3}$$

Note that $\int_{2/3}^{1} (3 \cdot \cos(6\pi t - \pi) + 3)\, dt = 1$, such that all the volume that has entered the ventricle during the diastole exits the ventricle during the systole.

From the ventricle volumes in Equation 4.1, the following two linear equations determine the pressures in the ventricles and therefore the outlet pressures:

$$P_{LV} = V_{LV} \cdot E_{LV} + P_{LV_0}, \tag{4.4a}$$

$$P_{RV} = V_{RV} \cdot E_{RV} + P_{RV_0}, \tag{4.4b}$$

with P_{LV} and P_{RV} the pressures in mmHg of the left and right ventricles, respectively. E_{LV} and E_{RV} are the elastances in mmHg/m^3 of the left and right ventricles, respectively, which determine how much the pressures rise for a given rise in volume. Finally, P_{LV_0} and P_{RV_0} are the pressures of the left and right ventricles at the start of the simulation, respectively.

Considering the volumes of the reservoirs representing the systemic and pulmonary circulations, another two ODEs similar to Equation 4.1 are implemented in the model:

$$\frac{dV_S}{dt} = Q_{AoV} - Q_{VCe}, \tag{4.5a}$$

$$\frac{dV_P}{dt} = Q_{PVa} - Q_{PVs}. \tag{4.5b}$$

In this case, V_S and V_P are the volumes in m^3 of the systemic and pulmonary reservoirs, respectively. Q_{AoV} and Q_{PVa} are the previously-introduced flow rates leaving the ventricles that are now entering the reservoirs. Q_{VCe} and Q_{PVs} are the inlet flow rates in m^3/s through the vena cavae and pulmonary veins, respectively.

Similar to Equation 4.4, the final two linear equations describing the Windkessel system are responsible for the pressures in the systemic and pulmonary reservoirs and hence for the inlet pressures:

$$P_S = V_S \cdot E_S + P_{S_0}, \tag{4.6a}$$

$$P_P = V_P \cdot E_P + P_{P_0}, \tag{4.6b}$$

with P_S and P_P the pressures in mmHg of the systemic and pulmonary reservoirs, respectively, E_S and E_P the systemic and pulmonary elastances in mmHg/m^3, respectively, and P_{S_0} and P_{P_0} the pressures of the systemic and pulmonary reservoirs at the start of the simulation, respectively.

With the Windkessel coupling implemented in the model, ten parameter values are required. Equation 4.4 requires the initial pressures of the ventricles, P_{LV_0} and P_{RV_0}, along with the elastances of the left and right ventricles, E_{LV} and E_{RV}. Similarly, Equation 4.6 requires the initial pressures of

the reservoirs, P_{S_0} and P_{P_0}, along with the systemic and pulmonary elastances, E_S and E_P. As in the steady-state simulations, also initial values for the left and right atrial pressures are set (P_{LA_0} and P_{RA_0}, respectively). For the transient simulations, P_{LA_0} and P_{RA_0} are set equal to the initial pressures of the pulmonary and systemic reservoirs, respectively. These initial pressures as well as the elastances have been adapted iteratively to achieve physically relevant inlet and outlet pressures throughout the cardiac cycle that correspond to data from Lumens et al. [35]. The required parameters and their values are presented in Table 4.4.

Domain	Parameter	Value
Pulmonary	E_P	1700 mmHg/m^3
	P_{P_0}	20 mmHg
LA	P_{LA_0}	20 mmHg
LV	E_{LV}	1540 mmHg/m^3
	P_{LV_0}	5.6 mmHg
Systemic	E_S	525 mmHg/m^3
	P_{S_0}	2 mmHg
RA	P_{RA_0}	2 mmHg
RV	E_{RV}	830 mmHg/m^3
	P_{RV_0}	-0.1 mmHg

Table 4.4: Parameter values for the transient simulation

From a simulation of five cardiac cycles, it was concluded that the results have converged after three cardiac cycles. This was found from an analysis of the peaks and troughs of the systemic and pulmonary reservoir pressures, as shown in Figure 4.7. The peak-to-peak and trough-to-trough differences are presented in Table 4.5. In these results, the initial condition is taken as the first peak. As all the differences are below 1% after three cycles, i.e. between peaks and troughs 4-5, the fourth cardiac cycle is deemed to provide results of sufficient accuracy and will therefore be used in the following analyses.

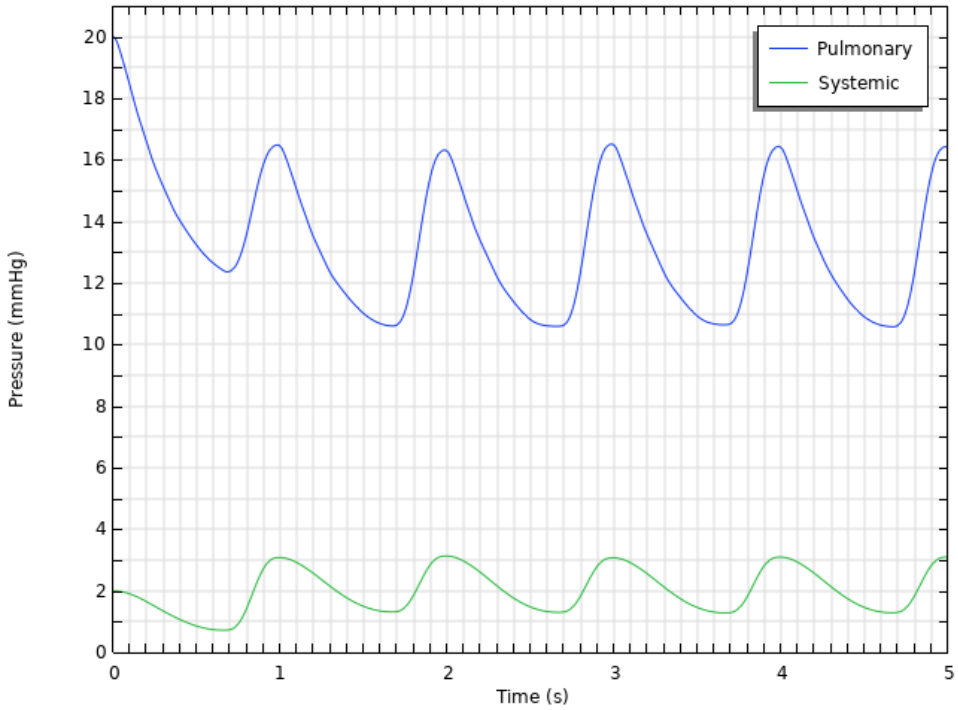

Figure 4.7: Convergence of the systemic and pulmonary reservoir pressures over five cardiac cycles for a simulation in absence of an interatrial shunt

Reservoir	Heart cycle	Difference in peaks	Difference in troughs
Pulmonary	1-2	17.6%	14.5%
	2-3	1.00%	0.05%
	3-4	1.19%	0.47%
	4-5	0.48%	0.61%
Systemic	1-2	54%	83%
	2-3	1.69%	0.84%
	3-4	1.88%	1.46%
	4-5	0.75%	0.39%

Table 4.5: Convergence of the systemic and pulmonary reservoir pressures over five cardiac cycles for the transient simulation in absence of an interatrial shunt

4.3.1. Results

Velocity field

Figures 4.8 to 4.10 show the progression of the velocity field over the cardiac cycle in absence (a) and presence (b) of an 8 mm interatrial shunt. Figure 4.8 shows the moment halfway through the diastole ($t = 0.35$ s), Figure 4.9 shows the moment at the end of diastole ($t = 0.65$ s) just before the atrioventricular valves close, and Figure 4.10 shows the moment at the end of systole ($t = 0.95$ s) just before the valves open again.

Figure 4.8 shows a similar flow field as shown in section 4.2 in Figure 4.4 for the steady-state simulation. This is because the steady-state simulation represents the average flow field during the diastole, when the valves are open. Similar flow features can be distinguished, such as the jets from the inlets merging towards the outlets and the recirculation zones in the corners of the atria and between the inlets. A significant difference between the steady-state and transient flow fields, however, is that the jets from the steady-state simulation are much more straight-lined than in the transient simulation. This shows the unsteady behavior of the flow, as a single moment can differ greatly from the average situation. Furthermore, note the big difference in velocity magnitudes of around 1 m/s between the steady-state and transient flow fields. The origin of this difference lies in the geometry being two-dimensional, which necessitated scaled inlet diameters. As the inlets in the steady-state simulation are described by velocities that have been scaled to achieve realistic Reynolds numbers, i.e. higher velocities, the inlet pressures in the steady-state simulations (Figure 4.5) are unrealistically high. These pressures should namely not exceed 15 mmHg in the simulated conditions [46]. On the other hand, the inlets in the transient simulation are described by realistic static pressures that therefore result in lower velocities and Reynolds numbers. The exception to this is the upper inlet to the right atrium, the superior vena cava, which shows a higher velocity magnitude in the current simulation compared to the steady-state simulation. This is because the transient simulation assumes equal inlet pressures between the two vena cavae [35], whereas the steady-state simulation sets a much lower velocity for the SVC than for the IVC, as Kemmerling [31] assumes a low Reynolds number for the SVC. As a result, the SVC has a much bigger influence on the right atrial flow field in the current simulation than in the steady-state simulation. It now produces a jet of higher velocity magnitude that manages to reach further into the atrium, which decreases the size of the big recirculation zone near the interatrial septum that was seen in Figure 4.4a.

As the diastole continues, blood from the systemic and pulmonary circulations moves via the atria, through the atrioventricular valves into the ventricles. This reduces the volume and pressure in the systemic and pulmonary reservoirs and increases the volume and pressure in the left and right ventricles, therefore reducing the pressure difference between the in- and outlets of the atria. This results in a decrease in inlet velocities through the diastole, which can be seen in Figure 4.9. Here, the velocity field is shown at the end of the diastolic phase of the cardiac cycle, moments before the valves close and the systole starts. It can be seen that velocity magnitudes have largely died out, apart from the shunt flow in Figure 4.9b. This indicates that the intra-atrial pressure gradients have largely vanished, whereas an interatrial pressure gradient is still present. From the inlet jets, only the SVC still has a significant contribution to the atrial flow field, which is likely because of its size, carrying more momentum than the smaller inlet veins. This imbalance between the SVC and IVC causes reversed flow through the latter, both with and without a shunt. This behavior is not seen in the left atrium, as all inlet veins have the same diameter and carry approximately the same momentum.

When the mitral and tricuspid valves close, the systole begins and the ventricles contract, ejecting the volumes from the left and right ventricles into the systemic and pulmonary circulations, respectively. In contrast to the diastole, the systemic and pulmonary reservoirs are now being filled with blood, increasing their pressures and therefore the pressures at the inlets of the atria. Although the inlet pressures are increasing, the outlet valves are closed, which creates a stagnant flow field in the atria in absence of an interatrial communication (Figure 4.10a). However, this phase of the heart cycle is arguably where a shunt makes the biggest difference in terms of the flow field, as can be seen in Figure 4.10b. Because there is a big pressure gradient between the pulmonary veins and the vena cavae, and the interatrial shunt allows a communication between the two, blood starts to flow from the high pressure pulmonary veins into the lower pressure vena cavae. This causes reversed flow through the vena cavae, filling the systemic reservoir further, rather than emptying it. In Figure 4.10b, the jets from the four pulmonary veins can be seen to merge into one jet that contracts through the interatrial communication, increasing its velocity magnitude. In the right atrium, this jet flows towards the lower of the two vena cavae, the IVC, where a part splits off that flows towards the SVC. This shunt jet splits the right atrium into two, resulting in two counter-rotating recirculation zones in the lower half of the right atrium and one big recirculation zone in the upper half. Also the lower half of the left atrium is characterized by a stagnant flow field, as Figure 4.10b shows one big recirculation zone of low velocity magnitude in this area. The biggest recirculation zones, however, are found in absence of a shunt, as Figure 4.10a shows. These flow fields in the right and left atria are the result of the flow fields at the end of the diastole (Figure 4.9a), just before the valves close. After closure of the valves, blood no longer flows in or out of the atria and the velocity magnitudes fall as momentum is dissipated through viscosity. This leaves two recirculation zones that span almost the entire atria.

In reality, however, blood does still enter the atria during the systole, as the atria expand during this phase of the cardiac cycle. Therefore, the flow field discussed in this section is largely an artefact of the assumption of the current simulation that the geometry does not deform. This means that the current simulation underestimates the velocity magnitudes in the atria during the systole, which will be shown in section 4.4.

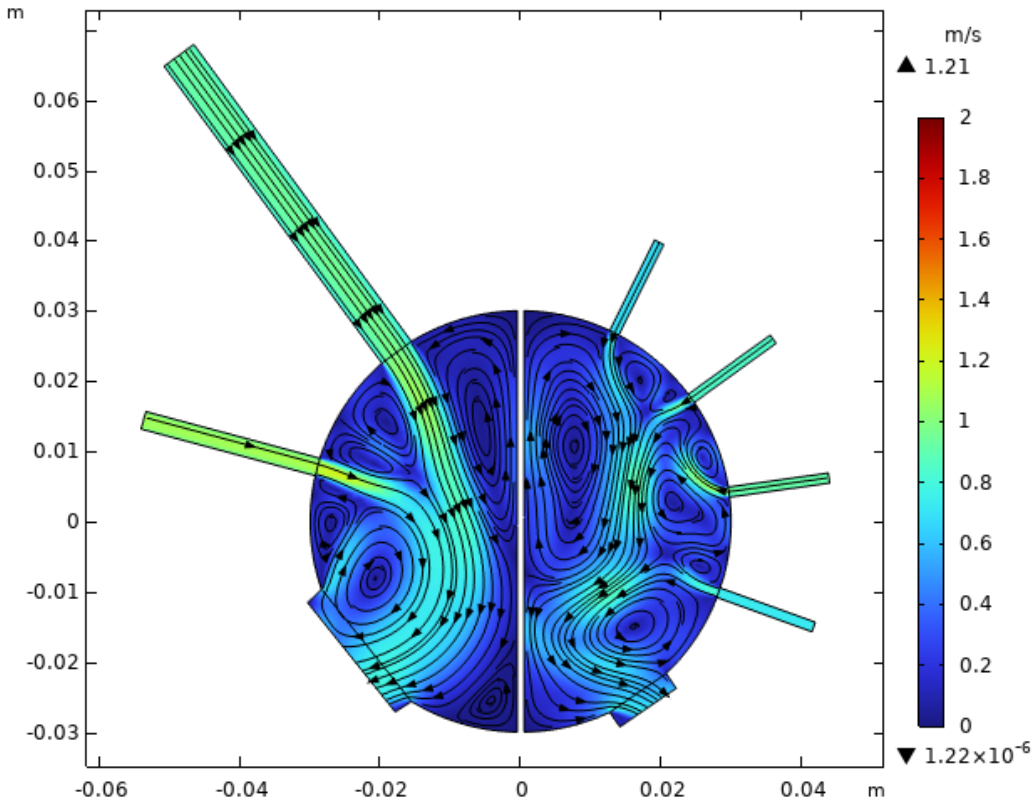

(a) Without shunt

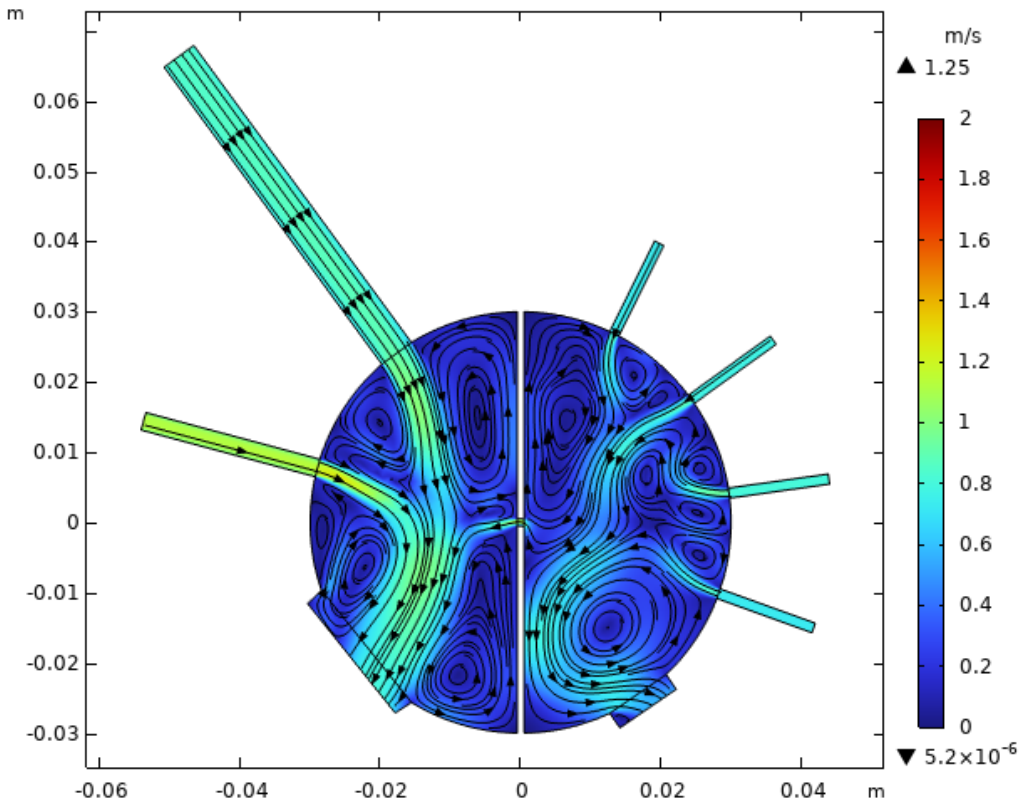

(b) 8 mm shunt

Figure 4.8: Velocity field of the transient CFD simulation halfway through the diastole ($t = 0.35$ s) in absence (a) and presence (b) of an 8 mm shunt

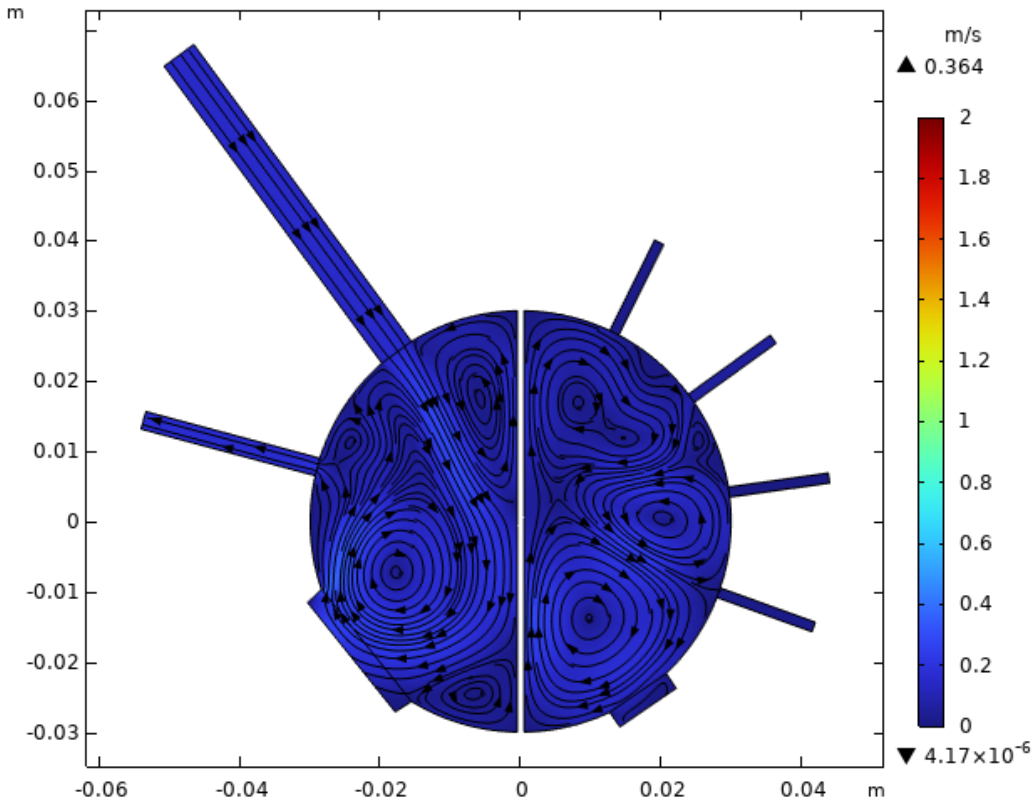

(a) Without shunt

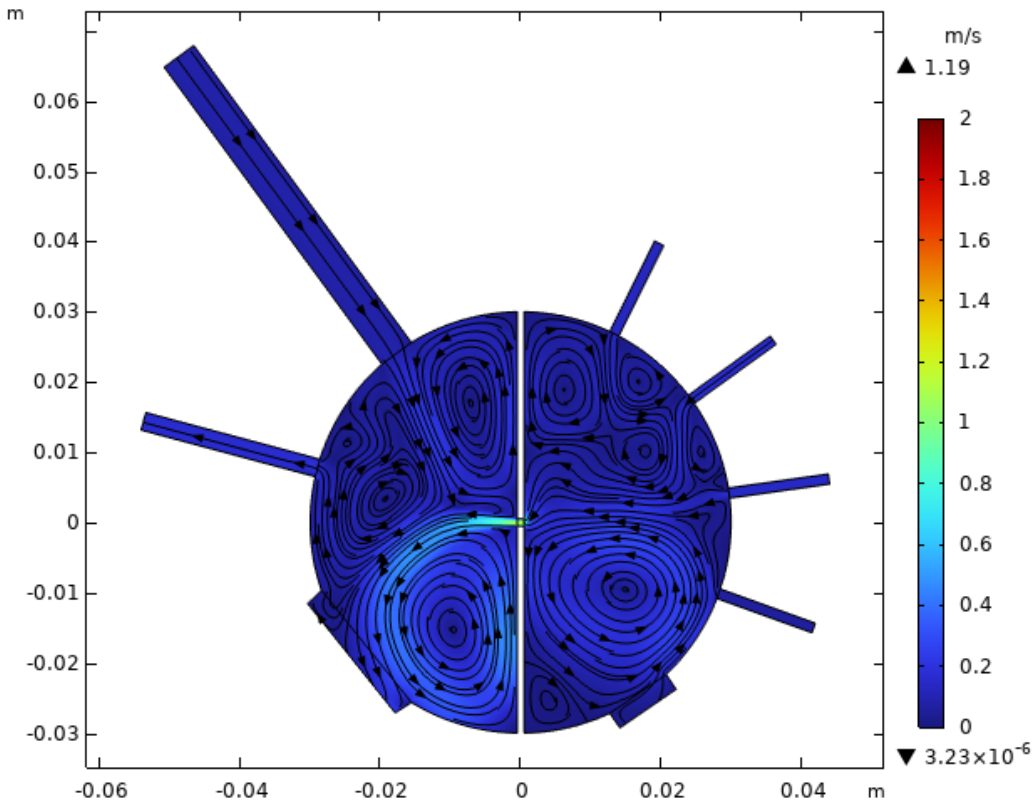

(b) 8 mm shunt

Figure 4.9: Velocity field of the transient CFD simulation at the end of diastole ($t = 0.65$ s) in absence (a) and presence (b) of an 8 mm shunt

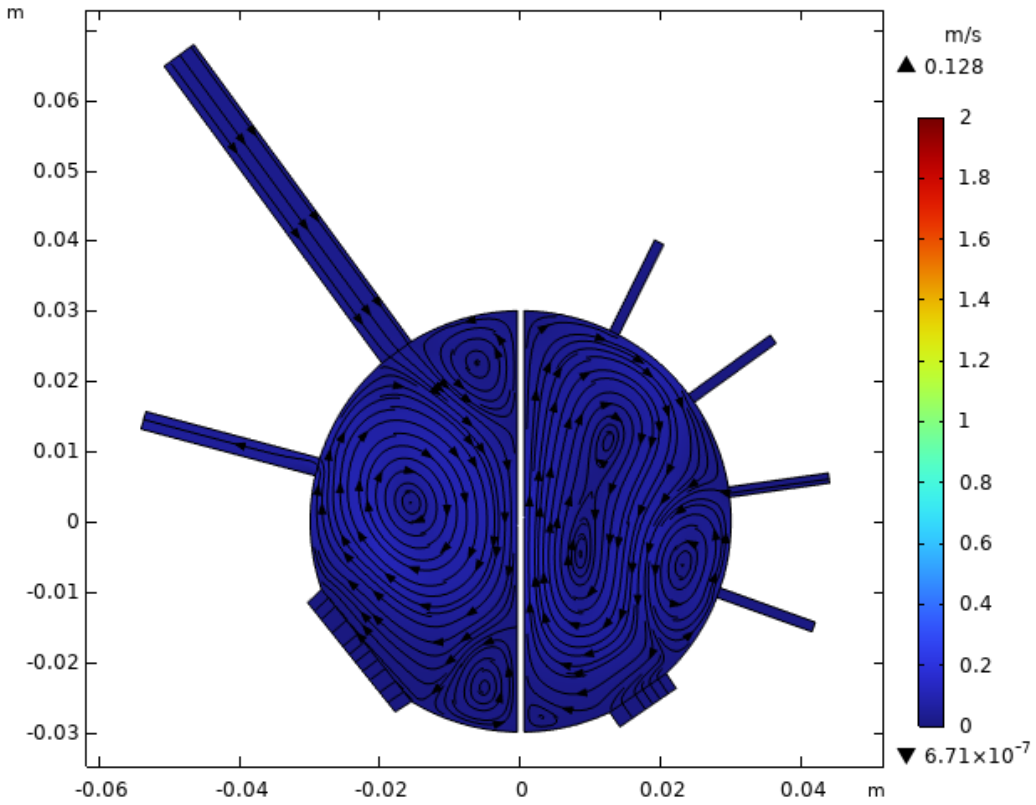

(a) Without shunt

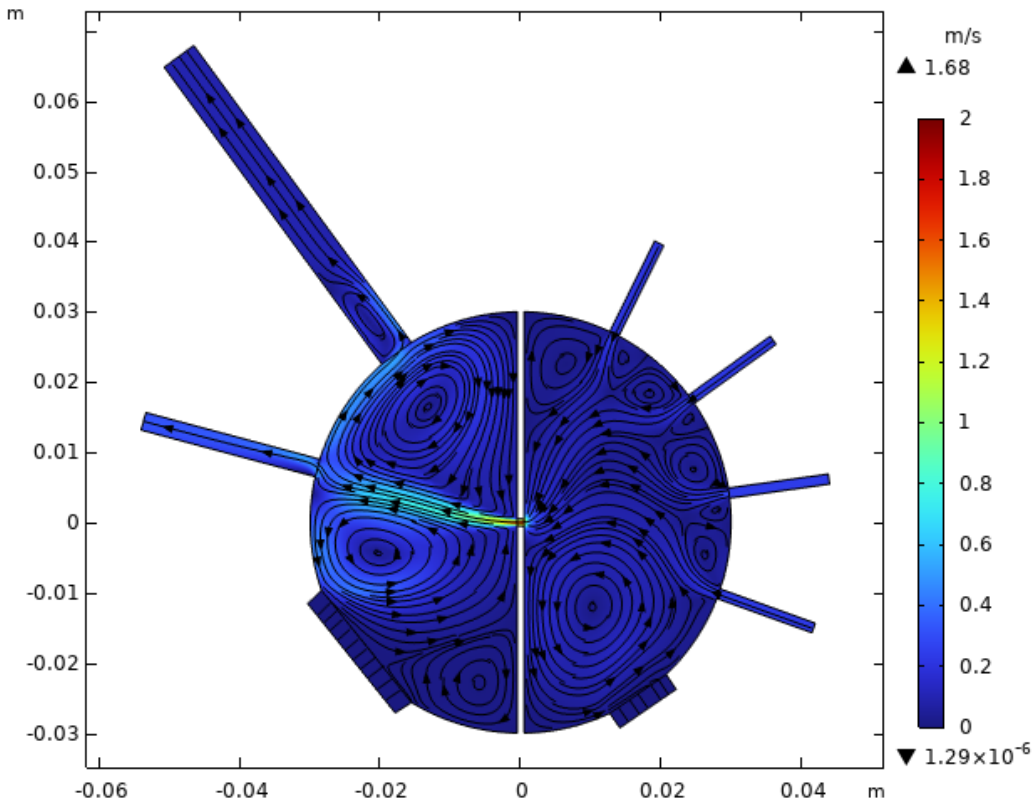

(b) 8 mm shunt

Figure 4.10: Velocity field of the transient CFD simulation at the end of systole ($t = 0.95$ s) in absence (a) and presence (b) of an 8 mm shunt

Flow rates

Figure 4.11 shows the flow rates through the inlets, outlets and interatrial shunt over one cardiac cycle in absence (Figure 4.11a) and presence (Figure 4.11b) of an 8 mm shunt. In these figures, positive values indicate blood flow exiting the domain and negative values indicate blood flow entering the domain. Therefore, the positive values are mostly occupied by the mitral (MV) and tricuspid (TV) valves and the negative values are mostly occupied by the inlets. For the shunt, a negative value indicates a flow from the left atrium to the right atrium and vice versa.

Considering the situation without an interatrial communication (Figure 4.11a), the combined flow rate through the inlets equals the flow rate through the outlet in each atrium. This is because blood is assumed incompressible and the atria do not deform in the current simulation. For this reason, the flow rate through the pulmonary veins is equal but opposite to the flow rate through the mitral valve. Similarly, the flow rate through the SVC plus the flow rate through the IVC equals the flow rate through the tricuspid valve. Naturally, the shunt flow rate is zero in absence of an interatrial communication. At the start of the diastolic phase, Figure 4.11a shows that the inlets start to bring blood into the atria. The pulmonary veins are already at their peak flow rate after a little over 0.1 s into the heart cycle, whereas the vena cavae only reach this point after 0.25 s. This is the result of the higher pressure difference between the PVs and the MV compared to the VCe and the TV. After the peaks, the flow rates can be seen to steadily decrease due to the reduction of the pressure difference between the in- and outlets: the inlet pressures drop due to the emptying of the systemic and pulmonary reservoirs and the outlet pressure rise due to the filling of the left and right ventricles. At the start of the systolic phase, the atrioventricular valves close. As noted in the previous section on the velocity field, the inferior vena cava shows reversed flow just before and during the systole as a result of the momentum imbalance between the two vena cavae. Here, this flow from the SVC to the IVC can be clearly seen after 0.6 s into the heart cycle. Also note that this flow dies out during the systolic phase, as momentum is dissipated through viscosity.

Figure 4.11b shows what happens to the flow rates when an 8 mm shunt is introduced in the interatrial septum. Overall, similar behavior is observed between the two situations, with the flow rates rapidly building up to a peak before gradually falling. The biggest difference during the diastole is that the flow rate through the tricuspid valve is now significantly higher than before, where the flow rate through the mitral valve is significantly lower than before. As discussed in section 4.2 for the steady-state simulation, this is a direct result of the interatrial shunt, transporting part of the blood flow that enters the left atrium into the right atrium. This increases the blood flow through the pulmonary circulation and decreases that through the systemic circulation, thus increasing the Qp:Qs ratio. Figure 4.12 shows the instantaneous Qp:Qs ratio over the diastole. Note that the systole is not shown in this figure as the Qp:Qs ratio is irrelevant during this phase. Here, it can be seen that the Qp:Qs ratio increases from around 0.1 at the start of diastole to around 3 after half a second into the diastole. After this, the ratio blows up as the flow rate through the mitral valve drops to zero and becomes negative at $t = 0.61$ s. This indicates reversed flow through the mitral valve outlet, which can also be seen in Figure 4.11b. The instantaneous Qp:Qs ratio confirms that the flow rate through the TV is higher than the flow rate through the MV for most of the diastole. Only at the start, as the flow rate through the mitral valve peaks early, Qp:Qs is temporarily smaller than 1 and more blood flows into the left ventricle than into the right ventricle at that particular moment. After that, the mitral valve flow rate is quickly overtaken by the flow rate through the tricuspid valve, where their ratio keeps increasing as the mitral valve flow rate starts to decrease. Even though the Qp:Qs ratio is smaller than 1 for the final part of the diastole as it is negative, this actually increases the Qp:Qs ratio overall. This is because the Qp:Qs ratio depends on the end-diastolic volumes of the left and right ventricles. Therefore, this bit of reversed flow through the mitral valve at the end of the diastolic phase increases the Qp:Qs ratio as it reduces $V_{LV_{ED}}$. From the simulation, it follows that $V_{LV_{ED}} = 2.74 \cdot 10^{-3}$ m^3 and $V_{RV_{ED}} = 3.83 \cdot 10^{-3}$ m^3, resulting in a ratio of pulmonary to systemic blood flow Qp:Qs = 1.40. This is slightly higher than the value of 1.24 that was estimated from the steady-state simulation.

Considering the flow rate through the interatrial shunt, it is fairly constant around 10^{-3} m^3/s throughout the heart cycle. As the systolic phase commences, note that the flow rates through the inlets do not drop to zero, which does happen in absence of the shunt. As discussed in the previous section, the jets from the pulmonary veins merge before flowing through the shunt towards the vena cavae during the systole. This means that the flow rate through the pulmonary veins is equal to the shunt flow rate and equal to the combined SVC and IVC flow rates, which is confirmed by Figure 4.11b.

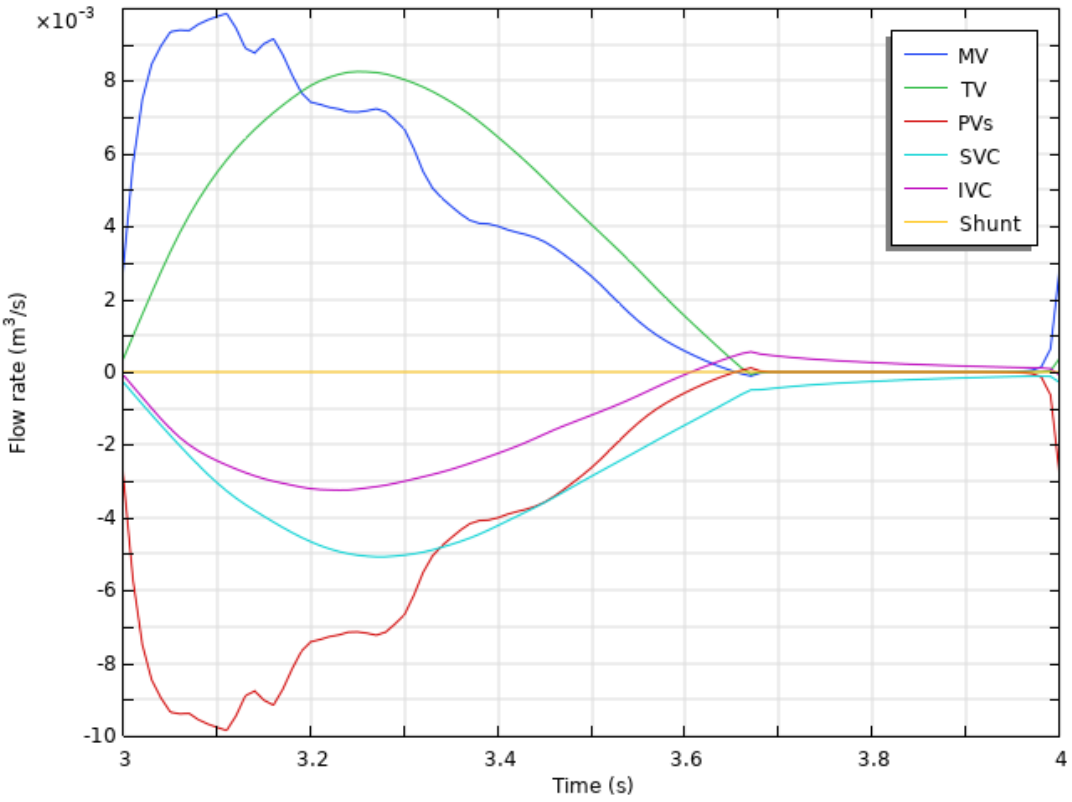

(a) Without shunt

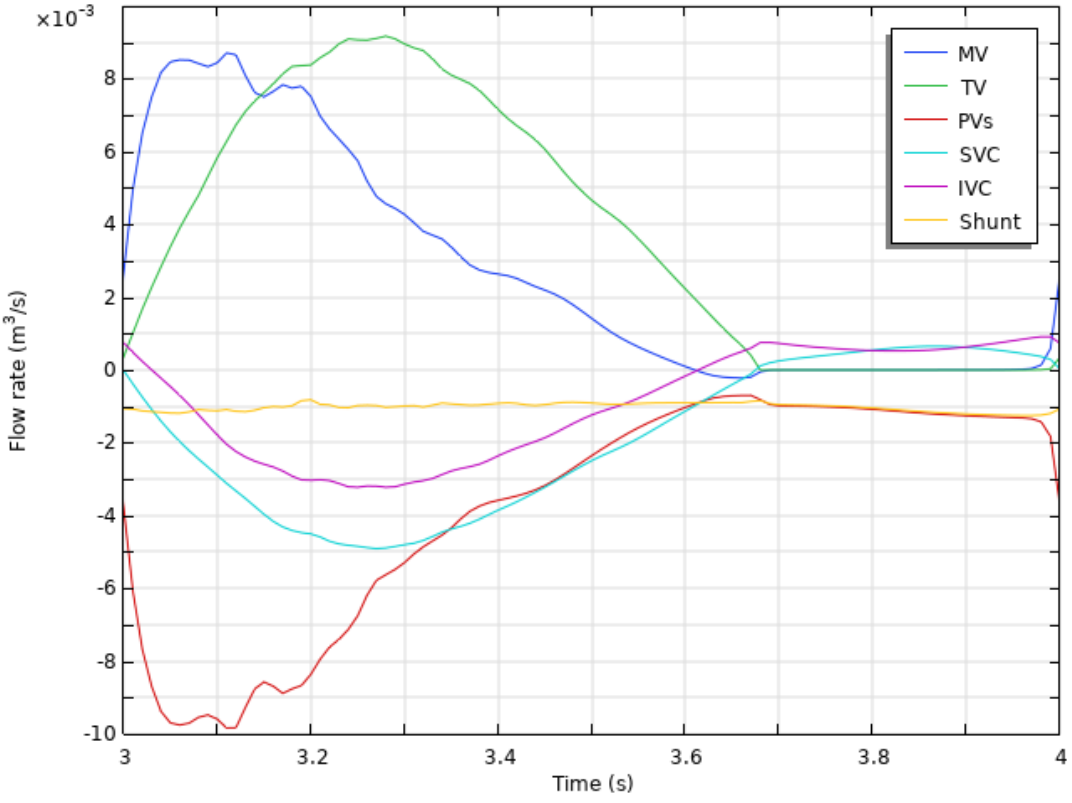

(b) 8 mm shunt

Figure 4.11: Flow rates through the inlets, outlets and interatrial shunt of the transient CFD simulation over one cardiac cycle in absence (a) and presence (b) of an 8 mm shunt. Positive values indicate flow rate exiting the domain and negative values indicate flow rate entering the domain. For the shunt, a negative value indicates a flow from left to right.

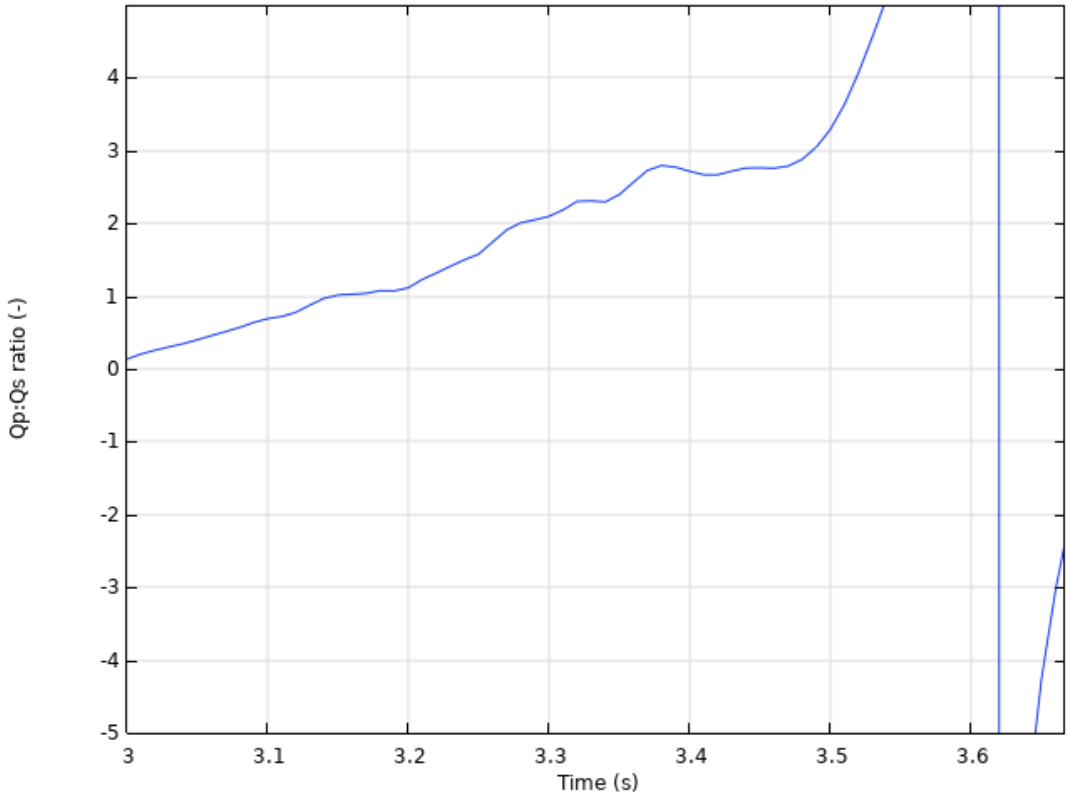

Figure 4.12: Instantaneous ratio of pulmonary to systemic blood flow over the diastolic phase of one cardiac cycle in presence of an 8 mm shunt

Pressure field

Figures 4.14 to 4.16 show the progression of the pressure field over the cardiac cycle in absence (a) and presence (b) of an 8 mm interatrial shunt. These results are taken at the same moments as the results of the velocity field presented in Figures 4.8 to 4.10. These moments are halfway through the diastole (Figure 4.14 at $t = 0.35$ s), at the end of diastole (Figure 4.15 at $t = 0.65$ s) and at the end of systole (Figure 4.16 at $t = 0.95$ s). Comparing these figures to Figure 4.5 for the steady-state simulation, it must be noted that the scales have changed for this transient simulation. This is because of the previously discussed Reynolds-scaled inlet velocities describing the steady-state simulation, which have resulted in unrealistically high pressures. Therefore, a fair comparison of the pressure field between this simulation and the steady-state simulation cannot be made.

Figure 4.14 shows the pressure field at $t = 0.35$ s. Comparing Figure 4.14a to Figure 4.14b shows the expected behavior of the interatrial shunt, namely that the left atrial pressure is decreased and the right atrial pressure is slightly increased with the introduction of a shunt. This is especially well visible by comparing the left atria, where the yellow/orange in Figure 4.14a has made place for yellow/green in Figure 4.14b. On the contrary, the blue colors in the right atrium in Figure 4.14a have become just a bit lighter in Figure 4.14b, indicating a slight increase in right atrial pressure. Furthermore, from a comparison of the pressure fields in Figure 4.14 to the corresponding velocity fields in Figure 4.8, many flow features can be recognized, such as the relatively low-pressure recirculation zones between the inlets.

Towards the end of the diastole, the velocity magnitudes decrease as discussed in the previous sections. This is because the systemic and pulmonary reservoirs are drained, with a reduction of inlet pressures as a result. Meanwhile, the left and right ventricles are filled, resulting in an increase in outlet pressure and hence a decreasing pressure difference between in- and outlets. Since less kinetic energy is added to the system, the intra-atrial pressure gradients die out, causing a nearly constant pressure throughout each atrium. This can be seen in Figure 4.15, which shows the pressure fields at the end of the diastolic phase at $t = 0.65$ s. Once again, comparing Figure 4.15a to Figure 4.15b clearly shows that the shunt results in a reduction of left atrial pressure and an increase in right atrial

pressure.

The systolic phase of the heart cycle is characterized by the closed atrioventricular valves. In the current simulation, this is modeled by locally increasing the viscosity in the domains near the outlets such that no fluid passes through. Of course, this is physically unrealistic, although it models a physically realistic condition by closing the outlet valves. Therefore, it must be noted that the pressures in the outlet domains during the systole are not relevant and will be omitted from the analysis of the results. These results are presented in Figure 4.16, showing the pressure fields at the end of systole ($t = 0.95$ s) in absence (Figure 4.16a) and presence (Figure 4.16b) of an 8 mm shunt. Comparing the two gives slightly different pressure fields, similar to the comparison of the velocity fields at this moment (Figure 4.10). Assuming no movement of the walls in this simulation, the systole is the phase where blood flow no longer enters the atria if a shunt is not present. Therefore, viscous effects become dominant and velocity magnitudes and pressure gradients die out, similar to what was seen at the end of the diastole. At the same time, the ventricles are emptied, increasing the pressures of the pulmonary and systemic circulations. In turn, this increases the pressures of the atria, resulting in the pressure field presented in Figure 4.16a: equalized pressure throughout each atrium. Still, it can be seen that an interatrial communication has a significant effect on the pressure field at the end of systole. As the left atrial pressure is higher than the right atrial pressure, blood flows from the left atrium to the right and reduces the pressure in the left atrium at the expense of the right atrium. Furthermore, Figure 4.16b also shows that velocity magnitudes and intra-atrial pressure gradients are no longer zero, as flow features can be recognized in the pressure field. The relatively high pressure near the IVC inlet in the right atrium, for instance, is a result of the shunt jet impinging on the wall. However, to study the small intra-atrial pressure gradients in more detail, Figure 4.17 is added for reference. This figure shows the same pressure fields as in Figure 4.16, but with the left and right atria described by different legends. Here, the relatively high pressure near the IVC inlet in the right atrium is more clearly visible and also the recirculation zones between the pulmonary vein inlets in the left atrium can be recognized. Also note that the intra-atrial pressure fluctuations in both atria are much larger in presence of a shunt (see Figure 4.17b) than in absence of one (see Figure 4.17a).

Figure 4.18 presents how the pressures of the different chambers and reservoirs evolve over the cardiac cycle. This considers the pulmonary and systemic reservoirs and the four chambers of the heart. Figure 4.18a shows this evolution in absence of a shunt, whereas Figure 4.18b shows this in presence of the 8 mm shunt. Looking at the pulmonary and systemic pressures, it can be seen that these pressures start the diastole at their peak values. As fluid flows from the blood circulations into the atria, this decreases their volumes and pressures before they are refilled during the systole to start the cycle again. On the other hand, the ventricular pressures start the diastole at their minimum values, as they are filled and increase in pressure during this phase. In Figure 4.18, it can be seen that the ventricular pressures even exceed the inlet pressures towards the end of the diastole. This means that the inlet-to-outlet pressure gradient becomes negative and starts to decelerate the flow from the inlets to the outlets. This is in line with the observation made in Figure 4.11, which showed reversed flow through the mitral valve. In reality, this inlet-to-outlet pressure gradient is even more negative, but the blood flow does not reverse through the inlets or outlets. As an example, realistic waveforms of the pulmonary and left ventricular pressures according to Lumens et al. [35] are presented in Figure 4.13a. Here, the diastole starts when the left ventricular pressure drops below the pulmonary pressure around $t = 0.6$ s. This namely opens the mitral valve, as confirmed by its flow velocity in Figure 4.13b. The left ventricular pressure quickly reaches its minimum (around $t = 0.7$ s) and increases again as the ventricle is filled with blood. Shortly after, the left ventricular pressure already exceeds the pulmonary pressure early in the diastole. This is the moment where the mitral valve flow rate peaks, as the flow is decelerated after this due to the reversed pressure gradient. Even though the flow rate is decreasing, blood still keeps flowing from the left atrium into the left ventricle due to its momentum. In the current simulation, the blood has a lot less momentum than in reality, as the CFD model does not consider the mass of the entire blood circulation but only that of the blood in the computational domain. Therefore, a reversed pressure gradient in the current simulation decelerates the flow quicker than in reality, underestimating the effect of its momentum. As a result, this affects the pulmonary pressures, that can be seen to become as low as 4 mmHg in reality, whereas it does not even reach 10 mmHg in the current simulation. This makes the underestimation of the blood's momentum a limitation of the CFD simulations.

In the last part of the diastole, just before the mitral valve flow velocity reaches zero and would

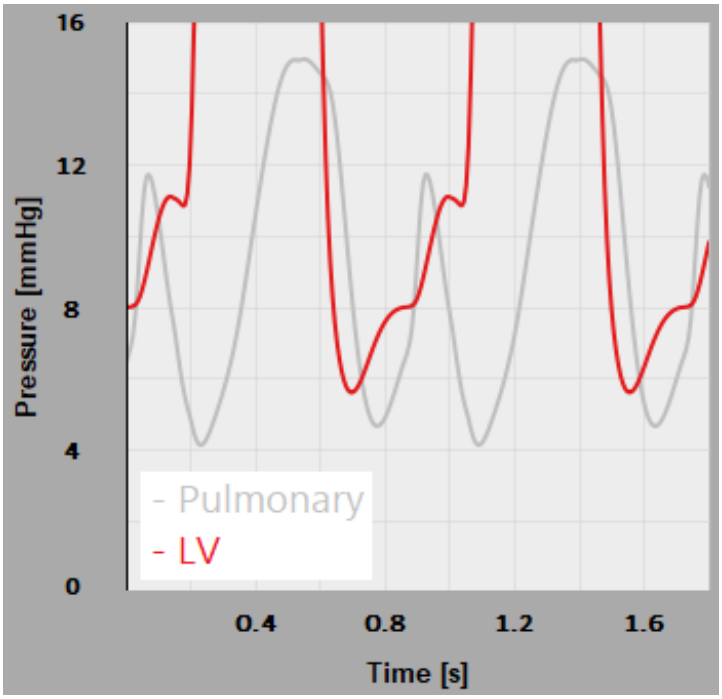

(a) Pulmonary and left ventricular pressures

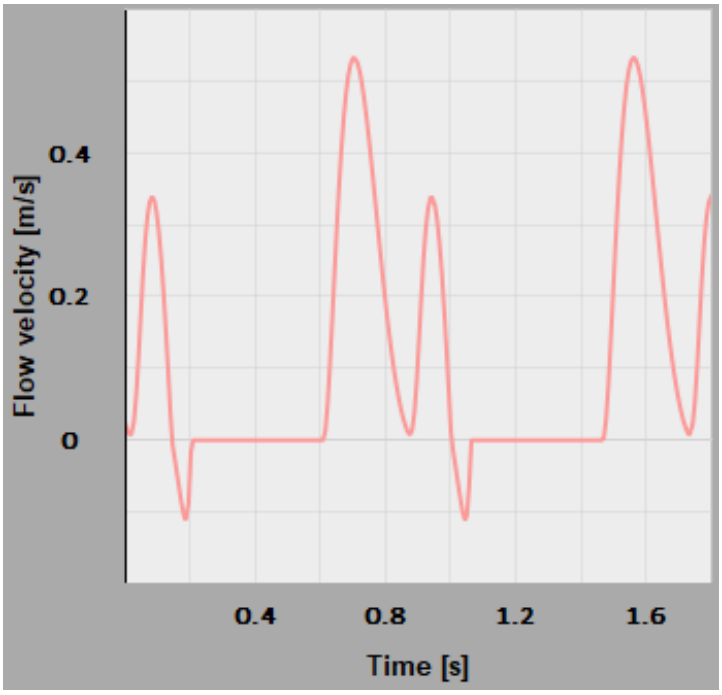

(b) Mitral valve flow velocity

Figure 4.13: Realistic pulmonary and left ventricular pressures (a) and mitral valve flow velocity (b) according to Lumens et al. [35]

become negative, the pulmonary pressure is increased due to the contraction of the atria. As a result, the pulmonary pressure exceeds the left ventricular pressure, reversing the pressure gradient again. This causes the second peak in mitral valve flow rate. In the current simulation, however, the atrial contraction is not included as a static domain is considered. In the transient simulation including wall movement in section 4.4, this will be included. Finally, note that in reality (see Figure 4.13a), the highest ventricular pressures are found during the systole as this is the phase of the cardiac cycle that the ventricles contract. In the current model, such a ventricular contraction is not modeled and the ventricular volume is simply moved to the pulmonary and systemic reservoirs through the equations presented previously. Therefore, rather than peaking in pressure, the ventricular pressures decline as they are emptied during the systole (see Figure 4.18). This is also the reason why the ventricular pressures are at their minimum at the start of the diastole, whereas in reality the diastole commences the moment that the ventricular pressures drop below the atrial/pulmonary pressures as can be seen in Figure 4.13. Thus, the current research neglects the relatively high, reducing ventricular pressures at the very start of the diastole and instead assumes them to start from their minimum values.

In Figure 4.18, also the spatial averages of the atrial pressures are shown. The difference in elastance between the inlet and outlet reservoirs is expected to have an influence on the evolution of these pressures over the diastole. The left atrium is connected to the pulmonary reservoir as inlet ($E_P = 1700$ mmHg/m^3) and the left ventricle as outlet ($E_{LV} = 1540$ mmHg/m^3). Considering the situation without an interatrial shunt, this means that if fluid flows from the pulmonary reservoir, through the left atrium into the left ventricle, the pressure in the pulmonary reservoir drops more than the pressure rises in the left ventricle. Therefore, a slight decrease in left atrial pressure is expected over the diastole. On the other hand, the right atrium is connected to the systemic reservoir ($E_S = 525$ mmHg/m^3) and the right ventricle ($E_{RV} = 830$ mmHg/m^3). As the elastance of the outlet reservoir is higher than the inlet reservoir in this case, an increase in right atrial pressure is expected over the diastole. Figure 4.18a confirms this for the right atrial pressure, which is seen to almost follow the curve of the RV pressure. No decrease in left atrial pressure is observed, however, as the left atrial pressure stays relatively constant over the diastole. This discrepancy could be due to the small difference between E_P and E_{LV} (10%), making this effect negligible, whereas the difference between E_S and E_{RV} is much bigger (58%).

At the start of the systolic phase of the heart cycle, the valves suddenly close, altering the pressure in the atria. This can be seen in Figure 4.18 around $t = 0.67$, though the peaks are very small as velocity magnitudes have largely died out at this point (see Figure 4.9). Also note that the peak in the average left atrial pressure is pointing down as there is reversed flow through the mitral valve at this point (see Figure 4.11), whereas the peak in average right atrial pressure is pointing up. In absence of the shunt, the left atrial pressure is now equal to the pulmonary pressure and follows its pressure rise through the systole. Similar behavior is seen for the right atrial pressure with the pressure of the systemic reservoir. Including a shunt, however, blood keeps flowing during the systole as (small) pressure differences remain between and within the atria. In Figure 4.18b, it can be seen why blood flows from the pulmonary circulation into the left atrium, through the interatrial shunt to the right atrium and into the systemic circulation, as the different pressures during the systole highlight.

Considering the effectiveness of the shunt, it can be seen that the pulmonary pressures are lowered throughout the cardiac cycle by comparing Figure 4.18a to Figure 4.18b. The peak pulmonary pressure is reduced by 1.1 mmHg from 16.5 to 15.4 mmHg and the minimum pressure is reduced by the same amount from 10.6 mmHg to 9.5 mmHg. In turn, the lowest systemic pressure has slightly increased from 1.3 to 1.8 mmHg while the peak pressure has increased from 3.1 to 3.4 mmHg. This difference in pressure delta is due to the much lower systemic elastance ($E_S = 525$ mmHg/m^3) compared to the pulmonary elastance ($E_P = 1700$ mmHg/m^3) as shown in Table 4.4. Also the spatial average of the left atrial pressure is significantly lowered by the shunt. The pressure at the end of systole has reduced by approximately 1.2 mmHg from around 16.3 mmHg without a shunt to around 15.1 mmHg including an 8 mm shunt. Meanwhile, the minimum LA pressure shows a reduction of 1.0 mmHg from 9.1 mmHg to 8.1 mmHg. On the other hand, the right atrial pressure at the end of systole has increased by 0.3 mmHg from around 3.1 mmHg to 3.4 mmHg and the minimum RA pressure at the start of the diastole has remained fairly constant, going from 0.2 to 0.3 mmHg. Similar behavior is observed for the ventricular pressures, with the peak LV pressure at the end of diastole reducing by 1.1 mmHg from 10.9 to 9.8 mmHg and $P_{RV_{ED}}$ increasing by 0.3 mmHg from 3.1 to 3.4 mmHg. By design, the minimum ventricular pressures have remained the same, as these are set in the model.

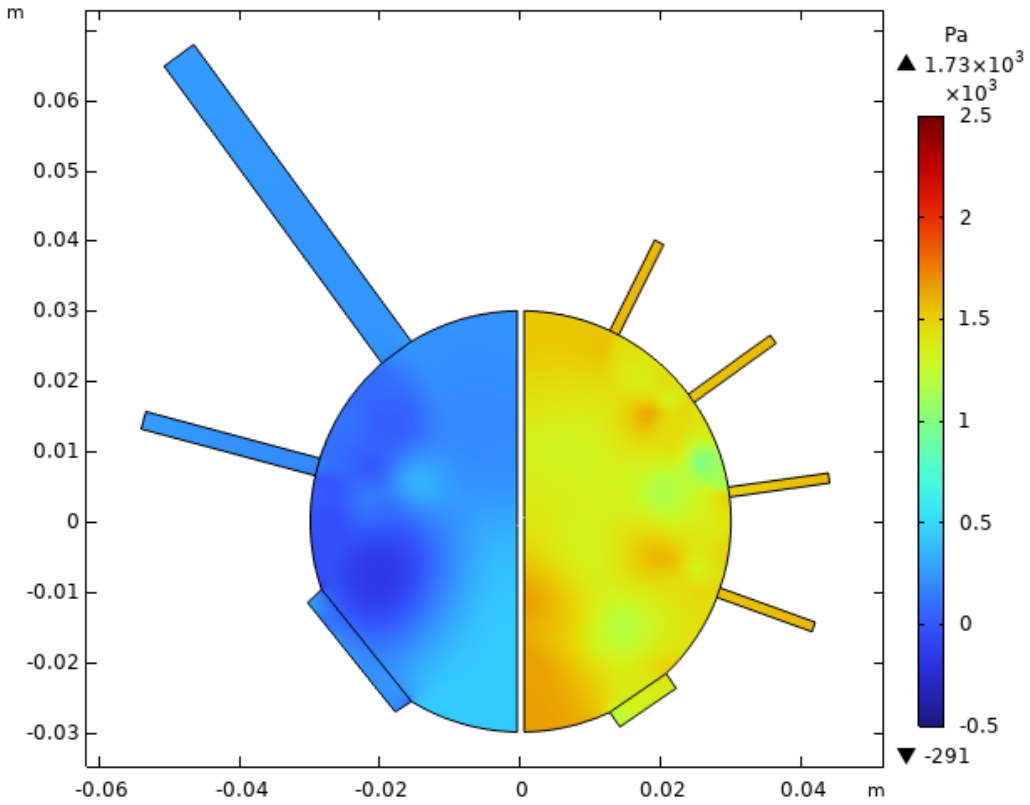

(a) Without shunt

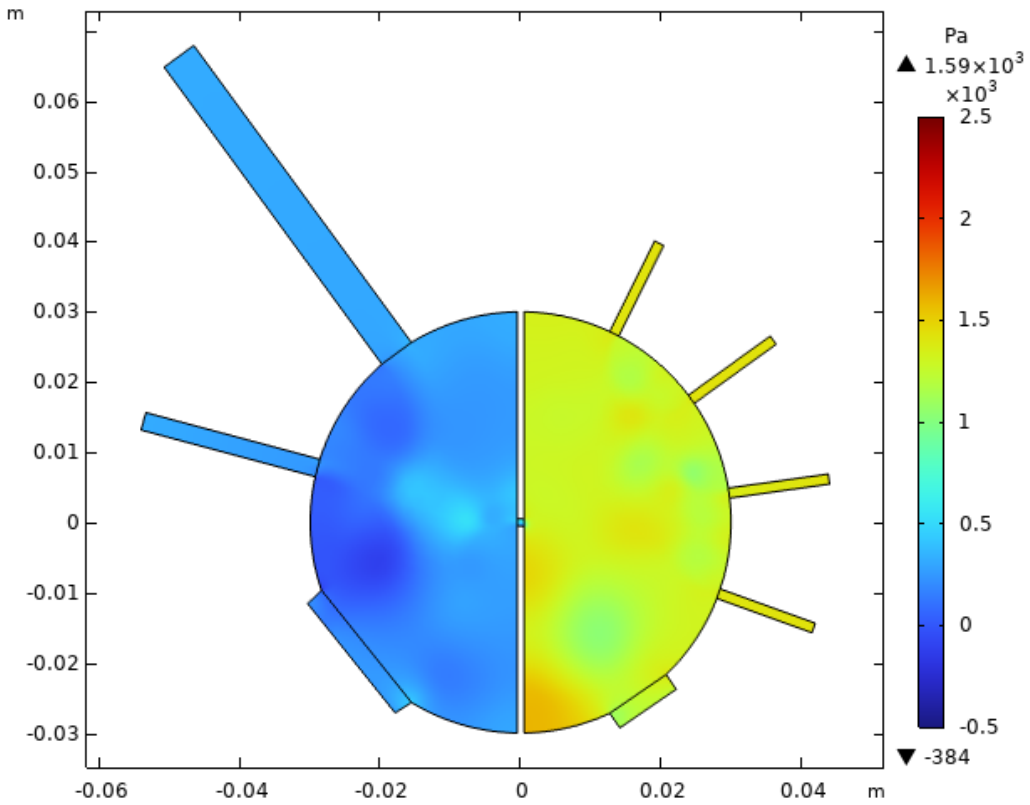

(b) 8 mm shunt

Figure 4.14: Pressure field of the transient CFD simulation halfway through the diastole ($t = 0.35$ s) in absence (a) and presence (b) of an 8 mm shunt

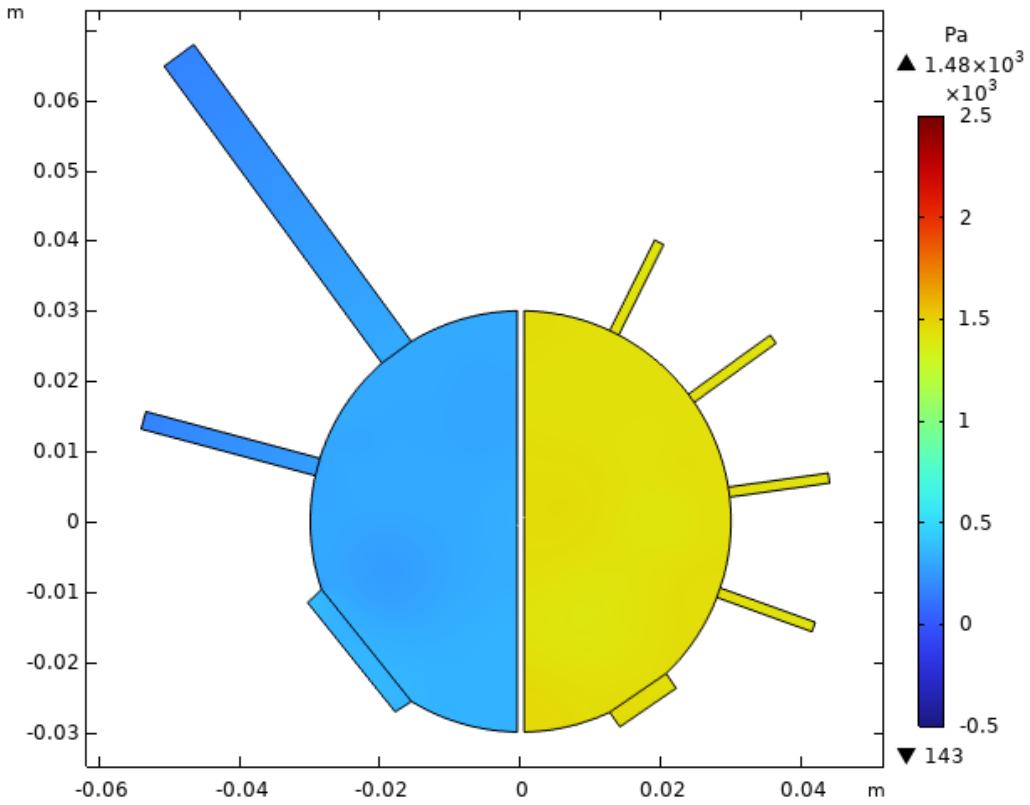

(a) Without shunt

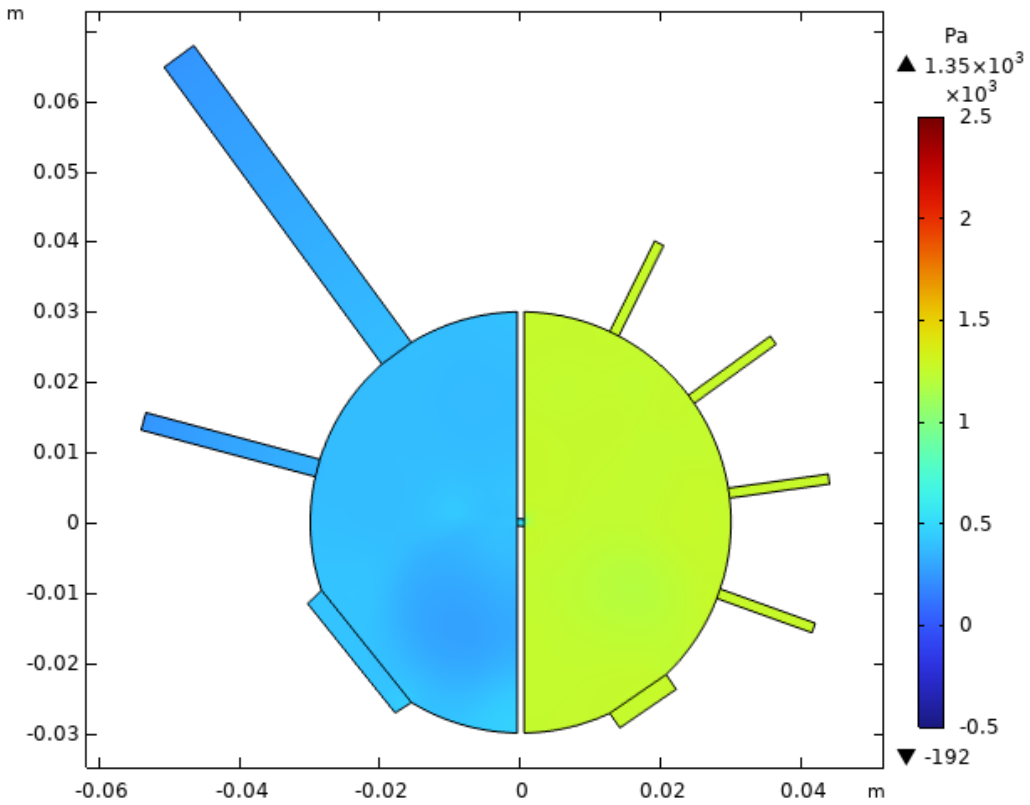

(b) 8 mm shunt

Figure 4.15: Pressure field of the transient CFD simulation at the end of diastole ($t = 0.65$ s) in absence (a) and presence (b) of an 8 mm shunt

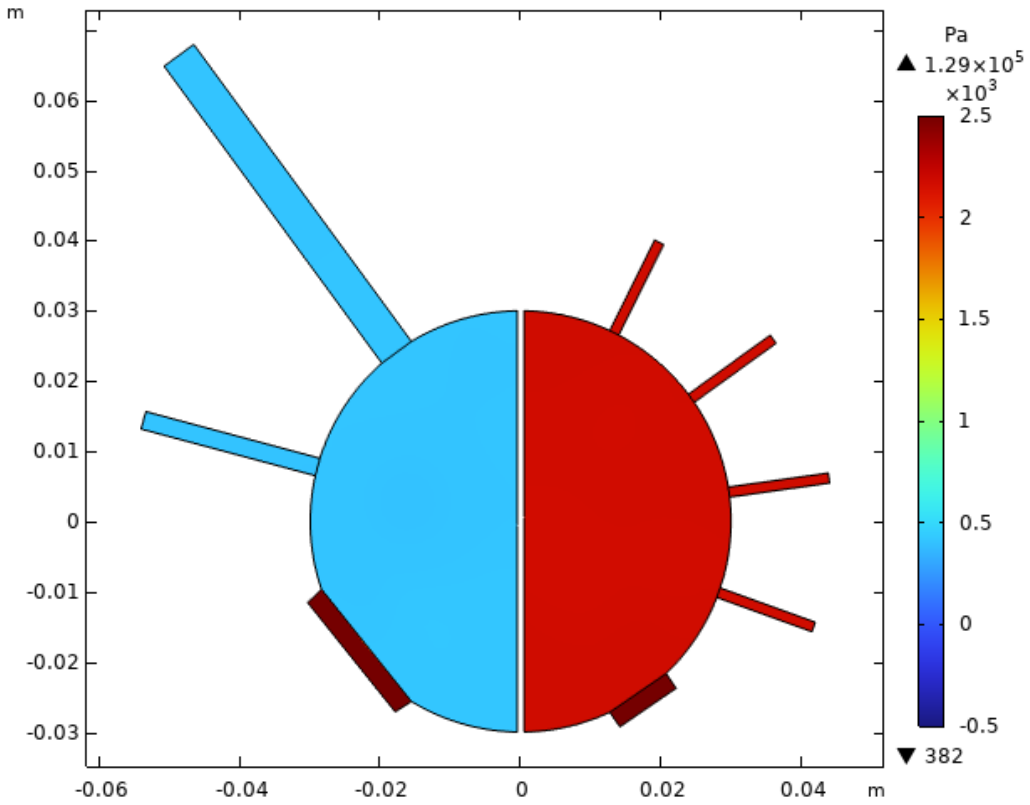

(a) Without shunt

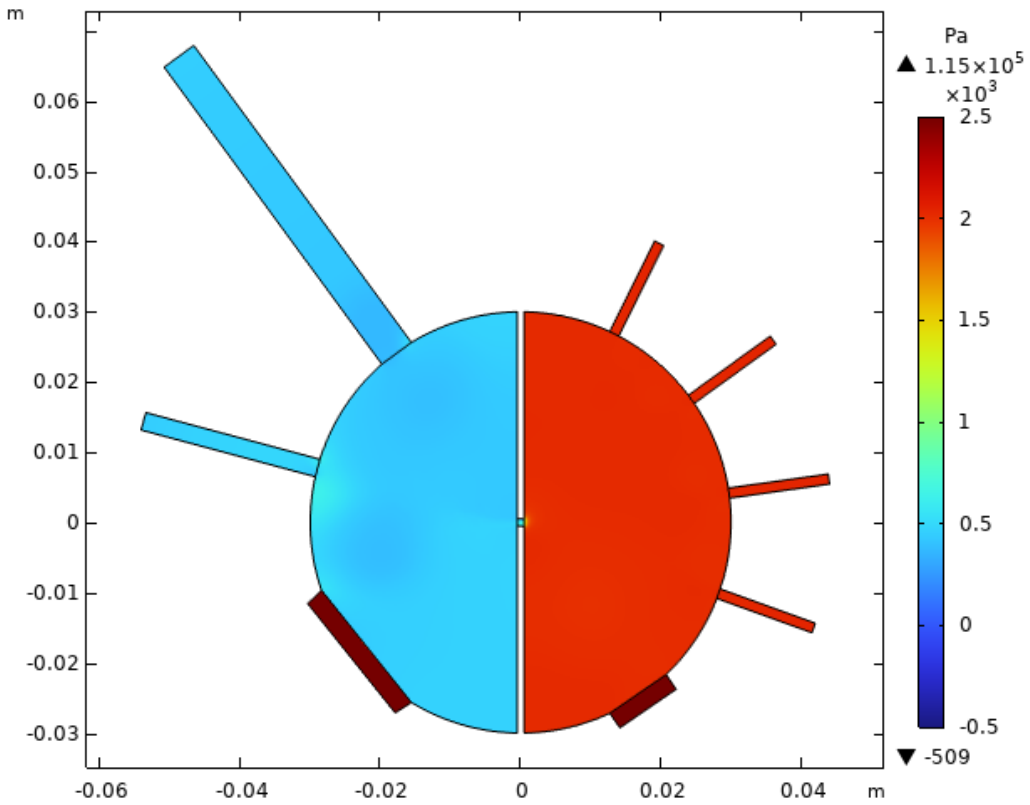

(b) 8 mm shunt

Figure 4.16: Pressure field of the transient CFD simulation at the end of systole ($t = 0.95$ s) in absence (a) and presence (b) of an 8 mm shunt

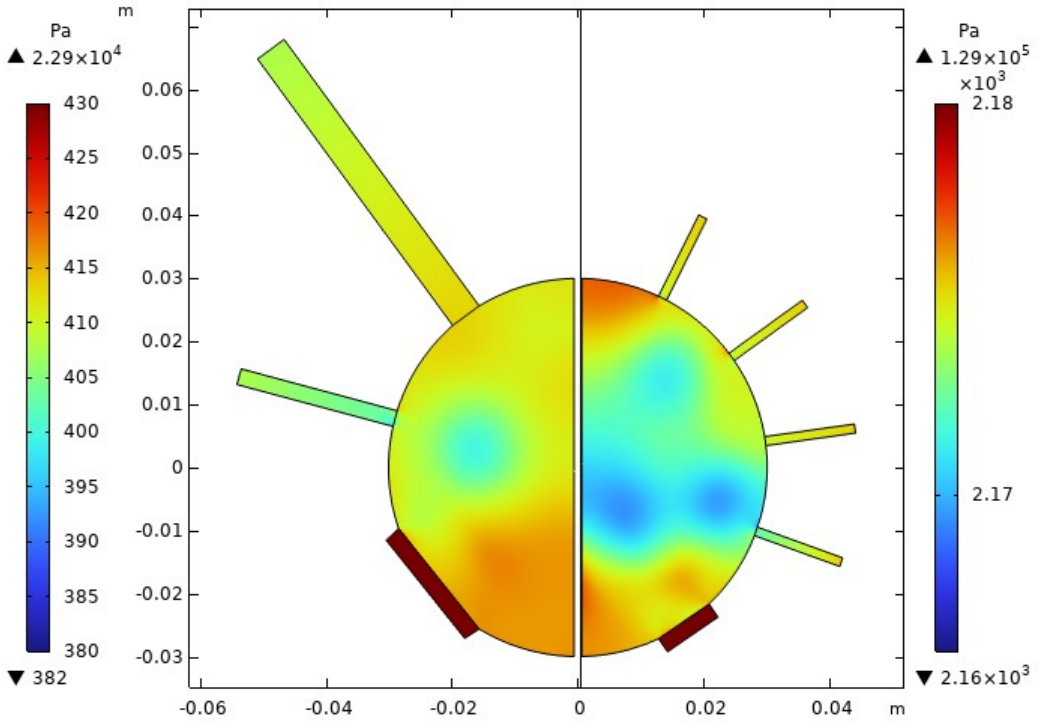

(a) Without shunt

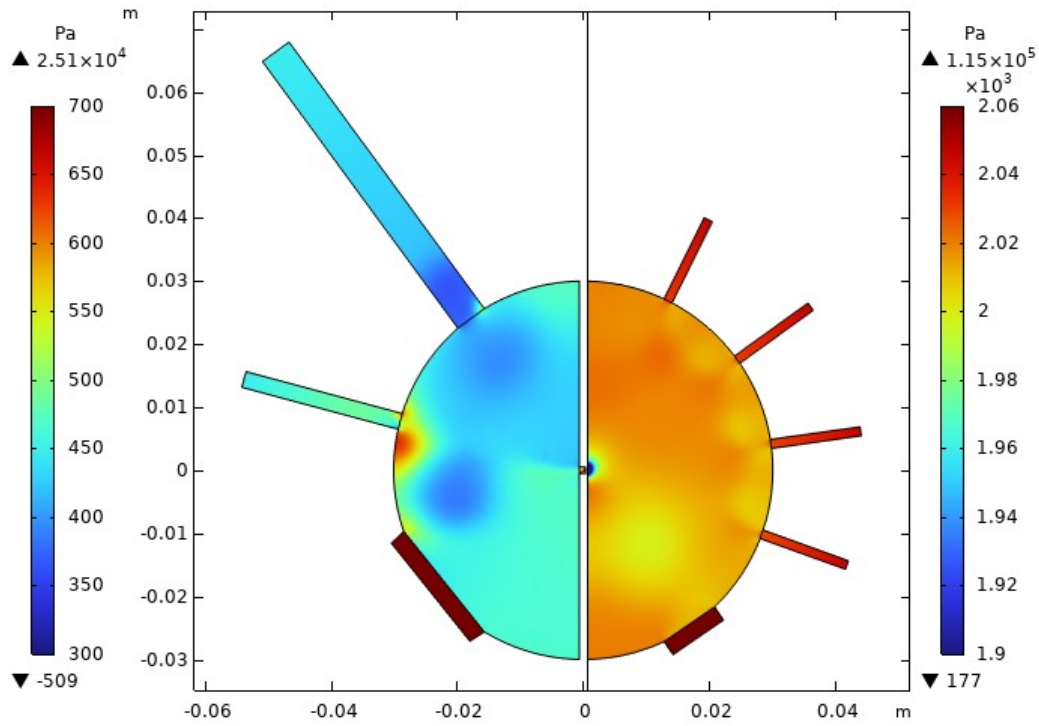

(b) 8 mm shunt

Figure 4.17: Pressure field of the transient CFD simulation at the end of systole ($t = 0.95$ s) in absence (a) and presence (b) of an 8 mm shunt, with the left and right atria described by different legends to study the intra-atrial fluctuations. The legend on the left side of the image describes the pressure field left of the vertical line and vice versa.

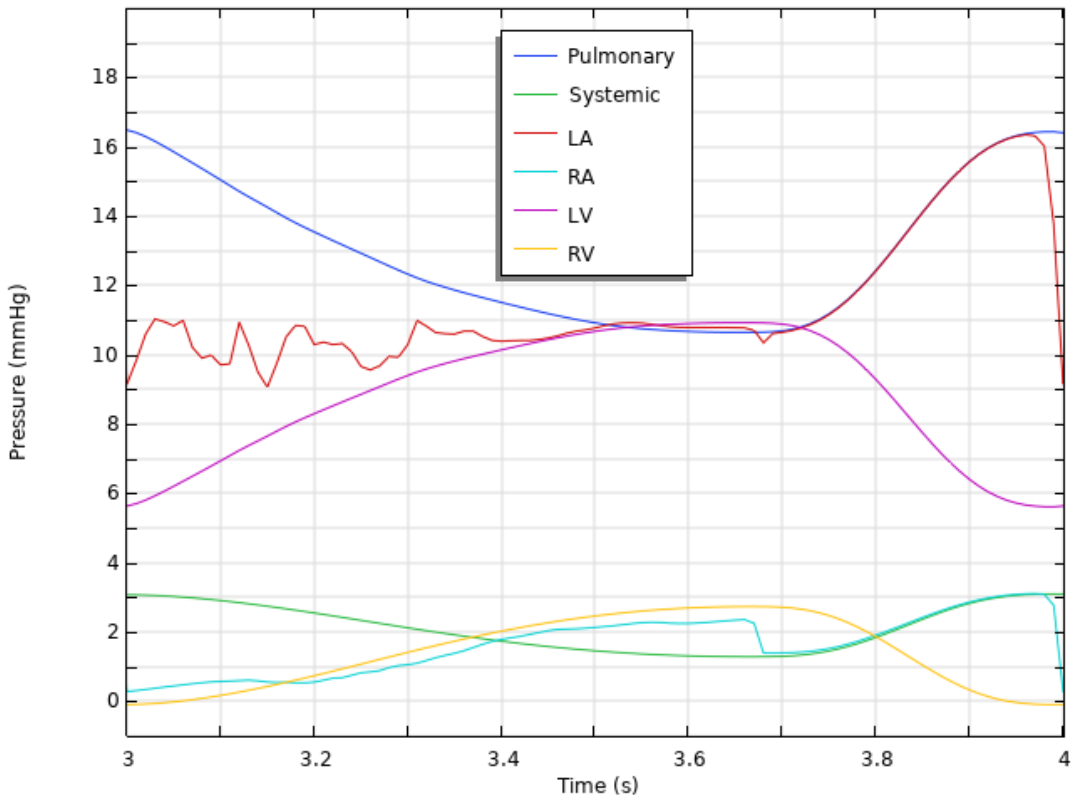

(a) Without shunt

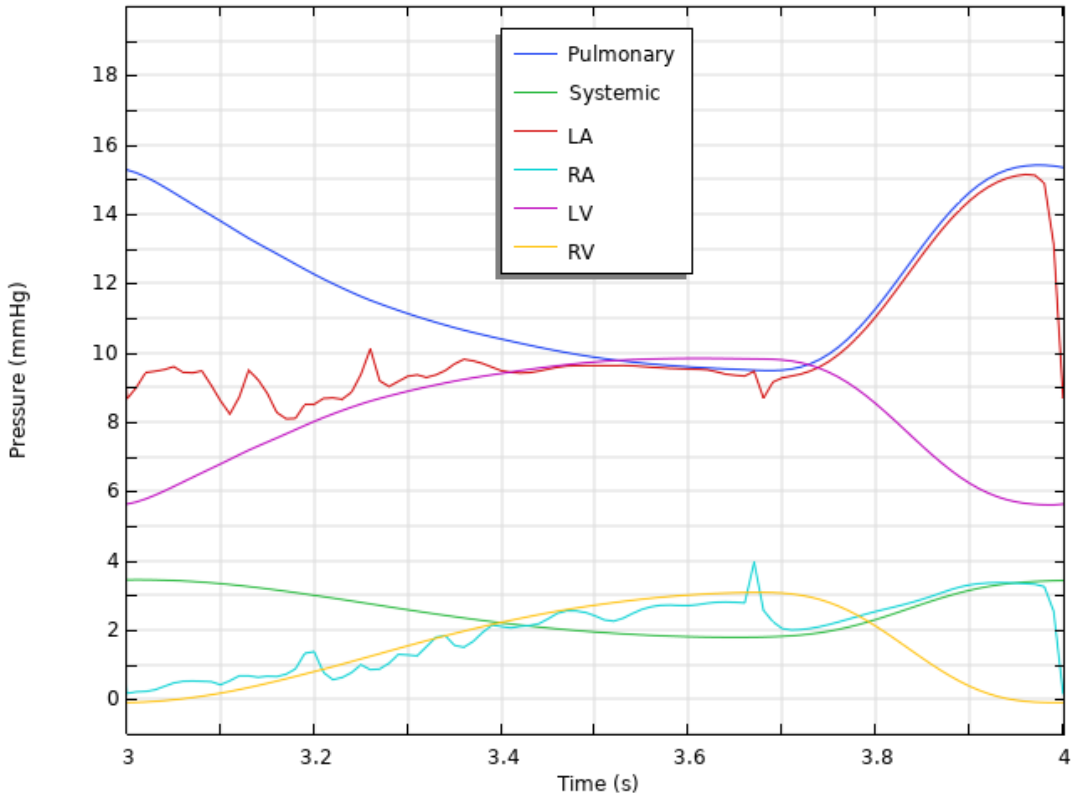

(b) 8 mm shunt

Figure 4.18: Pulmonary, systemic, left (LA) and right (RA) atrial and left (LV) and right (RV) ventricular pressures of the transient CFD simulation over one cardiac cycle in absence (a) and presence (b) of an 8 mm shunt

4.4. Moving mesh

The two-dimensional model is further extended by taking into account the deformation of the atria during the cardiac cycle. The deformation is prescribed *a priori* and is derived from the progression of the atrial volume over the cardiac cycle. This information is extracted from the computer program CircAdapt, which is developed by the Department of Biomedical Engineering from Maastricht University [35]. The data is adapted such that the diastole lasts 2/3 of the cardiac cycle and the minimum and maximum atrial volumes are adjusted to suit HFpEF patients according to Kaye et al. [30], which are 74 mL and 172 mL, respectively.

The deformation assumes only the radius to be a function of time by prescribing displacement of the outer walls in the normal direction. The walls where this movement is prescribed are marked in blue in Figure 4.19. The unmarked walls naturally adapt to this movement and remain unchanged where they can. Therefore, the shunt diameter remains constant. Though the inlet and outlet diameters are not explicitly modeled to change in size, they do deform at the edge of the atria. This is because the arc length of the inlet/outlet changes with the radius.

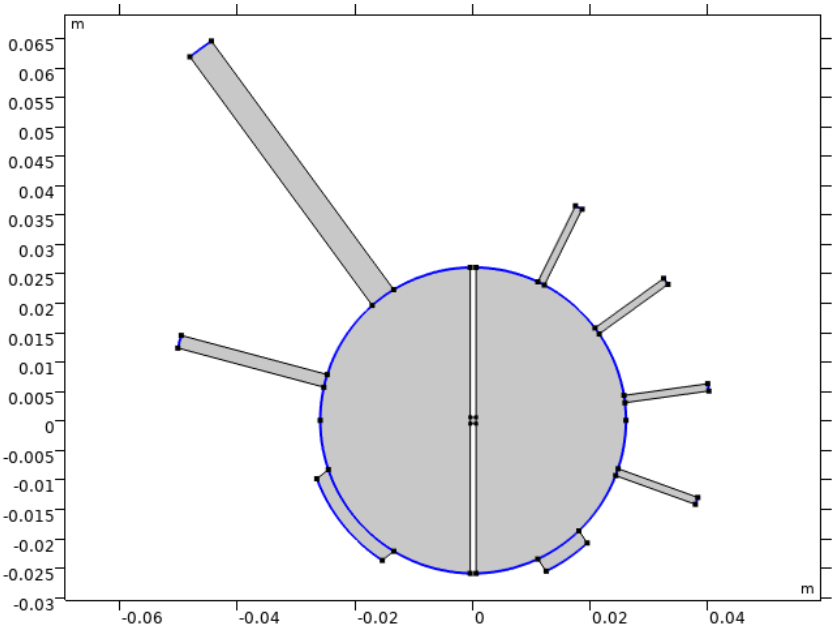

Figure 4.19: 2D double atrium geometry with walls with prescribed normal deformation marked in blue

Since the deformation is prescribed as a displacement of the wall, the volumes extracted from Lumens et al. [35] are converted to radii. The smallest atrial volume (74 mL) has a radius of $r = (\frac{3V}{4\pi})^{\frac{1}{3}} = 26$ mm corresponding to a deformation of 0 mm, whereas the largest atrial volume (172 mL) has a radius of 34.5 mm corresponding to a deformation of 8.5 mm. Finally, a curve-fitting is applied to this data to smooth out the deformation in order to accelerate the simulation. Figure 4.20 shows the deformation of the atria over the cardiac cycle, both in terms of the volume (a) and difference in radius compared to the smallest radius (b). Note that Figure 4.20b is the curve that actually describes the deformation of the atria.

In these figures, it can be seen that the heart cycle starts by increasing its size, which happens during the systolic phase. This is in contrast to the transient simulation without moving walls, which found the systole in the last 1/3 of the cardiac cycle. This means that the heart cycle commences with the outlet valves closed in the current simulation. The decision to invert these phases was driven by the implementation of the wall movement. It was namely found that the simulation in COMSOL is more stable if it commences with the domain first increasing in size and then decreasing. To keep the analyses of the results consistent with the previous in section 4.3, however, the diastole is still considered as the start of the cardiac cycle. In Figure 4.20, it can be seen that this phase starts at peak deformation ($t = 0.33$ s), when the atrial volume is at its maximum. Initially, atrial volume decreases in what is in reality a passive phase: as the ventricles start to relax, ventricular pressures decline until they drop below the atrial pressures. This causes the atrioventricular valves to open and blood to flow

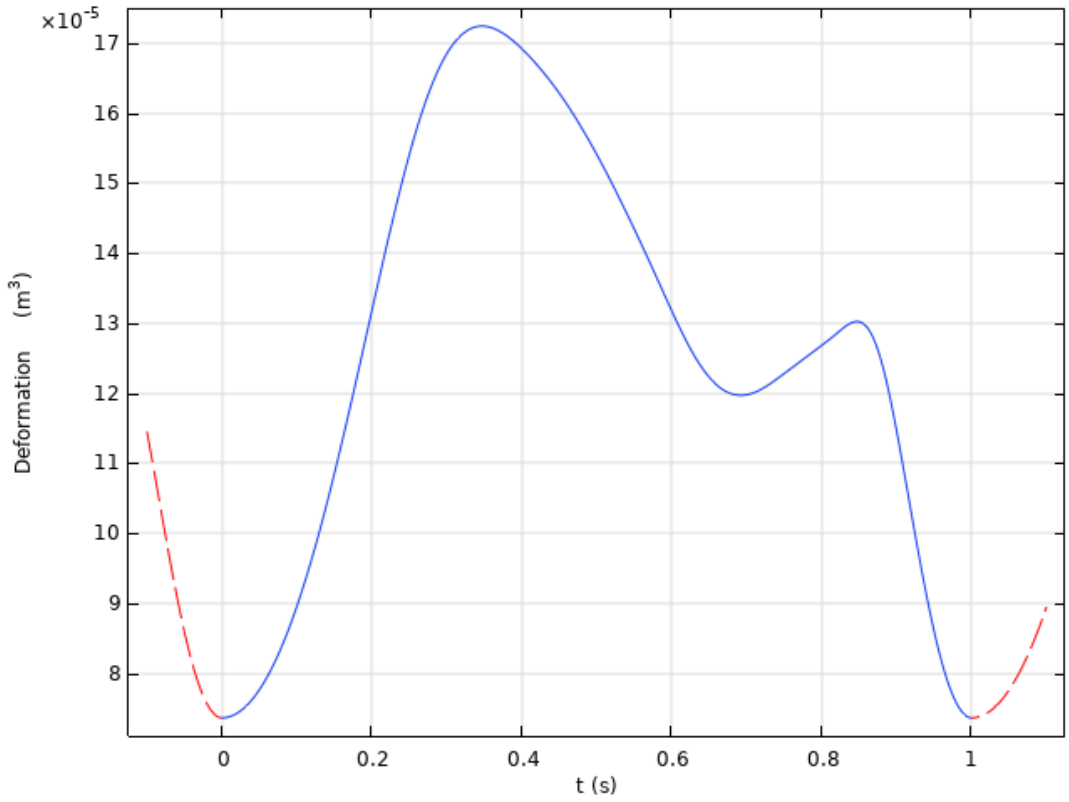

(a) Volume

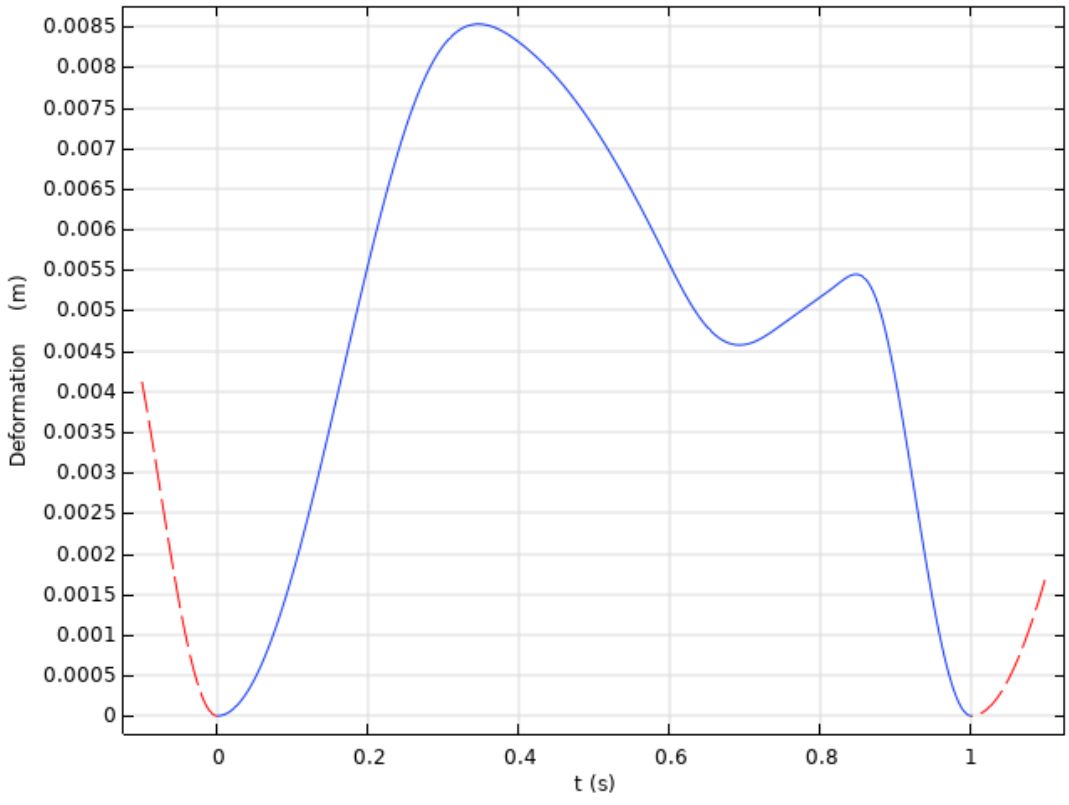

(b) Difference in radius

Figure 4.20: Deformation of the atria over the heart cycle in terms of volume (a) and difference in radius (b)

from the atria into the ventricles. As this continues, the ventricular pressures rise and the flow rates through the atrioventricular valves decrease. As blood keeps flowing into the left and right atria from the pulmonary and systemic circulations, respectively, the atrial volume temporarily starts to increase again around $t = 0.7$ s. This is until the atria contract in approximately the last 10% of the cardiac cycle, increasing the atrial pressures again and squeezing the last bit of blood into the ventricles. This conclusion to the cardiac cycle is known as the atrial systole or the atrial contraction and is the only active contribution of the atria to the heart cycle.

Due to the inversion of the diastole and systole in the current simulation, the boundary conditions that were applied to the transient simulation without wall movement (see Table 4.4) do not result in similar physically relevant inlet and outlet pressures. Therefore, some of these parameter values were adjusted in order to restore this. In Table 4.6, the parameter values for the transient simulation with a moving mesh are presented. From this, it can be seen that only the initial pressures of the pulmonary reservoir (P_{P_0}) and the left atrium (P_{LA_0}) have been altered compared to Table 4.4. Importantly, none of the elastances have been altered, such that this simulation represents a characteristically similar HFpEF patient.

Domain	Parameter	Value
Pulmonary	E_P	1700 mmHg/m^3
	P_{P_0}	0 mmHg
LA	P_{LA_0}	0 mmHg
LV	E_{LV}	1540 mmHg/m^3
	P_{LV_0}	5.6 mmHg
Systemic	E_S	525 mmHg/m^3
	P_{S_0}	2 mmHg
RA	P_{RA_0}	2 mmHg
RV	E_{RV}	830 mmHg/m^3
	P_{RV_0}	-0.1 mmHg

Table 4.6: Parameter values for the transient simulation with a moving mesh

Another difference caused by switching the two phases of the cardiac cycle considers the filling of the pulmonary and systemic reservoirs during the first systole. As described in section 4.3, the volume of blood that is stored in the ventricles during the diastole is ejected into the blood circulations during the systole. In the simulation described in section 4.3, these ventricles were filled before the first systole, as the simulation started with the diastole. In the current simulation, however, the ventricles are empty at the start of the simulation and no volume is transferred from the ventricles to the pulmonary and systemic reservoirs. To compensate for this, the pulmonary and systemic reservoirs are artificially filled during the first systolic phase of the cardiac cycle by mathematically adding a fixed amount of volume. These volumes were determined iteratively by considering the volumes that are added to these reservoirs during the second systole.

Regarding the modeling of the outlet valves, the current simulation models this with a damping function in the form of a weak contribution at the outlets. This weak contribution sets the velocity at the outlet equal to zero when the valves are closed. This method is different from the one applied in the transient simulation without moving walls, where this was modeled by locally increasing the viscosity in the outlet domains. The latter method was namely found to be ineffective for a simulation with a moving mesh, which drove the decision for another method.

Compared to the transient simulations without moving walls, also the spatial discretization is adjusted for the current simulations. It was found that the mesh presented in subsection 4.1.1 produces physically unrealistic results in the transient simulations with moving walls (see Appendix D). Refining the mesh aggravates these effects, whereas no physically unrealistic behavior is observed on the coarser default mesh from Appendix B. Effort has been put into resolving the issue on the refined mesh, first by refining the time step as it was believed that its cause lied in the Courant number being too high. The time step was refined both through reducing the relative tolerance to as low as $3 \cdot 10^{-4}$ and by running the simulation with very small constant time steps to as low as $5 \cdot 10^{-5}$ s. However, this has not managed to significantly change the results of the simulation. Furthermore, values of the relative tolerance/fixed time step smaller than those mentioned result in the simulation crashing. Other attempts

have been made to resolve the problem by applying different turbulence models in combination with various wall treatment methods, but without any improvement. Extension of the inlets of the domain was found to have a significant positive influence on the results, but was concluded to be due to the extra resistance of the inlets, which is not preferred. Also, this method only partly resolves the issue. Prescribing total rather than static pressure at the inlets and outlets was found to resolve the physically unrealistic results. However, since the simulations consider a problem driven by static pressure, it is deemed that prescribing the total pressure would result in larger errors in the results than a coarser mesh would. Finally, it was therefore decided to perform the transient simulations with moving walls on a coarser mesh in which the physically unrealistic flow is not present. This considers a mesh similar to the one presented in subsection 4.1.1, but with a coarser boundary layer maximum element size of 2.74 mm.

Similar to the transient simulation without a moving mesh, a simulation of five cardiac cycles was conducted to study the convergence of the results by analysing the systemic and pulmonary reservoir pressures, see Figure 4.21. From this, it was concluded that the results have converged after three cardiac cycles, as all peak-to-peak and trough-to-trough differences have reduced to less than 1%, see Table 4.7. In these results, the initial condition is taken as the first trough. Therefore, the fourth cardiac cycle is deemed to provide results of sufficient accuracy and will be used in the following analyses.

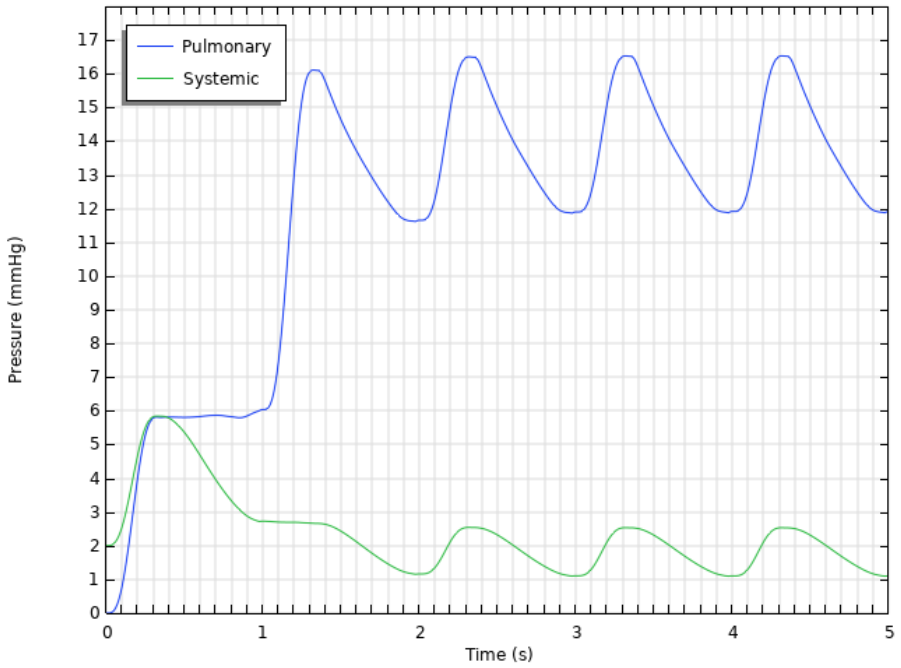

Figure 4.21: Convergence of the systemic and pulmonary reservoir pressures over five cardiac cycles for a simulation in absence of an interatrial shunt

Reservoir	Heart cycle	Difference in peaks	Difference in troughs
Pulmonary	1-2	178%	N/A
	2-3	2.48%	100%
	3-4	0.15%	2.15%
	4-5	0.01%	0.13%
Systemic	1-2	54%	35%
	2-3	4.15%	57%
	3-4	0.28%	4.35%
	4-5	0.03%	0.36%

Table 4.7: Convergence of the systemic and pulmonary reservoir pressures over five cardiac cycles for the transient simulation with moving mesh in absence of an interatrial shunt

4.4.1. Results

Velocity field

Similar to section 4.3, Figures 4.22 to 4.24 show the progression of the velocity field over the cardiac cycle in absence (a) and presence (b) of an 8 mm interatrial shunt. Figure 4.22 shows the moment halfway through the diastole, which is now at $t = 0.65$ s rather than at $t = 0.35$ s due to the inversion of the systole and the diastole. Furthermore, Figure 4.23 shows the moment at the end of diastole ($t = 0.95$ s) just before the outlet valves close, and Figure 4.24 shows the moment at the end of systole ($t = 0.3$ s) just before the valves open again.

In Figure 4.22, it can directly be seen that this simulation considers movement of the walls. Outlined in black, one can namely see the original geometry from which the fluid domain has deformed. As discussed, this original geometry is the one that describes the atria at the end of diastole/the start of systole, when the atrial volume is at its minimum. Therefore, the fluid domain is larger than or equal to this geometry throughout the cardiac cycle. Regarding the flow field, Figures 4.22a and 4.22b are very similar to Figures 4.8a and 4.8b, respectively. This is of course expected, as the only difference is the movement of the walls. One could note that the results from the current simulation look less chaotic, as the inlet jets are more straight-lined than in Figure 4.8 and are actually more similar to the steady-state flow field in Figure 4.4. However, this is simply a coincidence, as this only shows a single moment. Another difference between Figure 4.22 and Figure 4.8 considers the velocity magnitudes, as these are lower in the current simulation compared to the simulation without a moving mesh. This is likely a result of the higher pressure in the atria due to the wall movement, as the atria are shrinking at this point.

As the diastole continues, the ventricles continue to be filled while the atria continue to shrink. Especially during the atrial contraction, the atrial volume rapidly decreases. Figure 4.23 shows the flow field during this phase at $t = 0.95$ s, 0.05 s before the outlet valves close and the systole commences. As in section 4.3, a relatively stagnant flow field is expected compared to halfway during the diastole. This is because the inlet pressures have decreased at this stage, while the outlet pressures have increased, resulting in a much smaller (or even negative) pressure difference between the inlets and outlets at the end of the diastole. Therefore, the velocities in the inlets have decreased. However, as the atria are contracting, there is still a flow through the outlets into the ventricles. Since this is mostly driven by the movement of the walls, this results in a significantly different flow field compared to Figure 4.9. The latter shows a more stagnant flow field in this case, as no such driving force is present. The wall movement is especially well visible in Figure 4.23 by looking at the streamlines near the walls. As the streamlines point into the domain, this means that the velocity at the wall is nonzero as blood is pushed inwards. Following these streamlines finds that this blood is moving towards the outlet and into the ventricle. In presence of a shunt in Figure 4.23b, however, blood is also moved from the left to the right atrium.

In section 4.3, it was discussed that the systole results in the most stagnant flow field during the cardiac cycle, at least for the situation in absence of a shunt. This is because the outlet valves are closed, meaning that the blood has nowhere to go. As a consequence, large recirculation zones characterize the atrial flow fields, in which the momentum is slowly dissipated through viscosity during this phase. In reality, however, the systole is the phase in which the atria are filled with blood from the systemic and pulmonary circulations. This can only be modeled through movement of the walls, which is why a significant difference between the results of the current simulation and the one in section 4.3 is found in this phase. Although the velocity magnitudes are low, Figure 4.24 clearly shows that the atria are being filled, which was not the case in Figure 4.10. This can also be seen by the numerous amounts of smaller recirculation zones instead of one large recirculation zone, as the inlet jets still add energy to the flow field. Moreover, note that the streamlines are now pointing into the walls, indicating the outward movement of these walls and the increasing volume of the atria. In Figure 4.24b, it can also be seen that an 8 mm shunt flow no longer causes reversed flow through both the vena cavae, as was the case in Figure 4.10b. In the current simulation, the right atrium is now being filled by the SVC and the shunt flow, while a small reversed flow is still present through the IVC as previously seen.

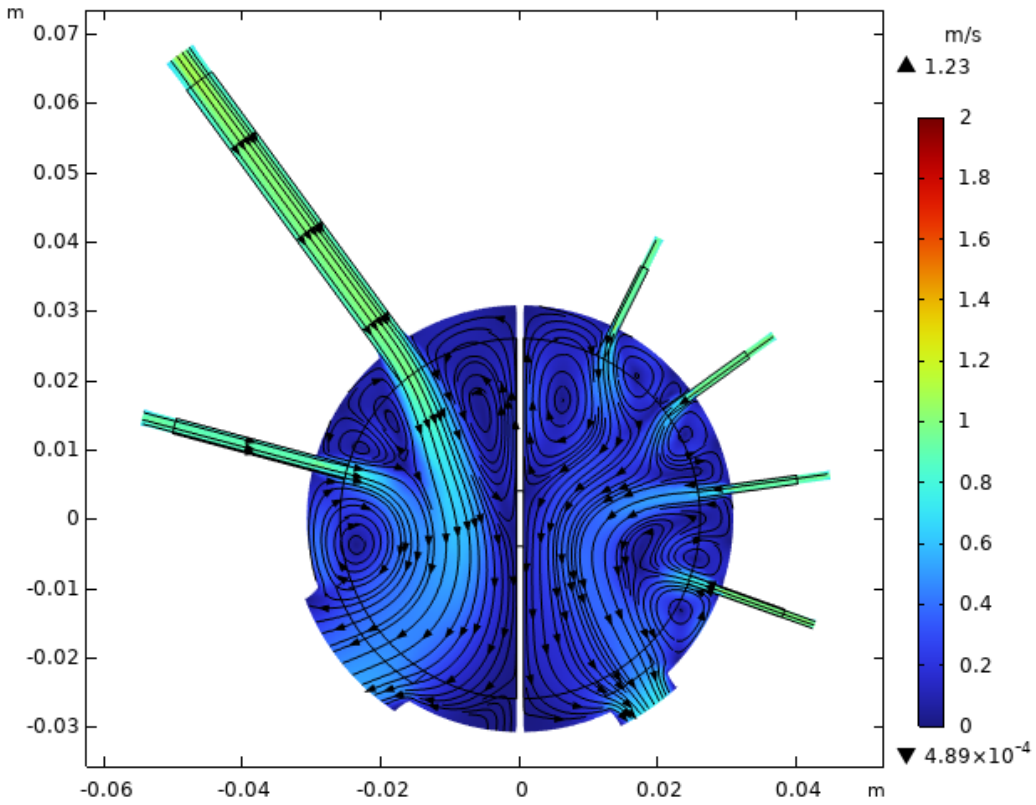

(a) Without shunt

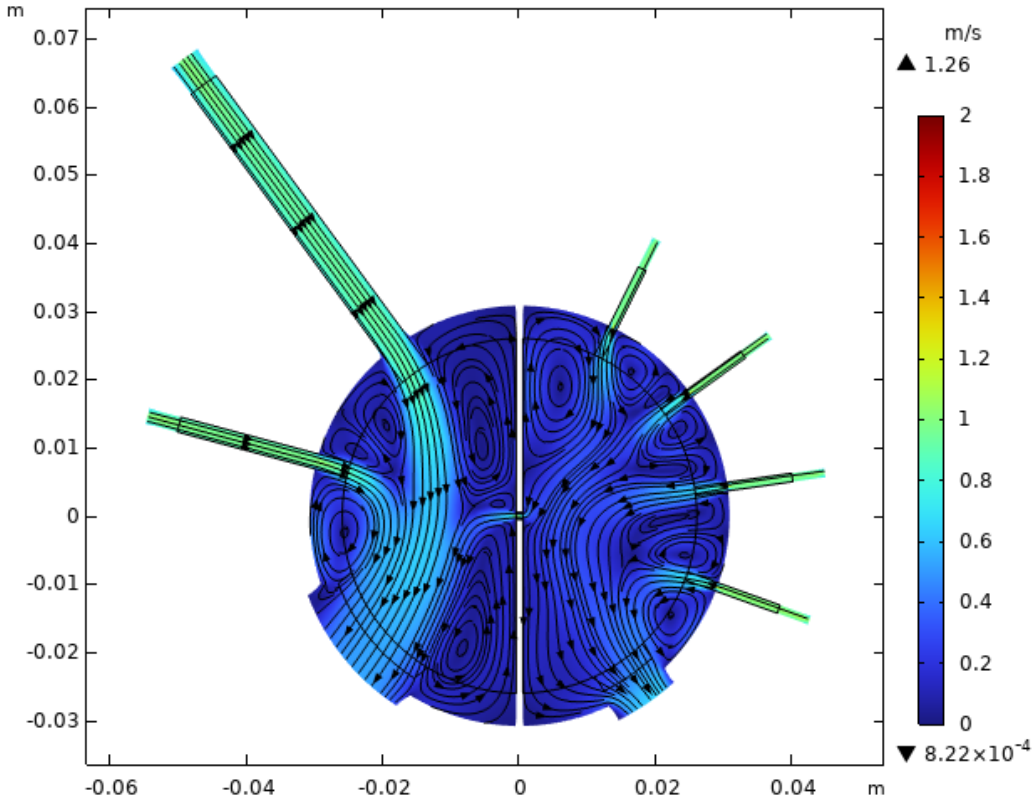

(b) 8 mm shunt

Figure 4.22: Velocity field of the transient CFD simulation halfway through the diastole ($t = 0.65$ s) in absence (a) and presence (b) of an 8 mm shunt

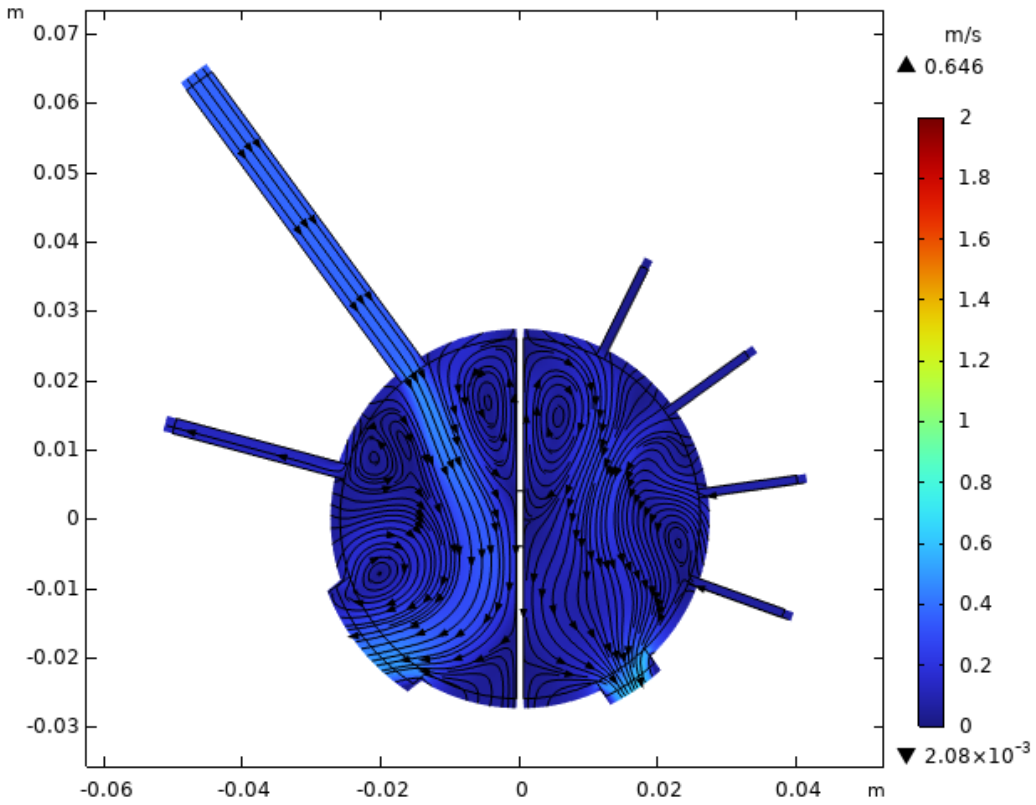

(a) Without shunt

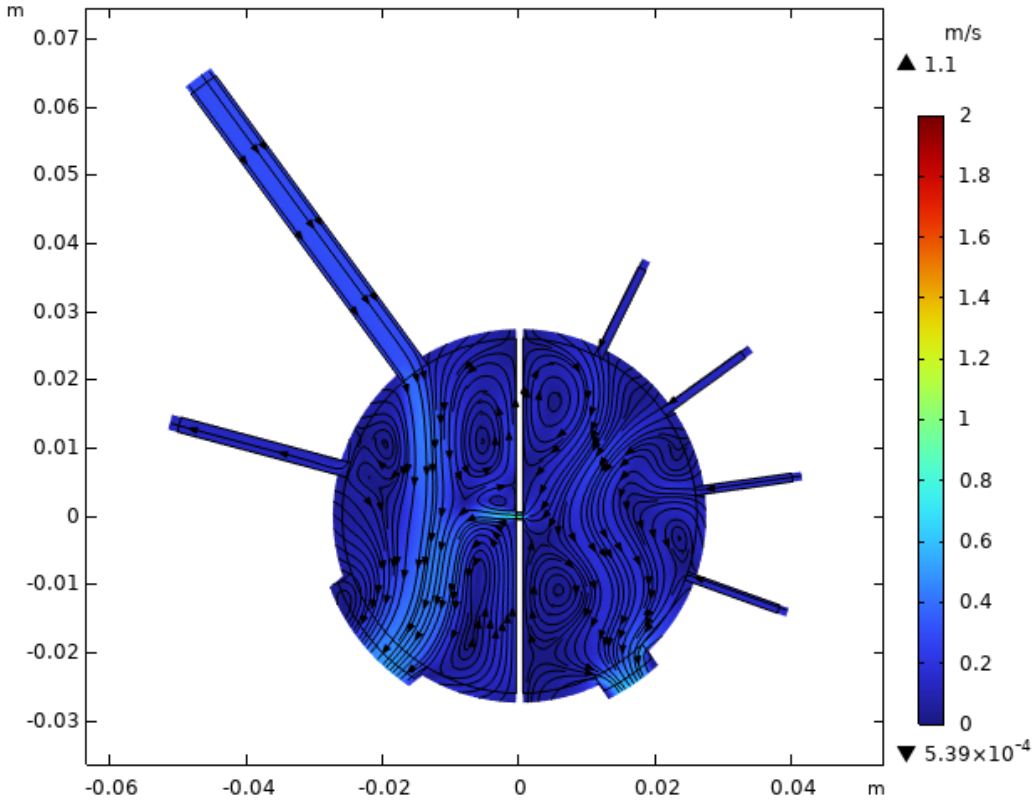

(b) 8 mm shunt

Figure 4.23: Velocity field of the transient CFD simulation at the end of diastole ($t = 0.95$ s) in absence (a) and presence (b) of an 8 mm shunt

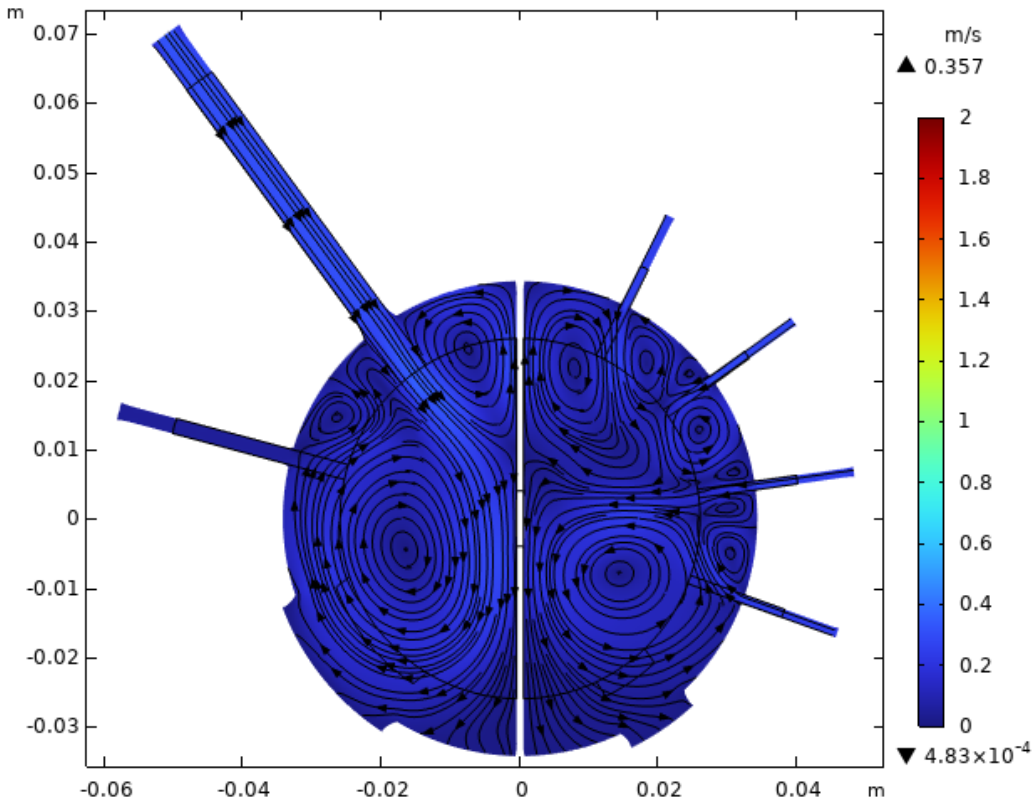

(a) Without shunt

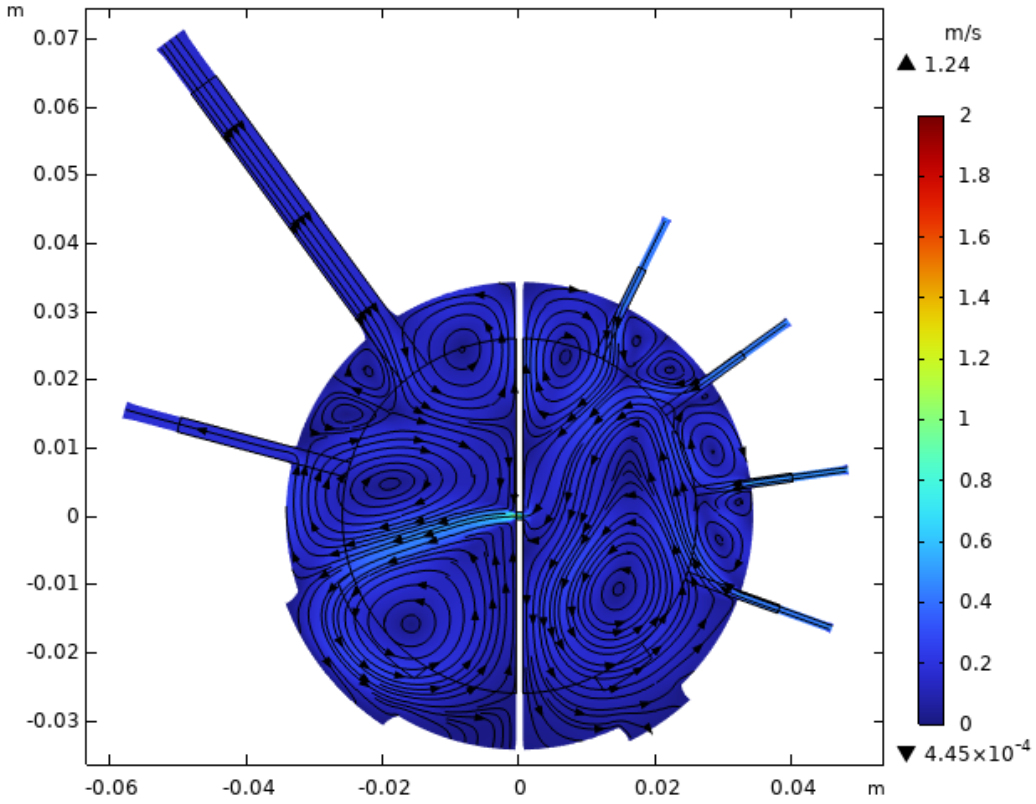

(b) 8 mm shunt

Figure 4.24: Velocity field of the transient CFD simulation at the end of systole ($t = 0.3$ s) in absence (a) and presence (b) of an 8 mm shunt

Flow rates

In Figure 4.25, the flow rates through the inlets, outlets and interatrial shunt are shown in absence (a) and presence (b) of an 8 mm interatrial shunt. By comparing the shapes of the graphs in Figure 4.25 to the graphs in Figure 4.11, it can be seen that this considers a simulation with moving walls. For easy comparison, the results from both figures are combined in Figure 4.26, where the solid lines show the results from Figure 4.25 and the dashed lines show the results from Figure 4.11. Note that the results from Figure 4.11 have been shifted in time due to the different setups of the two simulations. Especially the curves for the mitral and tricuspid valves clearly show the atrial contraction, which corresponds to the peak in flow rate around $t = 0.9$ s. However, the deformation can also, more subtly, be detected before the atrial contraction. Following the deformation from the start of the diastole ($t = 0.33$ s) in Figure 4.20, it can be seen that the decline in atrial volume is accelerating until about $t = 0.6$ s, where an inflection point is found. From this inflection point, the shrinking of the atria is slowing down, causing the flow rates through the outlet valves to decrease more rapidly. This can be seen in Figure 4.25 around $t = 0.6$ s. About 0.1 s later, at $t = 0.7$ s, this deceleration of the decrease in atrial volume has become an increase in atrial volume. As this increase happens almost linearly (see Figure 4.20), the acceleration of the increase in atrial volume has reduced to zero. Consequently, this causes the flow rates through the outlet valves to decrease less rapidly again, as can be seen in Figure 4.25 around $t = 0.7$ s. Finally, the deceleration of the increase in atrial volume around $t = 0.85$ s leads to the atrial contraction which has yet been discussed.

Furthermore, similar features can also be observed between the solid and dashed lines in Figure 4.26, such as the quick rise of the MV and PV flow rates and the slower rise of the TV and VC flow rates. As discussed previously, this is due to the difference in inlet-to-outlet pressure gradient between the left and right sides of the heart. After the peaks in flow rates, these start to decrease as the inlet pressures drop and the outlet pressures rise. Other than in the transient simulation without wall movement, however, the flow rates do not decrease almost linearly to zero, but fluctuate much more due to the wall movement. Also note that this has a significant influence on the magnitudes of the flow rates. At the start of the diastole, the peak mitral and tricuspid valve flow rates are now lower than they are without wall movement. Naturally, this is because also the PV and VC flow rates have reduced, respectively. A possible reason behind their reduction is that the computational domain in the current simulation is bigger than the static domain (used for the simulations in sections section 4.2 and section 4.3) for almost the entire diastole, see Figure 4.20. This likely increases the resistance between the inlets and outlets, therefore decreasing the flow rate.

Moreover, note that in absence of a shunt, the flow rate through the outlet is no longer equal to the flow rate through the inlets in each atrium. If the atria are decreasing in volume, such as during most of the diastole, the outlet flow rate is higher than the combined inlet flow rates of that atrium. If the atria are increasing in volume, such as during the systole, the inlet flow rates are higher than the outlet flow rates. Especially the latter is easy to see by comparing the results from the two simulations in Figure 4.26a. In both figures, the flow rates through the outlets are zero during the last 1/3 of the cardiac cycle. In the simulation without wall movement, this means that also the combined inlet flow rates are zero, which is shown by the dashed line. With wall movement, however, the atria are filled by the inlets during this phase. The amount of blood entering the atria during the systole is now equal to the increase in volume of the atria.

Another similarity between the current simulation and the one without wall movement is that the inferior vena cava inlet temporarily shows reversed flow. In section 4.3, it was seen that this starts at the end of the diastole and continues through the entire systolic phase. Including the deformation of the atria, it also starts at the end of the diastolic phase, but changes twice through the systole. Once again, the higher kinetic energy jet from the superior vena cava results in a reversed flow through the IVC in the stagnating flow field towards the end of the diastole. As the atrioventricular valves close and the atria start to expand, blood is sucked into the atria from both the inferior and superior vena cava, temporarily undoing the reversed flow through the IVC. As the atrial expansion stagnates towards the end of the systole, the higher kinetic energy SVC jet reverses the flow through the IVC again. Note that this description only applies to the current simulation. In reality, of course, the atrial deformation during the systole is not an active process, but is the result of the increased pressures in the pulmonary and systemic circulations. Blood is therefore not *sucked into* the atria, but the atrial walls are pushed outwards by the blood pressure.

Comparing the results from the transient simulations with and without wall movement in Figure 4.26b

shows the expected behavior of the interatrial shunt. As seen previously, the introduction of the shunt lowers the flow rate through the mitral valve, while it increases the flow rate through the tricuspid valve. In Figure 4.27, the instantaneous ratio of pulmonary to systemic blood flow over the diastole is shown. As in section 4.3, this figure shows that Qp:Qs is temporarily lower than 1 around the start of the diastole, which is the phase in which the MV flow rate peaks early. Once the flow rate through the tricuspid valve has reached the mitral valve flow rate at $t = 0.5$ s, however, Qp:Qs stays higher than 1 for the rest of the diastole. At first, it steadily grows as both outlet flow rates steadily decrease by the same amount. Only during the atrial contraction, both outlet flow rates rise by approximately the same amount, with a drop in Qp:Qs as a result. At the very end of the systole, a high peak can be seen in Figure 4.27. As the outlet valves close, both MV and TV flow rates drop to zero. Because this data point is generated in the time that these flow rates are reduced, Qp:Qs is temporarily very high as the MV flow rate is already much closer to zero than the TV flow rate. At the end of the diastole, the left ventricular volume is $2.92 \cdot 10^{-3}$ m^3, where $V_{RV_{ED}} = 3.64 \cdot 10^{-3}$ m^3. Therefore, the average Qp:Qs = 1.25, which is very close to the value of 1.24 that was estimated from the steady-state simulation and a bit lower than the value of 1.40 that was calculated from the transient simulation without wall movement.

Finally, considering the shunt flow itself, it is once again relatively constant throughout the cardiac cycle, hovering around $0.4 \cdot 10^{-3}$ m^3/s. Note that this is more than twice as low as the value of $1 \cdot 10^{-3}$ m^3/s found in section 4.3. The next section will show that the left-to-right pressure gradient has not significantly changed, so this is not the cause. Rather, this is likely the result of the deformation-induced flow field. Firstly, the inlet velocities are now lower as indicated by the flow rates in Figure 4.26. Secondly, another reason could be that the inlets are further away from the shunt during most of the diastole, directing less blood straight into the shunt as the jet has diverged more.

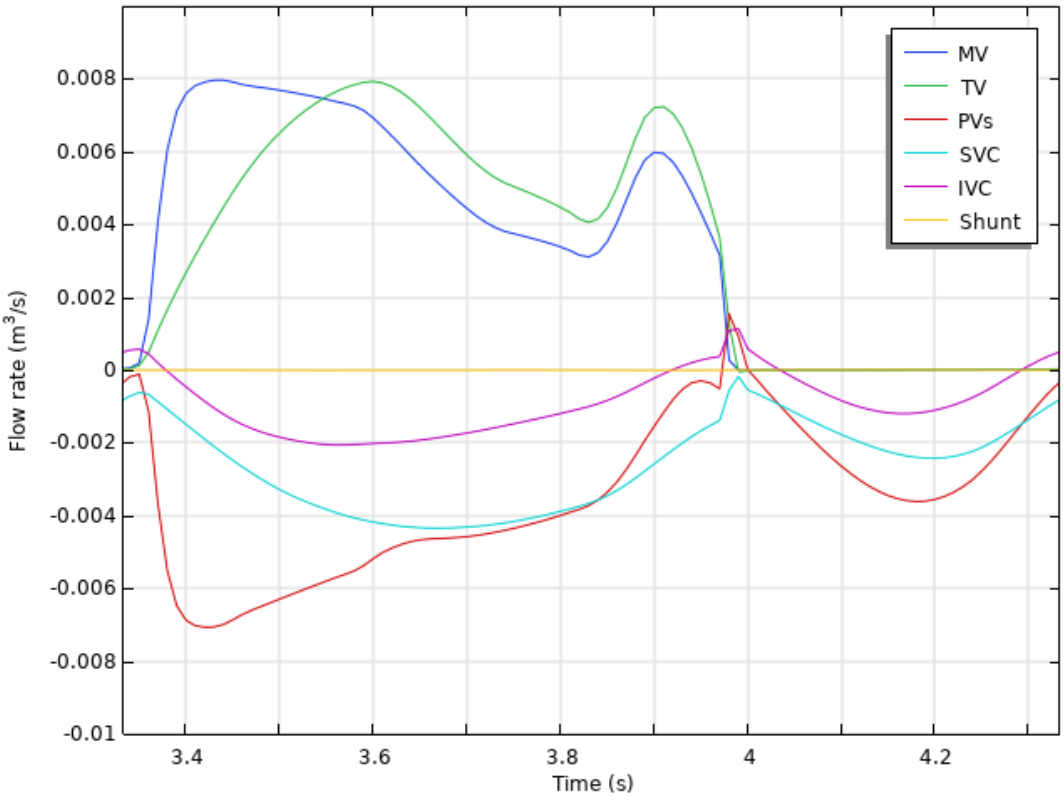

(a) Without shunt

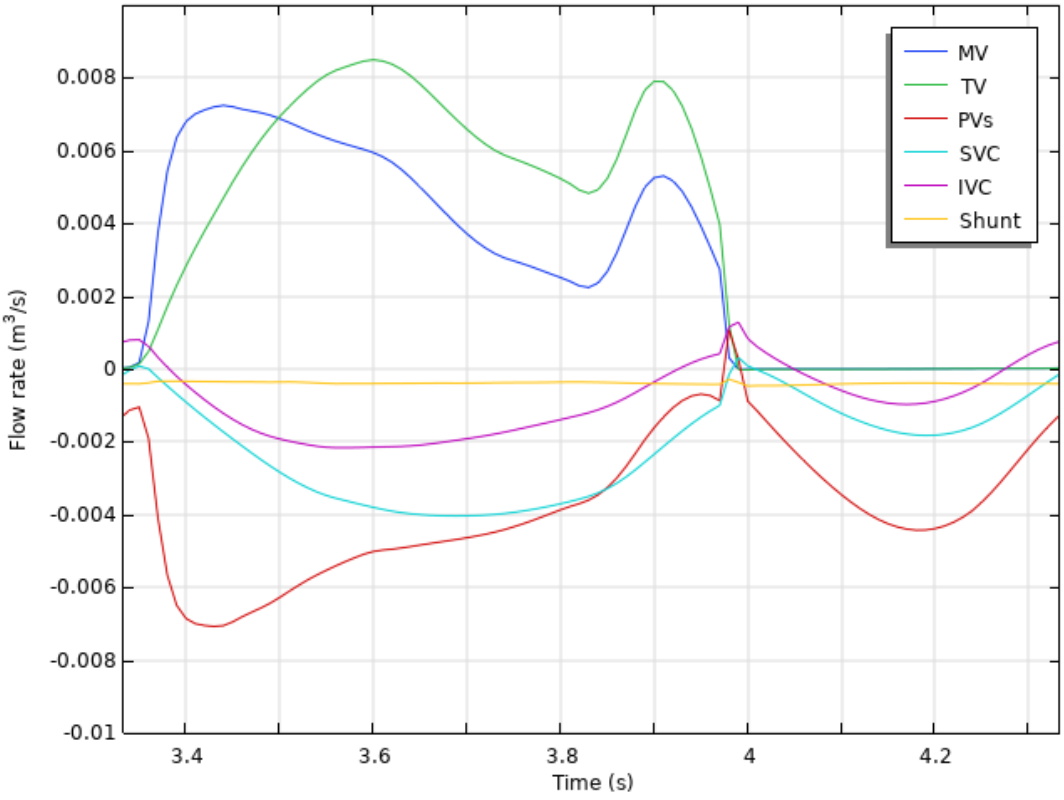

(b) 8 mm shunt

Figure 4.25: Flow rates through the inlets, outlets and interatrial shunt of the transient CFD simulation over one cardiac cycle in absence (a) and presence (b) of an 8 mm shunt. Positive values indicate flow rate exiting the domain and negative values indicate flow rate entering the domain. For the shunt, a negative value indicates a flow from left to right.

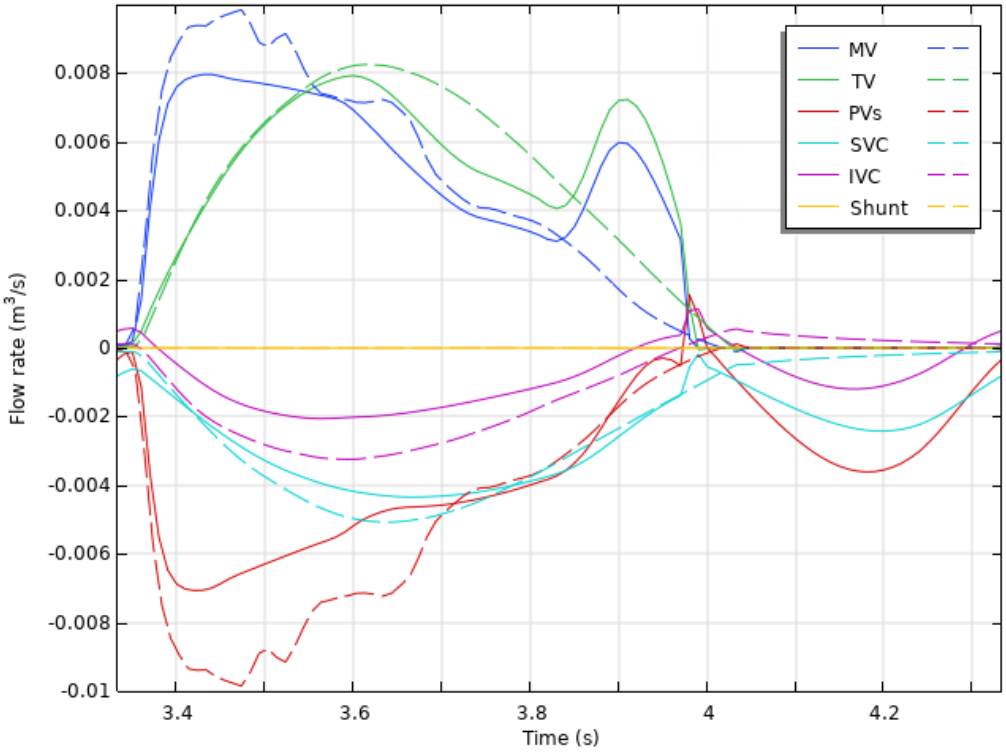

(a) Without shunt

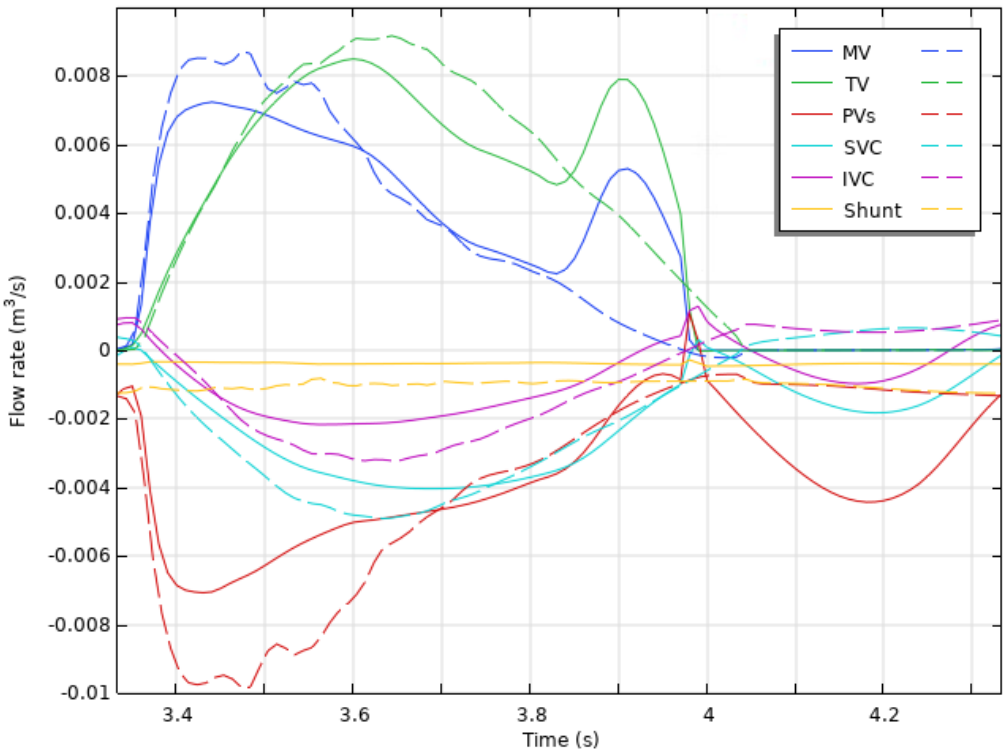

(b) 8 mm shunt

Figure 4.26: Comparison of the flow rates through the inlets, outlets and interatrial shunt between the transient CFD simulations with (solid line) and without (dashed line) wall movement in absence (a) and presence (b) of an 8 mm shunt. Positive values indicate flow rate exiting the domain and negative values indicate flow rate entering the domain. For the shunt, a negative value indicates a flow from left to right.

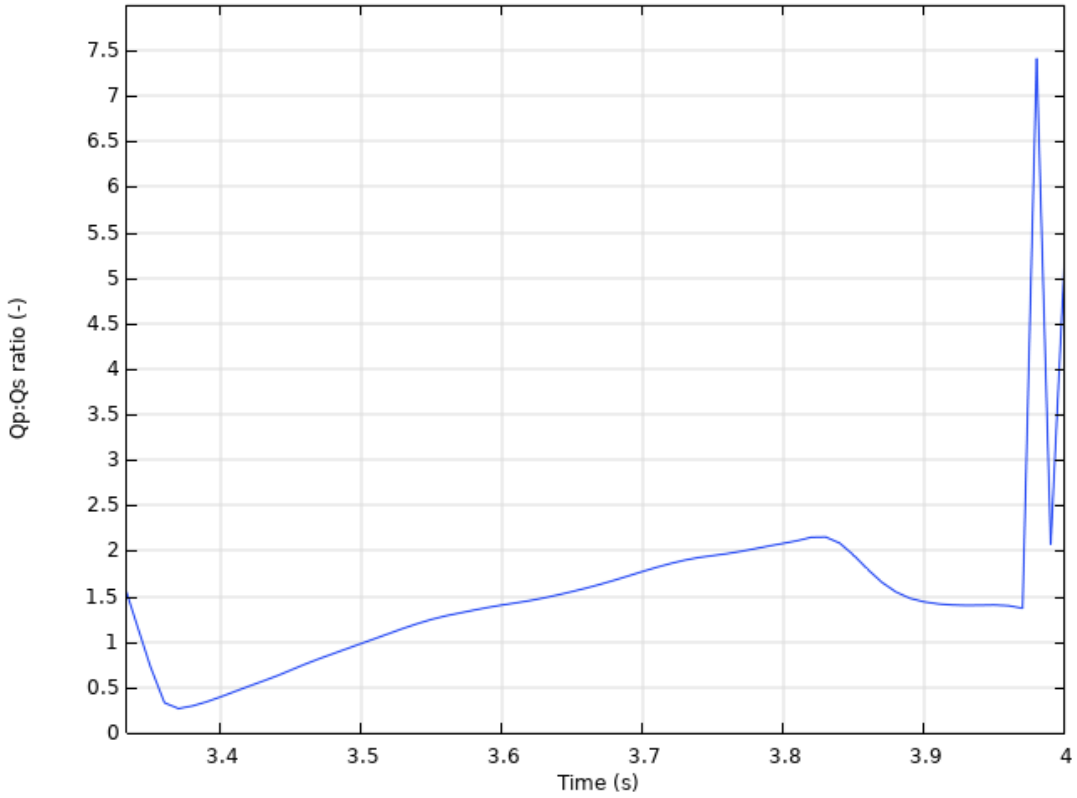

Figure 4.27: Instantaneous ratio of pulmonary to systemic blood flow over the diastolic phase of one cardiac cycle in presence of an 8 mm shunt

Pressure field

Figures 4.28 to 4.30 show the pressure fields in the atria in absence (a) and presence (b) of an 8 mm interatrial shunt at the three previously-introduced moments during the cardiac cycle. These moments are halfway through the diastole (Figure 4.28 at $t = 0.65$ s), at the end of diastole (Figure 4.29 at $t = 0.95$ s) and at the end of systole (Figure 4.30 at $t = 0.3$ s).

Halfway through the diastole, Figure 4.28 shows the pressure fields in absence (Figure 4.28a) and in presence (Figure 4.28b) of an 8 mm interatrial shunt. Compared to the transient simulation without wall movement, a similar pressure field is seen. The main difference is that the velocities through the inlets are lower for the current simulation, causing a slightly more stagnant flow field with fewer pressure fluctuations. This can be seen in Figure 4.28, where the pressure fields show a nearly constant value throughout each atrium, quite different from those in Figure 4.14. Another difference between the two simulations is found in the pulmonary vein inlets in Figure 4.28. As the inlets move together with the walls of the atria, the inlets are moving inwards at $t = 0.65$ s. In the simulation, this has resulted in pressure fluctuations in these inlets, which can be seen as the orange color in the pulmonary veins. In reality, this would not be the case as such a boundary is not present. However, as these pressure fluctuations are restricted to the inlet veins only, they are not expected to have a significant influence on the overall results. Considering the 8 mm interatrial shunt, it can once again be seen that left atrial pressure is lowered, as the difference in color between the left atria in Figure 4.28a and Figure 4.28b indicates. Although difficult to see from the pressure fields, right atrial pressure has slightly risen as a result, as will later be shown.

In the transient simulation described in section 4.3, the end of the diastolic phase is characterized by a stagnant flow field and few pressure fluctuations, as inlet and outlet pressures have converged to one another. As discussed previously for the velocity field, this is significantly different in the current simulation due to the atrial contraction. Next to a less stagnant velocity field as seen in Figure 4.23 compared to Figure 4.9, a different pressure field is seen in Figure 4.29 compared to Figure 4.15. Though both pressure fields are relatively constant, the magnitudes are quite different. This is a direct result of the atrial contraction, as the rapid decrease in atrial volume causes an elevated pressure in the atria.

Consequently, this causes a high velocity jet through the outlets, which is why the outlets show significantly lower pressures. This is especially well visible for the mitral valve outlet in Figure 4.29. Once again, note that Figure 4.29b shows a much lower pressure throughout the left atrium than Figure 4.29a does. In this case, the increased pressure in the right atrium can also be seen, which is indicated by the lighter color in the bottom figure.

When the atrioventricular valves have closed and the systole commences, the pulmonary and systemic circulations are filled with blood from the ventricles. Though the expansion of the atria is prescribed in the current simulation, this expansion is a result of the rise in pulmonary and systemic pressures in reality. In contrast to the simulation described in section 4.3, this causes significant flow rates through the inlets during this phase of the heart cycle, as could be seen in Figures 4.24 and 4.25. In terms of the pressure field, however, this is not evident, as Figure 4.30 shows pressure fields without any visible fluctuations. Rather, the pressures are distributed almost evenly throughout each atrium, both in absence and presence of an interatrial shunt. At this point in the cardiac cycle, the atrial pressures are at their highest, as the pulmonary and systemic reservoirs are at their maximum volumes and pressures, influencing the pressures in the atria. This is clearly seen by comparing Figure 4.30 to Figure 4.28 and Figure 4.29. Where the left atria now color dark red, indicating pressures high on the scale, the left atria colored green (Figure 4.28) to orange (Figure 4.29) during the diastole. Similarly, the blue-colored right atria are of a much lighter shade in Figure 4.30 than in Figures 4.28 and 4.29. Also note the effectiveness of the interatrial shunt by comparing the intra-atrial pressures between Figure 4.30a and Figure 4.30b.

Looking at the evolution of the pulmonary, systemic, left and right atrial, and left and right ventricular pressures over the cardiac cycle in Figure 4.31, various similarities and differences can be seen compared to Figure 4.18. For easy comparison, the results from both figures are combined in Figure 4.32, where the solid lines show the results from Figure 4.31 and the dashed lines show the results from Figure 4.18. Note that the results from Figure 4.18 have been shifted in time due to the different setups of the two simulations. Considering the pulmonary pressure, this is 16.5 mmHg at the start of the diastole in both simulations without a shunt. In the current simulation, the minimum pulmonary pressure drops to around 12 mmHg[1] at the end of the diastole, whereas it drops to below 11 mmHg at the end of the diastole in absence of wall movement. This means that the pulmonary reservoir is emptied less in the current simulation, which is in line with the observation that the inlet flow rates are lower. Meanwhile, the left ventricular pressure rises from 5.8 to 11 mmHg in both simulations without a shunt, meaning that the left ventricle is filled as much with or without wall movement. This difference in volume added by the pulmonary reservoir is due to the wall movement. In the transient simulation without wall movement, atrial volume stays constant, so all blood entering the atrium through the inlet instantly exits the atrium through the outlet. This means that the volume entering the atrium equals the volume exiting the atrium. The application of the moving walls in the current simulation has altered this. At the start of the diastole, the atrial volume is namely bigger than the atrial volume at the end of the diastole. This difference in volume is the extra volume that is added to the ventricle on top of the volume from the pulmonary circulation. Considering the opposite side of the heart, the systemic pressure starts around 2.5 mmHg at the start of diastole and reduces to 1 mmHg at the end of it. Similar to the left heart, this reduction in systemic pressure is slightly larger in the transient simulation without moving walls for an equal rise in ventricular pressure.

The biggest difference between the current simulation and the simulation described in section 4.3 can be seen in the atrial pressures. At the start of the diastole, the outlet valves open, releasing the pressure and volume built up in the atria during the systolic phase. This is clearly visible in Figure 4.31 around $t = 0.33$ s. As the atrial volume decreases, the atrial pressures slowly but steadily increase. In reality, however, atrial pressures would decrease more slowly over the first half of the diastole and surely would not rise [35]. This could mean that the outlets offer too little resistance in the CFD simulations, causing the outlet flow rates to become too high and the pressures to drop too quickly. Possibly, this is due to the simple modeling of the atrioventricular valves, whereas the valve leaflets might be more resistant in reality. From halfway through the diastole, the atrial pressures stay relatively constant around 10 and 1 mmHg for the left and right atrium, respectively. This is until the clear bump in atrial pressures from around $t = 0.8$ s, followed by a spike. This indicates the atrial contraction followed by the closure of the outlet valves. As discussed previously, this is the clearest indication that this

[1] As mentioned in section 4.3, the minimum pulmonary pressure is much lower in reality, around 4 mmHg. This is not achieved in the CFD simulations due to the blood's momentum being underestimated.

simulation considers wall movement, as this is not visible in the results from the simulation without wall movement. Firstly, the rapid decrease in volume of the atria during the atrial systole significantly increases the pressure in the atria at the end of the diastole. As a result, this causes a second peak in flow rate through the mitral and tricuspid valves, as seen in Figure 4.25. Note that this also affects the ventricular pressure curves, which suddenly show a steeper rise due to this atrial contraction. Since this is quickly followed by the closure of these valves, the pressure rapidly rises in the atria. The resulting pressure peaks are much higher in the current simulation than they are in the simulation without wall movement. Naturally, this is due to the higher outlet flow rates at the moment that the valves close. Also note the dip in pressure right after the pressure peak.

After the closure of the valves, the atrial pressures are lower than before the pressure peak. This is because the atria are rapidly contracting at the end of the diastole, causing a high pressure, whereas the atria are relaxing and increasing in volume at the start of the systole. As the pulmonary and systemic pressures increase over the systole, also the atrial pressures increase, although these are lower than the inlet pressures for most of this phase. In the transient simulation without wall movement in absence of a shunt, the inlet and atrial pressures are equal during the entire systolic phase. Once more, this difference is caused by the wall movement, as the increasing volume of the atria causes an inlet-to-atrium pressure gradient with an inflow through the inlet veins as a result. In reality, of course, the elevated pulmonary and systemic pressures are the cause of this pressure gradient, causing inflow through the inlet veins and the increase in atrial volume, rather than the other way around. Therefore, the temporary decrease in atrial pressure at the start of the systole is not realistic, but is an artefact of the prescribed deformation. Towards the end of the systole, it can be seen that the atrial pressures rise above the inlet pressures. Also this is due to the movement of the walls, as the inlet jets have gained momentum during the systole. Now that the increase in atrial volume decelerates, this momentum results in an overshoot in atrial pressure, temporarily reversing the inlet-to-atrial pressure gradient.

The effectiveness of the shunt is determined by comparing Figure 4.31a to Figure 4.31b, studying the pressure drops and rises that have come as a result of the interatrial shunt. Considering the left side of the heart, the pulmonary pressure peak has reduced by 0.8 mmHg from 16.5 to 15.7 mmHg and its minimum has reduced by 1 mmHg from 12 to 11 mmHg. Peak left atrial pressure has experienced an even greater drop of 1.1 mmHg from 16.9 to 15.8 mmHg, where this pressure at the start of the diastole has reduced by 0.5 mmHg from 8.8 to 8.3 mmHg. Meanwhile, the peak left ventricular pressure has dropped from 10.8 to 10.1 mmHg: a reduction of 0.7 mmHg. As previously explained in section 4.3, the minimum ventricular pressures have remained the same by design. On the right side of the heart, the shunt has increased the systemic, right atrial and right ventricular pressures. Without an interatrial communication, the pressure in the systemic reservoir fluctuates between 1.1 and 2.5 mmHg, whereas this fluctuates between 1.4 and 2.8 mmHg in presence of a shunt. This is a rise of 0.3 mmHg of the systemic pressure over the entire cardiac cycle. Similarly, peak right ventricular pressure has risen from 2.6 to 2.9 mmHg. Peak right atrial pressure has increased by 0.5 mmHg from 3.9 to 4.4 mmHg, while the start-of-diastole pressure has remained unchanged at 0.2 mmHg. Note that the peak right atrial pressure is found just before the end of the systole, as this is caused by the momentum from the inlet jets.

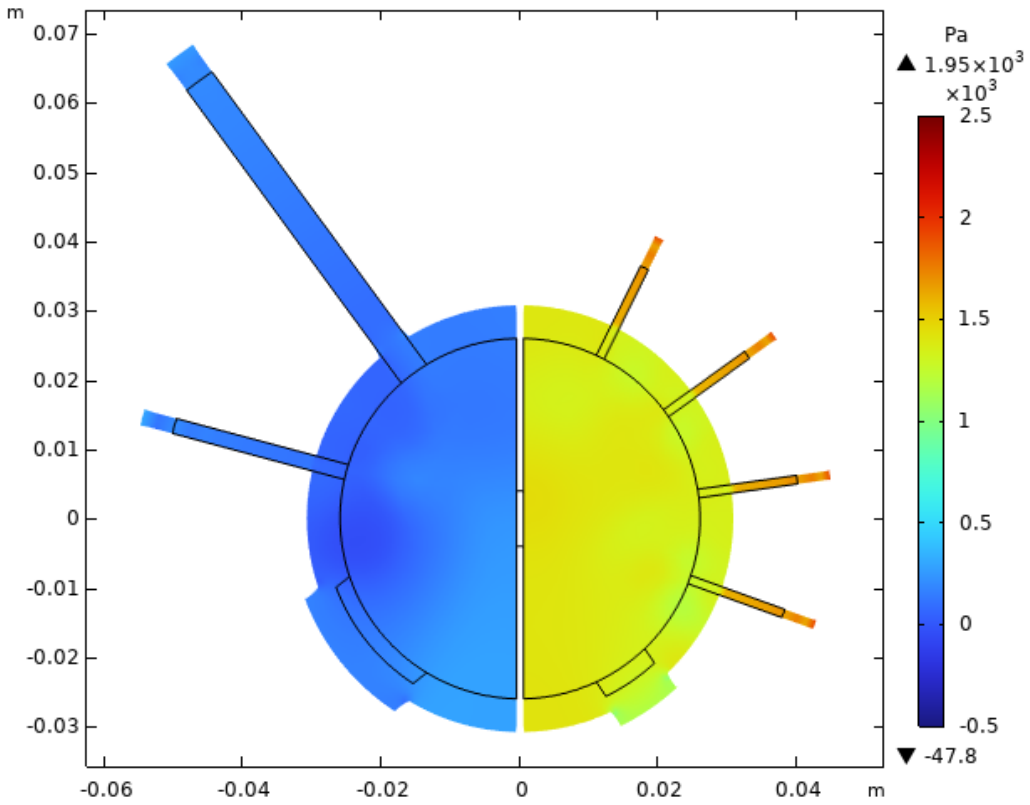

(a) Without shunt

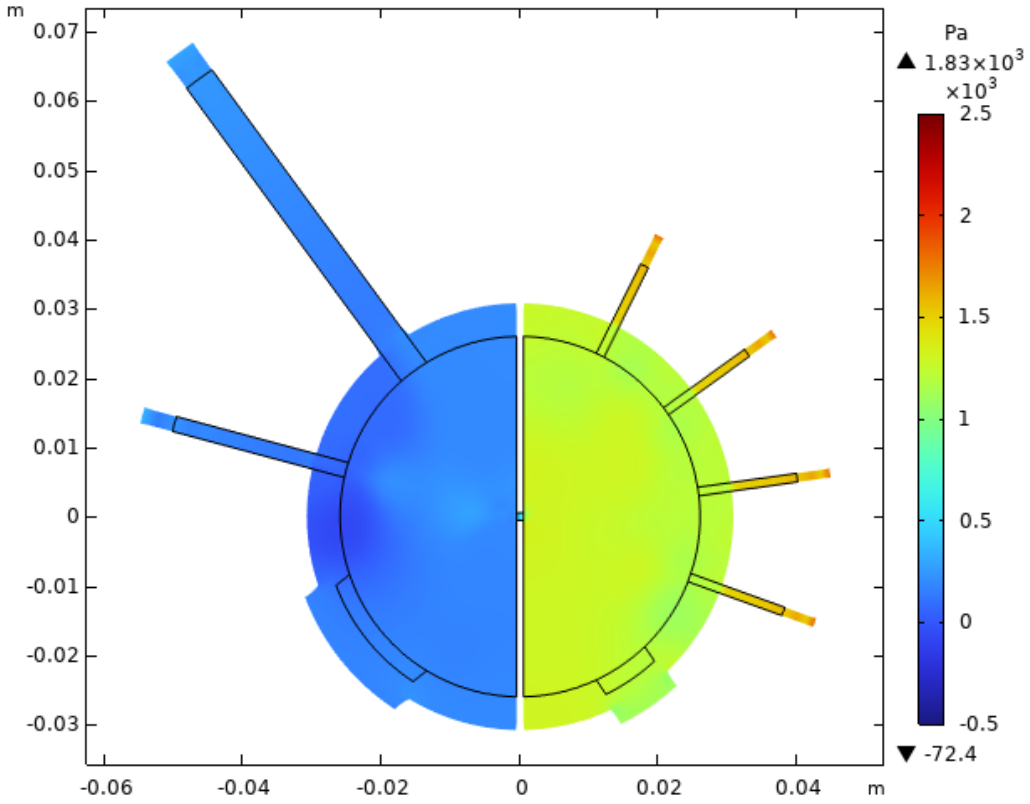

(b) 8 mm shunt

Figure 4.28: Pressure field of the transient CFD simulation halfway through the diastole ($t = 0.65$ s) in absence (a) and presence (b) of an 8 mm shunt

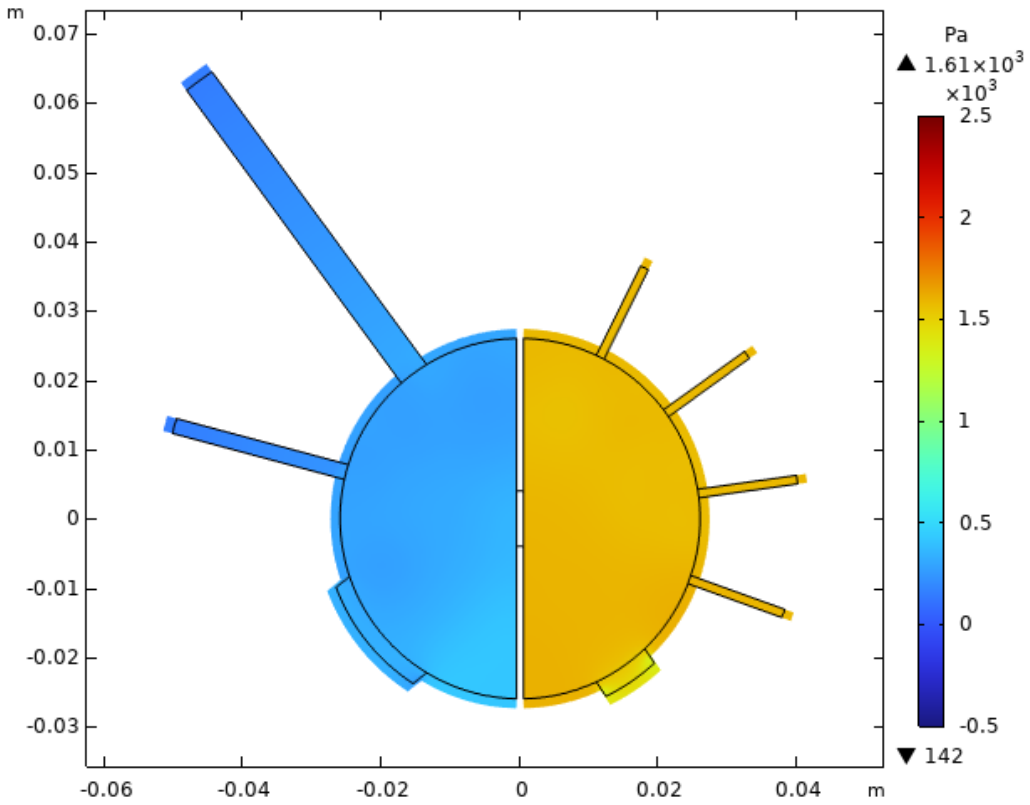

(a) Without shunt

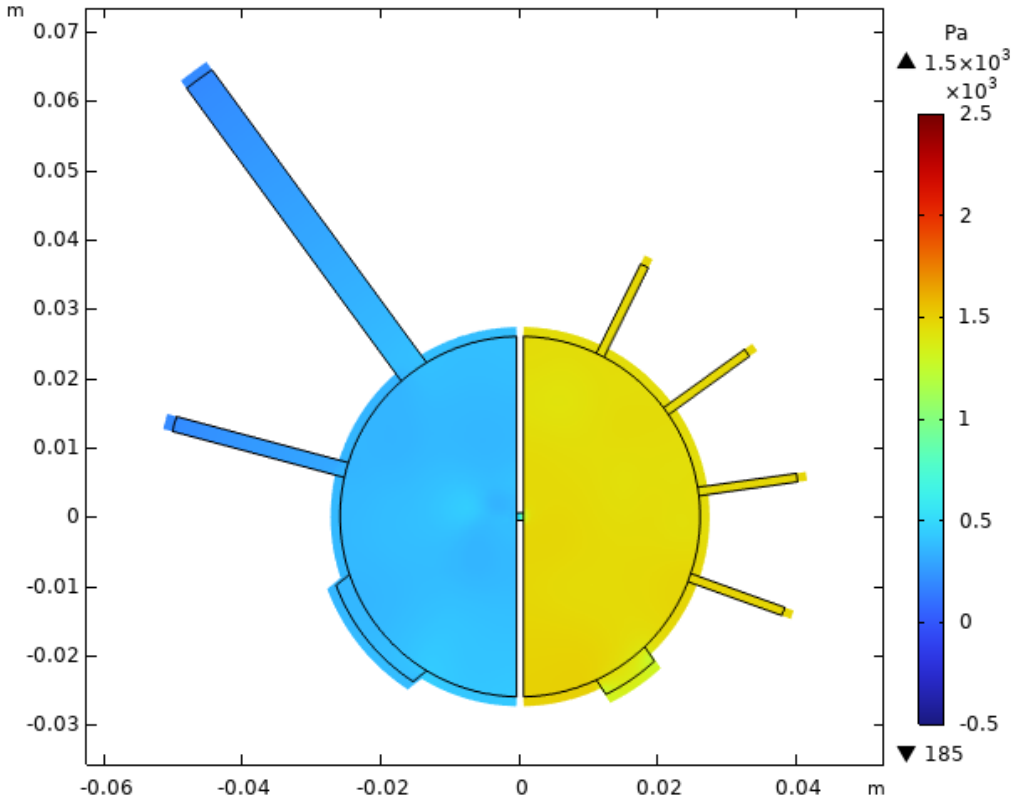

(b) 8 mm shunt

Figure 4.29: Pressure field of the transient CFD simulation at the end of diastole ($t = 0.95$ s) in absence (a) and presence (b) of an 8 mm shunt

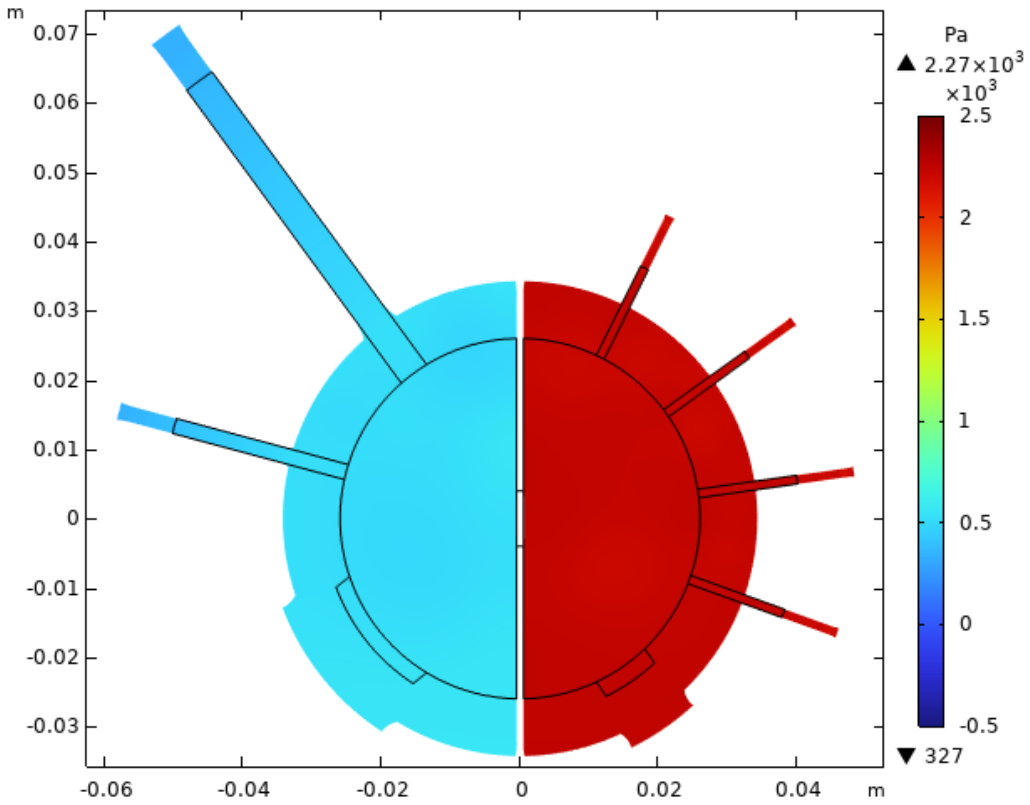

(a) Without shunt

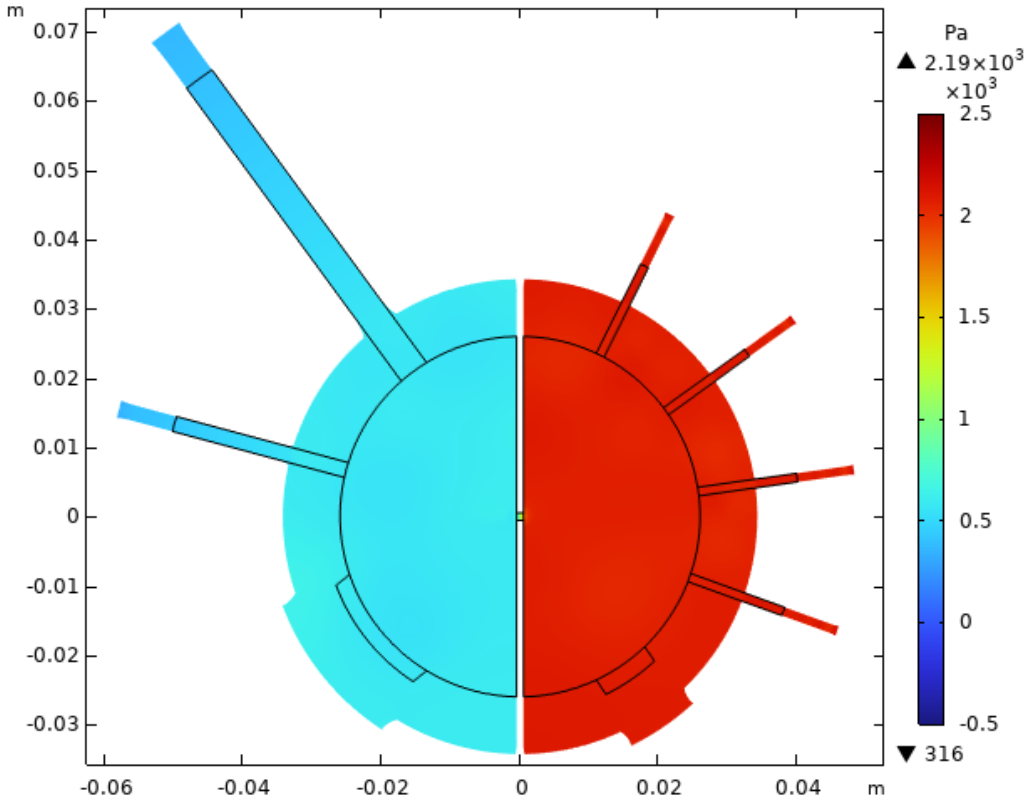

(b) 8 mm shunt

Figure 4.30: Pressure field of the transient CFD simulation at the end of systole ($t = 0.3$ s) in absence (a) and presence (b) of an 8 mm shunt

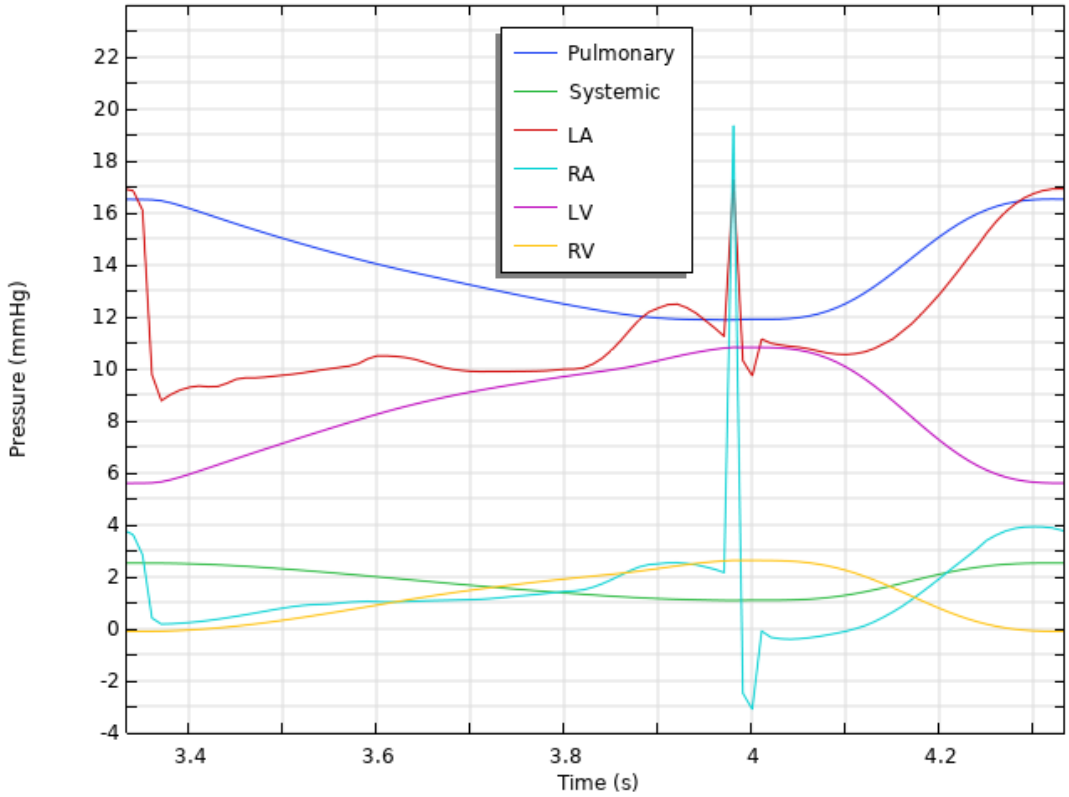

(a) Without shunt

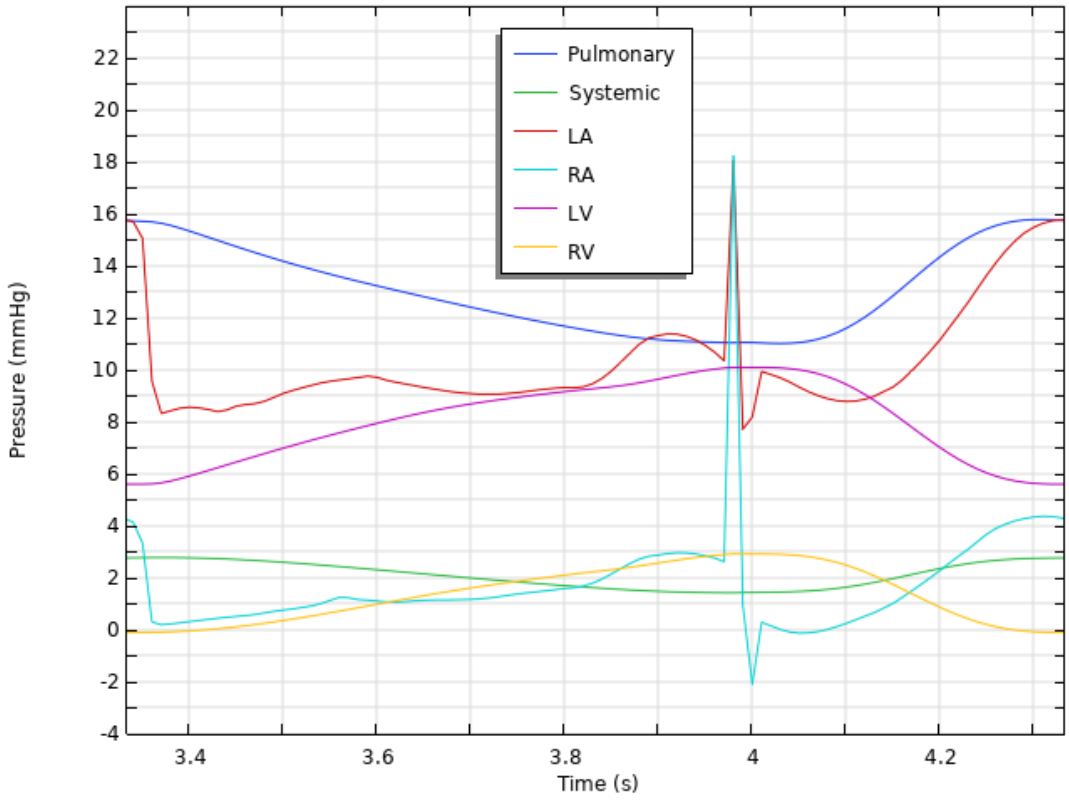

(b) 8 mm shunt

Figure 4.31: Pulmonary, systemic, left (LA) and right (RA) atrial and left (LV) and right (RV) ventricular pressures of the transient CFD simulation over one cardiac cycle in absence (a) and presence (b) of an 8 mm shunt

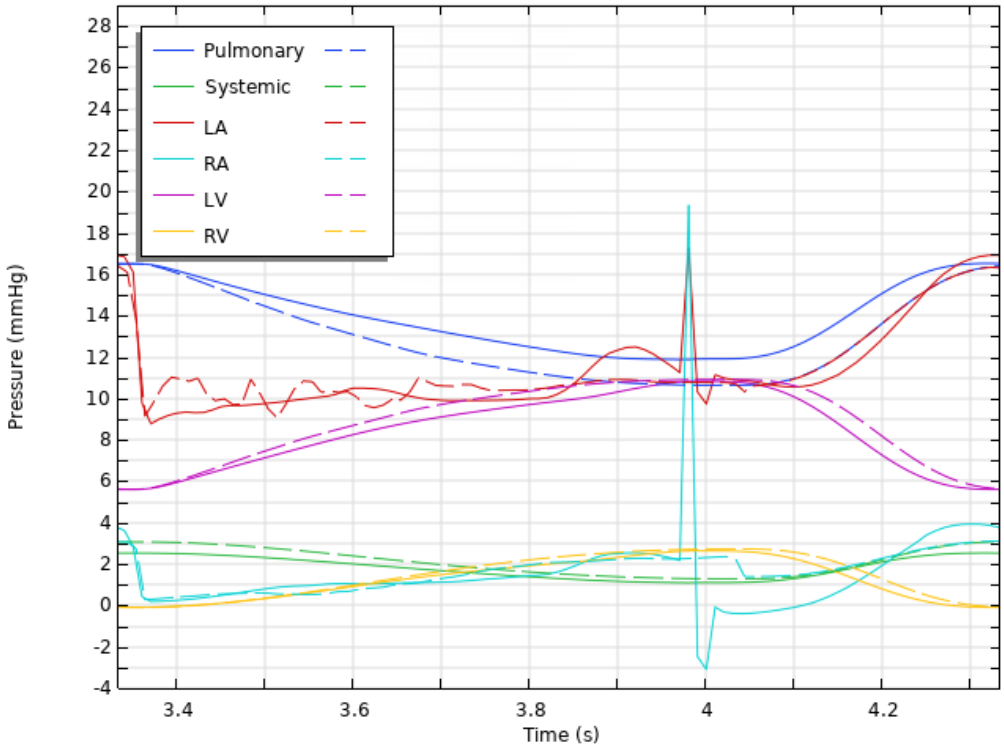

(a) Without shunt

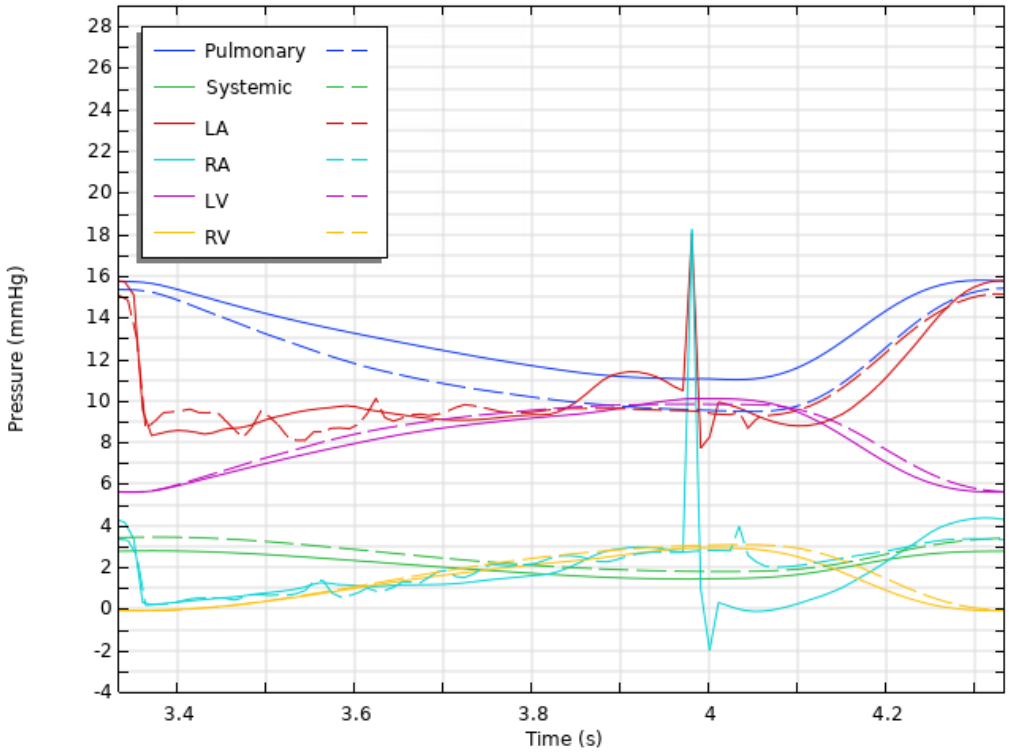

(b) 8 mm shunt

Figure 4.32: Comparison of the pulmonary, systemic, left (LA) and right (RA) atrial and left (LV) and right (RV) ventricular pressures between the transient CFD simulations with (solid line) and without (dashed line) wall movement in absence (a) and presence (b) of an 8 mm shunt

4.4.2. Patient-specific optimal shunt diameter

This part of the report investigates the patient-specific optimal shunt diameter in order to answer the research question:

> *What is the optimal diameter of an interatrial shunt for different patients with heart failure with preserved ejection fraction?*

This question is answered by applying a range of shunt sizes to a range of patients and finding the optimal shunt diameter for each patient. The different patients are obtained by changing the boundary conditions of the simulation and in particular the elastance of the left ventricle E_{LV}. Increasing this value namely causes the left ventricular pressure to rise more for a given increase in volume. This behavior represents a patient with a left ventricle of increased stiffness, which is a hallmark feature of heart failure with preserved ejection fraction [24]. Therefore, left ventricular elastance is a suitable parameter to vary to represent patients with HFpEF of different severity. To determine the optimal shunt diameter for each patient, note that the simulated conditions represent a patient at rest. In these conditions, pulmonary (capillary wedge) pressure should not exceed 15 mmHg for healthy patients [30]. Therefore, the diameter of a shunt is considered optimal if it is the smallest diameter that manages to reduce the peak pulmonary pressure to below 15 mmHg. In the current research, shunts with diameters from 2 to 20 mm are applied to each patient in steps of 2 mm.

Patient 1

The first patient considers the pressure characteristics previously presented in Figure 4.31a. As discussed in section 4.4, this patient has a left ventricular elastance $E_{LV} = 1540$ mmHg/m^3 (see Table 4.6), resulting in a peak pulmonary pressure of 16.5 mmHg. Section 4.4 has already shown the results if an interatrial shunt with a fenestration diameter of 8 mm is applied. The results in this section will show the effects of various shunt sizes on this patient. Since the left ventricular pressures of this patient correspond to those of a healthy person, this patient is referred to as 'normal' in the results.

Patient 2

For the second patient, the left ventricular elastance E_{LV} is increased by 50% compared to the first patient. Therefore, patient 2 is characterized by a left ventricular elastance of $E_{LV} = 2310$ mmHg/m^3. As this patient has a stiffer left ventricle than the first patient, 'stiffer' refers to this patient in the results.

Patient 3

The third and final patient has an even stiffer left ventricle than the second patient. This is modeled by doubling the left ventricular elastance of the first patient. Therefore, the left ventricular elastance of patient 3 is $E_{LV} = 3080$ mmHg/m^3. Since this patient has the stiffest left ventricle of all the patients, this patient is referred to as 'stiffest' in the results.

Results

Pressures

In Figures 4.33 and 4.34, the results are shown regarding the peak pulmonary pressure. Figure 4.33a shows how the peak pulmonary pressure is affected by different shunt sizes in each of the patients. Figure 4.34a is a direct result of the former, since the latter shows the drop in peak pulmonary pressure as a result of different shunt sizes in each of the patients. Finally, Figure 4.34b shows the sensitivity of different shunt sizes, defined as the derivative of Figure 4.34a. In all figures, a shunt diameter of 0 mm naturally represents the situation in absence of an interatrial shunt.

First of all, it can be seen in Figure 4.33a that varying left ventricular elastance has indeed resulted in patients with different pressure characteristics. As expected, a stiffer left ventricle results in elevated pulmonary pressures and therefore a higher peak pulmonary pressure. From this, it can be seen that patient 1 has a peak pulmonary pressure of 16.5 mmHg (as determined earlier), patient 2 has a peak pulmonary pressure of 17.2 mmHg and patient 3 has a peak pulmonary pressure of almost 18 mmHg. In all the patients, it can be seen that any shunt manages to reduce this peak pulmonary pressure and a larger shunt always results in a larger reduction. It is however interesting to note from both Figure 4.33a and Figure 4.34a that the smallest as well as the largest shunts show somewhat of a plateau. For the smallest shunts up to 6 mm, the reductions in peak pulmonary pressure are relatively small, whereas the introduction of an 8 mm interatrial shunt suddenly causes a much more significant pressure drop

and a 10 mm shunt even more. From a 12 mm shunt on, the reductions in peak pulmonary pressure between two shunts start to decrease again, forming another plateau for the largest shunts. This means that the smallest shunts are little effective and also that there is little difference between the effects of very large shunts. The highest sensitivity to shunt diameter is found in the range between 8 and 12 mm. Another way to show this is through the derivative of Figure 4.34a, which is shown in Figure 4.34b and is termed the shunt sensitivity. This figure confirms that the reduction in peak pulmonary pressure is the most sensitive to shunt diameter in the range between 8 and 12 mm.

The described behavior matches the findings by Kaye et al. [30] (see Figure 4.33b), as the Pulmonary Capillary Wedge Pressure (PCWP) in their research corresponds to the pulmonary pressure in the current research. Although Figure 4.33b shows the highest sensitivity for a different range of shunt diameters, similar behavior is clearly present.

Another effect of the shunt diameter that can be concluded from Figure 4.33 is that the pressure drop that results from a shunt is a function of the left ventricular elastance E_{LV}. In Figure 4.34a, it can namely be seen that the pressure drop for each shunt is always highest for patient 3. This is the patient with the stiffest left ventricle and the highest E_{LV}. In Figure 4.33a, this effect can also be seen by the peak pulmonary pressure curves converging as the shunt diameter increases. Whereas the difference in peak pulmonary pressure is about 1.5 mmHg between patients 1 and 3 in absence of a shunt, it is reduced to less than 0.5 mmHg in presence of a 20 mm interatrial shunt due to its higher pressure drop in patient 3. From this observation, it is expected that enlarging the shunts even further would result in all peak pulmonary pressure curves converging to approximately the same plateau. This would mean that very large shunts would result in similar peak pulmonary pressures, regardless of a patient's peak pulmonary pressure in absence of an interatrial shunt.

Finally, the optimal shunt diameter as defined previously can be determined from Figure 4.33a for each of the three patients. In this figure, it can be seen that a shunt diameter between 10 and 12 mm is optimal for patient 1, as it is the smallest shunt that reduces its peak pulmonary pressure to below 15 mmHg. For patient 2, a shunt with a diameter between 12 and 14 mm is optimal, whereas patient 3 requires a shunt between 14 and 16 mm diameter.

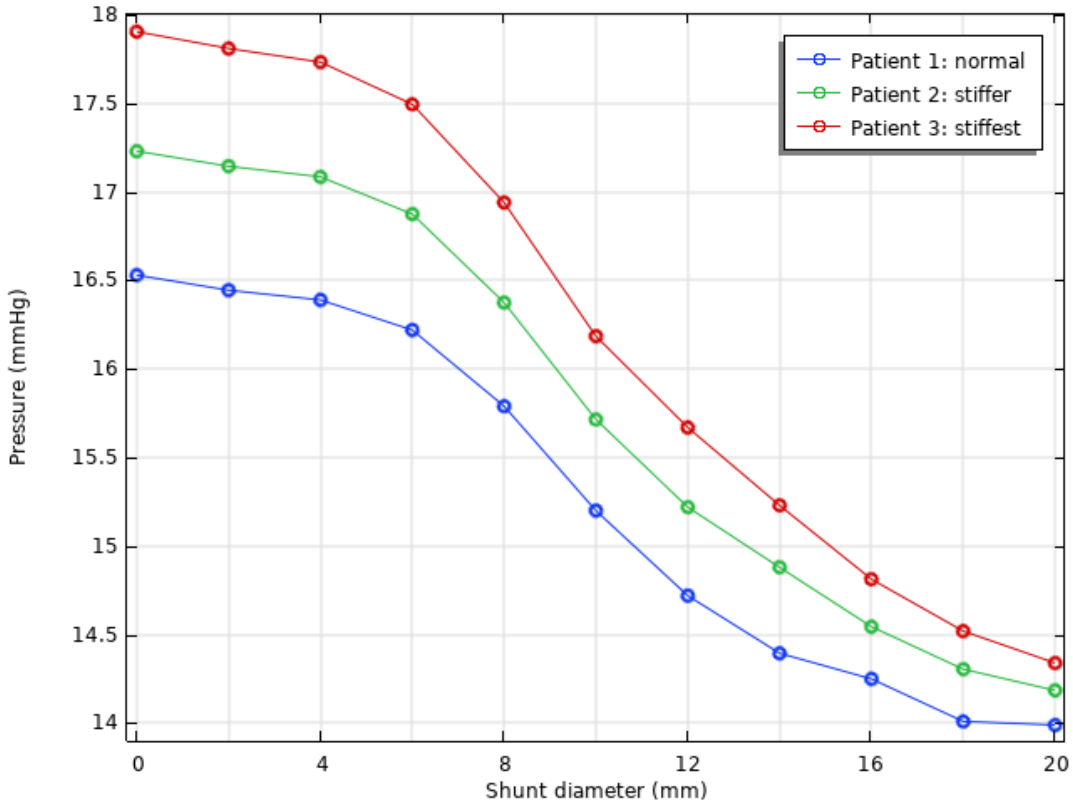

(a) Peak pulmonary pressure

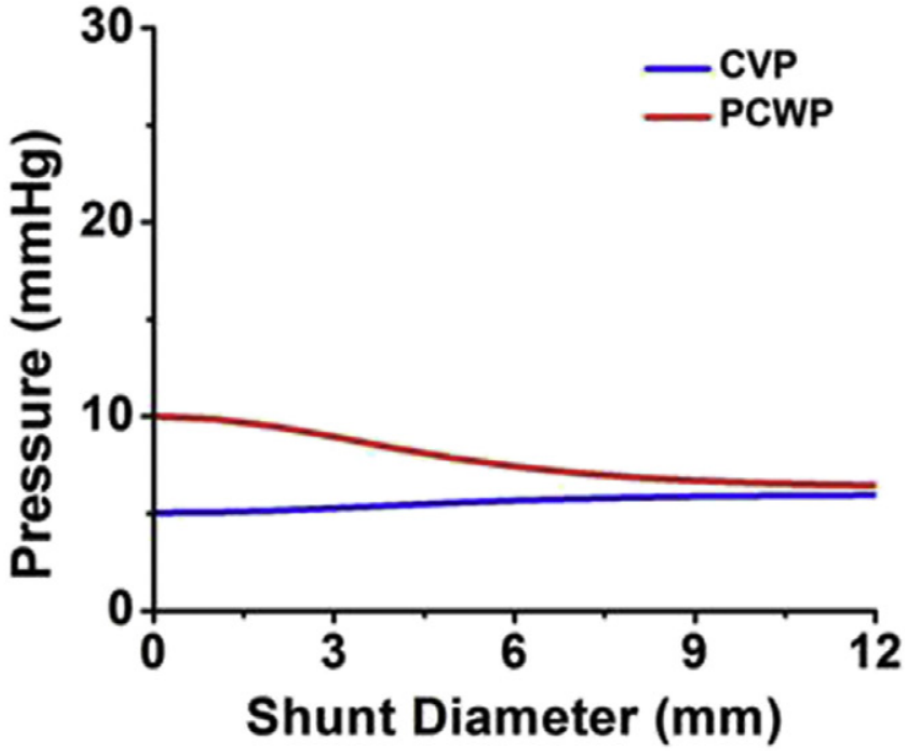

(b) Drop in peak pulmonary pressure

Figure 4.33: Peak pulmonary pressure as a function of shunt diameter for three patients of varying left ventricular stiffness (a) compared to Pulmonary Capillary Wedge Pressure (PCWP) and Central Venous Pressure (CVP) as a function of shunt diameter according to a lumped element model by Kaye et al. [30] (b)

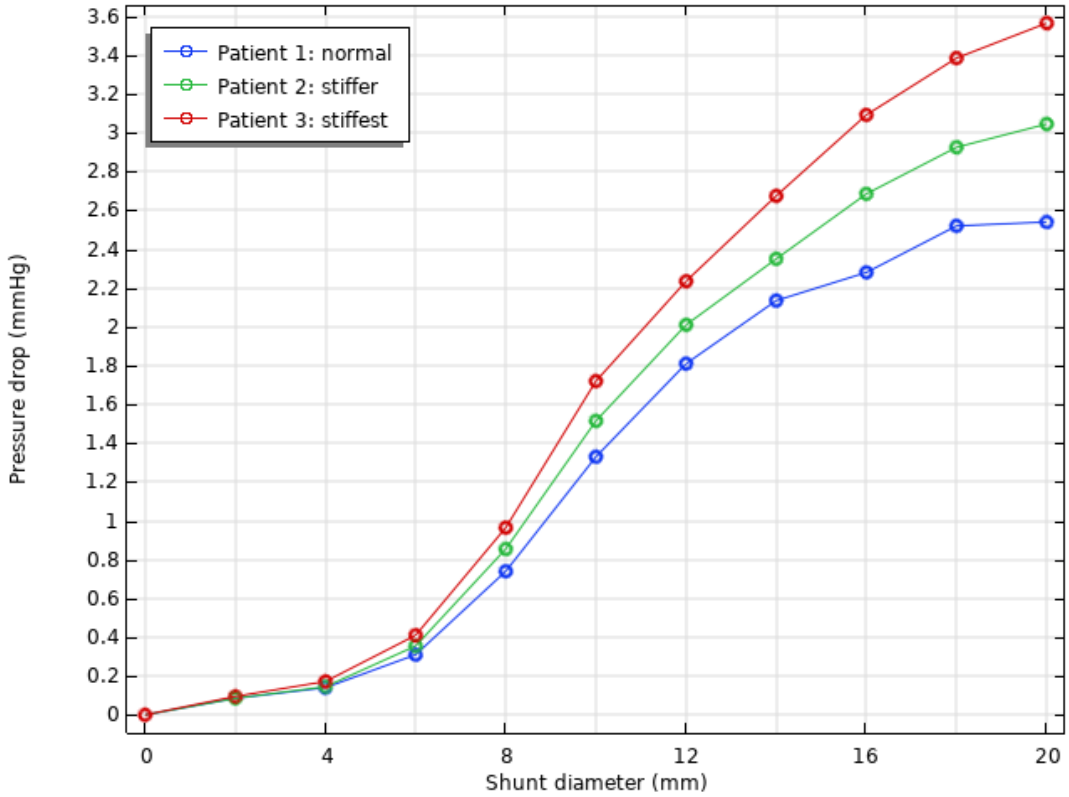

(a) Drop in peak pulmonary pressure

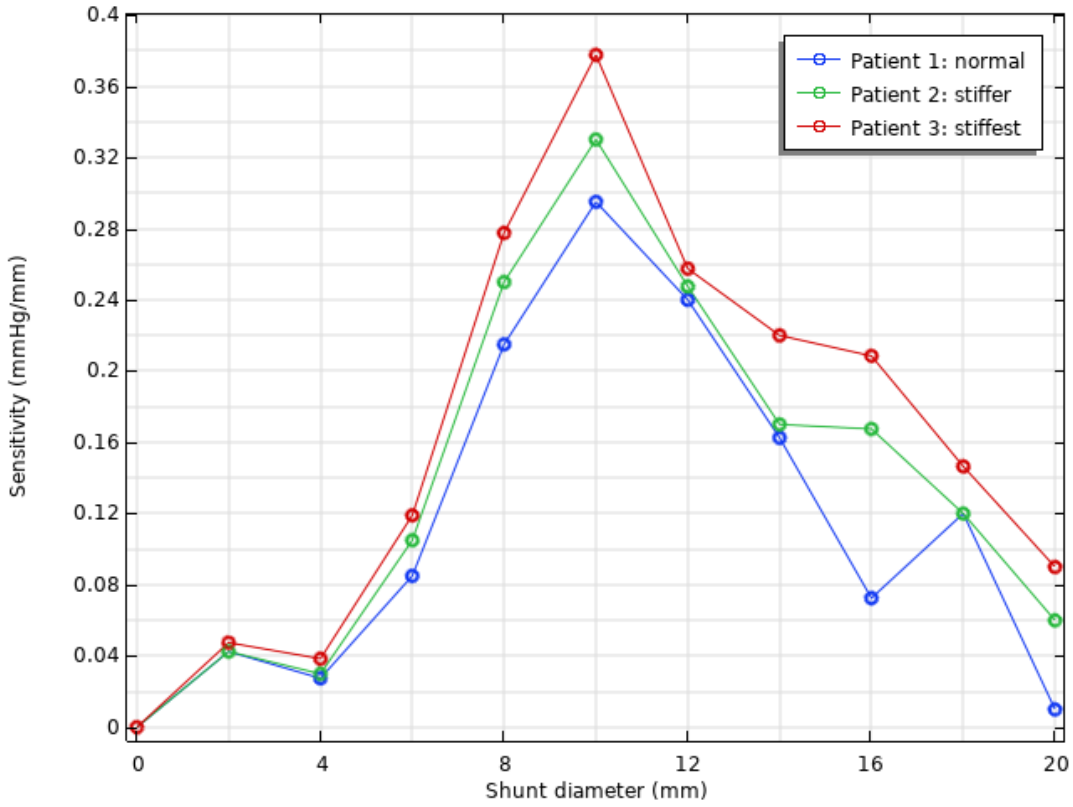

(b) Shunt sensitivity

Figure 4.34: Drop in peak pulmonary pressure (a) and its derivative representing the shunt sensitivity (b) as a function of shunt diameter for three patients of varying left ventricular stiffness

Ratio of pulmonary to systemic blood flow

In Figure 4.35, Figure 4.35a shows the left and right ventricular stroke volumes as a function of shunt diameter for the three patients of varying left ventricular stiffness. The stroke volume is the difference between the end-diastolic and end-systolic ventricular volumes, which correspond to the maximum and minimum ventricular volumes, respectively. Therefore, the stroke volume is the volume that exits the ventricle during each heartbeat. Since the blood exiting the right ventricle enters the pulmonary circulation and the blood exiting the left ventricle enters the systemic circulation, the ratio between the right and left ventricular stroke volumes determines the ratio of pulmonary to systemic blood flow, also known as the Qp:Qs ratio. The latter is shown in Figure 4.36.

As has yet been discussed in this report, the Qp:Qs ratio is equal to unity in absence of a shunt. This is because the blood circulation is a closed system, so the blood volume passing through the pulmonary circulation is the same volume that will pass through the systemic circulation. This means that the right and left ventricular stroke volumes are equal in absence of a shunt. In Figure 4.35a, it can be seen that this is close, but not exactly the case in the simulations, although this is barely visible in Figure 4.36. At a shunt diameter of 0 mm, i.e. in absence of a shunt, the right ventricular stroke volume is 3% smaller than the left ventricular stroke volume, which could be due to numerical errors in the discretization of the problem. Nevertheless, an error of 3% is acceptable for the calculation of the Qp:Qs ratio considering the other errors caused by model assumptions and by the spatio-temporal discretization (see Appendices B and C).

Firstly, the effect of the left ventricular elastance E_{LV} on the result is studied. Once again, it can be seen that the different values of E_{LV} for the different patients have affected the results. Figure 4.35a shows that right and left ventricular stroke volumes decrease with increasing left ventricular elastance. This is according to the expectation, as a stiffer left ventricle causes its pressure to rise more for a given rise in volume. Therefore, the left ventricular pressure rises more rapidly during the diastole and less volume enters the left ventricle. In absence of a shunt where the Qp:Qs ratio is equal to unity, this also directly affects the right ventricular volume. This highlights why increased left ventricular stiffness is problematic, as a reduction in stroke volume means that less blood is transported through the body. To counter this, the heart rate is increased, which means that the heart needs to work harder, eventually leading to heart failure.

In Figure 4.35a, it can be seen that the right ventricular stroke volume increases with shunt diameter, whereas the left ventricular stroke volume decreases by the same amount. As mentioned in the previous section for the peak pulmonary pressure, also these results are little sensitive to the shunt diameter for the smallest shunts. However, from a diameter of around 6 mm on, the interatrial shunts cause significant changes in right and left ventricular stroke volumes. These shunts seem to cause an almost linear increase and decrease in right and left ventricular stroke volume with shunt diameter, respectively. Figure 4.35b however shows the derivative of Figure 4.35a, from which it can be seen that the largest shunts are becoming less sensitive to shunt diameter, following the same behavior as seen previously. It is also expected that this sensitivity reduces for larger shunts, as the left ventricular stroke volume cannot become smaller than zero.

Another observation from Figure 4.35a is the convergence of the curves for each of the three patients. This is especially well visible for the right ventricular stroke volumes, as the volumes for the three patients are almost identical for the shunt diameters exceeding 16 mm. The left ventricular stroke volumes are slightly further apart, but can also clearly be seen to converge with shunt diameter. This behavior is also confirmed by Figure 4.35b, as the right ventricular stroke volume of patient 3 starts the lowest and has the highest derivative, whereas the right ventricular stroke volume of patient 1 starts the highest and has the lowest derivative. For the left ventricular stroke volumes on the other hand, patient 1 has the largest negative derivative and patient 3 has the smallest negative derivative, also indicating convergence.

Finally, the Qp:Qs ratio is considered in Figure 4.36. With the right ventricular stroke volume steadily increasing and the left ventricular stroke volume steadily decreasing, their ratio increases rapidly with shunt diameter. This figure also shows that it is a function of left ventricular elastance, meaning that it is not only a function of the shunt diameter. Furthermore, although the previous section has concluded the optimal shunt diameter for each patient based on the resulting peak pulmonary pressure, it must be noted that interatrial shunts can be dangerous if Qp:Qs exceeds 1.5 [18, 40, 45]. If the ratio of pulmonary to systemic blood flow is too high, there is simply not enough oxygen transported through the systemic circulation. Although this maximum of 1.5 is merely an estimation, it does indicate that

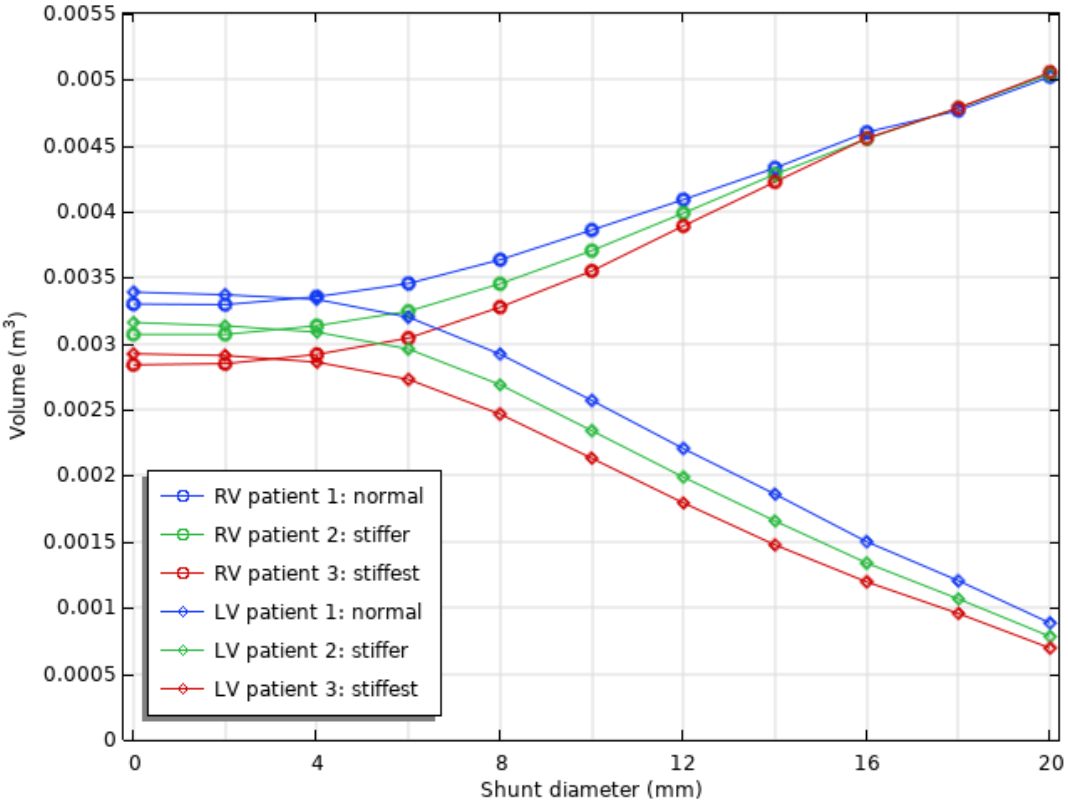

(a) Right and left ventricular stroke volumes

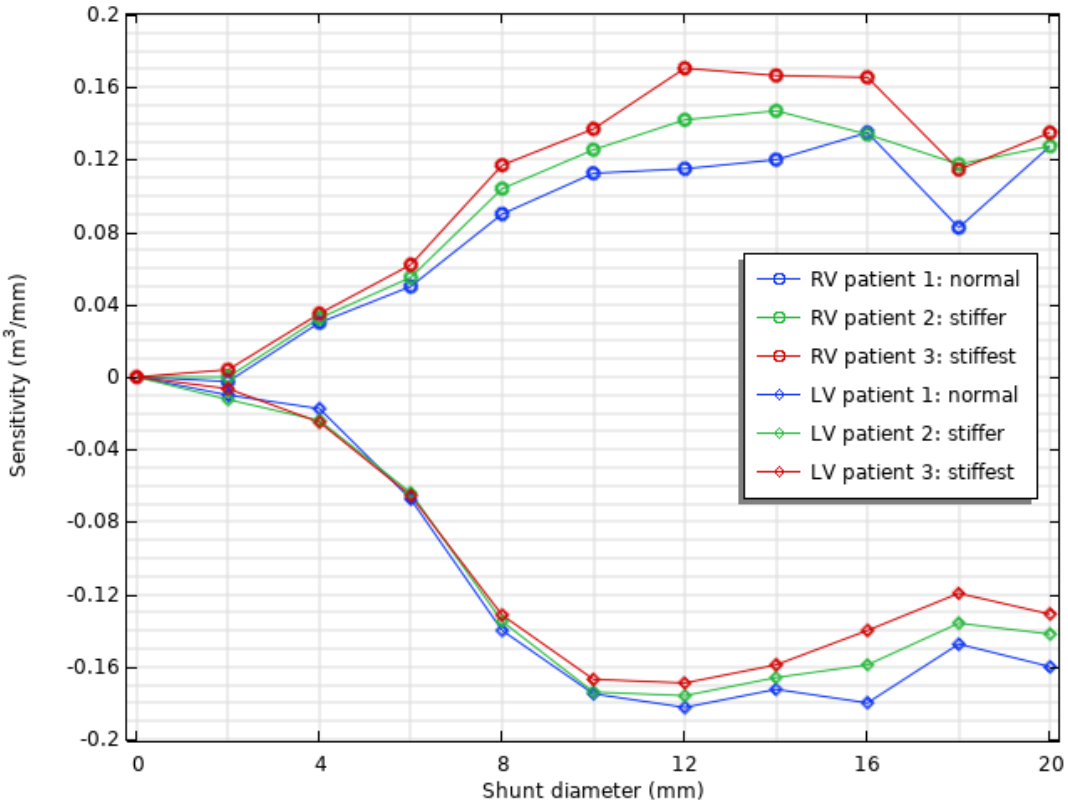

(b) Shunt sensitivity

Figure 4.35: Right and left ventricular stroke volumes (a) and its derivative representing the shunt sensitivity (b) as a function of shunt diameter for three patients of varying left ventricular stiffness

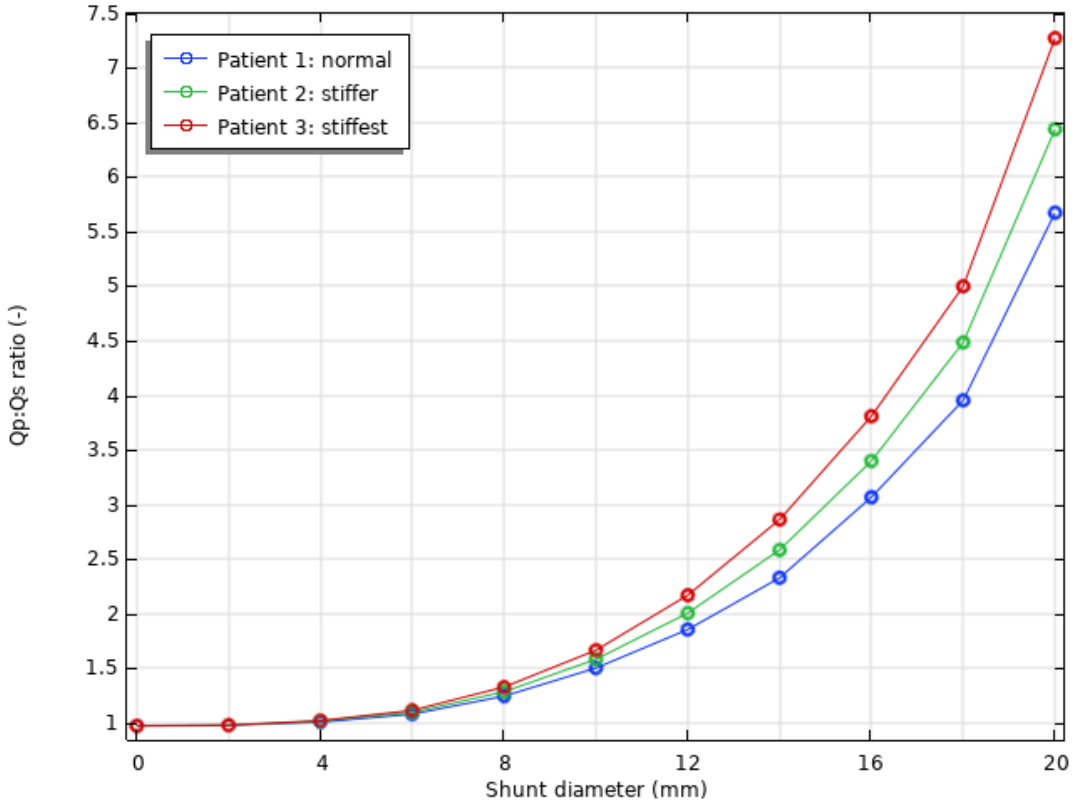

Figure 4.36: Ratio of pulmonary to systemic blood flow as a function of shunt diameter for three patients of varying left ventricular stiffness

the biggest shunts simulated in the current research could be lethal considering their Qp:Qs ratios. In the previous section, it was concluded that patient 1 requires a shunt with a diameter between 10 and 12 mm, which already results in a Qp:Qs ratio of 1.5 to 1.85, therefore exceeding the maximum of 1.5. Patient 2 would require a shunt that results in a Qp:Qs ratio between 1.85 and 2.33, whereas this would be between 2.33 and 3.07 for the third patient. This indicates that it is not possible to reduce the peak pulmonary pressure to below 15 mmHg for every patient while still adhering to a safe ratio of pulmonary to systemic blood flow. Instead, a weigh-off would have to be made between a patient's symptoms due to elevated pulmonary pressures and those due to excessive Qp:Qs ratios.

Resistance

This section of the results considers the resistance of the shunt as a function of its diameter. Since the shunt resistance is defined as the ratio of pressure difference to flow rate, Figures 4.37 and 4.38, respectively, show these variables as a function of shunt diameter for the three patients of varying left ventricular elastance E_{LV}.

Figure 4.37 shows the difference in spatial average of the left and right atrial pressures, which have been temporally averaged over the diastole of a single heart cycle. First of all, this figure shows that the left ventricular elastance significantly influences the left-to-right atrial pressure gradient. This is according to expectation, as an increased E_{LV} causes elevated left atrial pressures, therefore increasing the pressure difference between the two atria. Furthermore, Figure 4.37 shows that this pressure difference decreases with increasing shunt diameter. Also in this result, similar behavior is observed as in the results of the peak pulmonary pressure and the right and left ventricular stroke volumes. This includes the small sensitivity of the results to the shunt diameter for the smallest shunts, as well as the converging behavior of the curves with increasing diameter. The latter once again indicates the observed trend that larger shunts make the differences between patients smaller. Moreover, note how much the pressure gradient is influenced by the largest shunts: the pressure difference in presence of a 20 mm interatrial shunt is less than half of the pressure gradient in absence of a shunt for all three patients. This highlights how shunts of these sizes almost result in the two atria becoming a single

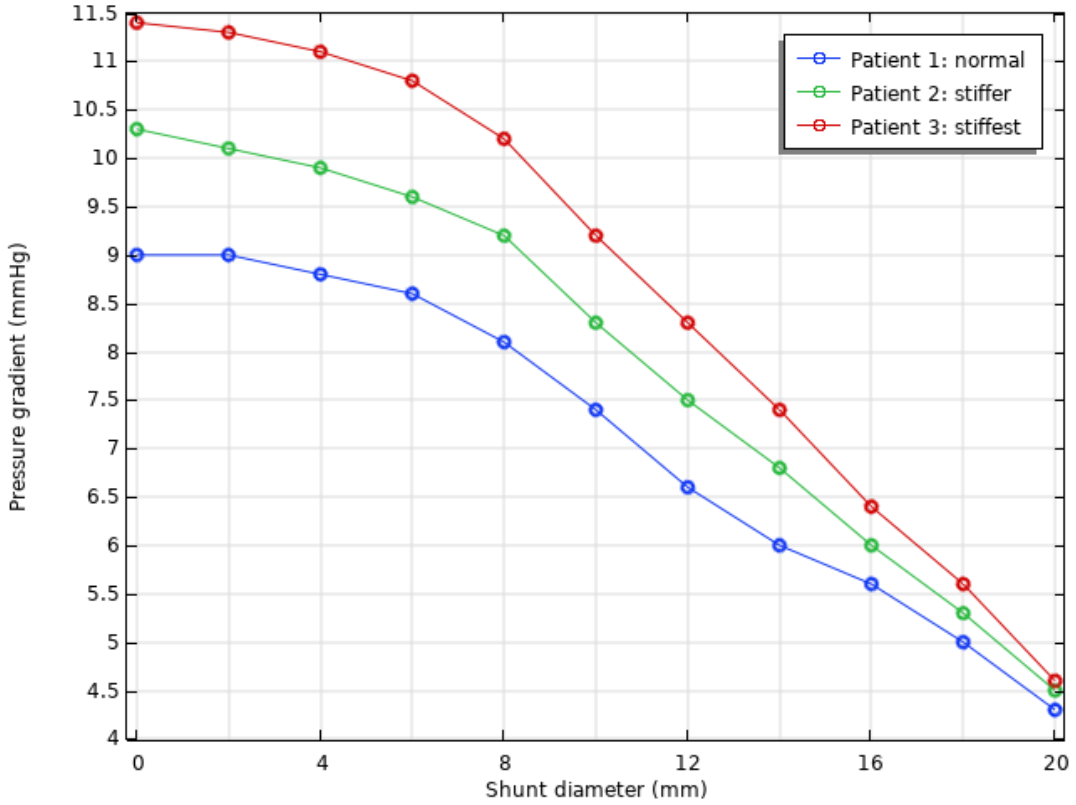

Figure 4.37: Left-to-right atrial pressure gradient as a function of shunt diameter for three patients of varying left ventricular stiffness

heart chamber.

In Figure 4.38, the flow rates through the shunts of varying diameters are presented. Due to the large differences in flow rates between the smallest and the largest shunts, the flow rates are plotted on a logarithmic scale in Figure 4.38a. Note that the zero flow rate in absence of a shunt is not included in this figure. For the smallest simulated shunt of 2 mm, the shunt flow rate is around 10^{-7} m^3/s, whereas the flow rates for the largest shunts are four orders of magnitude larger. In Figure 4.38b, the shunt flow rate is presented on a linear scale. Although this makes it difficult to study the flow rates of the smallest shunts, this gives a better idea of the flow rates for the largest shunts. From this figure, it can be seen that the sensitivity of the flow rate to the shunt diameter is lowest for the smallest shunt diameters, which is in line with the previous results. In contrast to the previous results, however, the shunt flow rate shows a divergence of the results with increasing diameter. Furthermore, between the three patients, it can be seen that patient 3 shows the highest shunt flow rate for all the diameters considered. This is also expected considering the higher pressure difference between the left and right atria for the third patient.

Finally, by dividing the left-to-right atrial pressure gradient from Figure 4.37 by the shunt flow rate from Figure 4.38, the shunt resistance is obtained, which is presented in Figure 4.39. Due to the very small flow rates for the smallest shunts, this has resulted in very large resistances for these diameters. Therefore, the shunt resistance has also been presented on a logarithmic scale in Figure 4.39a. Here, it can be seen that a 2 mm interatrial shunt has a resistance of around $3.5 \cdot 10^7$ mmHg·s/m^3. The largest shunts, however, have a resistance that is four orders of magnitude smaller than this, similar but opposite to what was found for the shunt flow rate. If the results are presented on a linear scale and only from 0 to $3.5 \cdot 10^4$ mmHg·s/m^3, this allows a closer look at the resistances of the largest shunts, see Figure 4.39b. From this figure, it becomes clear that the shunt resistance is the most sensitive to its diameter for the smallest shunts, since the resistance is inversely proportional to the shunt diameter. According to the research paper *Effects of an Interatrial Shunt on Rest and Exercise Hemodynamics: Results of a Computer Simulation in Heart Failure* by Kaye et al. [30], the shunt resistance is defined by the equation previously introduced in chapter 3 (see Equations 3.13 and 3.14):

$$R_{3D} = \frac{1}{K \cdot \text{Area}} = \frac{1}{K \cdot 0.25\pi d^2}. \tag{4.7}$$

This expression for the resistance has been included in Figure 4.39, where R_{3D} is the shunt resistance assumed to be in mmHg·s/mL, K is a proportionality constant assumed to be in cm/(mmHg·s), Area is the shunt area in cm^2 and d is the shunt diameter in cm. As can be seen in Figure 4.39a, this equation provides a rough estimation of the resistance of the smallest shunts as it is in the same order of magnitude as the values from the simulation. For the largest shunts, however, the resistances obtained from the equation proposed by Kaye et al. [30] are two orders of magnitude larger than the resistances according to the simulation. Therefore, the equation proposed by this research paper does not provide a good fit to the measurements.

However, since the simulations are two-dimensional, the geometry employed in the current research is actually a cylinder, rather than a sphere. This means that an increase in shunt diameter does not increase the shunt area quadratically, but linearly. Therefore, an adaptation is made to Equation 4.7 as follows:

$$R_{2D} = \frac{1}{K \cdot \text{Area}} = \frac{1}{K \cdot L \cdot d}, \tag{4.8}$$

where L is the length of the domain, which is 1 m or 100 cm in COMSOL. With the shunt diameter d also in cm, this altered expression for the shunt resistance is included in Figure 4.39. Both on the logarithmic and on the linear scale, it can be seen that this equation provides a much better fit with the simulation results for the largest shunts. For the smallest shunt, however, Equation 4.8 underestimates its resistance by more than three orders of magnitude. Therefore, it is concluded that also this expression is not a suitable fit to the measurements.

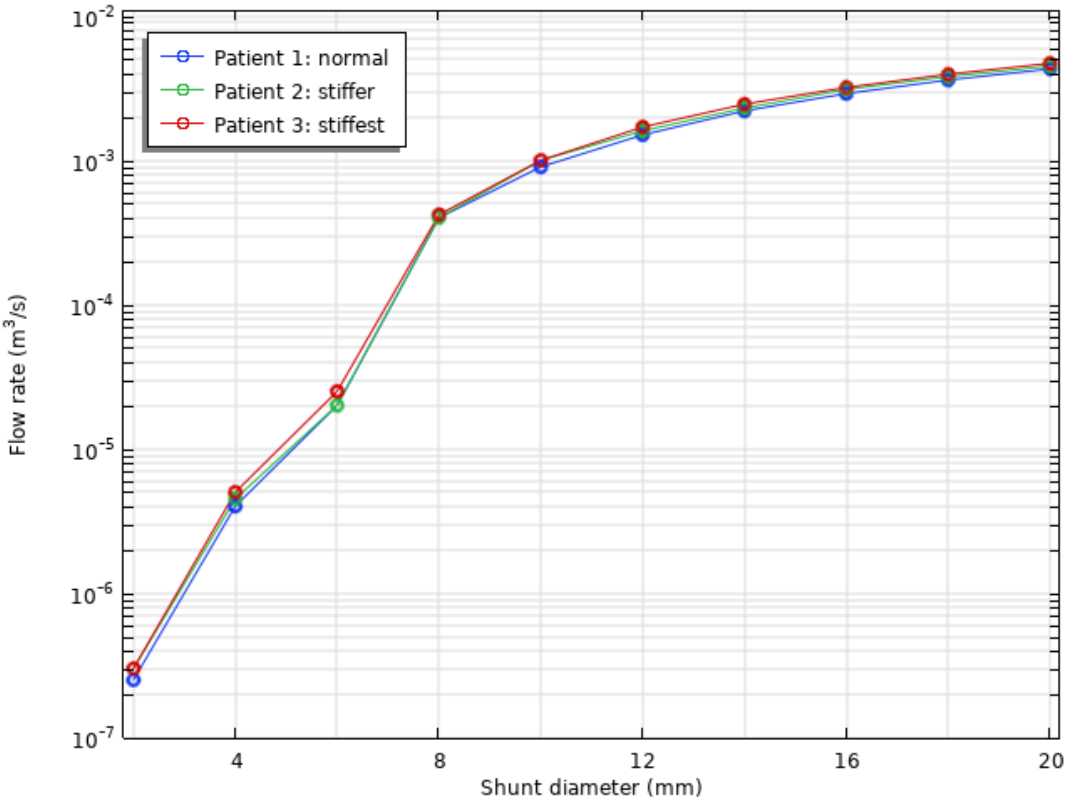

(a) Logarithmic

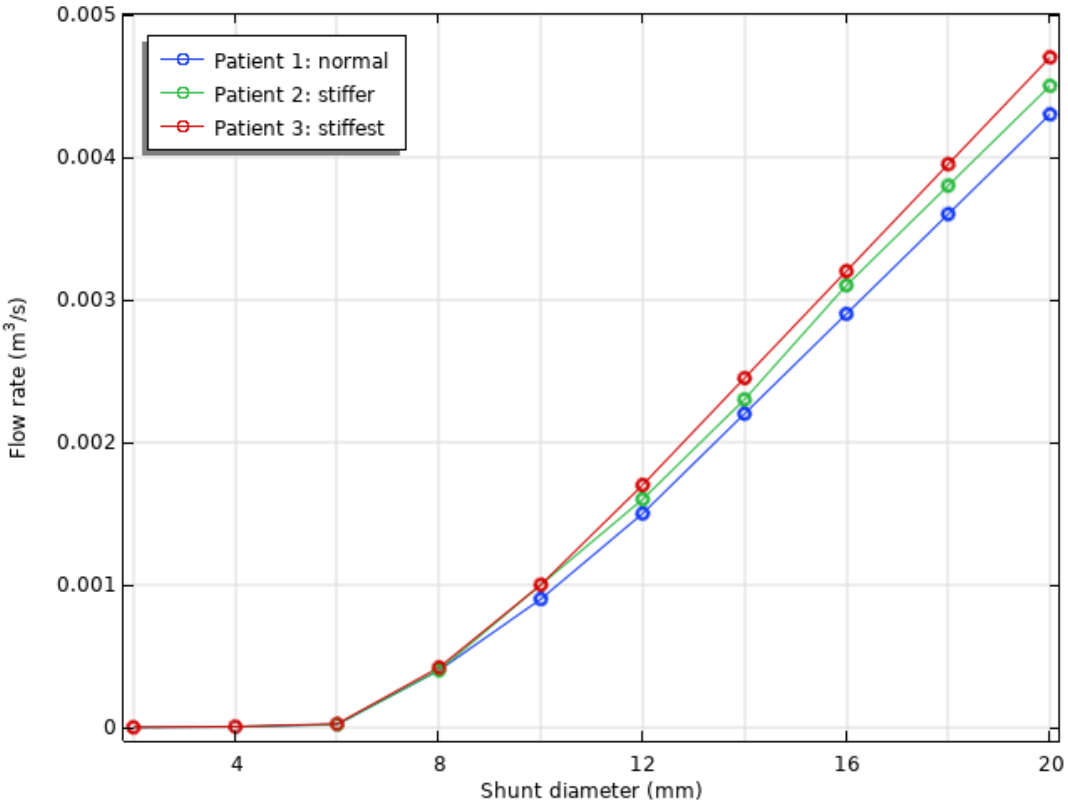

(b) Linear

Figure 4.38: Shunt flow rate on a logarithmic (a) and linear (b) scale as a function of shunt diameter for three patients of varying left ventricular stiffness

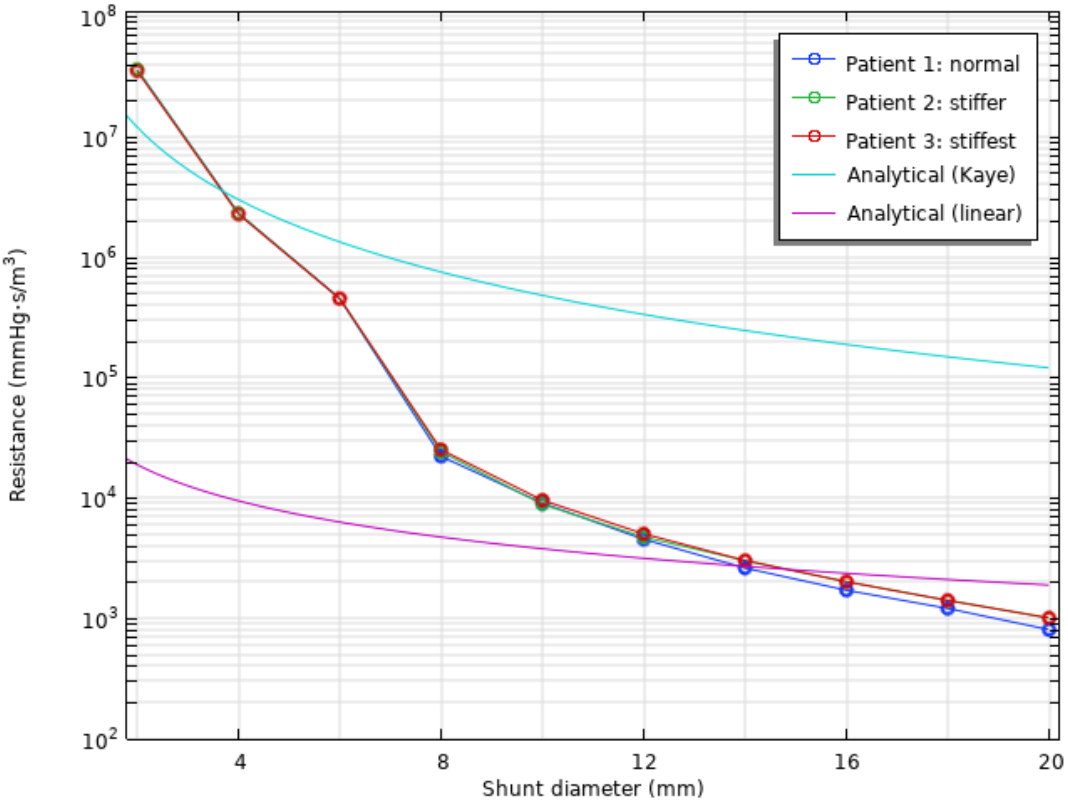

(a) Logarithmic

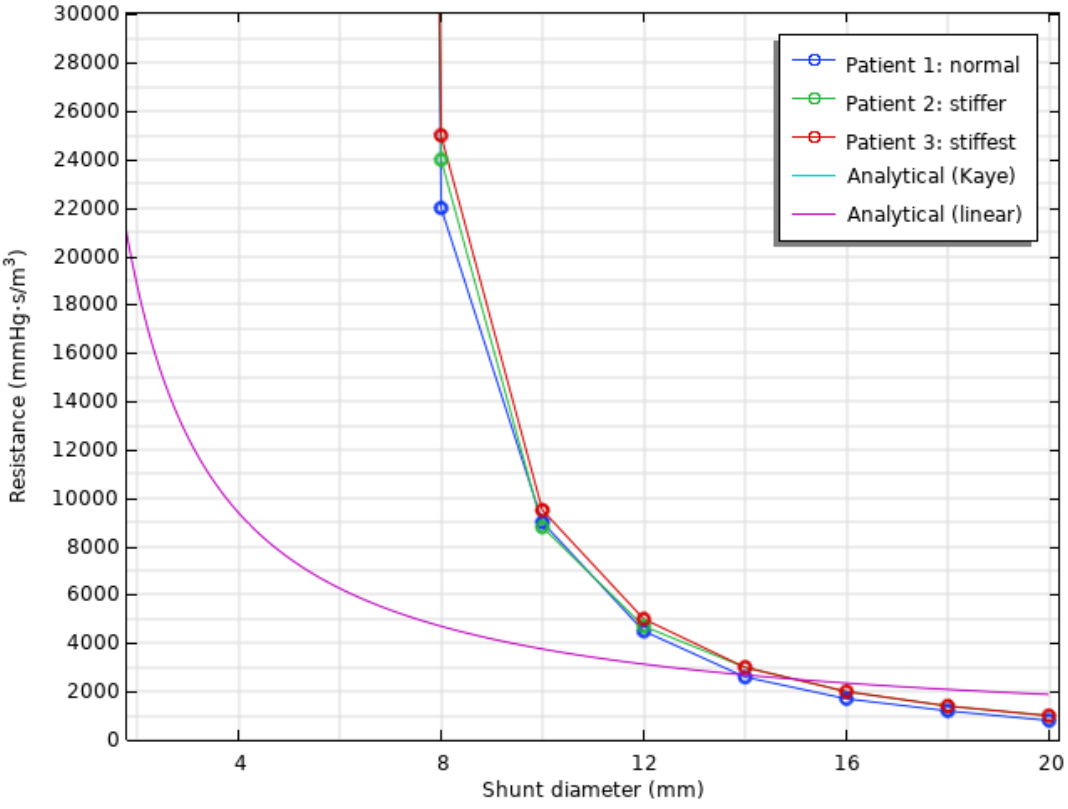

(b) Linear

Figure 4.39: Shunt resistance on a logarithmic (a) and linear (b) scale as a function of shunt diameter for three patients of varying left ventricular stiffness, compared to an analytical equation by Kaye et al. [30] and a linear adaptation thereof. Note that the analytical equation by Kaye et al. [30] is not visible in (b), as it goes beyond the limits of this figure.

5 Discussion

This chapter of the report discusses the validity of the results of the current research and the assumptions they are based on. Similar to the research itself, the discussion is split into two parts: the first part considers lumped element modeling and the second part considers the simulations performed using computational fluid dynamics.

5.1. LEM

In the current research, an attempt has been made to reproduce a three-element Windkessel model proposed by Kaye et al. [30] to study interatrial shunting. As discussed in chapter 3, a good match between the results of the reproduced lumped element model and the results from the research paper by Kaye et al. [30] is not achieved. Together with the limited time for the research project, it was therefore decided to not pursue lumped element modeling for the interatrial shunt research.

Due to the lack of information on the model provided in the research paper by Kaye et al. [30], many assumptions were made in reproducing the lumped element model. It is expected that this has adversely influenced the match between the results from the reproduced LEM and those provided by Kaye et al. [30]. The first of these assumptions is the interpretation of the hydraulic units provided by the research paper as electrical SI units, since the lumped element model uses an electrical description rather than a hydraulic one. This has possibly resulted in erroneous values prescribed to the elements in the model and the parameters in the equations. It was assumed that the results would not differ even if the values do, as long as the ratios between the values are the same as in reality, i.e. the same as in the research paper. This might hold for the resistance, impedance and capacitance elements in the circulation, as their relationships are linear, but this might not be true for the parameters in Equations 3.5 and 3.7, which are nonlinear.

Furthermore, Equation 3.4 is given in the research paper by Kaye et al. [30] as the equation governing the time-varying elements representing the heart chambers. In the reproduced model, however, only the expression for the time-varying elastance in Equation 3.7 is used, as it is assumed that the inverse of this should be prescribed to the time-varying capacitance elements. Moreover, the equations for the end-diastolic and end-systolic pressures (Equations 3.5 and 3.6, respectively) do not correspond to the results in the research paper in the form of pressure-volume loops. This begs the question how the authors have implemented Equations 3.4 to 3.7 into the lumped element model.

Finally, the research paper by Kaye et al. [30] provides incomplete information on the parameter values necessary for the model. This includes the systemic arterial resistance Ras and the end-systolic elastances E_{es} for the two atria, whereas E_{es} values for both ventricles are given. Also the end-diastolic or minimum values of the elastance E_{ed} are missing from the research paper, although the need for these is based on the assumption that the elastance cannot become zero, which is not supported by evidence but only by logic. Though not influencing the results presented in chapter 3, assumptions are also made regarding the units of the shunt resistance, proportionality constant and flow rate in Equation 3.12, since units are partly missing from this equation presented in the research paper by Kaye et al. [30].

Even though the results from the reproduced lumped element model do not match the results provided by Kaye et al. [30], pressure-volume loops of similar shape are observed in the results. Therefore, the work on lumped element modeling performed in the current research serves as a proof of principle that cardiovascular research can be performed through lumped element modeling. However, the model needs more time and effort for it to produce more realistic results such that it can be used as a reliable research tool.

5.2. CFD

The research presented in this report mainly considers simulations using computational fluid dynamics. Due to the many points of discussion considering this method, the discussion on CFD is split into parts that will be treated separately.

5.2.1. Two-dimensional

The main assumption in the computational fluid dynamics simulations is that these simulations are performed in a two-dimensional computational domain, whereas the human heart is clearly three-dimensional. A direct effect of this assumption is naturally that three-dimensional effects in the blood flow are not considered. Therefore, all the flow fields described in this report are not a true description of the flow fields in the heart during the different phases of the cardiac cycle. The reasoning behind the described flow fields and the effects of the interatrial shunt can however be extrapolated to the three-dimensional flow field. Flow features such as recirculation zones between the inlets of the atria and the presence of a relatively stagnant flow field towards the end of the diastole are examples of this [15].

Another effect of the two-dimensional representation of the two atria considers the inlets and outlets. As they only have a length rather than a surface area, the diameters of these inlets and outlets in reality are scaled down as described in chapter 4. As discussed in section 4.2, this causes a mismatch in the flow rates of the steady-state simulation as the inlet Reynolds numbers are kept constant, since the inlet velocities scale linearly while the scaling of the inlet and outlet diameters considers a quadratic relationship. For similar reasons, the two-dimensional computational grid also affects the relationship between the results and the shunt size. As explained previously, the shunt area in the computational domain increases linearly with shunt diameter in the current simulations, whereas it increases quadratically in three dimensions, i.e. in reality.

Furthermore, since the two-dimensional computational domain is extruded by 1 m in the simulations software COMSOL Multiphysics, the two atria are actually modeled as a long cylinder, rather than as a sphere. Therefore, the blood flows in the simulations consider much larger volumes than in reality, which is why the 2D assumption affects all volume-based values such as flow rate, elastance and resistance. Naturally, volumes and flow rates are bigger due to the larger volume of the extruded computational domain. Also, since the transient simulations are driven by static pressures and these pressures depend on volumes through elastances, these elastance values are much smaller than in reality. A given change in the pressure of a reservoir namely corresponds to a much larger change in volume in the current simulations compared to reality. Similarly, resistance values are much smaller than in reality due to the larger flow rates.

Finally, the two-dimensional assumption also affects the deformation of the atria and therefore the results of the transient simulation with wall movement. Section 4.4 states that the volume of the two atria varies between 74 and 172 mL, corresponding to radii of 26 and 34.5 mm, respectively. During the diastole, the atria decrease from their maximum end-systolic volume to their minimum end-diastolic volume, with the radius of the computational domain thus decreasing from 34.5 to 26 mm. In reality, this is a decrease in volume of 44%, since $(\frac{26}{34.5})^3 = 0.56$ for a sphere. In the two-dimensional CFD simulations, however, this is a decrease in volume of only 32%, since $(\frac{26}{34.5})^2 = 0.68$ for a circle/cylinder. Therefore, a three-dimensional heart contracts more than the two-dimensional heart considered in the CFD simulations in the current research.

5.2.2. Geometry

The current section is closely-linked to the previous one, since the geometry is naturally two-dimensional in the simulations. However, this section considers the assumptions regarding the geometry itself, rather than its two-dimensional nature. Also this section is split in multiple parts that will be discussed

separately.

Idealized model

First of all, the CFD simulations consider an idealized geometry of the two atria of the human heart. Even if it were three-dimensional, the two atria are assumed a perfectly circular sphere. In reality, however, the two atria are not circular and also contain intricate details such as papillary muscles. Furthermore, the left atrium includes a small extra chamber called the Left Atrial Appendage (LAA) which is not modeled. There is also no effect of the atrioventricular valve leaflets, as the outlet valves of the computational domain are simply modeled by semi-instantaneous closure through an increase of the viscosity in the transient simulation without moving walls, or through a damping function in the simulation with moving walls. Although the time it takes for the atrioventricular valves to open and close (60 ms [13, 42]) is considered in the model, realistically this has little effect. For the transient simulation without moving walls, this is because the viscosity changes by almost eleven orders of magnitude (from 0.0035 to 10^8 Pa·s) in 60 ms, whereas most of the opening/closing happens in the viscosity's lowest orders of magnitude. This is similar to what happens in the transient simulation including wall movement when the damping function is altered, resulting in the outlet valves opening and closing almost instantaneously.

Moreover, the shunt is modeled as a hole in the interatrial septum, whereas the presence of an interatrial shunt device might influence the flow field. Also the placement of the inlets and outlets is idealized, as they are placed evenly over the left and right atrial walls, which is unlikely to be the case in reality. Moreover, only the pulmonary veins and vena cavae are considered as inlets, whereas the smaller coronary arteries are not included. Regarding the pulmonary veins, it is assumed that there are four of them, while 30 - 40% of people actually have three or five pulmonary veins [50]. The inlets and outlets are furthermore modeled as straight tubes with the inlets having a length of 10 diameters and the outlets having a length of 2.5 mm. As mentioned in section 4.1, the outlet length represents the valve thickness, but the inlet length is chosen such that it is long enough to obtain a fully developed flow profile [27, 48]. Since the no-slip boundary condition is applied to all walls of the computational domain, a significant pressure drop occurs over the inlet tubes which naturally has an effect on the results. However, this effect is the same for all the simulations as the inlet lengths are kept constant between and throughout the simulations. Also, the pressure of the pulmonary reservoir, which is prescribed at the pulmonary vein inlets, represents the pressure in the pulmonary capillaries (PCWP). Therefore, a pressure drop between the pulmonary capillaries and the left atrium is also present in reality. Purely based on the pulmonary veins, this pressure drop would be much smaller in reality. This is because the length of the pulmonary veins is similar between the simulations and reality [49], whereas the hydraulic diameter d_h is much larger in reality ($d_h = d = 10.5$ mm for a circular PV, see Table 4.1) than in the simulations ($d_h = 2 \cdot d = 2.88$ mm for a rectangular PV of high aspect ratio [25]). It is however difficult to estimate the entire pressure drop in reality, as this strongly depends on the lengths and diameters of all the blood vessels between the measurement location and the left atrium. The pulmonary capillaries namely cause a large pressure drop due to their extremely small diameter of approximately 6 μm [57]. On the right side of the heart, the pressure of the systemic reservoir is prescribed at the vena cava inlets. This data is obtained from the computer program CircAdapt [35], but the location where this pressure is representative is unknown. Therefore, it is also difficult to determine whether the pressure of the vena cava jets entering the right atrium is accurate, causing an uncertainty in the results.

All of these assumptions have a significant influence on the atrial flow fields, which is why an idealized model is only an approximation of reality. Therefore, most cardiovascular research studies consider patient-specific heart models [37]. Such a model provides a more realistic geometry, but is specific to a single patient.

Volumes

Regarding the volume of the double atrium model, this is based on the data provided by Kaye et al. [30], where an average combined left and right atrial volume is considered for the CFD simulations with a static domain. For the transient simulation with wall movement, the volume of the domain varies between the minimum and maximum volumes from Kaye et al. [30]. However, this data is based on only two research studies of 46 HFpEF patients in total. Furthermore, since an idealized double atrium model is used for the CFD simulations, this also assumes equal left and right atrial volumes as the interatrial septum is placed in the middle of the computational domain. In reality, however, the

left atrium can be up to twice as large as the right atrium at the end of the diastole according to the pressure-volume loops in the research paper by Kaye et al. [30]. Of course, this will have an influence on the atrial flow field, but importantly the most relevant results such as the pressures and flow rates are expected to barely be affected by this.

Another limitation of the geometry is that only the two atria are included in the computational domain, with the rest of the blood circulation virtually modeled through equations. Due to the reduced mass of blood in the computational domain compared to the entire blood circulation, the momentum of blood flow is underestimated. As discussed in section 4.3, this affects the results, as an adverse inlet-to-outlet pressure gradient overestimates the deceleration of the blood flow compared to reality. This results in the pulmonary reservoir not being emptied as much as in reality, causing the minimum pulmonary pressure to be much higher in the simulations.

Prescribed deformation

In the transient CFD simulation including wall movement, the deformation is prescribed in advance. This influences the results as mentioned in section 4.4, because it changes the relationship between cause and effect. In the current research, for instance, the atria are filled with blood during the systole by the prescribed increase in atrial volume, causing blood to be sucked into the computational domain. However, the atria deform due to the increased atrial pressure in reality, which is the other way around. Another thing to note regarding the prescribed deformation is that this is derived from the computer program CircAdapt [35] modeling a healthy person. Therefore, the atrial deformation of a healthy person is applied to the atrial volume and pressure characteristics of a heart failure patient. The atrial deformation of a heart failure patient is expected to differ from a healthy person, as a patient's atria likely require a stronger contraction in order to fill the stiffened ventricles with enough blood. Naturally, the CFD simulations also do not account for long-term effects of the shunt on the heart's geometry and its deformation, known as cardiac remodeling.

Furthermore, the prescribed deformation assumes that the shunt diameter stays constant throughout the cardiac cycle. It could however also be the case that the shunt diameter increases with the atrial volume as the interatrial septum is stretched. On the other hand, the inlet and outlet openings into the atria do vary in diameter as the computational domain deforms. Whether this also happens in reality and by how much is not clear. On the other end of the inlets, where the actual inlet pressures are prescribed to the computational domain, pressure fluctuations were observed in the results in section 4.4. This is because the decision was made to keep the inlets extended by 10 inlet diameters throughout the cardiac cycle, which necessitated the inlets to move together with the atrial walls. In reality, however, there is no such inlet that moves with the atrial walls and causes pressure fluctuations in the pulmonary veins and vena cavae. If the physically unrealistic results in the transient simulation with wall movement (see Appendix D) would not become present at higher mesh densities, refining the mesh would be the simple solution to this problem. Otherwise, these fluctuations could be removed by fixing the location of the inlets. This would however cause the inlets to become shorter with increasing atrial volume, varying the pressure drop over the inlets throughout the simulation. Another option would be to decrease the effect that these fluctuations have on the results by bringing them further away from the atria, i.e. by extending the inlets. However, this would increase the pressure drop over the inlets which also influences the results.

Rigid walls

Both the CFD simulations with and without wall movement do not include the deformation of the domain due to the flow itself. In other words, the geometry of the simulations considers rigid walls. Therefore, the elasticity of the walls and the interatrial septum is not modeled, which would require a simulation employing Fluid-Structure Interaction (FSI) [37]. This could possibly indicate a deformation of the septum if the shunt is introduced, which could have an influence on the atrial flow field. During most of the diastole when the heart is fully relaxed, the geometry is considered to passively adapt to the surrounding forces, whereas a cardiovascular CFD simulation also considers an active contribution of the geometry as the heart contracts. In a fluid-structure interaction simulation, this could be included by applying a force on the wall during the atrial and ventricular contractions. The drawback of applying FSI, however, is that it is more complex and therefore more computationally expensive. It also requires knowledge of the structural properties of the heart, which is not straight-forward and also adds uncertainty to the results. Another, cheaper, way to include wall movement without prescribing the deformation would

be to base the deformation on the pressure difference between the inside and outside of the heart, but this would still require estimations of the heart's elastance and the pressure surrounding the heart.

5.2.3. Windkessel coupling

Outside of the computational domain, the inlet and outlet pressures are mathematically coupled through a Windkessel, as explained in section 4.3. The Windkessel includes two reservoirs representing the ventricles and another two reservoirs representing the pulmonary and systemic circulations. This model ensures the closed-loop behavior of the circulatory system and varies the pressures of the ventricles and the circulations during the phases of the cardiac cycle. However, the Windkessel coupling does not take the resistance, impedance or inertance of the pulmonary and systemic circulations into account. In essence, this makes it a one-element Windkessel model as it only takes into account the Windkessel effect of the circulations which assumes that the pressures rise and fall linearly with a change in volume. Therefore, any nonlinearity in this is not included in the current model, but can easily be implemented through the mathematical equations presented in section 4.3.

Furthermore, the CFD model is tuned to represent physically relevant inlet and outlet pressures. This is done by altering the simulation's boundary conditions that influence the Windkessel coupling between the inlets and outlets, such as the initial pressures and the elastances of the different reservoirs. Similar to the prescribed deformation, these conditions are tuned according to the computer program CircAdapt by Lumens et al. [35] which is based on physiological hemodynamics. Therefore, the conditions of the Windkessel might not fully represent a heart failure patient.

Regarding the inlet pressures of the left atrium, Figure 4.13a in section 4.3 shows a realistic pulmonary pressure according to the computer program CircAdapt [35]. Here, it can be seen that the pulmonary pressure according to this source shows two peaks and troughs per heart cycle, whereas the current research considers a single peak and a single trough. In CircAdapt, this second peak corresponds to the atrial contraction and rises together with the left atrial pressure. Since CircAdapt is based on a lumped element model, it is assumed that the elements representing the pulmonary veins and the time-varying element representing the left atrium are next to one another. The atrial contraction therefore influences the pressure also in the elements representing the pulmonary veins. In the current research, the atrial contraction also raises the pressures in the pulmonary veins in the computational domain, but this is not visible in the curve of the pulmonary pressure. This would namely only rise if reversed flow through the inlets were present that would fill the pulmonary reservoir and increase its pressure. Therefore, the discrepancy in the pulmonary pressure between the current research and the results presented in Figure 4.13a is not due to an error in the model, but is a result of the different locations where this pulmonary pressure is measured between the two methods.

Finally, a limitation of the Windkessel coupling is that the minimum ventricular pressure is fixed in the current research. This is due to the assumption that all the blood that enters the ventricle, also exits the ventricle during the systole and directly enters the blood circulations. Since the initial pressures of the four reservoirs (at zero volume) are set by the boundary conditions, the ventricles return to this minimum pressure every cardiac cycle. This is a fair assumption, as the simulated conditions do not change between the heart cycles, but it does limit the CFD model from investigating the effect of different conditions or the introduction of an interatrial shunt on the minimum ventricular pressure. An accompanying assumption is the one discussed in section 4.3, which neglects the relatively high, reducing ventricular pressures at the very start of the diastole. Instead, the ventricular pressures are assumed to already be at their minimum when the atrioventricular valves open and the diastole commences.

5.2.4. Solver settings

Regarding the solver settings of the CFD simulations, there are also a few factors influencing the results. Firstly, the Reynolds-Averaged Navier-Stokes (RANS) equations are solved to perform the simulations. As explained in the literature report [37], RANS simulations are not well-suited for modeling cardiovascular flows due to their transitional nature between laminar and turbulent flow according to Parker et al. [48]. Therefore, the CFD simulations might not accurately predict the atrial flow features and a Large Eddy Simulation (LES) might provide more realistic results.

Furthermore, the RANS simulations are employed in combination with the k-ω turbulence model, which is an excellent turbulence model for wall-bounded flows [37]. However, the flow studied in the current research is not particularly wall-bounded but mainly considers free shear flow. For this application, a k-ϵ model might be more suitable, or a hybrid turbulence model in the form of the Shear Stress

Transport (SST) turbulence model could be used. This was attempted in the current research, but it was found that the simulations were the most stable with the k-ω turbulence model, whereas some simulations would even diverge with the k-ϵ or SST turbulence models.

Although the use of the Newtonian assumption is validated in Appendix A, it does introduce an error in the results. This error is found to be around 1% for the pressure field and up to 10% for the velocity field, which is deemed acceptable. However, this error is determined in the steady-state simulation, which represents the average flow field during the diastole. In the transient simulations, the shear rates are lower during the systolic phase of the cardiac cycle than they are during the diastole. Therefore, the error is expected to be larger during this phase in the transient simulations. Finally, blood is modeled as an incompressible fluid, which is also an assumption that affects the results, although it is not expected to do so significantly.

5.2.5. Discretization

The spatio-temporal discretization of the computational fluid dynamics problem is extensively discussed in Appendices B and C for the mesh and for the time step, respectively. Here, the effect of the discretization on the results is treated in brief.

Spatial

The spatial discretization of the computational grid, i.e. the mesh, introduces an error of around 5% for the pressure field and around 10% for the velocity field. This is determined from the mesh study presented in Appendix B. However, the simulations including wall movement are solved on a coarser mesh than the other simulations as described in section 4.4. Therefore, the errors due to the spatial discretization will be larger for this simulation. As previously discussed, the cause is unclear of the physically unrealistic behavior in the transient simulations with moving walls on the mesh presented in subsection 4.1.1. The Courant number was believed to be too high, but strong reductions of the time step either through reductions of the relative tolerance or by fixing the time step to very small values did not cause improved results. The simulation might however require even smaller time steps that could not be achieved. The physically unrealistic behavior could be resolved by prescribing total pressure at the inlets and outlets, rather than static pressure. Since the current research considers a problem driven by static pressure, however, it is deemed that prescribing the total pressure would result in larger errors in the results than a coarser mesh would.

Temporal

Regarding the temporal discretization, a study on the time step of the transient simulations is presented in Appendix C. From this, it is concluded that the instantaneous velocity and pressure fields are unreliable due to the time-dependent fluctuations of the inlet jets. Especially the instantaneous left atrial flow field showed large relative errors due to the fluctuations of the jets from the pulmonary veins. However, important results such as the pressures of the reservoirs in the Windkessel, the spatially averaged left and right atrial pressures and the inlet and outlet flow rates are concluded to have an error of less than 10% due to the temporal discretization. Smaller time steps can decrease this error due to the temporal discretization of the transient simulations, but will also result in more computationally expensive simulations. Therefore, an error within 10% is deemed acceptable.

5.2.6. Remaining questions

The final section of this chapter discusses remaining questions regarding the results that are discussed as follows. First of all, in the study on the patient-specific optimal shunt diameter in subsection 4.4.2, it is observed that doubling the left ventricular elastance E_{LV} in a patient without an interatrial shunt raises the peak pulmonary pressure from 16.5 mmHg for the first patient to just below 18 mmHg for the third patient. This is an increase in peak pulmonary pressure of less than 1.5 mmHg for a doubling of the left ventricular elastance. However, many heart failure patients have pulmonary capillary wedge pressures exceeding these values [37], which means that such patients are not modeled in the current research. Since a doubling of the left ventricular elastance is already an immense increase in the stiffness of the left ventricle, it is expected that other factors also contribute to these higher pulmonary pressures. Therefore, parameters other than the left ventricular elastance E_{LV} will likely also have to be adjusted to model patients with different severities of heart failure. This could include the boundary conditions such as the elastances of the other reservoirs, but also other simulated conditions such as the heart rate, the

temporal ratio between the two phases of the cardiac cycle and the heart's deformation. These are all kept constant throughout the simulations, which might not be realistic between patients. For instance, as previously mentioned in subsection 4.4.2, it is known that the heart compensates for a reduced ventricular stroke volume by increasing its heart rate to keep the cardiac output constant. Therefore, the heart rate of the third patient might be higher than that of the first patient in reality. Also, the diastole is assumed to last for 2/3 of the cardiac cycle in the CFD simulations according to Kemmerling [31], whereas the lumped element model uses a different approach. According to Kaye et al. [30], the systolic phase has a fixed duration depending on the moment of maximal chamber elastance T_{max}, with the diastole completing the rest of the cardiac cycle. This indicates that multiple approaches are possible to model the two phases of the cardiac cycle, which might apply to different patients.

Furthermore, subsection 4.4.2 also discusses the reductions in peak pulmonary pressures as a result of the different shunt sizes for the three patients. For the shunt diameters reported in literature, the results from the current research can be compared. This considers results from the clinical trials on the currently existing methods to create and maintain an interatrial shunt as discussed in chapter 2, but also results from *in silico* studies investigating interatrial shunts, such as in the research paper by Kaye et al. [30]. Considering the interatrial shunt device by Corvia Medical with a fenestration diameter of 8 mm, it is reported by Litwin, Borlaug, and Komtebedde [34] that mean PCWP at rest decreased by 5 mmHg from 19 mmHg to 14 mmHg in Corvia's first feasibility study. Although this considers the mean pulmonary capillary wedge pressure whereas the current research considers peak pulmonary pressure, a similar, if not larger, reduction is expected in the peak PCWP. In the current research, however, Figure 4.34a in subsection 4.4.2 shows that an 8 mm interatrial shunt results in a reduction of less than 1 mmHg in peak pulmonary pressure for all three patients. Also compared to the computational study by Kaye et al. [30] employing a lumped element model, the reduction in peak pulmonary pressure of an 8 mm shunt is underestimated, since Kaye et al. [30] report a PCWP reduction of 3 mmHg under simulated resting conditions. Due to the underestimation of the reduction in peak pulmonary pressure from the CFD simulations, the current research predicts that shunts that are too large are required for a certain pressure reduction. This results in excessive Qp:Qs ratios that can be lethal for the patient. The reason behind this underestimation of the shunt effectiveness is not understood, but could be due to the two-dimensional modeling of the three-dimensional problem. The shunt diameter is scaled down, following the same logic behind the scaling of the inlet and outlet diameters. It could be that this scaling has an exaggerated effect on the results, meaning that the shunt resistance is too high and therefore the pressure reduction is too low. Further research including three-dimensional simulations is required to investigate the cause of this underestimation.

6

Conclusion

This report has presented a research project on the patient-specific optimal diameter of an interatrial shunt for the relief of left heart and pulmonary pressures in patients suffering from heart failure through the following research question:

> *What is the optimal diameter of an interatrial shunt for different patients with heart failure with preserved ejection fraction?*

This research question is answered through a computational study into interatrial shunting. First, an attempt has been made at reproducing a three-element Windkessel model introduced by Kaye et al. [30], but a good match between the results from the reproduced model and those provided by the research paper could not be established. Since the reproduced lumped element model is unable to provide physically relevant conditions that could be used to study interatrial shunting, research is solely performed through simulations employing computational fluid dynamics. A circular, idealized two-dimensional CAD model including the left and right atria, four pulmonary veins, the two vena cavae and the two atrioventricular valves is used to study the intra- and interatrial velocity and pressure fields in absence and presence of an interatrial shunt through steady-state and transient simulations. For the steady-state simulation, the average diastolic flow field is studied in absence and presence of an interatrial shunt. Velocities are prescribed at the inlets that are scaled to equal realistic Reynolds numbers, while realistic ventricular static pressures are prescribed at the outlets. From the steady-state simulation, the introduction of an interatrial shunt is observed to influence the atrial flow field and increase the flow rate through the tricuspid valve while reducing the flow rate through the mitral valve, hence increasing the ratio of pulmonary to systemic blood flow (Qp:Qs). The transient simulations are performed with and without wall movement in which time-dependent static pressures are prescribed at the inlets and outlets and the opening and closing of the atrioventricular valves is modeled. The inlets and outlets are coupled through a Windkessel including four reservoirs, representing the two ventricles and the pulmonary and systemic circulations. This coupling represents the closed-loop behavior of the circulatory system and ensures realistic inlet and outlet pressures throughout the cardiac cycle. The transient simulation employing the same static computational domain from the steady-state simulation concludes a similar effect of the interatrial shunt, but provides these results throughout the cardiac cycle instead of at an averaged moment during the diastole. On top of that, the transient simulation including wall movement employs a prescribed deformation of the atrial walls, inlets and outlets, representing the deformation of the atria over the cardiac cycle. Results from this simulation highlight the effect of the atrial deformation, including the late diastolic peak in atrioventricular flow rates due to the atrial contraction. Furthermore, a shunt flow from the left atrium to the right atrium is observed in all the simulations throughout the heart cycle. As such, the shunt manages to reduce pulmonary, left atrial and left ventricular pressures while slightly increasing systemic, right atrial and right ventricular pressures.

To answer the research question regarding the patient-specific optimal shunt diameter, shunts with diameters ranging between 0 and 20 mm are applied to three different patients of varying left ventricular stiffness. This study is performed using the transient CFD simulations including wall movement, from which it is found that the smallest shunts (< 6 mm) as well as the largest shunts (> 12 mm) are little

sensitive to shunt diameter. The medium-sized shunts (6 - 12 mm), however, are found to be very sensitive to the shunt diameter, with a small change in shunt diameter resulting in a large change in peak pulmonary pressure. Moreover, larger shunts are observed to reduce the differences between patients in terms of peak pulmonary pressure, ventricular stroke volume and left-to-right atrial pressure gradient. The optimal shunt diameter is initially defined as the shunt with the smallest diameter that manages to reduce a patient's peak pulmonary pressure to below 15 mmHg. However, it is found from the current research that large shunts are needed to meet this requirement that result in excessive Qp:Qs ratios and could be lethal for the patient. Therefore, it is concluded that the optimal interatrial shunt for a heart failure patient is the one with the smallest diameter that manages to reduce a patient's peak pulmonary pressure to below 15 mmHg, as long as its Qp:Qs ratio does not exceed 1.5. Otherwise, the optimal shunt is the one with the largest diameter that does not exceed Qp:Qs = 1.5.

6.1. Recommendations

As discussed in the previous chapter, further research is required to validate the findings from the current research. The main limitation of this research is the two-dimensional nature of the computational fluid dynamics simulations. Therefore, it is recommended to extend the model presented in this report to three dimensions. This will allow the three-dimensional flow field of the heart to be studied and omits the need to scale the inlets, outlets and interatrial shunt. Also, this will consider more realistic values of volume-based quantities and provide a more accurate relationship between the shunt resistance and its diameter, allowing the resistance of an interatrial shunt to be modeled more accurately in a lumped element model. Medical professionals could benefit from this since LEM is a quick and easy method to obtain results on a patient's hemodynamics, for example to assess surgery outcomes before placing an interatrial shunt. Furthermore, the geometrical model could be improved, for instance by addressing the difference in left and right atrial volumes and by including more details such as the left atrial appendage, papillary muscles and atrioventricular heart valve leaflets. Also the deformation of the geometry could be improved by considering the atrial deformation of a heart failure patient, or even by performing a fluid-structure interaction simulation. A patient-specific heart model obtained through medical imaging techniques could also be considered. The coupling between the inlets and outlets through the Windkessel model also requires improvement, first of all by including the resistances of the pulmonary and systemic circulations to create a two-element Windkessel model. Arterial impedance and inertance of the pulmonary and systemic circulations can further be added, where the latter would be useful in tackling the underestimation of the blood's momentum in the current model. This would help resolve the minimum pulmonary pressures that are too high in the transient CFD simulations compared to reality. Also this coupling would provide more realistic results if it were tuned to pressure characteristics of heart failure patients rather than physiologic hemodynamics. Regarding the CFD models, the k-ϵ or SST turbulence models could provide a more accurate description of the atrial flow fields. Otherwise, a large eddy or even direct numerical simulation could be employed for more accurate results, which would also require a finer discretization. Other than improvements to the model, it is also recommended to consider different conditions by varying the heart rate, pressure characteristics, atrial volumes, number of pulmonary veins, temporal ratio between the phases of the cardiac cycle and more.

Finally, the full potential of computational fluid dynamics has not been extracted from the simulations in the current research. CFD simulations are able to provide any result at any place and at any time, whereas this research has mainly limited itself to studying flow rates and (spatially averaged) pressures. Metrics such as wall shear stress, residence times, viscosity and vorticity can easily be obtained from CFD simulations and are important determinants for several cardiovascular diseases [38, 47]. Studying such metrics could give a better idea of the instantaneous as well as the long-term effects of interatrial shunts, since changes in the flow field could indicate the initiation of any favorable or adverse effects, such as thrombus formation.

References

[1] *Alleviant*. 2023. URL: https://www.alleviantmedical.com/ (visited on 04/24/2023).

[2] *Anatomy of the heart*. 2023. URL: https://occlutech.com/anatomy-of-the-heart/ (visited on 03/07/2023).

[3] *Atrial Flow Regulator (AFR)*. 2023. URL: https://occlutech.com/afr/ (visited on 03/06/2023).

[4] A. Bilbao et al. "The Minnesota living with heart failure questionnaire: comparison of different factor structures". In: *Health and Quality of Life Outcomes* 14.23 (2016). DOI: 10.1186/s12955-016-0425-7.

[5] A. Biscopink, W. Mostertz, and J. Grewal. "Interatrial Septal Devices for HFpEF: What We Learned from REDUCE LAP-HF". In: *Current Treatment Options in Cardiovascular Medicine* 25 (2023), pp. 29–41. DOI: https://doi.org/10.1007/s11936-022-00975-0.

[6] B. A. Borlaug, J. Blair, and M. W. Bergmann. "Latent Pulmonary Vascular Disease May Alter the Response to Therapeutic Atrial Shunt Device in Heart Failure". In: *Circulation* 145 (2022), pp. 1592–1604. DOI: 10.1161/CIRCULATIONAHA.122.059486.

[7] B. A. Borlaug et al. "Exercise hemodynamics enhance diagnosis of early heart failure with preserved ejection fraction". In: *Circulation Heart Failure* 3.5 (2010), pp. 588–595. DOI: 10.1161/CIRCHEARTFAILURE.109.930701.

[8] D. Burkhoff, M. Dickstein, and T. Schleichter. *About Harvi*. 2023. URL: https://harvi.academy/about/ (visited on 04/16/2023).

[9] D. Burkhoff, M. Dickstein, and T. Schleichter. *Harvi TEACH: Training and Education in Advanced Cardiovascular Hemodynamics*. 2023. URL: https://harvi.academy/teach-mcs-workshop-prep/english/ (visited on 04/16/2023).

[10] V. Carvalho et al. "Blood Flow Modeling in Coronary Arteries: A Review". In: *Fluids* 6.2 (2021), pp. 53–67. DOI: https://doi.org/10.3390/fluids6020053.

[11] G. Chang. *Electric Circuits and the Hydraulic Analogy*. 2023. URL: https://ataridogdaze.com/science/hydraulic/index.html (visited on 04/16/2023).

[12] *COMSOL - Software for Multiphysics Simulation*. 2023. URL: https://www.comsol.com/ (visited on 11/01/2023).

[13] M. Corti et al. "Impact of atrial fibrillation on left atrium haemodynamics: A computational fluid dynamics study". In: *Computers in Biology and Medicine* 150 (2022). DOI: https://doi.org/10.1016/j.compbiomed.2022.106143.

[14] *Corvia Atrial Shunt System*. 2023. URL: https://corviamedical.com/corvia-atrial-shunt-system/ (visited on 04/24/2023).

[15] L. Dedè, F. Menghini, and A. M. Quarteroni. "Computational fluid dynamics of blood flow in an idealized left human heart". In: *International Journal for Numerical Methods in Biomedical Engineering* 37.11 (2019). DOI: 10.1002/cnm.3287.

[16] S.N. Doost et al. "The numerical analysis of non-Newtonian bloodflow in human patient-specific left ventricle". In: *Computer Methods and Programs in Biomedicine* 127 (2016), pp. 232–247. DOI: http://dx.doi.org/10.1016/j.cmpb.2015.12.020.

[17] A. Elagha et al. "Characterization of the interatrial septum by high-field cardiac MRI: a comparison with multi-slice computed tomography". In: *The Egyptian Heart Journal* 72.81 (2020). DOI: https://doi.org/10.1186/s43044-020-00109-6.

[18] S. Emani, D. Burkhoff, and S. M. Lilly. "Interatrial shunt devices for the treatment of heart failure". In: *Trends in Cardiovascular Medicine* 31.7 (2021), pp. 427–432. DOI: https://doi.org/10.1016/j.tcm.2020.09.004.

[19] L. Escamilla. *Pin on Human Body*. 2023. URL: https://www.pinterest.com/pin/561120434808817858/ (visited on 05/10/2023).

[20] *Exploratory Study of the Edwards Transcatheter Atrial Shunt System (ALt FLOW CANADA)*. 2023. URL: https://clinicaltrials.gov/ct2/show/NCT04000607 (visited on 04/24/2023).

[21] I. Fernández-Ruiz. "Interatrial shunting for the treatment of heart failure". In: *Nature Reviews Cardiology* 13 (2016), pp. 312–313. DOI: https://doi.org/10.1038/nrcardio.2016.56.

[22] J. M. Griffin, B. A. Borlaug, and J. Komtebedde. "Impact of Interatrial Shunts on Invasive Hemodynamics and Exercise Tolerance in Patients With Heart Failure". In: *Journal of the American Heart Association* 9 (2020). DOI: 10.1161/JAHA.120.016760.

[23] A. Gupta and S. R. Bailey. "Update on Devices for Diastolic Dysfunction: Options for a No Option Conditions?" In: *Current Cardiology Reports* 20 (2018), pp. 85–93. DOI: https://doi.org/10.1007/s11886-018-1027-2.

[24] *Heart Failure*. 2023. URL: https://occlutech.com/heart-failure-afr-2/ (visited on 03/06/2023).

[25] *Hydraulic diameter*. 2023. URL: https://en.wikipedia.org/wiki/Hydraulic_diameter (visited on 12/05/2023).

[26] *InterShunt*. 2023. URL: https://intershunt.com/ (visited on 04/24/2023).

[27] D. Jongerius. "A mathematical framework of left ventricular hemodynamics, focusing on wall motion and aortic valve jet flow". In: *Department of Biomedical Engineering, Eindhoven University of Technology* (2021). URL: https://research.tue.nl/en/studentTheses/a-mathematical-framework-of-left-ventricular-hemodynamics-focusin.

[28] T. H. Jørgensen and L. Søndergaard. "Transcatheter Implantation of Interatrial Shunt Devices to Lower Left Atrial Pressure in Heart Failure". In: *International Journal of Heart Failure* 4.1 (2022). DOI: https://doi.org/10.36628/ijhf.2021.0038.

[29] N. K. Kapur, J. N. Upshaw, and B. S. Wessler. "REDUCE LAP-HF II interatrial shunt trial: neutral, but necessary". In: *The Lancet* 399.10330 (2022), pp. 1094–1095. DOI: https://doi.org/10.1016/S0140-6736(22)00108-8.

[30] D. M. Kaye et al. "Effects of an Interatrial Shunt on Rest and Exercise Hemodynamics: Results of a Computer Simulation in Heart Failure". In: *Journal of Cardiac Failure* 20.3 (2014), pp. 212–221. DOI: http://dx.doi.org/10.1016/j.cardfail.2014.01.005.

[31] E. M. C. Kemmerling. "In Vitro Pressure Measurements Across an Interatrial Shunt for HFpEF Treatment". In: *Cardiovascular Engineering and Technology* 13.5 (2022), pp. 663–672. DOI: https://doi.org/10.1007/s13239-021-00607-x.

[32] L. Lauder et al. "Feasibility and efficacy of transcatheter interatrial shunt devices for chronic heart failure: a systematic review and meta-analysis". In: *European Journal of Heart Failure* 23 (2021), pp. 1960–1970. DOI: https://doi.org/10.1002/ejhf.2360.

[33] *Left-to-right shunt for Heart Failure*. 2023. URL: https://occlutech.com/heart-failure-afr/ (visited on 03/06/2023).

[34] S. E. Litwin, B. A. Borlaug, and J. Komtebedde. "Update on Atrial Shunt Therapy for Treatment of Heart Failure". In: *Structural Heart* 6.6 (2022). DOI: https://doi.org/10.1016/j.shj.2022.100090.

[35] J. Lumens et al. *CircAdapt*. 2023. URL: https://www.circadapt.org/ (visited on 07/17/2023).

[36] M. T. Maeder et al. "Hemodynamic basis of exercise limitation in patients with heart failure and normal ejection fraction". In: *Journal of the American College of Cardiology* 56.11 (2010), pp. 855–863. DOI: 10.1016/j.jacc.2010.04.040.

[37] G. R. Meindertsma. "Methods to study interatrial shunting in heart failure patients". In: *Department of Aerospace Engineering, Delft University of Technology* (2023).

[38] R. Mittal et al. "Computational modeling of cardiac hemodynamics: Current status and future outlook". In: *Journal of Computational Physics* 305 (2016), pp. 1065–1082. DOI: https://doi.org/10.1016/j.jcp.2015.11.022.

[39] D. Morley et al. “Hemodynamic effects of partial ventricular support in chronic heart failure: Results of simulation validated with in vivo data”. In: *The Journal of Thoracic and Cardiovascular Surgery* 133.1 (2007), pp. 21–28. DOI: 10.1016/j.jtcvs.2006.07.037.

[40] T. Nishikawa et al. “Prediction of haemodynamics after interatrial shunt for heart failure using the generalized circulatory equilibrium”. In: *ESC Heart Failure* 7 (2020), pp. 3075–3085. DOI: 10.1002/ehf2.12935.

[41] *NoYA RAISE Trial II (Radiofrequency Ablation-Based Interatrial Shunt for Heart Failure)*. 2023. URL: https://clinicaltrials.gov/ct2/show/NCT05375110 (visited on 04/24/2023).

[42] L. Obermeier et al. “CT-Based Simulation of Left Ventricular Hemodynamics: A Pilot Study in Mitral Regurgitation and Left Ventricle Aneurysm Patients”. In: *Frontiers in Cardiovascular Medicine* 9 (2022). DOI: 10.3389/fcvm.2022.828556.

[43] M. Obokata, Y. N. Reddy, and S. J. Shah. “Effects of Interatrial Shunt on Pulmonary Vascular Function in Heart Failure With Preserved Ejection Fraction”. In: *Journal of the American College of Cardiology* 74.21 (2019), pp. 2539–2550. DOI: https://doi.org/10.1016/j.jacc.2019.08.1062.

[44] D.C. de Oliveira et al. “Computational fluid dynamics of the right atrium: Assessment of modelling criteria for the evaluation of dialysis catheters”. In: *PLOS One* 16.2 (2021). DOI: https://doi.org/10.1371/journal.pone.0247438.

[45] C. Paitazoglou and M. W. Bergmann. “The atrial flow regulator: current overview on technique and first experience”. In: *Therapeutic Advances in Cardiovascular Disease* 14 (2020), pp. 1–8. DOI: https://doi.org/10.1177/1753944720919577.

[46] C. Paitazoglou et al. “One-year results of the first-in-man study investigating the Atrial Flow Regulator for left atrial shunting in symptomatic heart failure patients: the PRELIEVE study”. In: *European Journal of Heart Failure* 23.5 (2021), pp. 800–810. DOI: https://doi.org/10.1002/ejhf.2119.

[47] R. Pandey et al. “A review study on blood in human coronary artery: Numerical approach”. In: *Computer Methods and Programs in Biomedicine* 187 (2020). DOI: https://doi.org/10.1016/j.cmpb.2019.105243.

[48] L. P. Parker et al. “Computational Fluid Dynamics of the Right Atrium: A Comparison of Modeling Approaches in a Range of Flow Conditions”. In: *Journal of Engineering and Science in Medical Diagnostics and Therapy* 5.3 (2022). DOI: https://doi.org/10.1115/1.4054526.

[49] M. Polaczek et al. “Morphology and morphometry of pulmonary veins and the left atrium in multislice computed tomography”. In: *Surgical and Radiologic Anatomy* 41 (2019), pp. 721–730. DOI: https://doi.org/10.1007/s00276-019-02210-1.

[50] *Pulmonary Veins: Anatomy and Function*. 2022. URL: https://my.clevelandclinic.org/health/body/23242-pulmonary-veins (visited on 11/02/2023).

[51] *RESPONDER-HF Trial*. 2023. URL: https://clinicaltrials.gov/study/NCT05425459 (visited on 10/05/2023).

[52] W. P. Santamore and D. Burkhoff. “Hemodynamic consequences of ventricular interaction as assessed by model analysis”. In: *American Journal of Physiology* 260.1 Pt 2 (1991), H146–H157. DOI: 10.1152/ajpheart.1991.260.1.H146.

[53] A. Saunders and E. Michelakis. “Atrial Shunt Devices in Patients With Heart Failure and Preserved or Mildly Reduced Ejection Fraction and the Pulmonary Circulation: Promises and Concerns”. In: *Circulation* 145 (2022), pp. 1605–1608. DOI: 10.1161/CIRCULATIONAHA.122.059810.

[54] S. J. Shah, B. A. Borlaug, and E. S. Chung. “Atrial shunt device for heart failure with preserved and mildly reduced ejection fraction (REDUCE LAP-HF II): a randomised, multicentre, blinded, sham-controlled trial”. In: *The Lancet* 399 (2022), pp. 1130–1140. DOI: https://doi.org/10.1016/S0140-6736(22)00016-2.

[55] *SimulationX System Simulation Software*. 2023. URL: https://www.esi-group.com/products/simulationx (visited on 11/01/2023).

[56] T. Sochi. “Non-Newtonian Rheology in Blood Circulation”. In: *Department of Physics & Astronomy, University College London* (2013). DOI: https://doi.org/10.48550/arXiv.1306.2067.

[57] J. L. Sparling and M. F. V. Melo. *Cohen’s Comprehensive Thoracic Anesthesia*. Elsevier, 2022. Chap. Chapter 05 - Pulmonary Pathophysiology and Lung Mechanics in Anesthesiology, pp. 66–87. DOI: https://doi.org/10.1016/B978-0-323-71301-6.00005-6.

[58] N. Stergiopulos, J. J. Meister, and N. Westerhof. “Evaluation of methods for estimation of total arterial compliance”. In: *American Journal of Physiology* 268.4 Pt 2 (1995), H1540–H1548. DOI: 10.1152/ajpheart.1995.268.4.H1540.

[59] N. Stergiopulos, B. E. Westerhof, and N. Westerhof. “Total arterial inertance as the fourth element of the windkessel model”. In: *American Journal of Physiology* 276.1 (1999), H81–H88. DOI: 10.1152/ajpheart.1999.276.1.H81.

[60] H. Suga and K. Sagawa. “Instantaneous Pressure-Volume Relationships and Their Ratio in the Excised, Supported Canine Left Ventricle”. In: *Circulation Research* 35.1 (1974), pp. 117–126. DOI: https://doi.org/10.1161/01.RES.35.1.117.

[61] *V-Wave*. 2023. URL: https://vwavemedical.com/ (visited on 04/24/2023).

[62] N. Westerhof, J. W. Lankhaar, and B. E. Westerhof. “The arterial Windkessel”. In: *Medical & Biological Engineering & Computing* 47 (2009), pp. 131–141. DOI: 10.1007/s11517-008-0359-2.

A

Newtonian assumption

To review the assumption that blood flow in the atria can be modeled as a Newtonian fluid, a validation step is taken in this research. Considering the steady-state 2D CFD simulations, the shear rates in the atria are presented in Figure A.1. According to Doost et al. [16] and Sochi [56], the shear rate below which non-Newtonian effects are considered significant is around 100 s^{-1}. Therefore, a color scale has been chosen such that the red regions reflect a shear rate higher than this threshold, whereas non-Newtonian effects are considered significant in the blue regions. Without a shunt present, as shown in Figure A.1a, some of the main structures discussed for the velocity field in section 4.2 can be recognized. In the right atrium, the jets from the two vena cavae are visible, with especially the IVC jet causing high shear rates in the lower part of the right atrium towards the tricuspid valve. In the left atrium, the highest shear rates are also found near the inlets, where the recirculation zones are present. Very close to the wall, however, small zones of low shear rate are visible. In the right atrium, a much bigger region of low shear rate is found, as almost the entire upper half of the right atrium has a shear rate below the 100 s^{-1} threshold. Also the flow in the superior vena cava inlet has a low shear rate.

The shunt flow in Figure A.1b alters the shear rate field in the atria. As noted previously in section 4.2, the flow through the interatrial septum disturbs the big region of recirculation in the right atrium. This can also be seen in Figure A.1b, where the shear rate is now much higher around the shunt. This also holds for the left atrium, where the region of low shear rate near the interatrial septum has increased in size. Meanwhile, the shear rates in the upper parts of the atria have largely remained the same, with low shear rates in the right atrium and high shear rates in the left atrium.

As significant parts of the domain show shear rates below 100 s^{-1}, it cannot directly be concluded that the results of the steady-state 2D CFD simulation are reliable. Therefore, the simulations have been repeated by modeling blood as a non-Newtonian fluid with shear rate-dependent viscosity. According to Carvalho et al. [10], the Carreau model is the most suitable to mimic the non-Newtonian behavior of blood and therefore this model was chosen. The Carreau model describes the fluid viscosity as follows:

$$\mu(\dot{\gamma}) = \mu_\infty + (\mu_0 - \mu_\infty)[1 + (\lambda\dot{\gamma})^2]^{(n-1)/2}, \tag{A.1}$$

where μ is the apparent viscosity, $\dot{\gamma}$ is the shear rate, μ_∞ is the high shear rate viscosity, μ_0 is the zero shear rate viscosity, λ is the time constant and n is the power law index. To model blood, the following values are used: $\mu_\infty = 0.0035$ Pa·s, $\mu_0 = 0.056$ Pa·s, $\lambda = 3.313$ s and $n = 0.3568$ [16, 44]. Equation A.1 is graphically presented in Figure A.2, which shows the dynamic viscosity of blood as a function of shear rate. The Newtonian value is added as a reference, which confirms that blood viscosity stays relatively constant for shear rates exceeding 100 s^{-1}.

As the dynamic viscosity is now a function of the shear rate and therefore no longer constant throughout the domain, Figure A.3 shows the dynamic viscosity in absence (Figure A.3a) and presence (Figure A.3b) of an 8 mm interatrial shunt. From this, it can be seen that the regions with the highest shear rates from Figure A.1 are darkest blue in Figure A.3. This means that the viscosity is lowest and close to the value of 0.0035 Pa·s used in the simulations assuming blood as a Newtonian fluid. The regions where the shear rates are the lowest correspond to the brighter colors, indicating a higher viscosity which is further from the constant value. Standing out from the brighter colors are the central part of

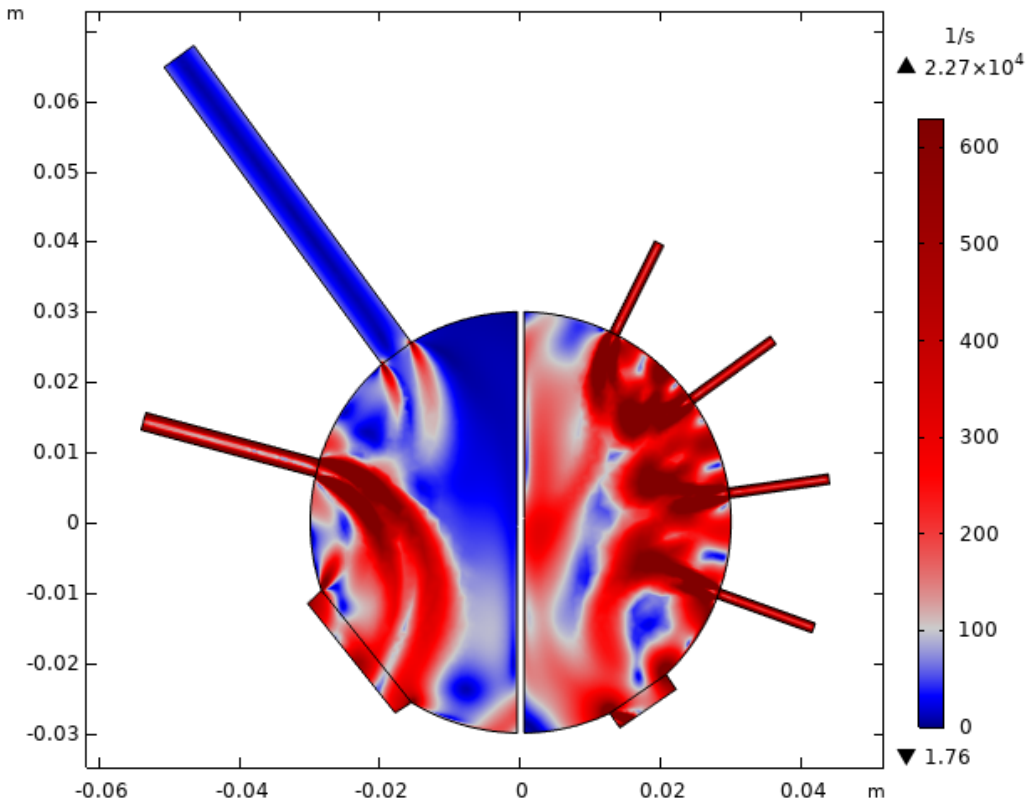

(a) Without shunt

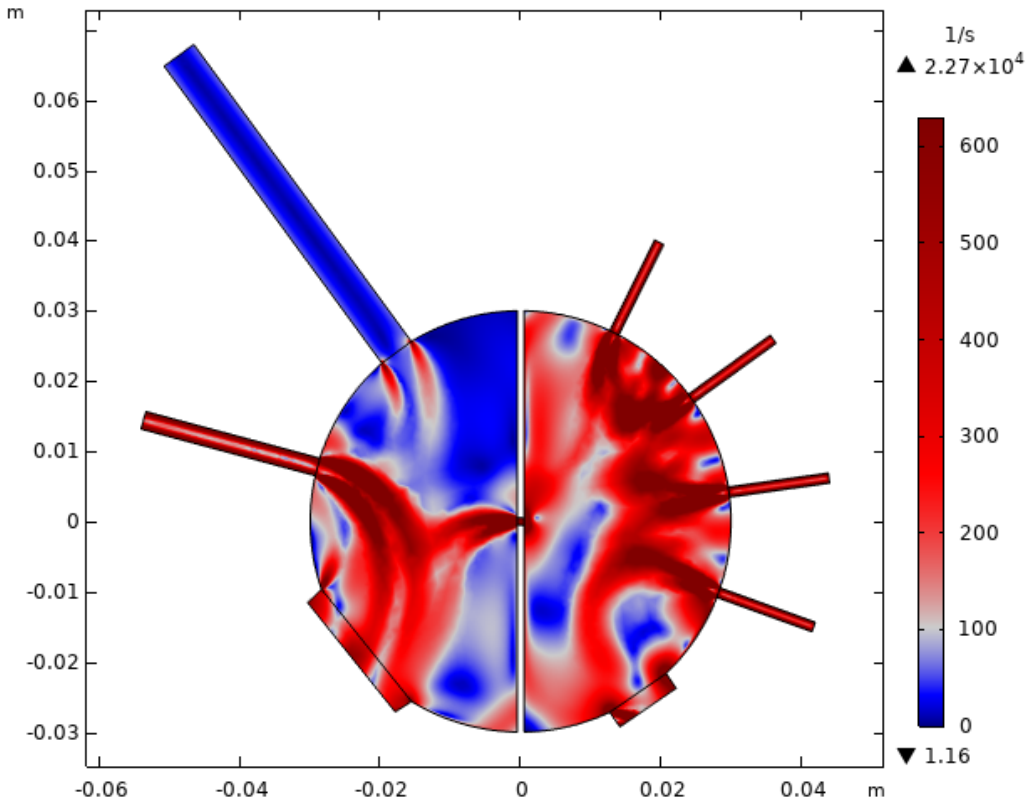

(b) 8 mm shunt

Figure A.1: Shear rate of the steady-state 2D CFD simulation in absence (a) and presence (b) of an 8 mm shunt

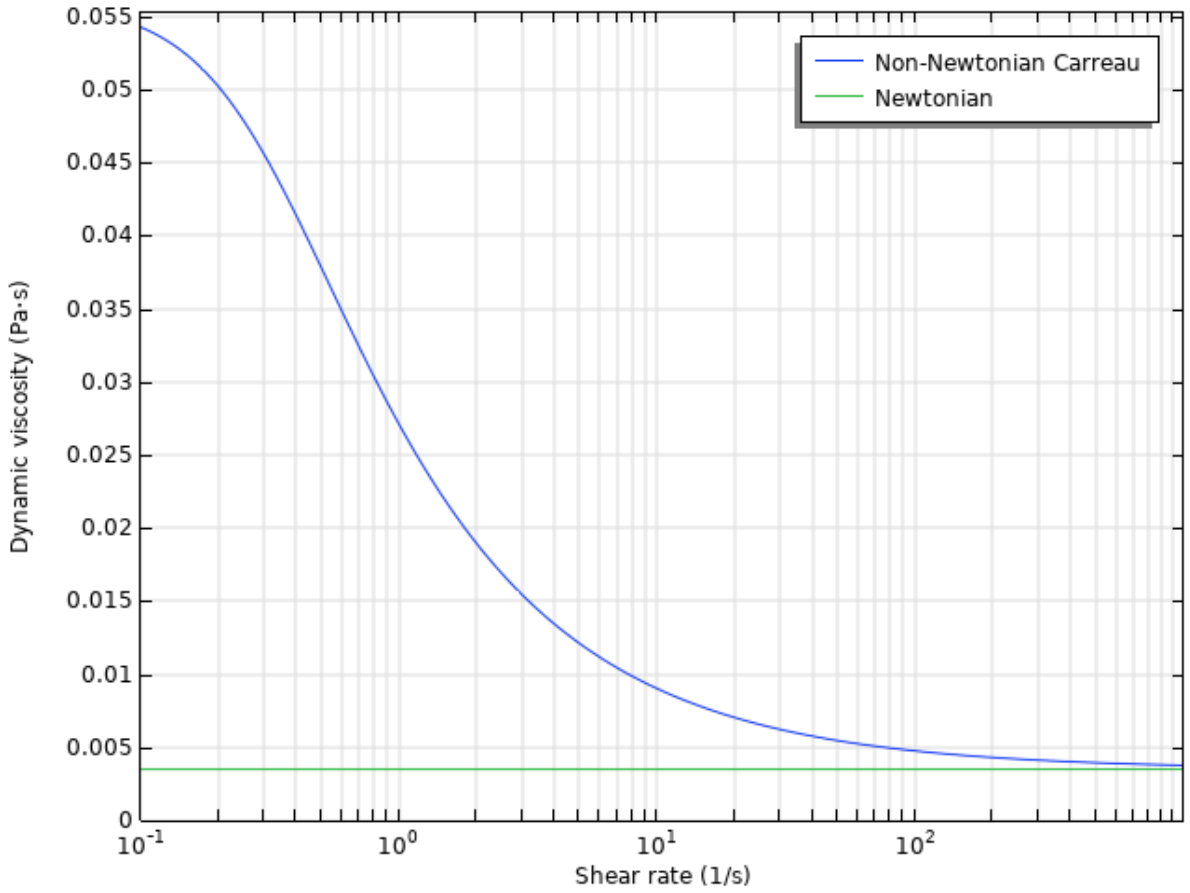

Figure A.2: Blood dynamic viscosity as a function of shear rate as modeled by the Carreau non-Newtonian fluid model and the Newtonian value as a reference

the superior vena cava and the right atrial upper corner, which show the highest dynamic viscosity in the domain. Although it is true that the shear rate is low here (5 s^{-1}), the viscosity should not be this high (0.025 Pa·s) in this region as found from Equation A.1 and Figure A.2. It is not fully understood why this is the case, but it could be due to a multi-way coupling between the shear rate and the dynamic viscosity. Overall, however, the presented result shows that the dynamic viscosity does not vary much throughout most parts of the atria.

The velocity field of this simulation is presented in Figure A.4. Comparing this result to Figure 4.4 presented in section 4.2 for the simulation assuming Newtonian viscosity, a visual difference cannot be established. Therefore, Figure A.5 shows the absolute difference in velocity magnitude between the simulation using the Newtonian assumption and the simulation using the Carreau non-Newtonian fluid model. In this figure, red regions reflect a higher velocity magnitude for the simulation assuming blood as a Newtonian fluid, whereas blue regions reflect a higher velocity magnitude for the simulation modeling blood as a non-Newtonian fluid. It can be seen that the Newtonian assumption mostly overestimates the velocity magnitude in the atria, but only by about 0.02 m/s. As this difference is more meaningful relative to the local velocity magnitude, Figure A.6 shows the absolute value of the difference in velocity magnitude between the two simulations, relative to the local velocity magnitude of the simulation assuming constant viscosity. The scale has been chosen in such a way that a red color indicates a relative difference greater than 10%, whereas a blue color indicates a relative difference smaller than 10%. This figure shows that the relative difference in velocity magnitude is very small throughout the domain, apart from only a few regions. These regions are either of low velocity magnitude, where a small difference in velocity can easily result in a large relative difference, of high velocity gradient, where a difference in velocity is easily found due to the high gradient, or a combination thereof. Figure A.7 shows the same result, but with an error threshold of 1%. This shows that the relative errors in the regions of highest shear rate are even less than 1%, whereas most of the higher errors are in the order of 2%.

Furthermore, Figure A.8 presents the pressure field of the simulation modeling blood using the Carreau non-Newtonian fluid model. As for the velocity field, no visual difference can be established between this result and Figure 4.5 for the simulation assuming a constant viscosity. Figure A.9 shows the absolute difference in pressure throughout the atria, where a red color indicates a higher pressure for the simulation assuming blood as a Newtonian fluid and a blue color indicates a higher pressure for the simulation assuming blood as a non-Newtonian fluid. From this, it can be seen that the Newtonian assumption over- and underestimates the pressure in various locations in the atria. However, the differences in pressure are mostly around 10 Pascal, which is relatively small compared to the local pressures. This is reflected by Figure A.10, which shows the absolute value of the difference in pressure between the two simulations, relative to the local pressure of the simulation assuming constant viscosity. This figure shows a very small relative difference throughout the atria, apart from the region between the inferior vena cava inlet and the tricuspid valve outlet in the right atrium. This great relative difference is caused by the low pressure in this area, which is very close to 0 Pa relative to the reference pressure. Therefore, a small absolute error in Figure A.9 still causes a large relative error in Figure A.10. How small the errors throughout most of the domain really are, is especially well reflected by Figure A.11, which shows the relative error with a threshold of only 1%.

In conclusion, this validation step has shown that there is a difference in results between the simulation assuming blood as a Newtonian fluid and the simulation modeling blood using the Carreau non-Newtonian fluid model. However, as Figures A.6 and A.7 have shown for the velocity field and Figures A.10 and A.11 have shown for the pressure field, the relative differences are very small (around 1%) for most of the domain. Therefore, it is concluded that the Newtonian assumption is valid for these simulations.

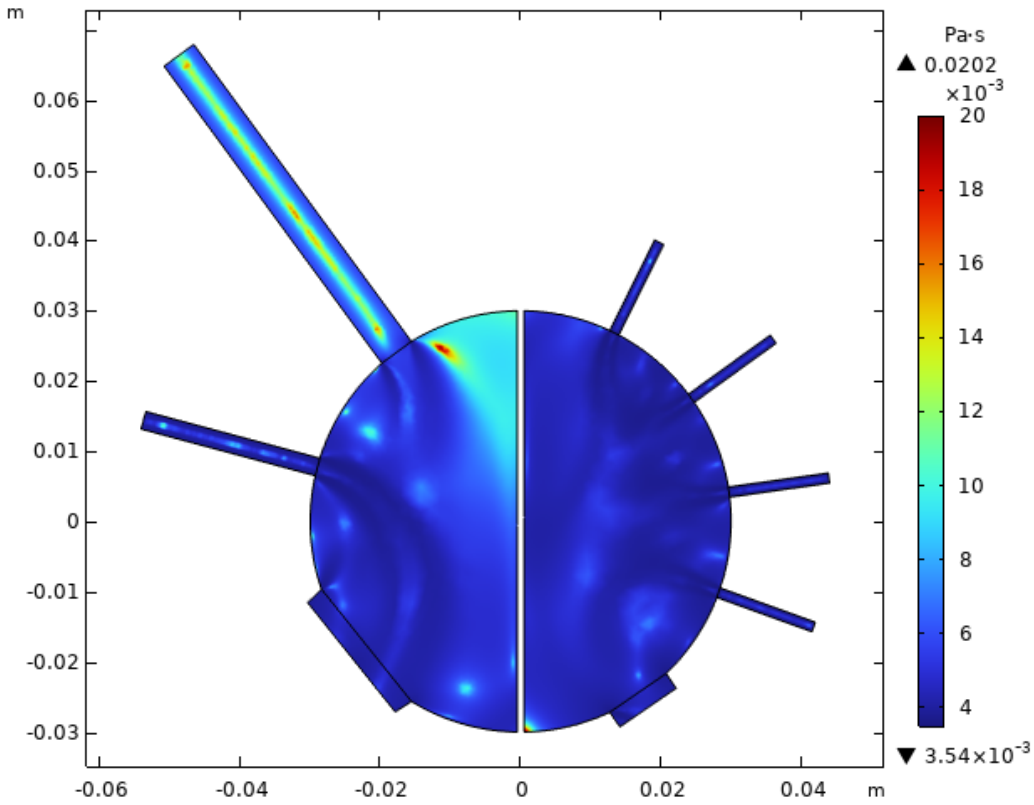

(a) Without shunt

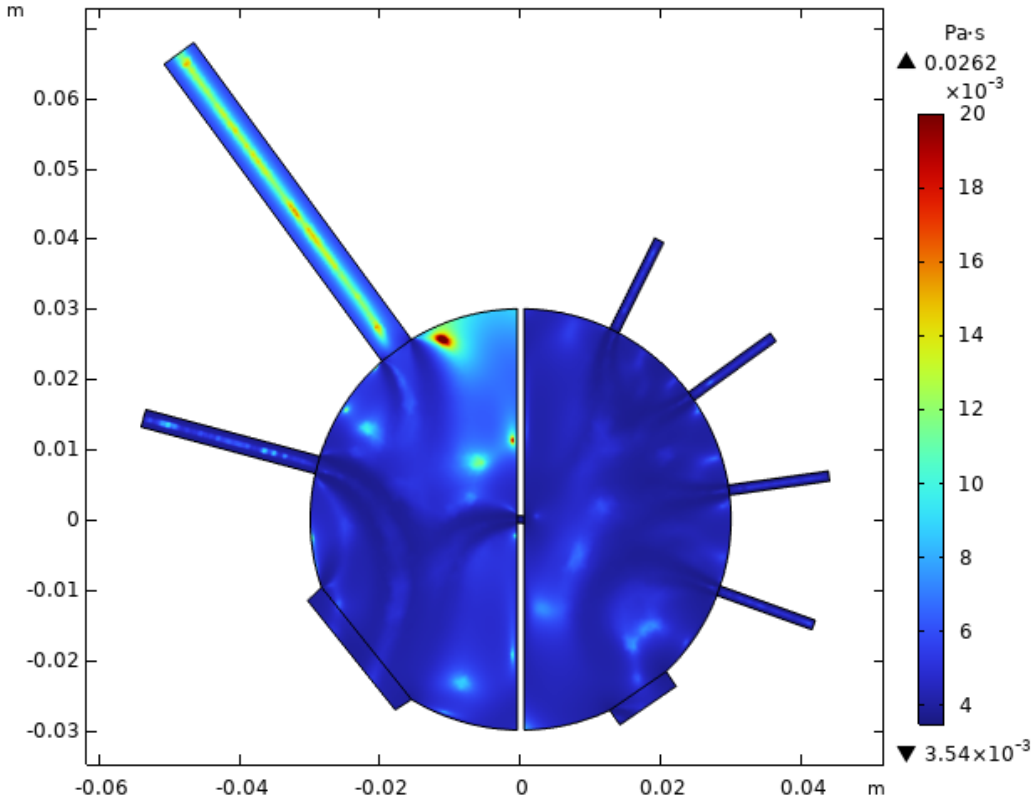

(b) 8 mm shunt

Figure A.3: Dynamic viscosity of the steady-state 2D CFD simulation using the Carreau non-Newtonian fluid model, in absence (a) and presence (b) of an 8 mm shunt

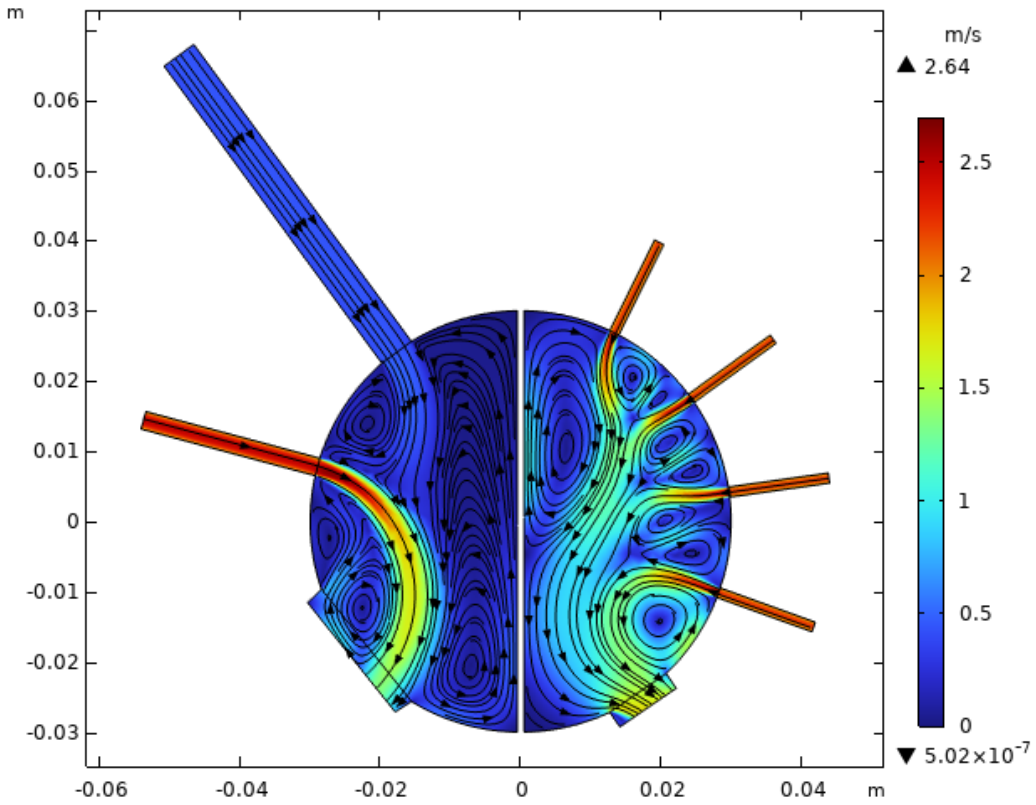

(a) Without shunt

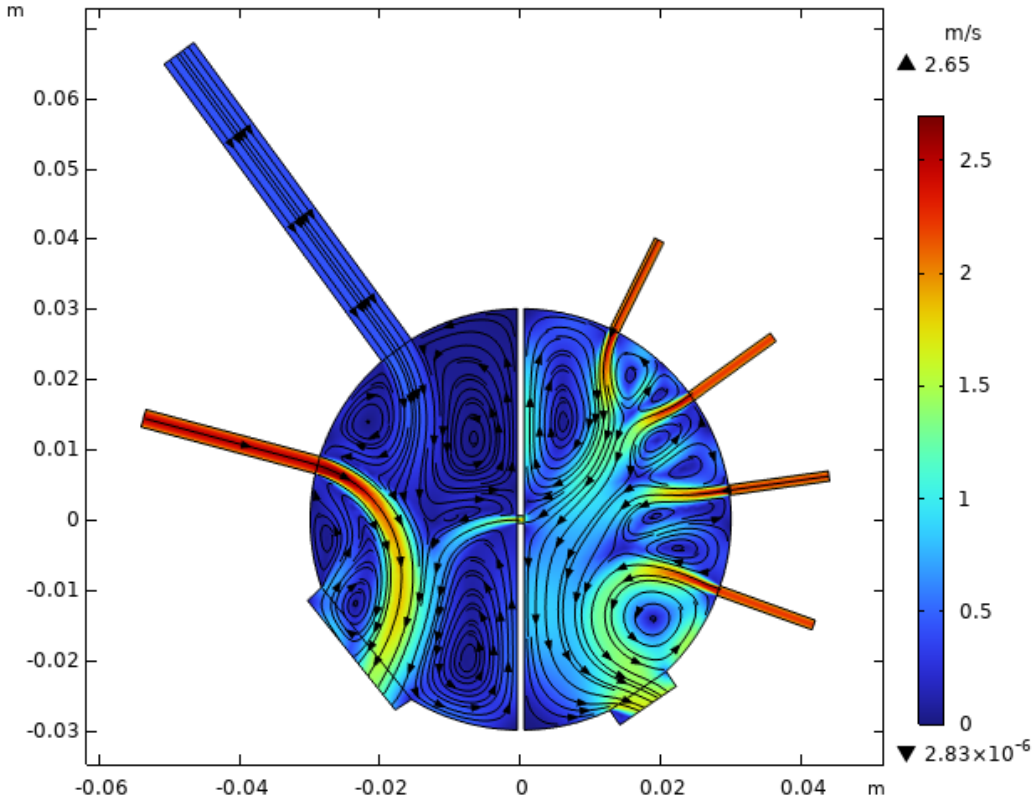

(b) 8 mm shunt

Figure A.4: Velocity magnitude and streamlines of the steady-state 2D CFD simulation using the Carreau non-Newtonian fluid model to describe the blood viscosity, in absence (a) and presence (b) of an 8 mm shunt

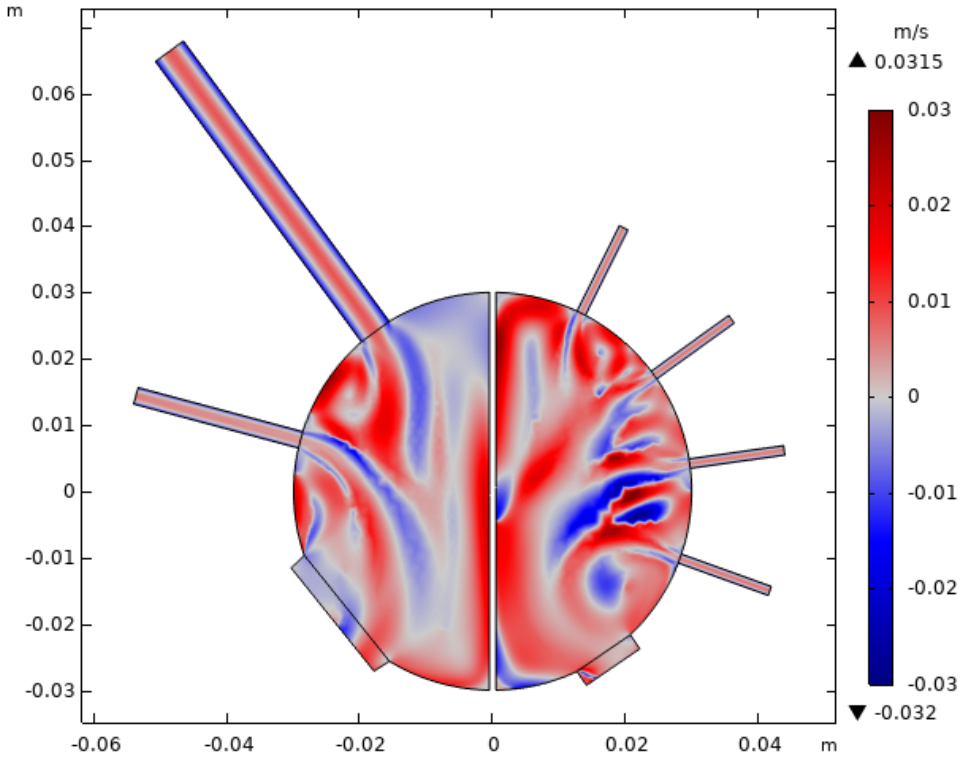

(a) Without shunt

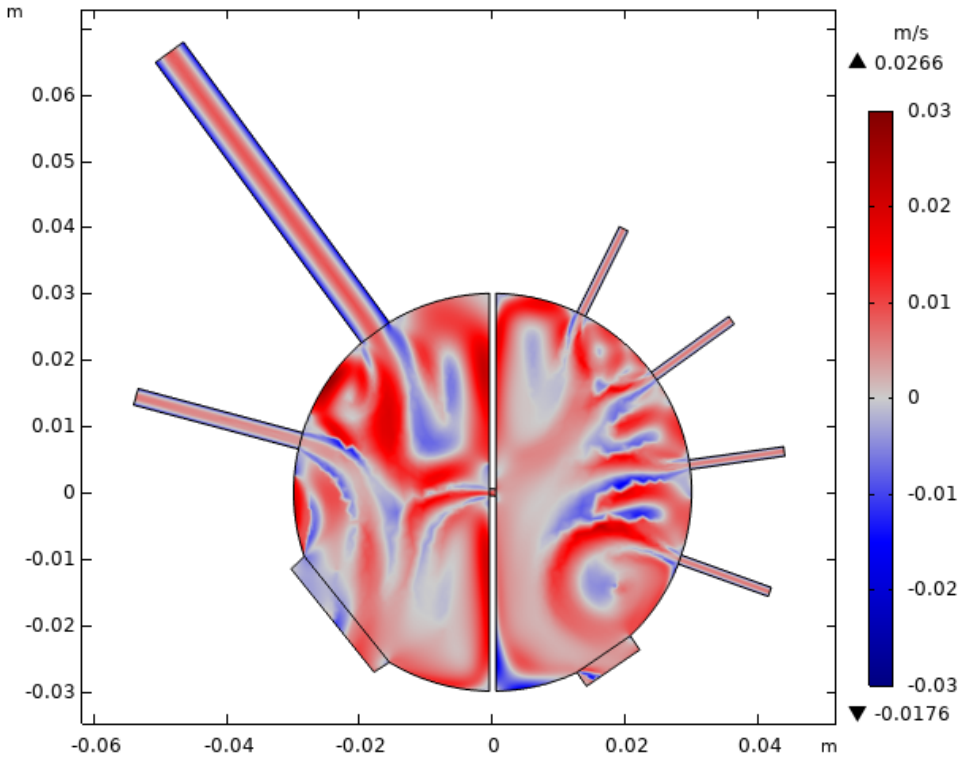

(b) 8 mm shunt

Figure A.5: Difference in velocity magnitude between the steady-state 2D CFD simulation using the Newtonian assumption and the simulation using the Carreau non-Newtonian fluid model to describe the blood viscosity, in absence (a) and presence (b) of an 8 mm shunt. A red color indicates a higher velocity magnitude for the Newtonian simulation, whereas a blue color indicates a higher velocity magnitude for the non-Newtonian simulation.

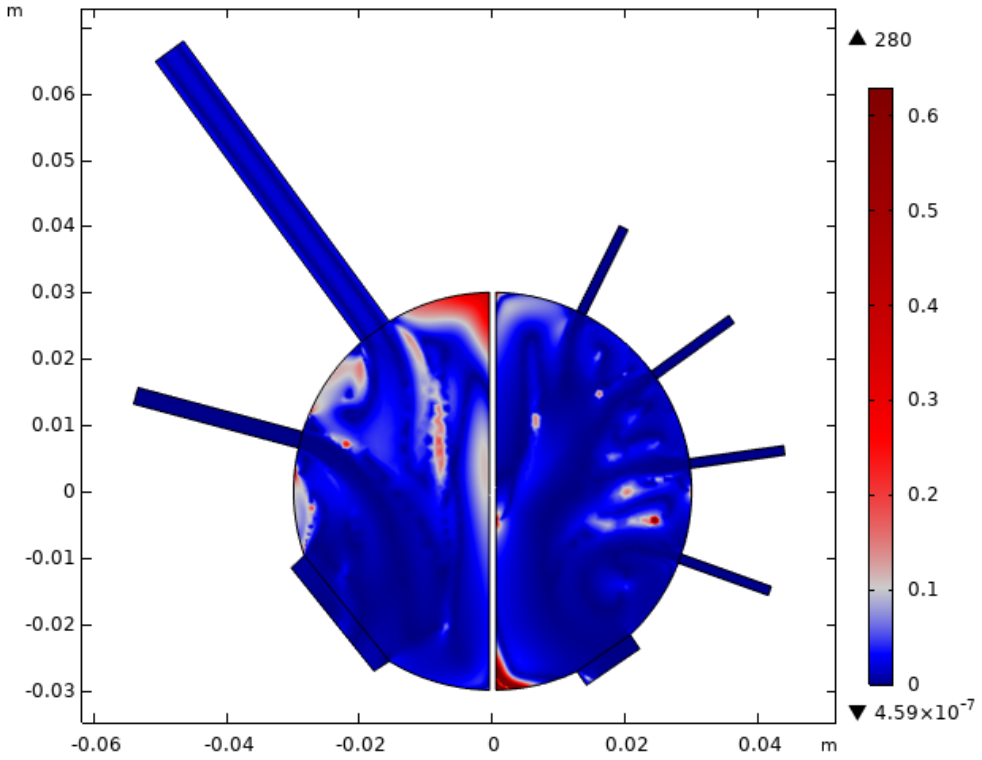

(a) Without shunt

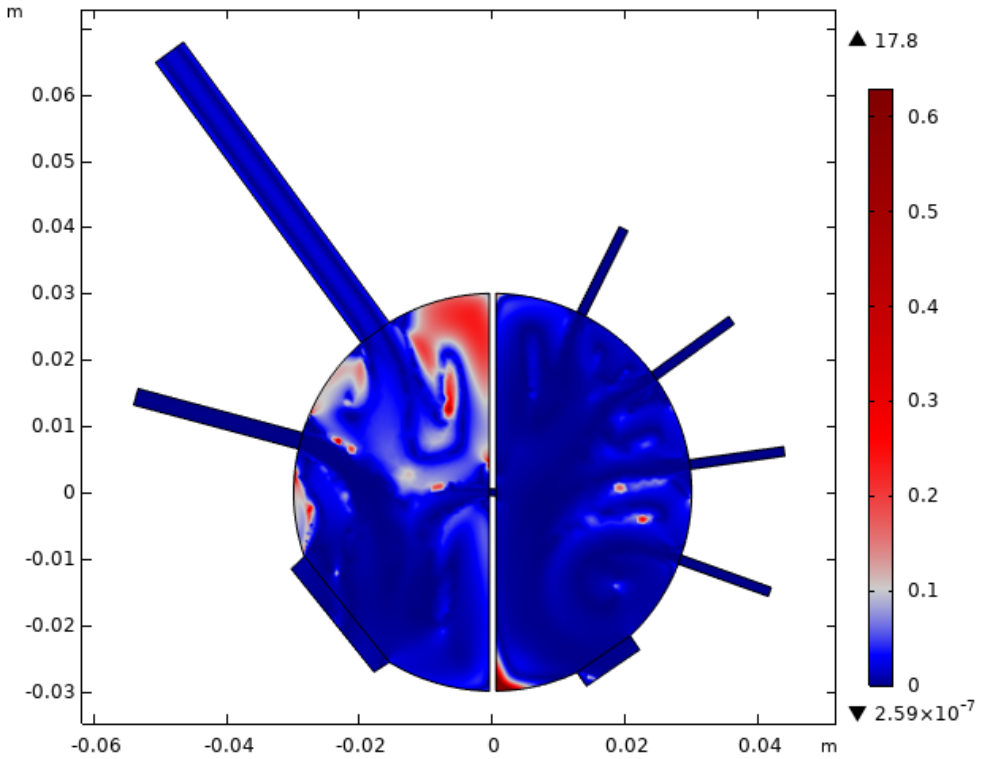

(b) 8 mm shunt

Figure A.6: Absolute value of the difference in velocity magnitude between the steady-state 2D CFD simulation using the Newtonian assumption and the simulation using the Carreau non-Newtonian fluid model to describe the blood viscosity, relative to the local velocity magnitude, in absence (a) and presence (b) of an 8 mm shunt. A red color indicates a relative difference greater than 10%, whereas a blue color indicates a relative difference smaller than 10%.

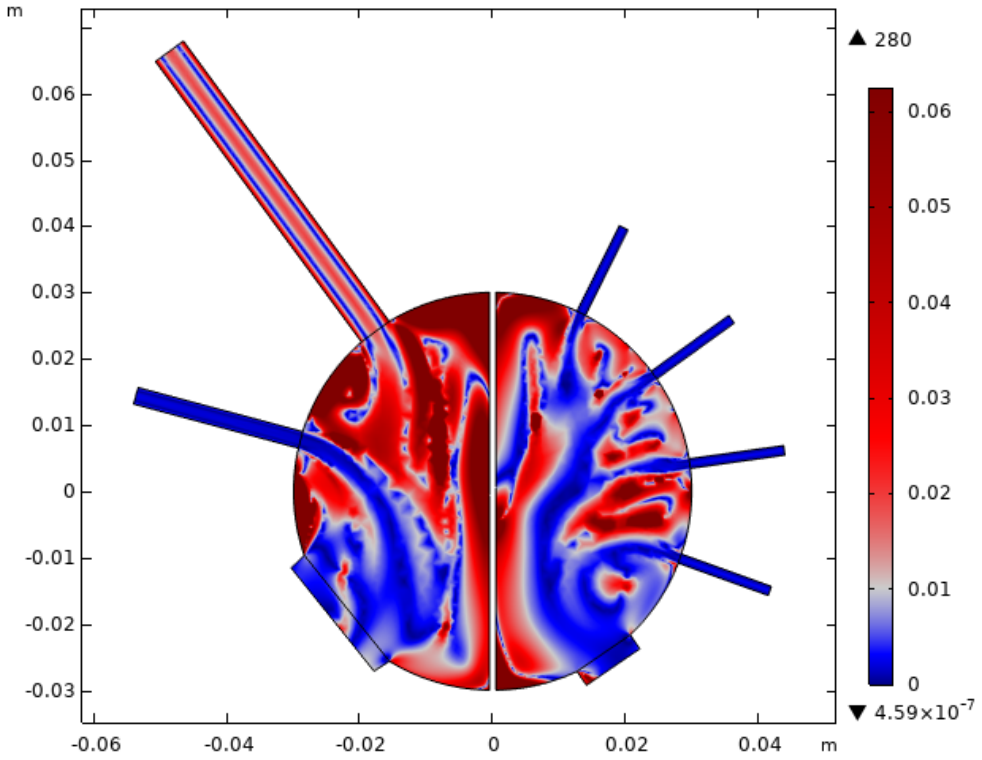

(a) Without shunt

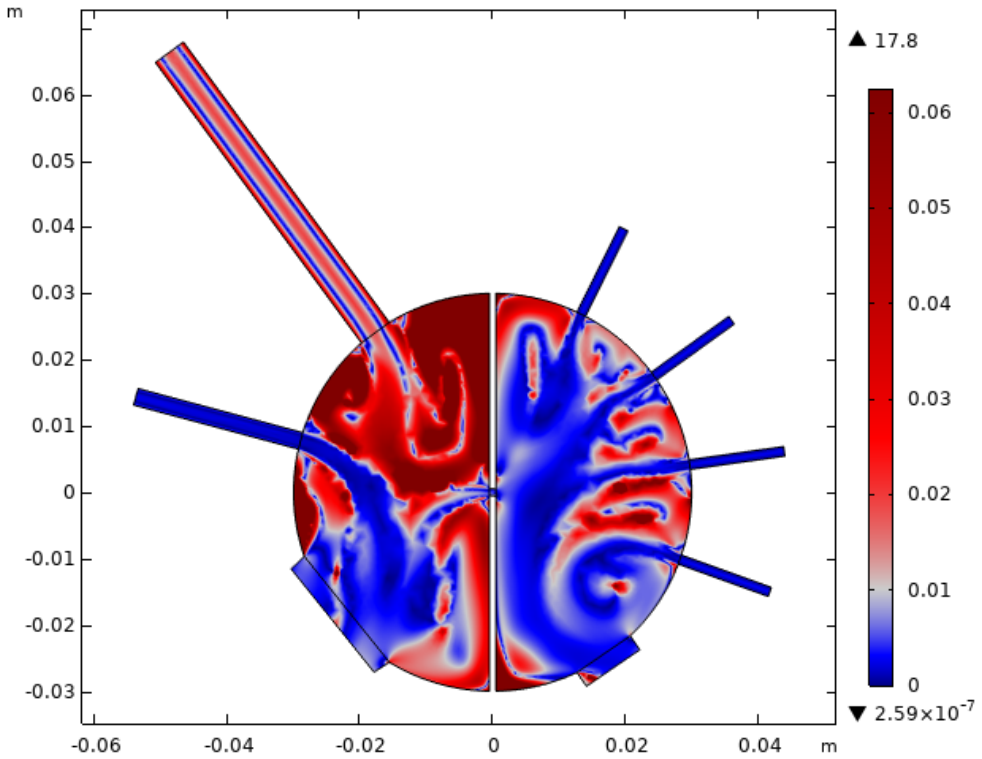

(b) 8 mm shunt

Figure A.7: Absolute value of the difference in velocity magnitude between the steady-state 2D CFD simulation using the Newtonian assumption and the simulation using the Carreau non-Newtonian fluid model to describe the blood viscosity, relative to the local velocity magnitude, in absence (a) and presence (b) of an 8 mm shunt. A red color indicates a relative difference greater than 1%, whereas a blue color indicates a relative difference smaller than 1%.

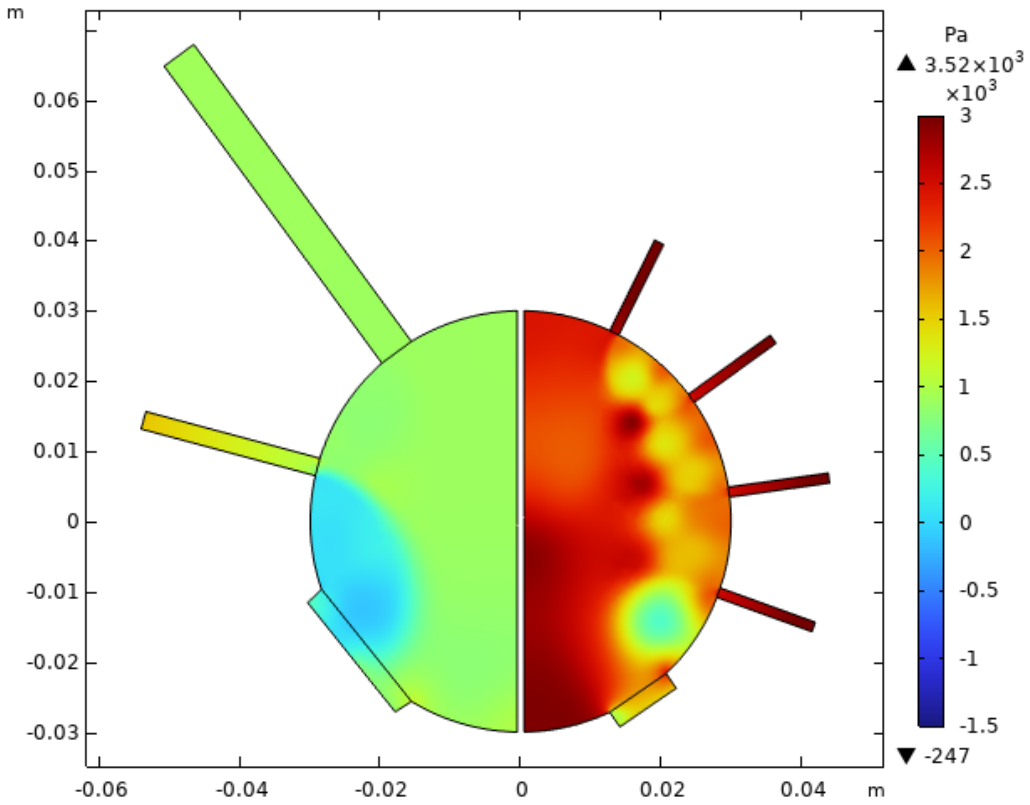

(a) Without shunt

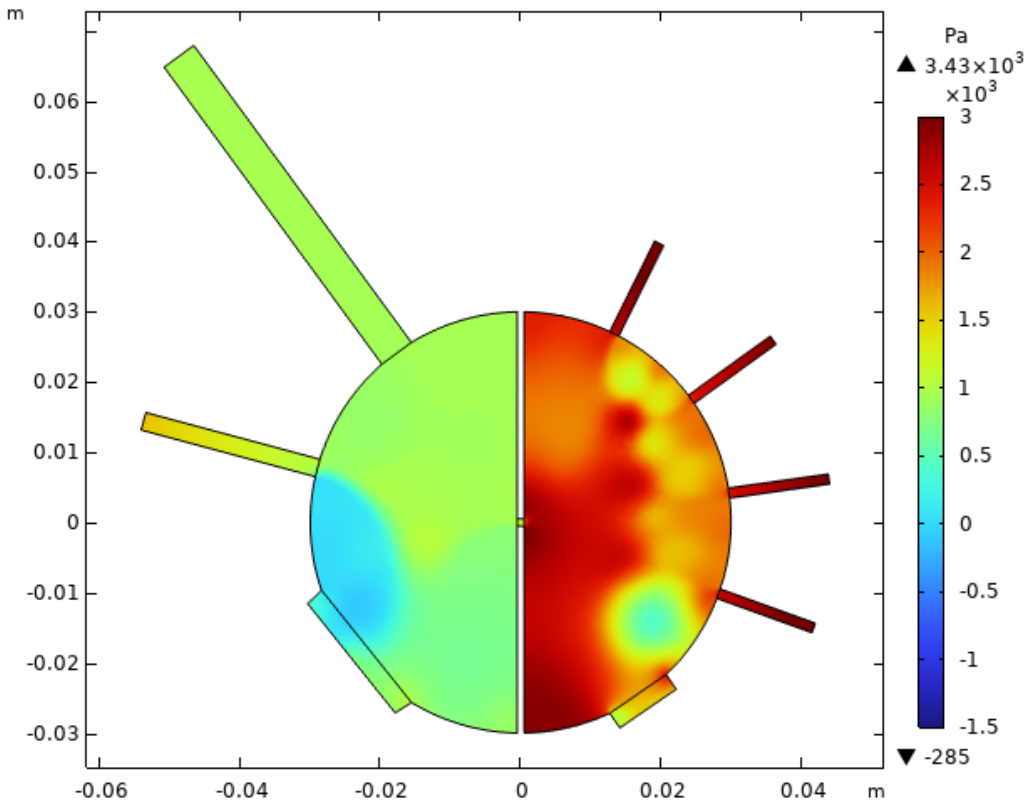

(b) 8 mm shunt

Figure A.8: Pressure field of the steady-state 2D CFD simulation using the Carreau non-Newtonian fluid model to describe the blood viscosity, in absence (a) and presence (b) of an 8 mm shunt

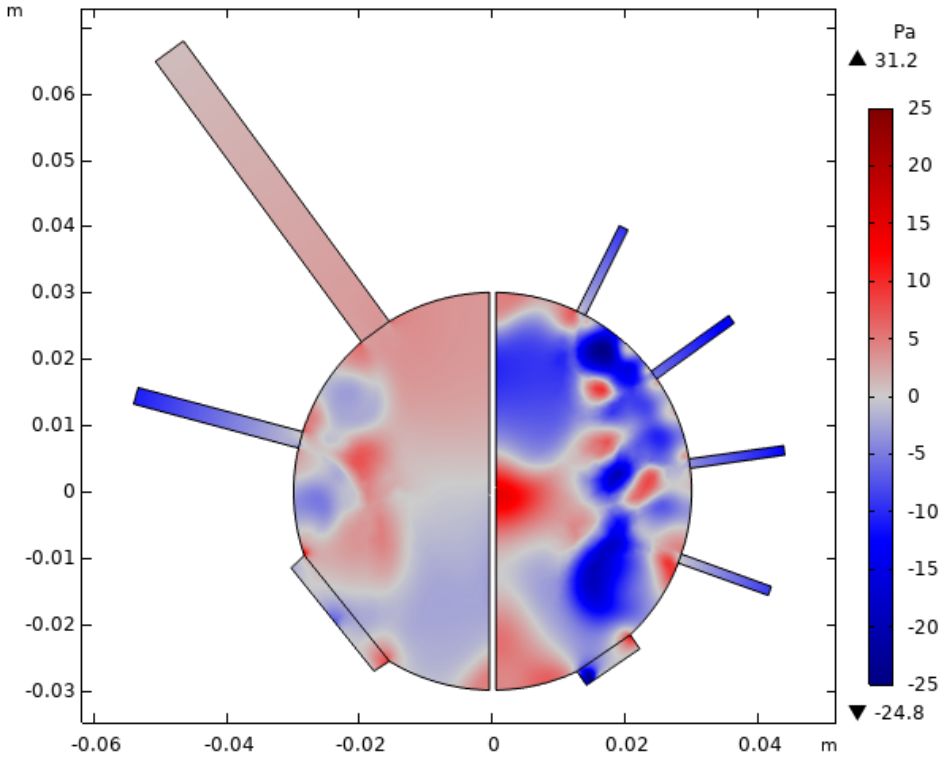

(a) Without shunt

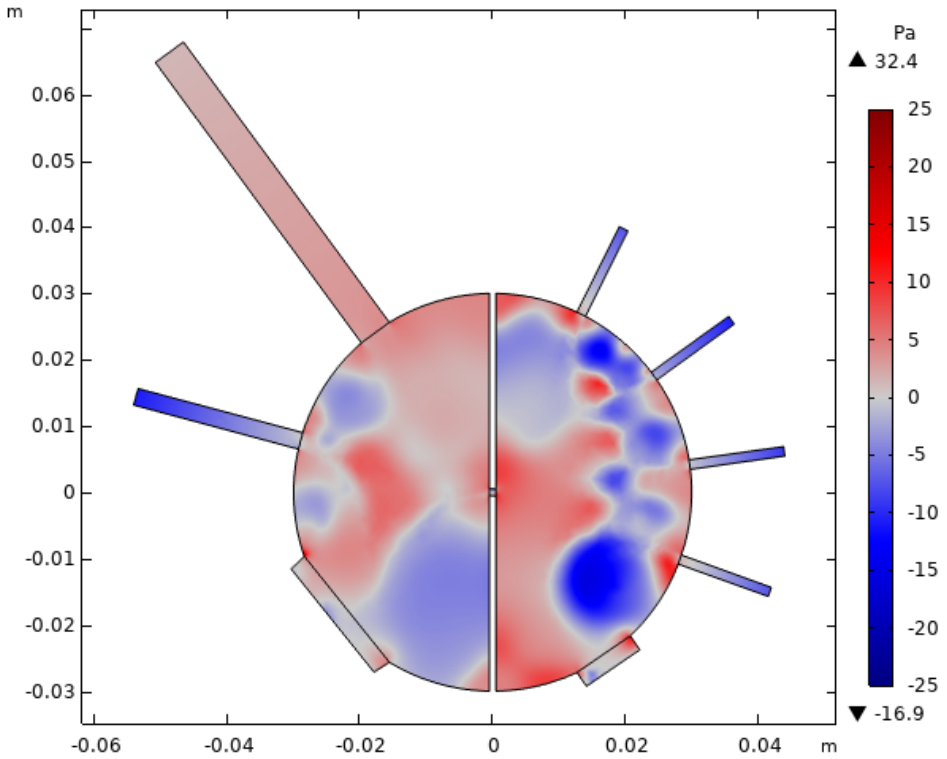

(b) 8 mm shunt

Figure A.9: Difference in pressure between the steady-state 2D CFD simulation using the Newtonian assumption and the simulation using the Carreau non-Newtonian fluid model to describe the blood viscosity, in absence (a) and presence (b) of an 8 mm shunt. A red color indicates a higher pressure for the Newtonian simulation, whereas a blue color indicates a higher pressure for the non-Newtonian simulation.

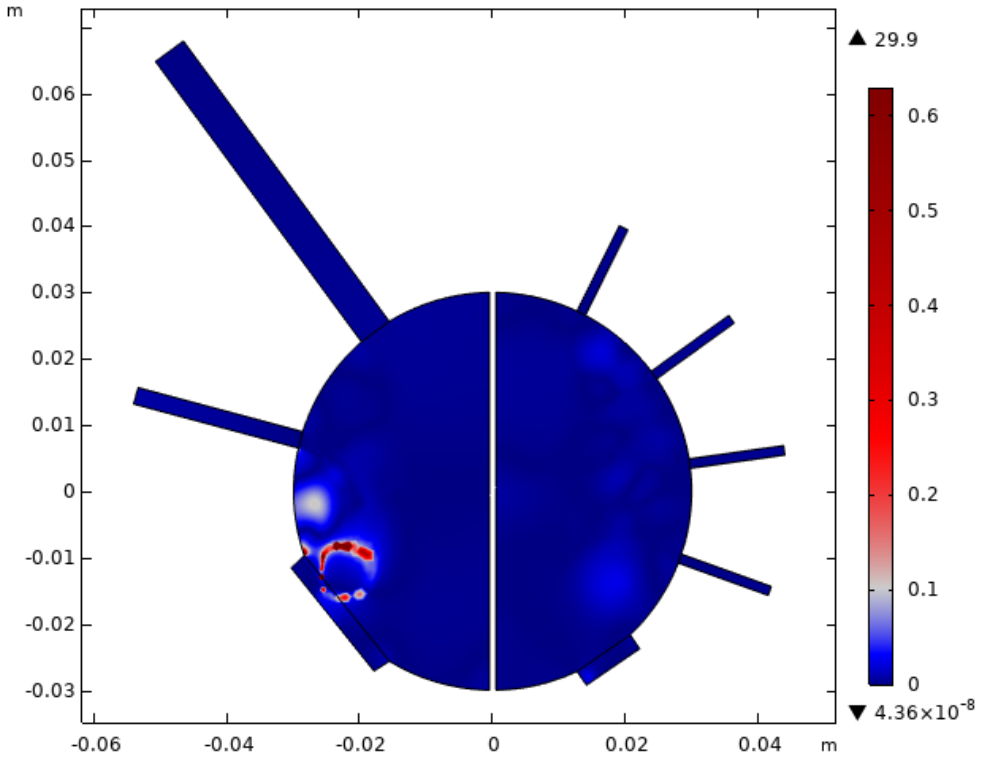

(a) Without shunt

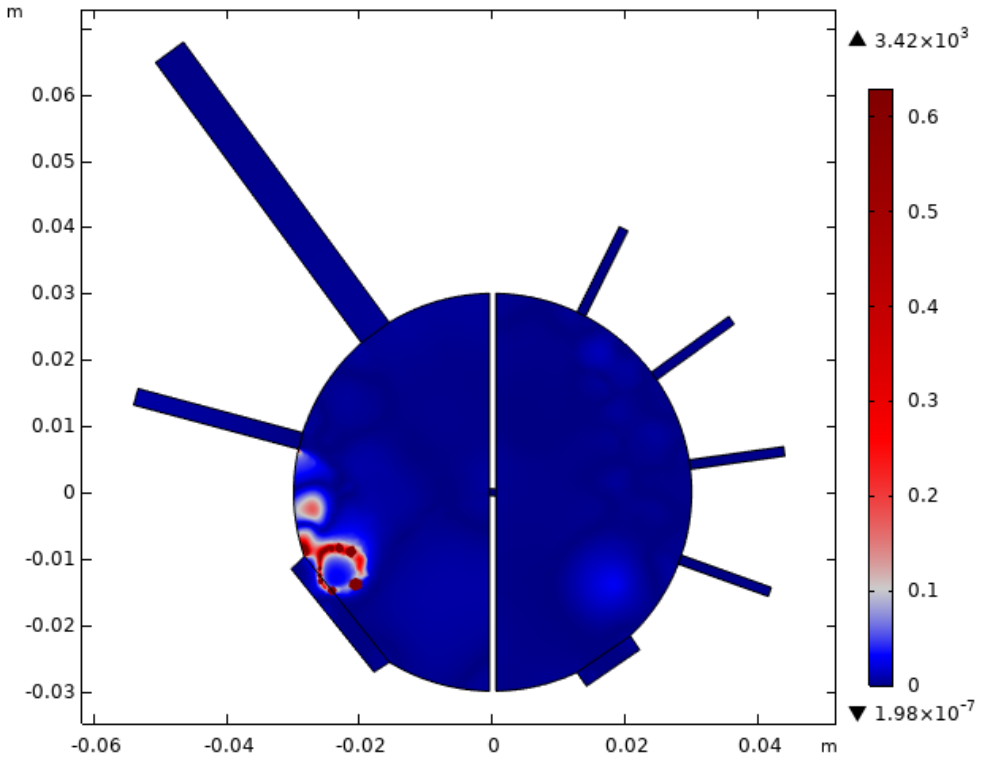

(b) 8 mm shunt

Figure A.10: Absolute value of the difference in pressure between the steady-state 2D CFD simulation using the Newtonian assumption and the simulation using the Carreau non-Newtonian fluid model to describe the blood viscosity, relative to the local pressure, in absence (a) and presence (b) of an 8 mm shunt. A red color indicates a relative difference greater than 10%, whereas a blue color indicates a relative difference smaller than 10%.

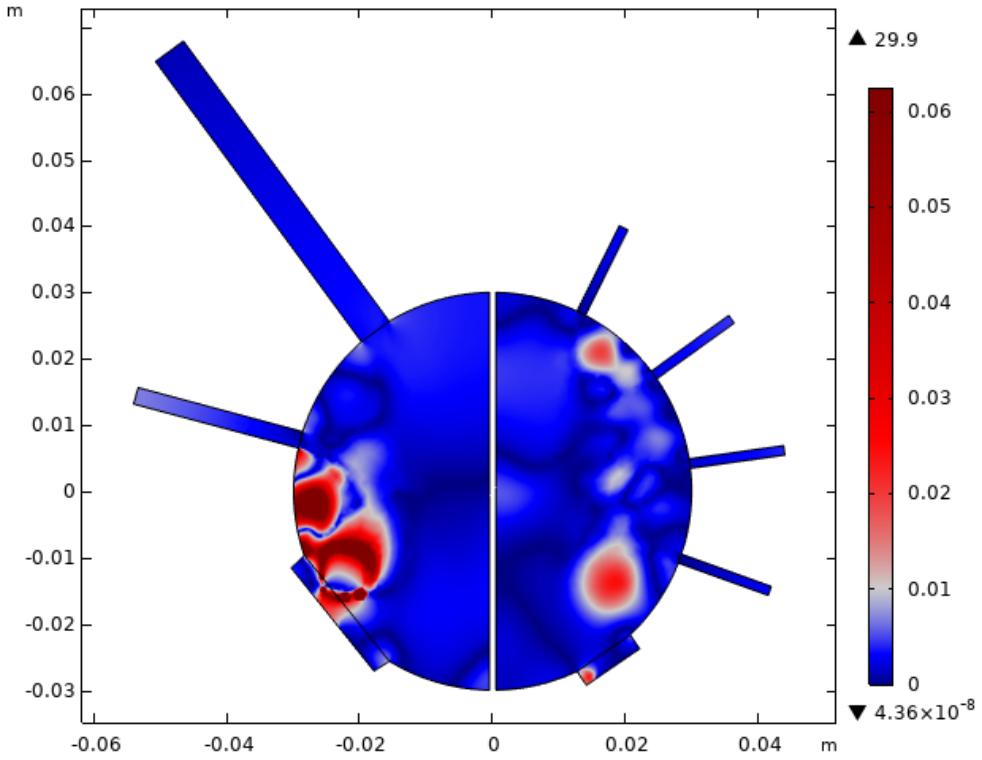

(a) Without shunt

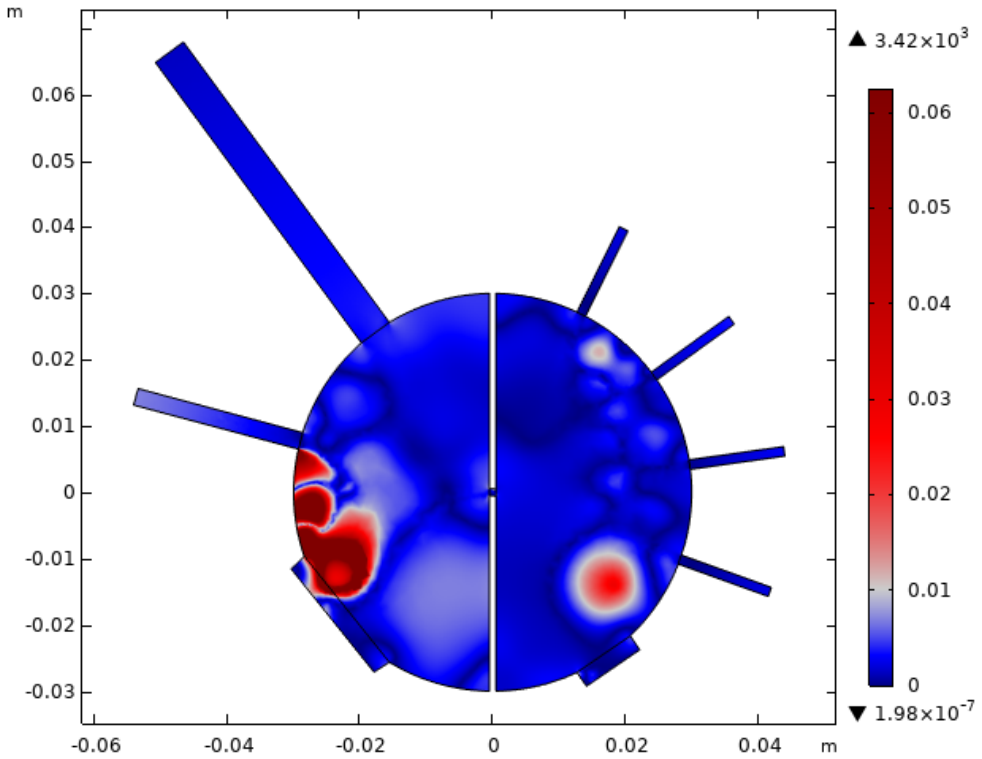

(b) 8 mm shunt

Figure A.11: Absolute value of the difference in pressure between the steady-state 2D CFD simulation using the Newtonian assumption and the simulation using the Carreau non-Newtonian fluid model to describe the blood viscosity, relative to the local pressure, in absence (a) and presence (b) of an 8 mm shunt. A red color indicates a relative difference greater than 1%, whereas a blue color indicates a relative difference smaller than 1%.

B

Mesh convergence and sensitivity

A study on the convergence and sensitivity of the mesh is performed as a verification step in this research. First, this appendix presents how the appropriate mesh size was chosen. Then, this mesh is further refined and its effect on the simulation results is analyzed. This analysis aims to quantify the error introduced by the spatial discretization of the problem, i.e. the mesh, to give an indication of the accuracy of the results.

Considering the steady-state simulation, initially the boundary layer is refined to increase the accuracy in the inlet veins, near the atrial walls and near the interatrial septum. The maximum element size is decreased from its default size of 2.74 mm by dividing it by 2, 4, 6, 8, 10, 12, 14, 16, 18 and 20. Figure B.1 presents the results of two parameters of this simulation as a function of the boundary layer maximum element size. Firstly, Figure B.1a shows the velocity magnitude squared (U^2) integrated over the domain. This parameter is chosen as a substitute for the kinetic energy, because it is a global parameter that should be conserved in the domain. Secondly, Figure B.1b shows the flow rate through the shunt, as this is a parameter of direct interest. By studying the convergence of these two parameters, a more founded choice for the mesh size can be made compared to studying only a single parameter. In both Figure B.1a and Figure B.1b, an increase in the parameter value is witnessed as the boundary layer is refined until somewhat of a plateau is reached. For the shunt flow rate (Figure B.1b), this is from the third data point from the right, whereas this is from the fifth data point from the right (circled in red) in Figure B.1a. Concluding from these two parameters, mesh convergence is reached from the fifth data point from the right, corresponding to a maximum element size of 0.343 mm, i.e. a boundary layer 8 times as fine.

For the default, non-refined mesh and for the mesh with a sufficiently refined boundary layer (the data point circled in red in Figure B.1), Figure B.2 shows the wall resolution in viscous units. As the k-ω turbulence model is used, the ideal wall resolution is obtained for $y^+ = 1$. For the default mesh (Figure B.2a), this is mostly not the case. Only in the superior vena cava and the walls in the top corner of the right atrium, the wall is sufficiently resolved. In the rest of the domain, y^+ is mostly between 2 and 3. Wall resolution is worst at the corners between the inlets/outlets and the walls, where y^+ goes up to 5 as indicated in the figure. This is due to the relatively coarse mesh in these regions, as the boundary layer refinement is not continued around sharp corners. For a boundary layer maximum element size that is 8 times smaller however, Figure B.2b shows that the walls are well-resolved nearly everywhere, i.e. $y^+ = 1$.

For the mesh with the sufficiently refined boundary layer with a maximum element size of 0.343 mm, the core is now refined in a similar fashion to the boundary layer, until the maximum element size of the boundary layer is reached. Therefore, the default maximum element size of the core of 4.41 mm is divided by 2, 4, 6, 8, 10, 12 and 12.9, the latter corresponding to the maximum element size of the boundary layer (0.343 mm). The values of the previously introduced substitute of the global kinetic energy and the shunt flow rate are presented in Figure B.3 as a function of core maximum element size. Both Figure B.3a and Figure B.3b show fluctuations in the parameter values. However, these are of the same order as the fluctuations in the plateaus in Figure B.1. Therefore, it is concluded that no refinement of the core mesh is necessary and that the appropriate mesh for the simulations has a boundary layer maximum element size of 0.343 mm and a core maximum element size of 4.41 mm.

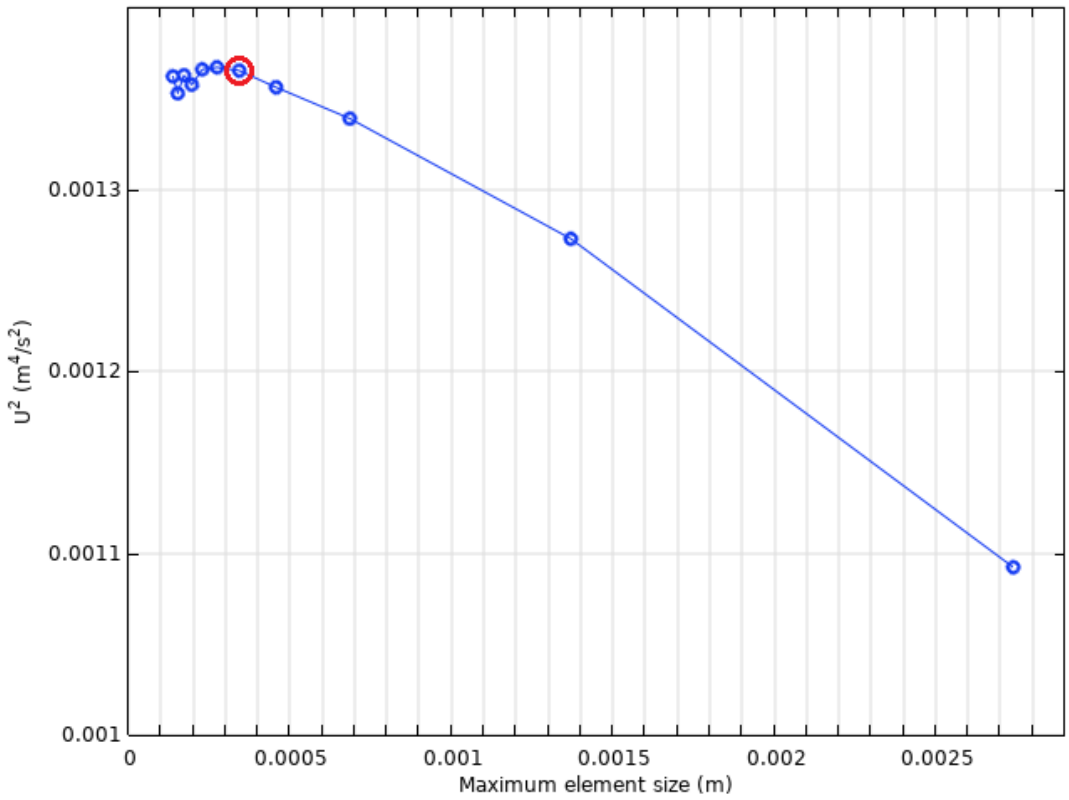

(a) Substitute of global kinetic energy

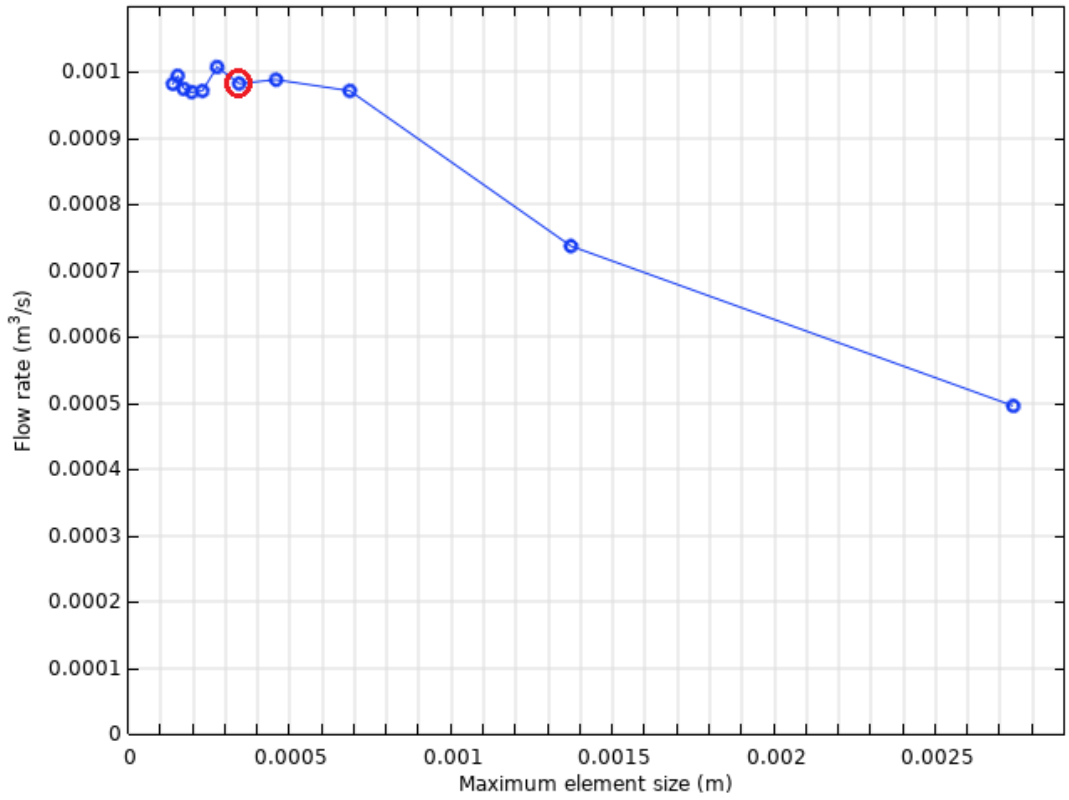

(b) Shunt flow rate

Figure B.1: Velocity magnitude squared (U^2) integrated over the domain (a) and shunt flow rate (b) as a function of boundary layer maximum element size. The data point circled in red indicates the converged mesh.

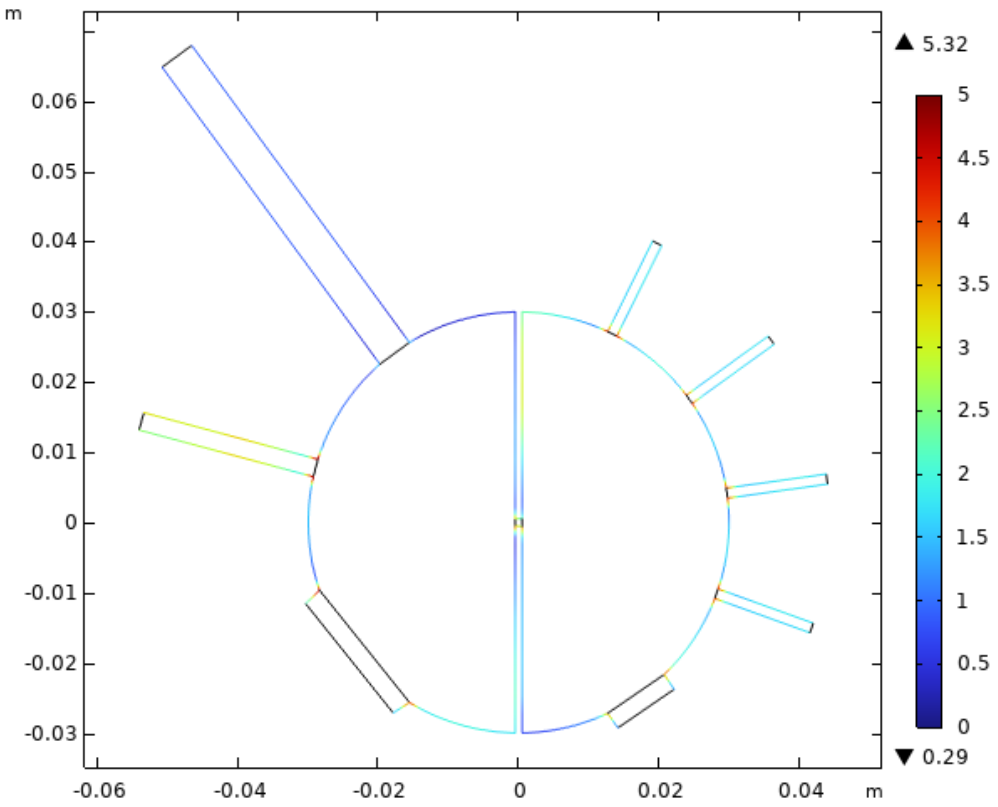

(a) Default mesh

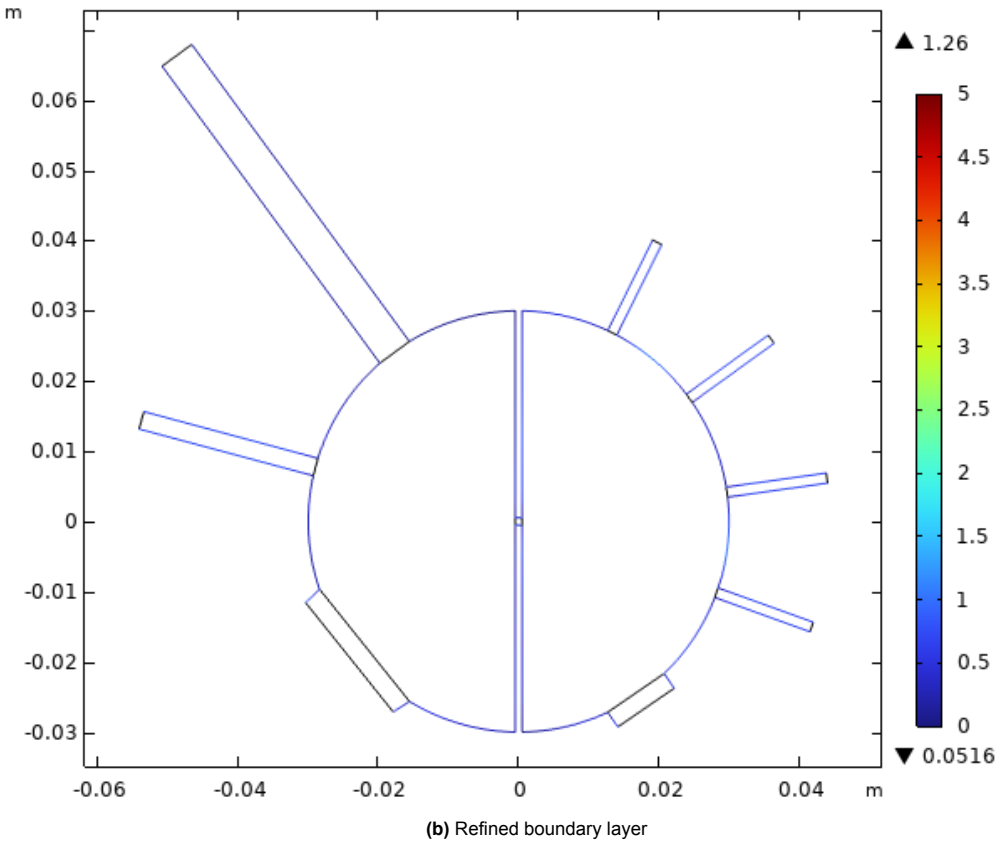

(b) Refined boundary layer

Figure B.2: Wall resolution in viscous units (y^+) of the default mesh (a) and the refined boundary layer mesh (b)

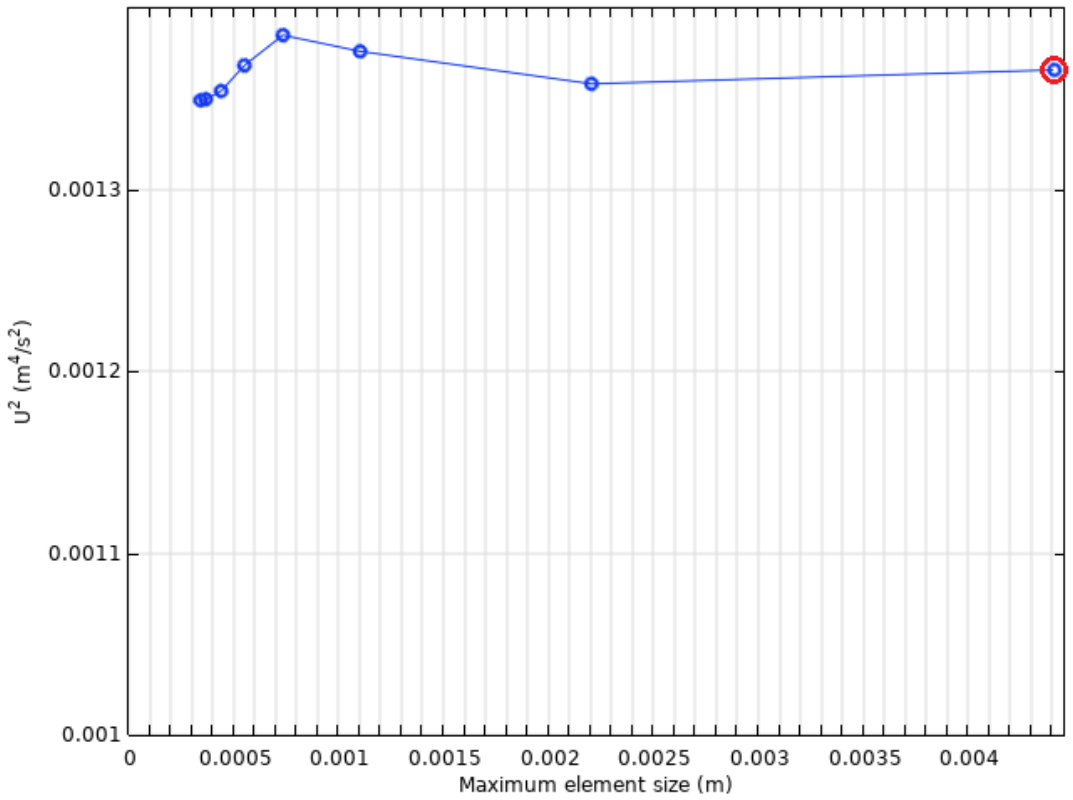

(a) Substitute of global kinetic energy

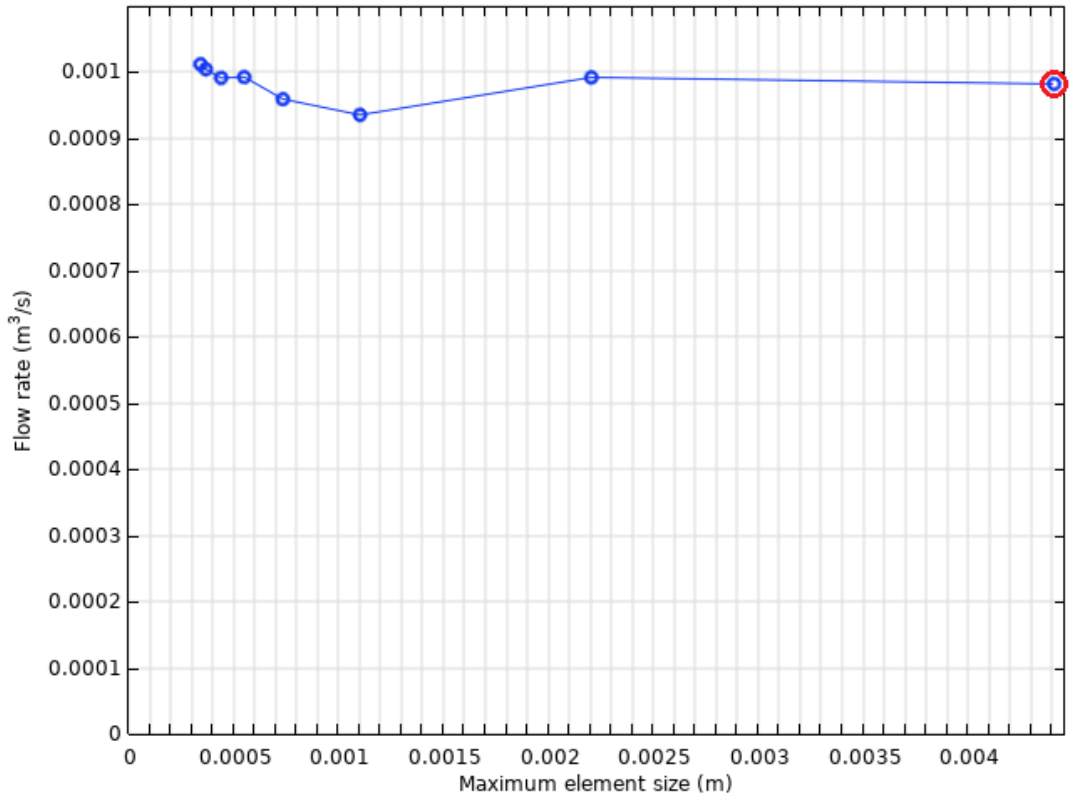

(b) Shunt flow rate

Figure B.3: Velocity magnitude squared (U^2) integrated over the domain (a) and shunt flow rate (b) as a function of core maximum element size. The data point circled in red corresponds to the data point in Figure B.1.

Though the mesh has converged towards a plateau in Figure B.1, there is still an error introduced by the discretization of the problem. To know this error, ideally a comparison would be made between the result of the sufficiently refined mesh and the result of a simulation with a mesh size of zero. However, as this is not possible, an estimation is made by extrapolating the results in Figure B.1 towards the y-axis, where the maximum element size would be zero. Since a plateau is reached, it is assumed that this plateau continues towards the y-axis, with the deviations from this plateau giving an indication of the mesh-induced error. In Figure B.1a, the sixth and tenth data points from the right show the maximum and minimum values around the plateau, respectively. Consequently, this gives an error of 1.04% relative to the value of the sufficiently refined boundary layer mesh. Similarly, Figure B.1b gives an error of 3.87%. Apart from estimating the error from the fluctuations of these two parameters, a direct comparison of the velocity and pressure fields can also be made between two solutions on this plateau. For this, the sufficiently refined mesh is compared to an even finer mesh. Here, it is assumed that the errors between all solutions on the plateau are approximately equal.

Figures B.4 and B.7 show the velocity and pressure fields, respectively, of a mesh that is even finer than the sufficiently refined mesh, with a boundary layer maximum element size of 0.274 mm. By comparing the results from this simulation with those of the sufficiently refined mesh as presented in section 4.2 (Figures 4.4 and 4.5), an estimation can be made of the mesh-induced errors. Since no clear visual difference can be established between the results of the two fine meshes, Figures B.5 and B.8 show the absolute errors between the two results, in absence (a) and presence (b) of an 8 mm shunt. For the velocity field in Figure B.5, it can be seen that the largest differences are found in and around the high velocity inlet jets. In the regions of low velocity magnitude, the absolute errors are generally smaller, apart from the recirculation zones in between the inlets of the left atrium. Overall, the errors are in the order of 0.1 m/s, where the velocity magnitudes of the high velocity regions are in the order of 2 m/s, resulting in an error of around 5%. More accurately, Figure B.6 presents the error relative to the local velocity magnitude, which shows that the errors in the velocity field are mostly within 10%. Only in the few regions that are colored red, the error is bigger than this. Note that most of these areas are of low velocity magnitude, such that a small absolute error can quickly result in a large relative error.

Studying the absolute differences in the pressure field, Figure B.8 shows that the largest errors are found in the left atrium. Once again, the biggest differences are found around the areas of high velocity magnitude, near the inlets. Throughout the right atrium, the error is fairly constant, apart from the region around the high velocity IVC jet. In absence of the shunt, the error is very close to zero, whereas the error is around 30 Pa in Figure B.8b. Most of the errors in the left atrium are in the order of 50 to 100 Pa, whereas the pressures are in the order of 1000 Pa, resulting in relative errors between approximately 5 and 10%. This is confirmed by Figure B.9, which shows that most errors in the pressure field are well within 10%. Figure B.10 even shows that most of these errors are actually only around 1%. As for the velocity field, the errors larger than 10% are mostly caused by the local pressures being close to zero, turning a small absolute error into a large relative error. This is especially the case for the red region between the IVC and the TV in the right atrium in Figure B.9, as Figure B.7 shows that the local pressures in these regions are very close to zero.

In conclusion, this study has shown that the simulation results converge towards a plateau if the boundary layer maximum element size is decreased, i.e. if the boundary layer mesh is refined. Refinement of the core mesh was deemed unnecessary, as the simulation results did not significantly change by decreasing the maximum element size in this area. The deviation of two parameter values around the plateau is around 1%, and most errors in the velocity and pressure fields are found to be around 5% and 1%, respectively. From this, it is concluded that the discretization of the problem introduces an error of approximately 5% in the results.

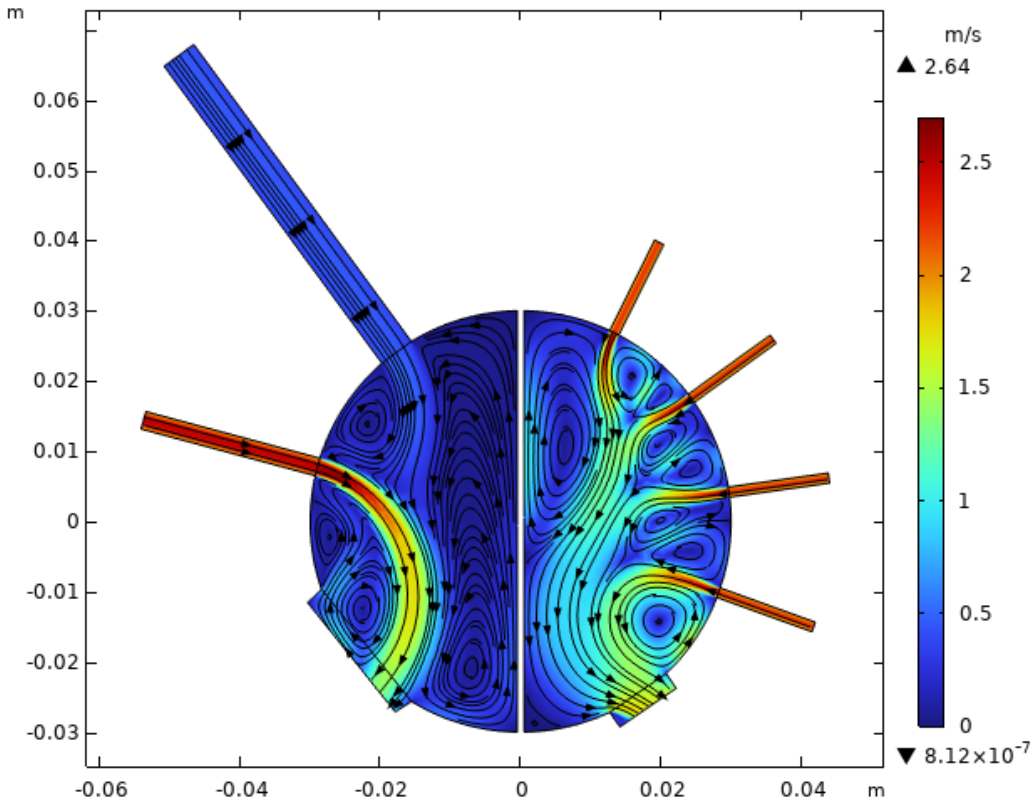

(a) Without shunt

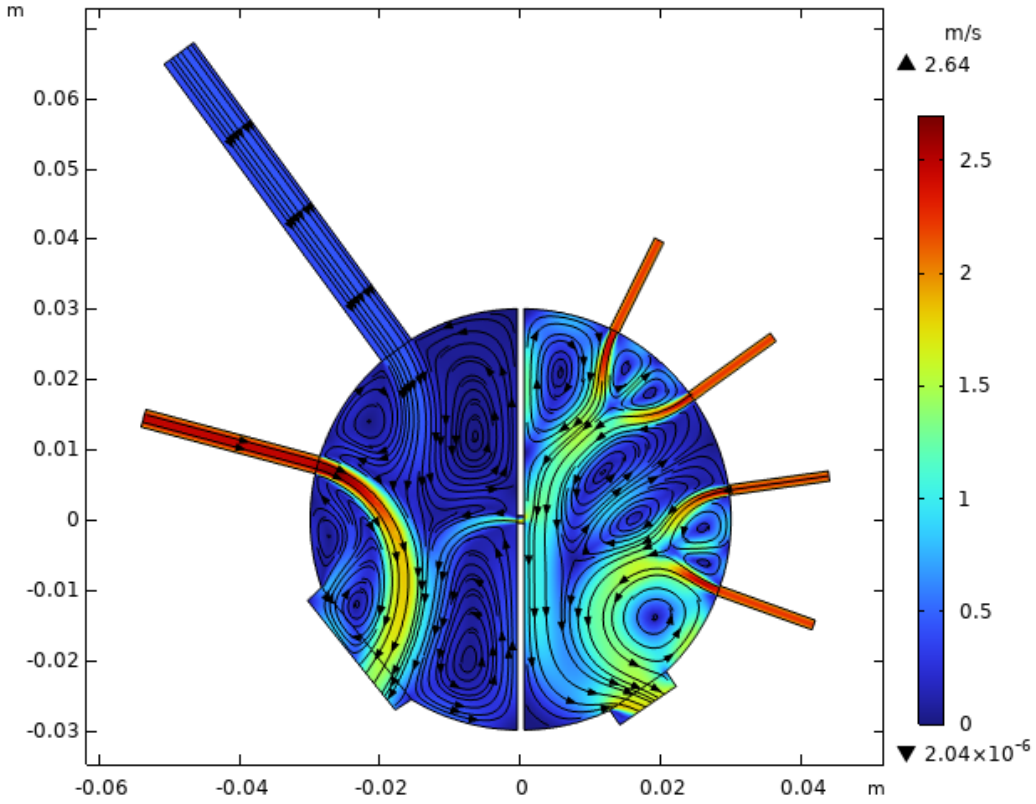

(b) 8 mm shunt

Figure B.4: Velocity magnitude and streamlines of the steady-state CFD simulation using a boundary layer maximum element size of 0.274 mm, in absence (a) and presence (b) of an 8 mm shunt

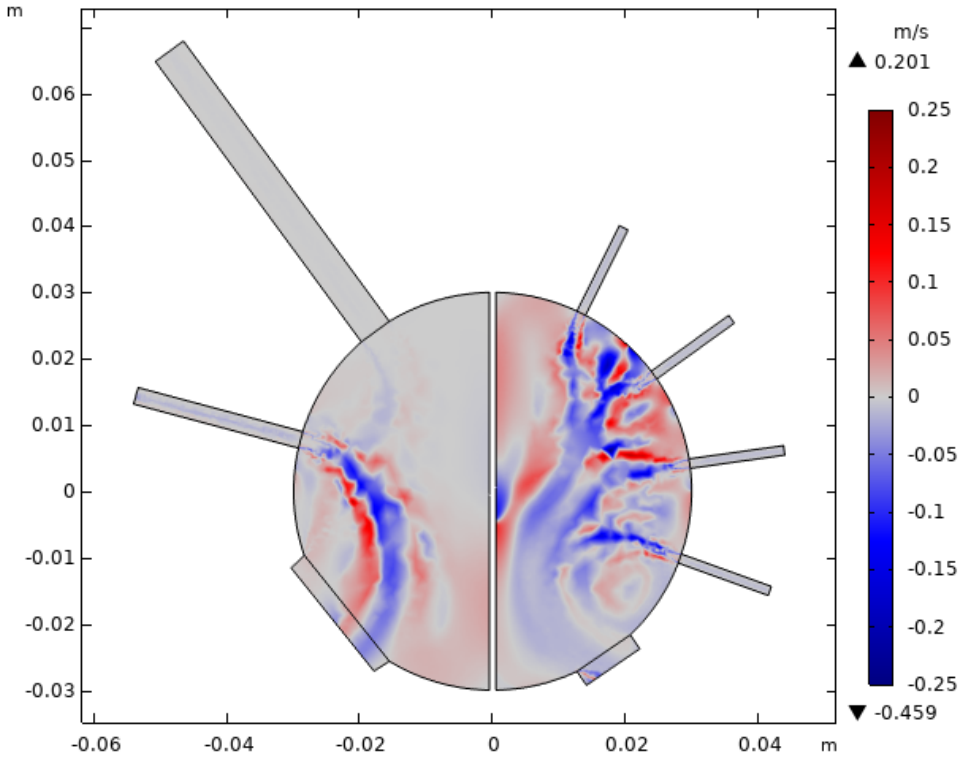

(a) Without shunt

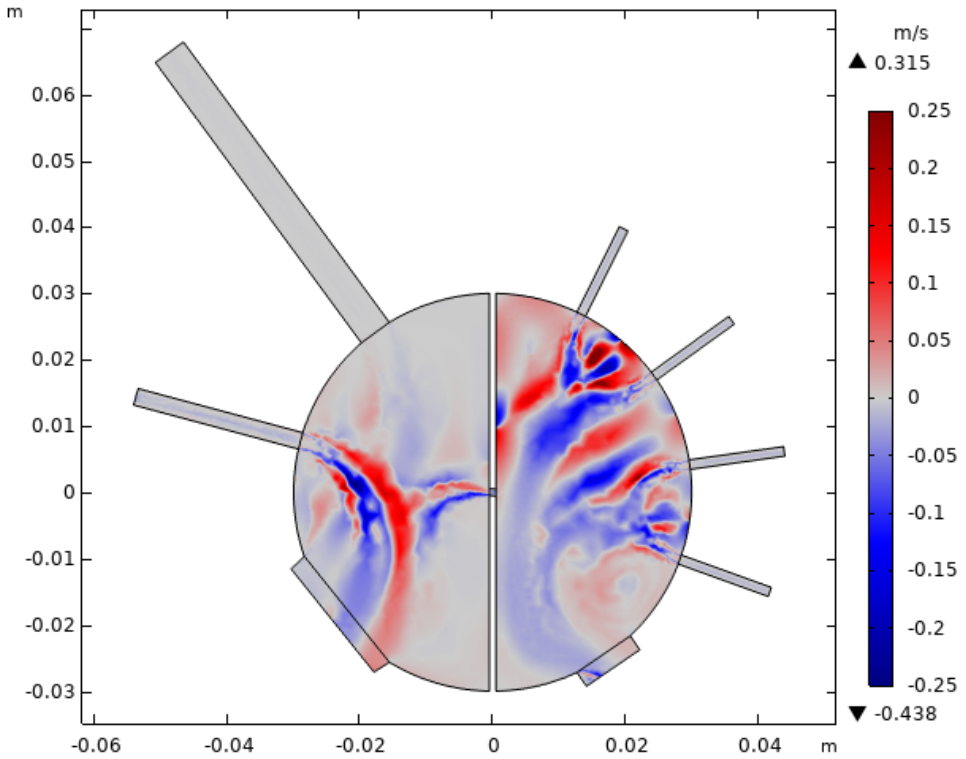

(b) 8 mm shunt

Figure B.5: Difference in velocity magnitude between the steady-state CFD simulation using a boundary layer maximum element size of 0.343 mm (the sufficiently refined mesh) and of 0.274 mm, in absence (a) and presence (b) of an 8 mm shunt. A red color indicates a higher velocity magnitude for the simulation with the sufficiently refined mesh, whereas a blue color indicates a lower velocity magnitude for the simulation with the sufficiently refined mesh.

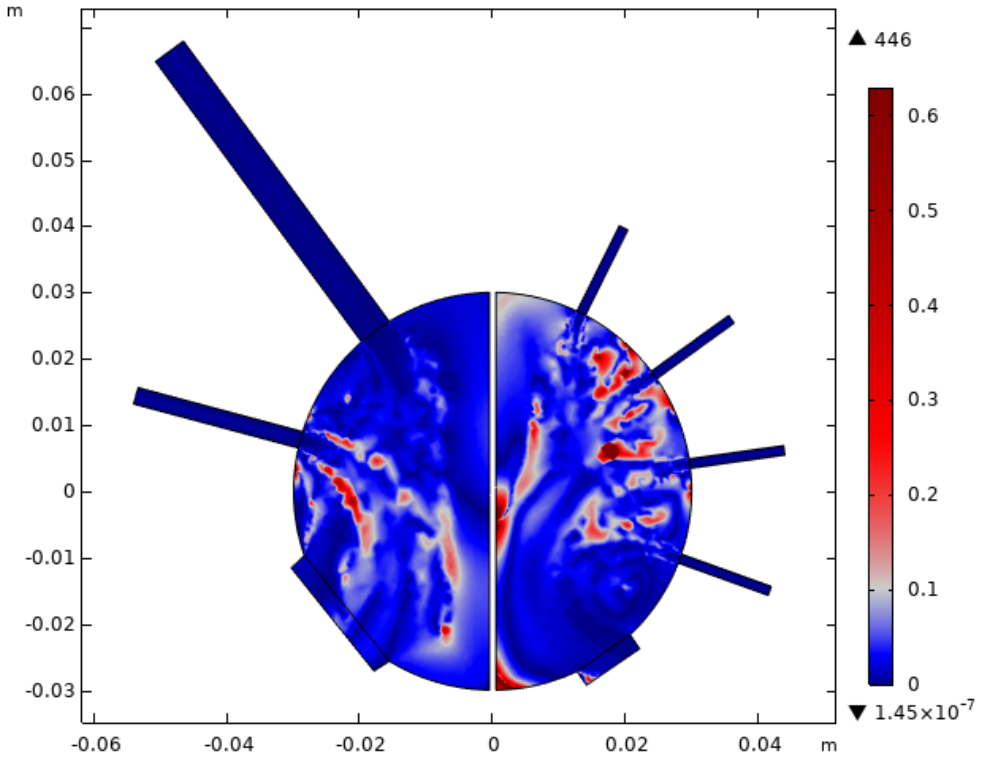

(a) Without shunt

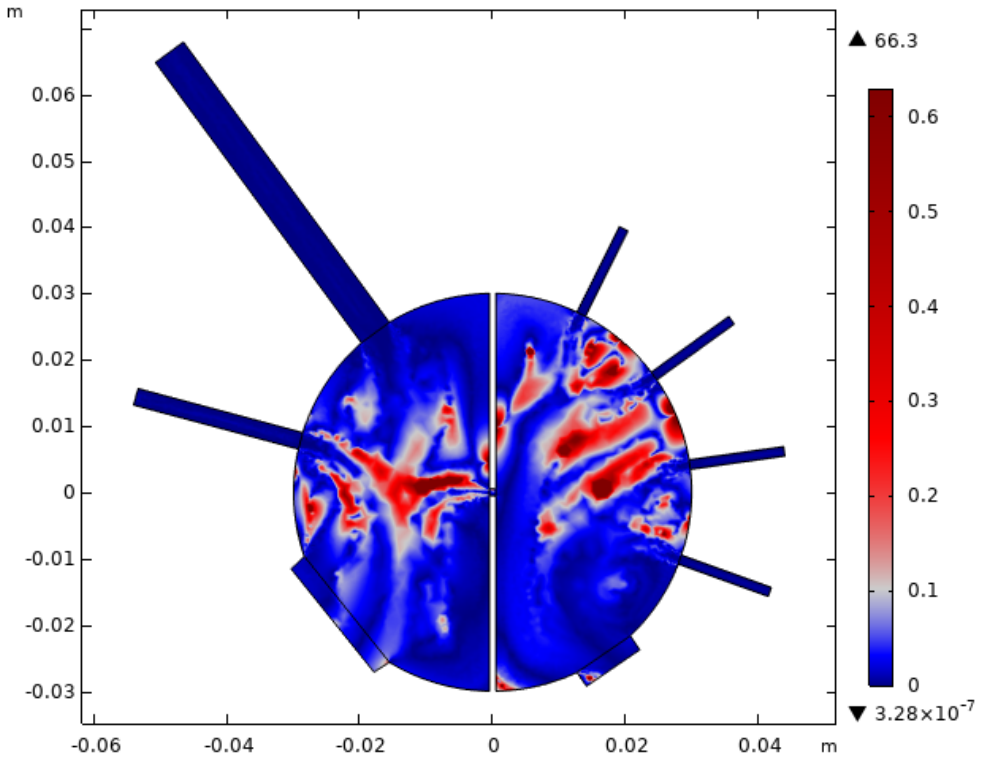

(b) 8 mm shunt

Figure B.6: Absolute value of the difference in velocity magnitude between the steady-state CFD simulation using a boundary layer maximum element size of 0.343 mm (the sufficiently refined mesh) and of 0.274 mm, relative to the local velocity magnitude, in absence (a) and presence (b) of an 8 mm shunt. A red color indicates a relative difference greater than 10%, whereas a blue color indicates a relative difference smaller than 10%.

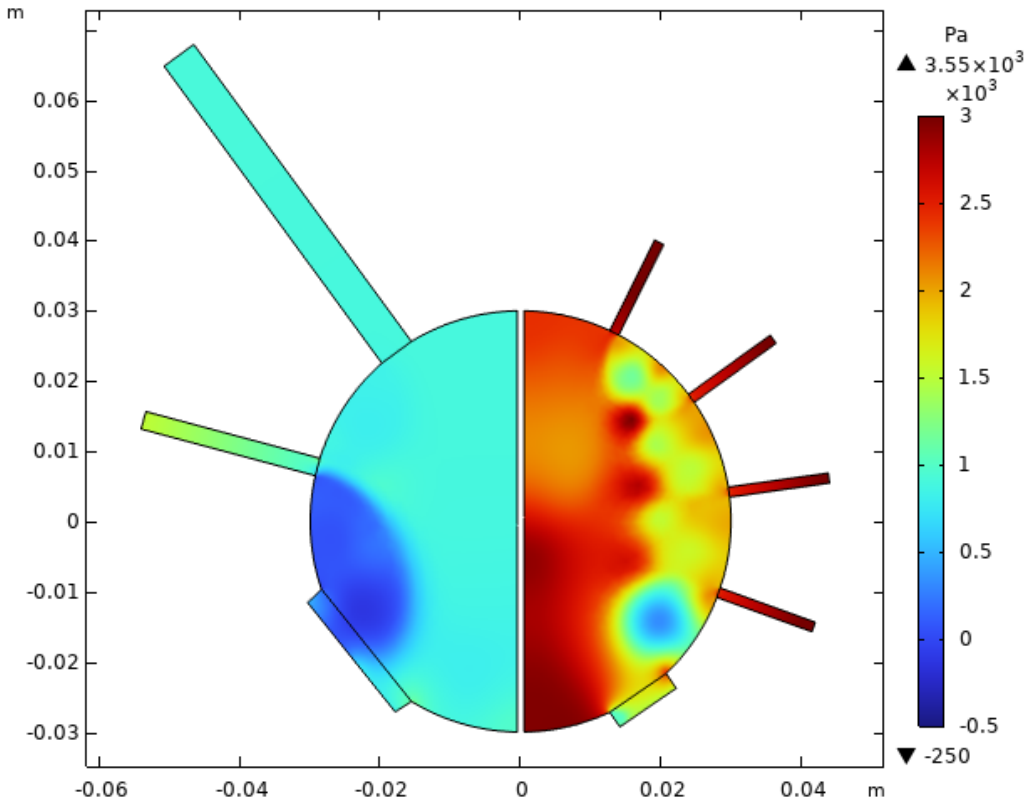

(a) Without shunt

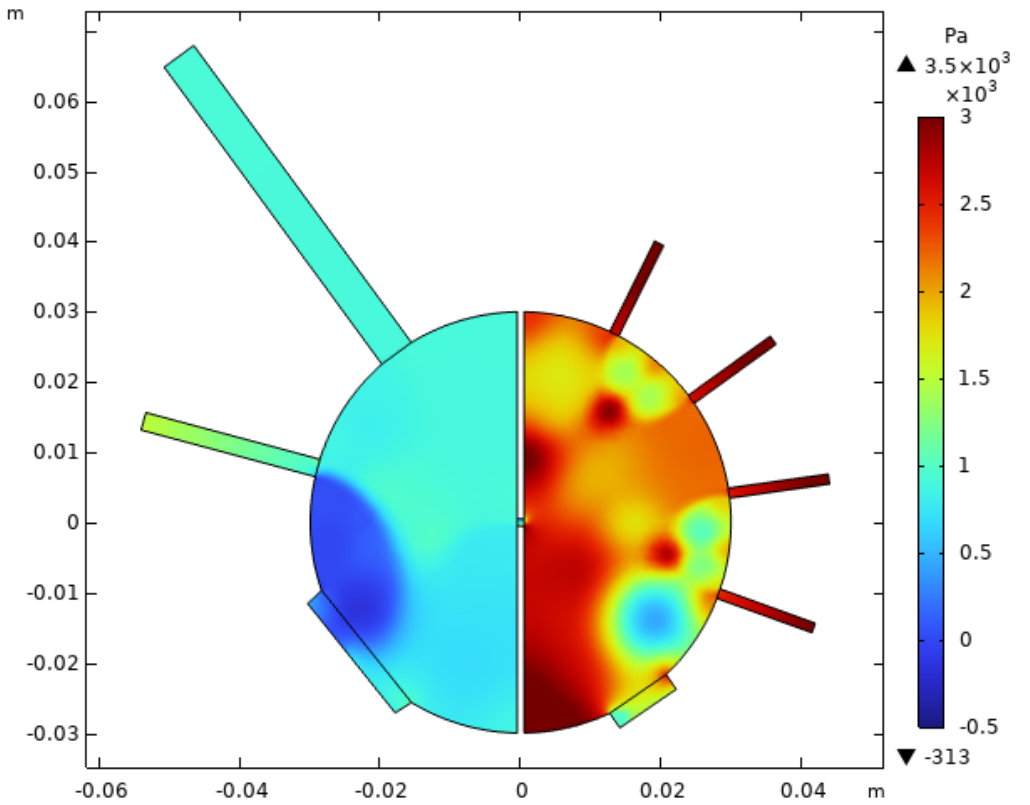

(b) 8 mm shunt

Figure B.7: Pressure field of the steady-state CFD simulation using a boundary layer maximum element size of 0.274 mm, in absence (a) and presence (b) of an 8 mm shunt

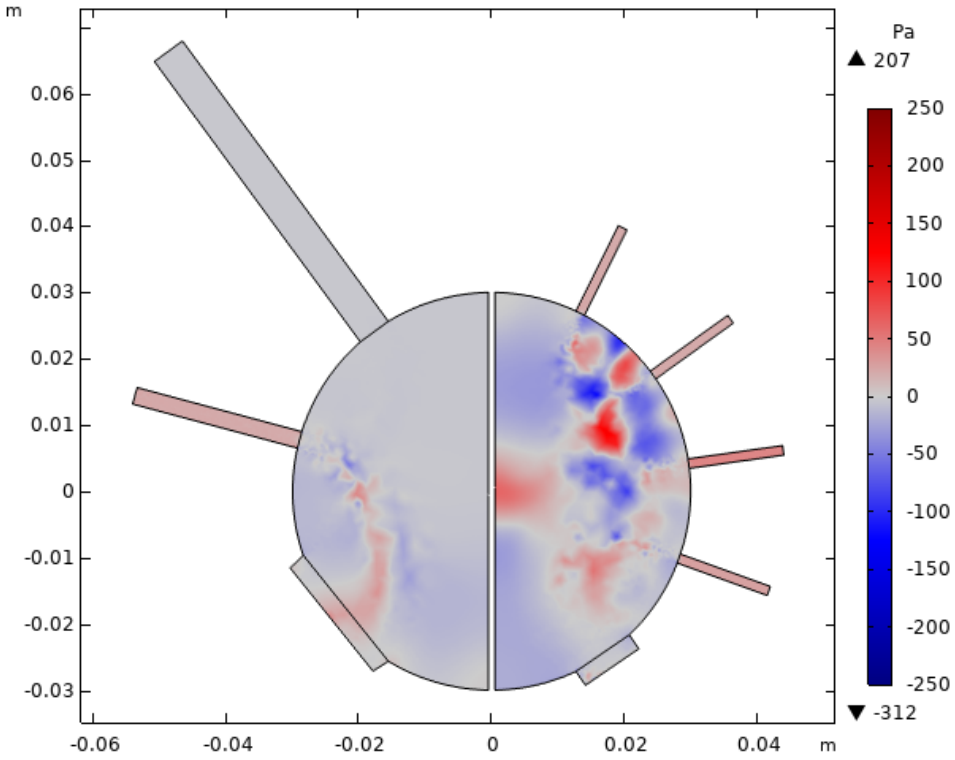

(a) Without shunt

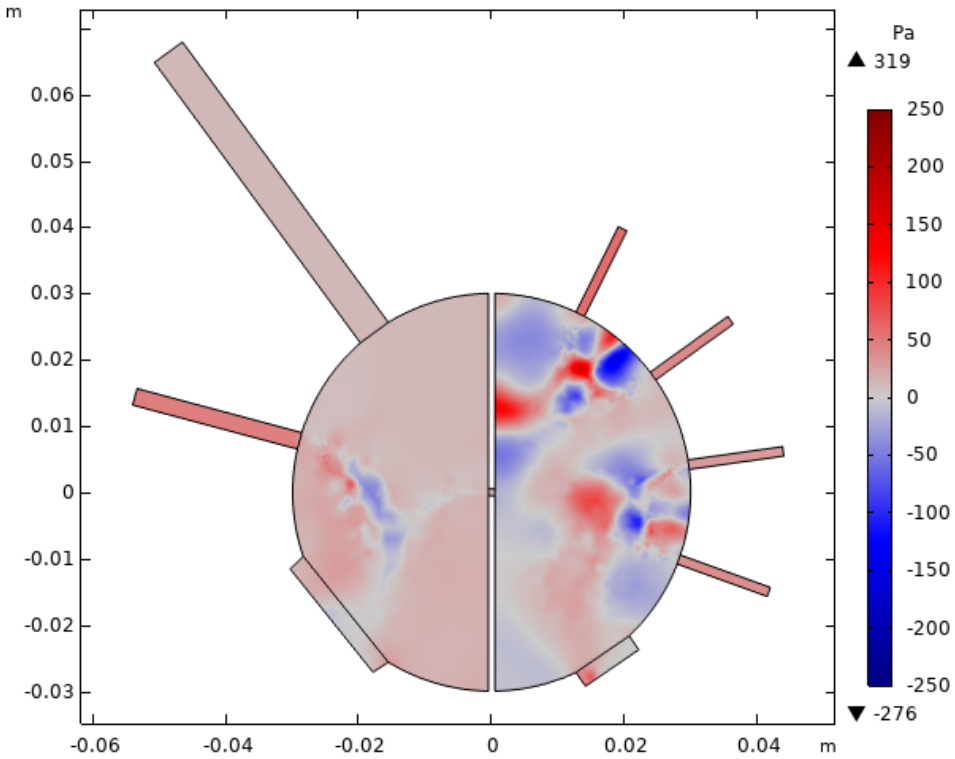

(b) 8 mm shunt

Figure B.8: Difference in pressure between the steady-state CFD simulation using a boundary layer maximum element size of 0.343 mm (the sufficiently refined mesh) and of 0.274 mm, in absence (a) and presence (b) of an 8 mm shunt. A red color indicates a higher pressure for the simulation with the sufficiently refined mesh, whereas a blue color indicates a lower pressure for the simulation with the sufficiently refined mesh.

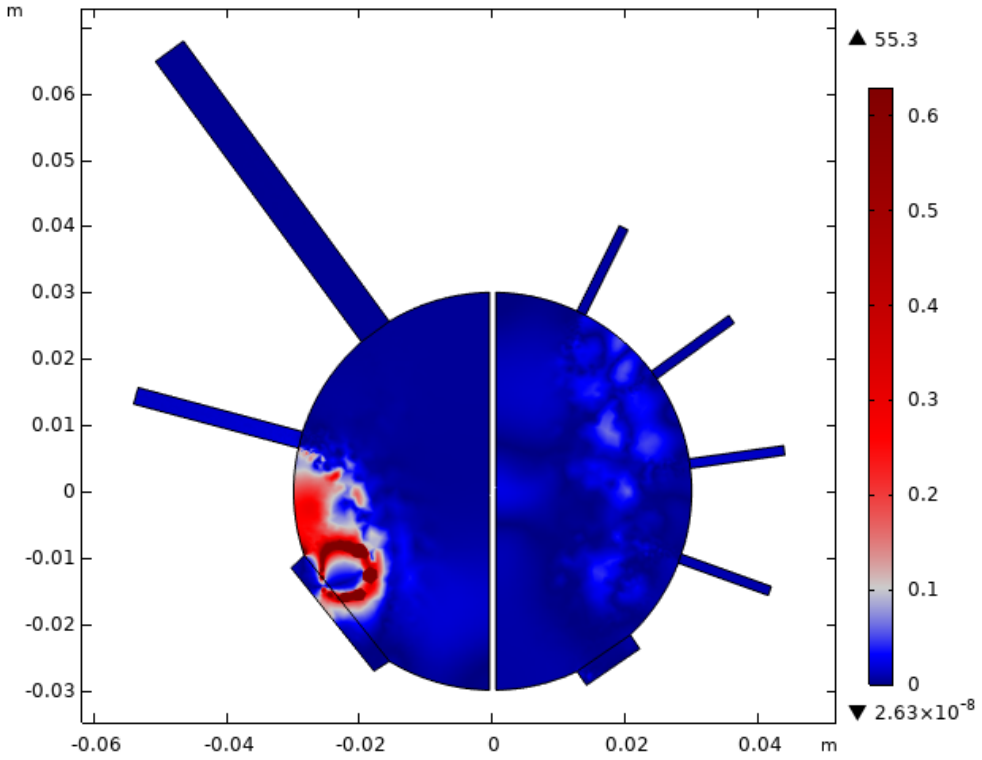

(a) Without shunt

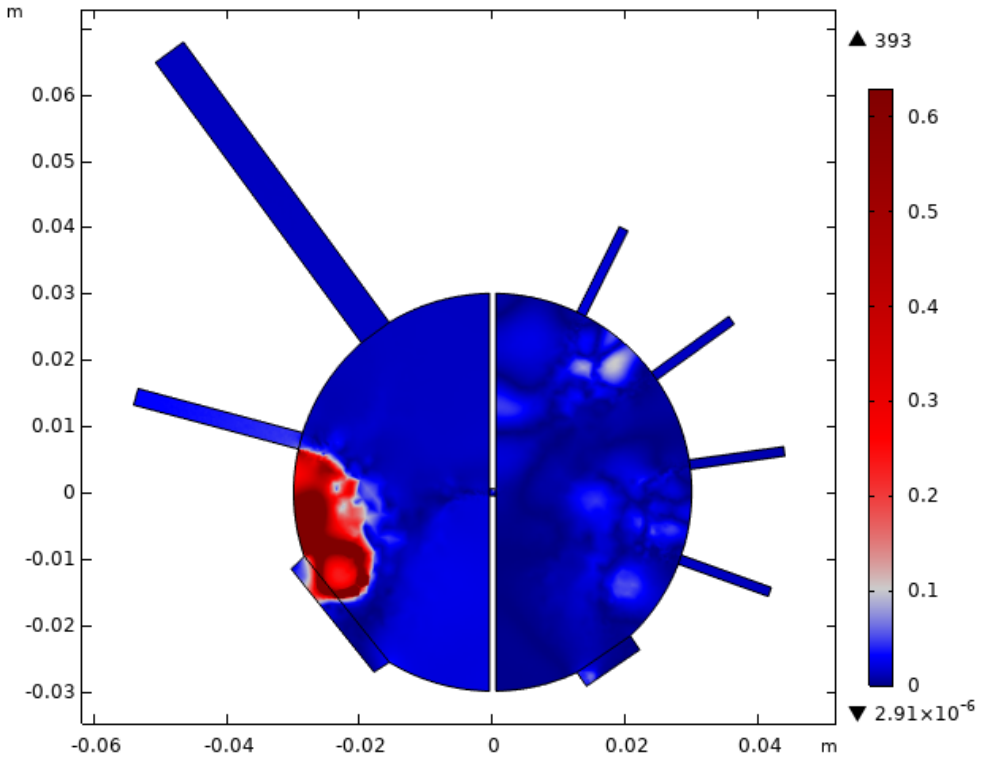

(b) 8 mm shunt

Figure B.9: Absolute value of the difference in pressure between the steady-state CFD simulation using a boundary layer maximum element size of 0.343 mm (the sufficiently refined mesh) and of 0.274 mm, relative to the local pressure, in absence (a) and presence (b) of an 8 mm shunt. A red color indicates a relative difference greater than 10%, whereas a blue color indicates a relative difference smaller than 10%.

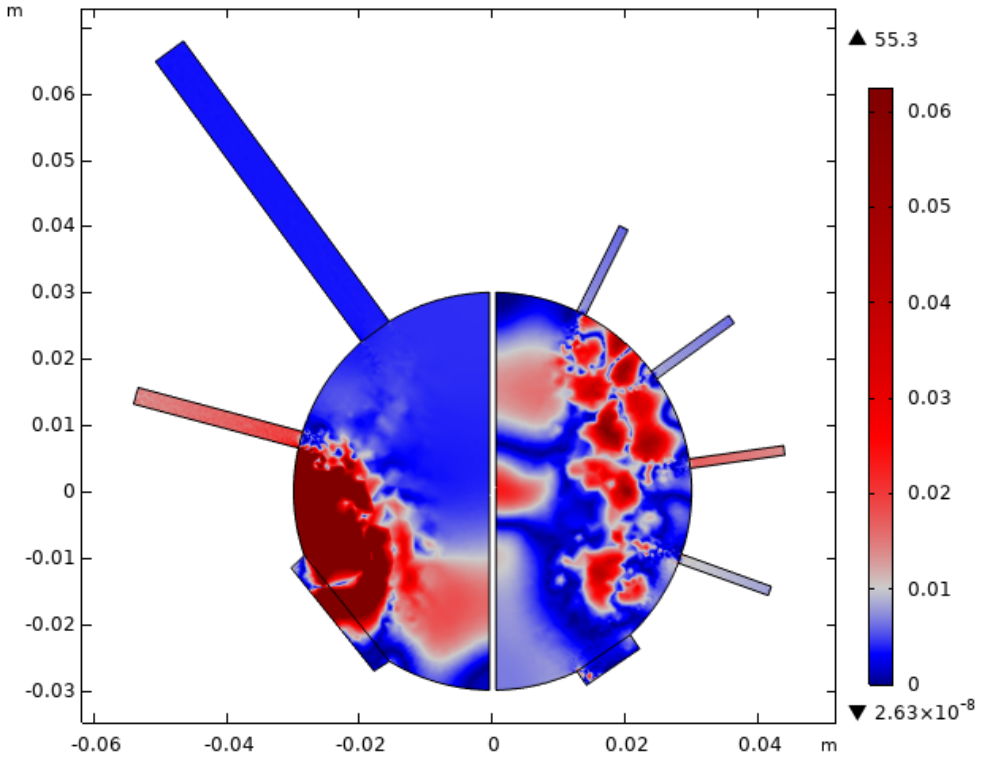

(a) Without shunt

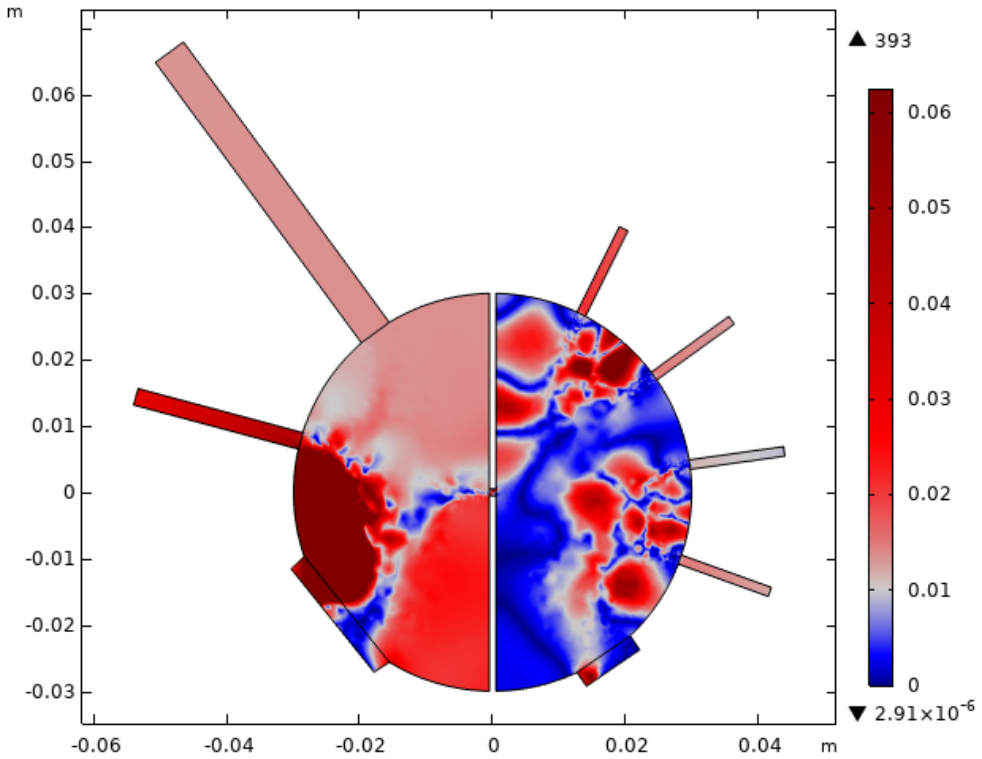

(b) 8 mm shunt

Figure B.10: Absolute value of the difference in pressure between the steady-state CFD simulation using a boundary layer maximum element size of 0.343 mm (the sufficiently refined mesh) and of 0.274 mm, relative to the local pressure, in absence (a) and presence (b) of an 8 mm shunt. A red color indicates a relative difference greater than 1%, whereas a blue color indicates a relative difference smaller than 1%.

C

Time step sensitivity

Next to the mesh convergence study presented in the previous appendix, another verification step is performed in the current research regarding the temporal discretization. In this appendix, the time step is refined and its effect on the results is analyzed.

The simulations performed in COMSOL Multiphysics use adaptive time stepping, meaning that the time step is not constant. Rather, it is determined based on the convergence criteria during the simulation. Therefore, the time step is not directly adjusted in this study, but is altered through the relative tolerance. For the simulations throughout this report, a relative tolerance value of 0.005 is used. This verification step has performed simulations with a smaller relative tolerance of 0.001. This appendix compares the results between the simulations employing the two different relative tolerances. For this, the transient simulation without a moving mesh is considered.

Due to the transient nature of the flow field, the errors in the velocity and pressure fields are locally very high. This is mainly caused by the fluctuations of the inlet jets, as can be seen in Figures C.1 and C.2 for the flow fields halfway through the diastole at $t = 0.35$ s, in absence and presence of an 8 mm interatrial shunt, respectively. In these figures, Figure C.1a and Figure C.2a show the same results as Figure 4.8a and Figure 4.8b from section 4.3, respectively, and have been repeated here for easy comparison. The resulting absolute errors in the velocity field are shown in Figure C.3, which correspond to the relative errors in Figure C.4. These results confirm the large errors between the two simulations in the instantaneous flow fields. Note that the errors in the left atrium are significantly larger than in the right atrium, which is due to the left atrial inlet jets fluctuating more. This is likely the result of the pulmonary veins having a smaller diameter.

Globally, however, the errors are much smaller. This is concluded from the differences in flow rates and pressures throughout the cardiac cycle. Figure C.5 shows the flow rates over a cardiac cycle for the simulation with the smaller relative tolerance, which is almost identical to Figure 4.11 from section 4.3 for the simulation with the larger relative tolerance. The absolute difference between the flow rates is shown in Figure C.6 and the corresponding relative difference is shown in Figure C.7. From this, it can be seen that the relative errors in flow rates are smaller than 10% for almost the entire cardiac cycle. The very high relative error peaks that are visible in Figure C.7 are due to the actual flow rates becoming very small at those moments. This is around the moments where the flow is reversing and therefore crossing zero flow rate, as can be seen in Figure C.5. Figure C.6 shows that the absolute errors in the flow rates are actually not much larger than normal at these moments. The only moment that a large relative error is directly caused by a large absolute error is at $t = 0.3$ s in absence of a shunt, see Figures C.6a and C.6b. Finally, note that the relative error in the shunt flow rate is omitted from Figure C.7a. This is because the shunt flow rate is naturally zero in absence of a shunt and this would result in dividing by zero flow rate.

Similar to the flow rates, the pressures in Figure C.8 for the simulation with a relative tolerance of 0.001 are also almost identical to the pressures in Figure 4.18 from section 4.3 for the simulation with a relative tolerance of 0.005. Figure C.9 presents the differences in pressures between the simulations with the different relative tolerances and Figure C.10 shows the resulting relative errors. From Figure C.9, it can be seen that the errors in the spatial average of the left atrial pressure are the largest, especially during the first half of the cardiac cycle. On the other hand, Figure C.10 shows that the rela-

tive error is the largest for the right atrial pressure, but only in presence of the shunt (see Figure C.10b). However, overall, the errors are within 10% for almost the entire cardiac cycle, which is deemed acceptable.

This appendix has presented a study on the temporal discretization of the simulations in the current research. This has been done by refining the time step through a reduction in the relative tolerance by a factor five. Though the errors in the instantaneous flow field are large, which is attributed to the transient nature of the flow, the relative errors in the flow rates and pressures over a single cardiac cycle are mostly within 10%, which is deemed an acceptable error.

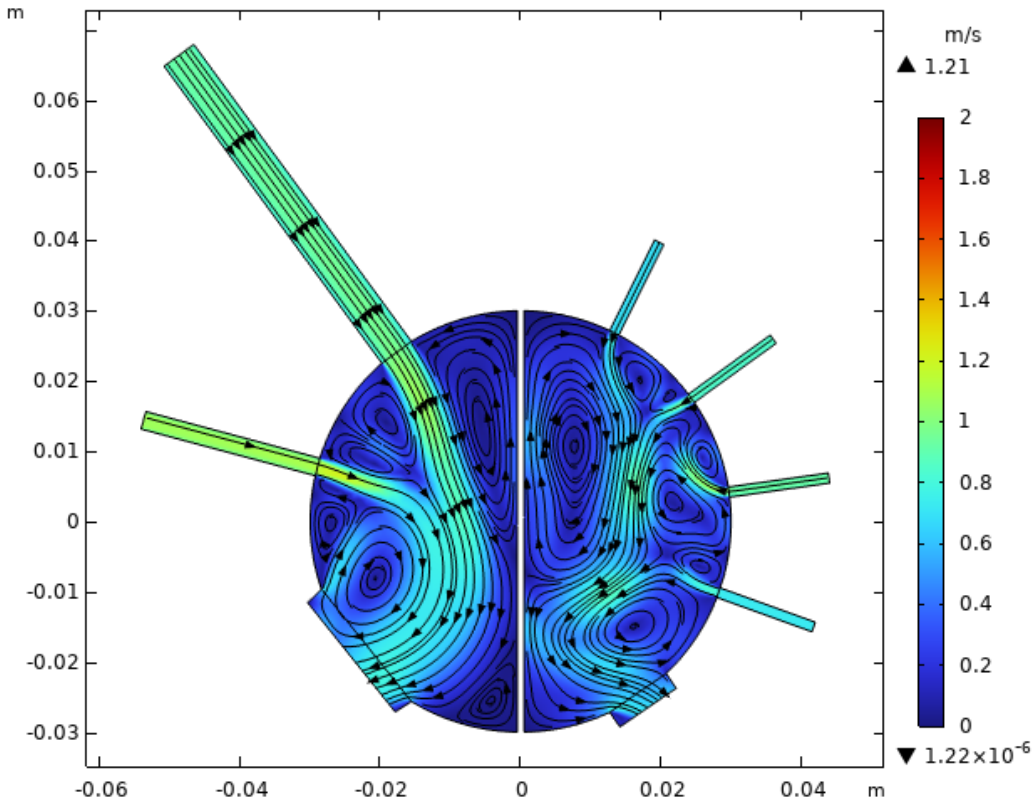

(a) Relative tolerance = 0.005

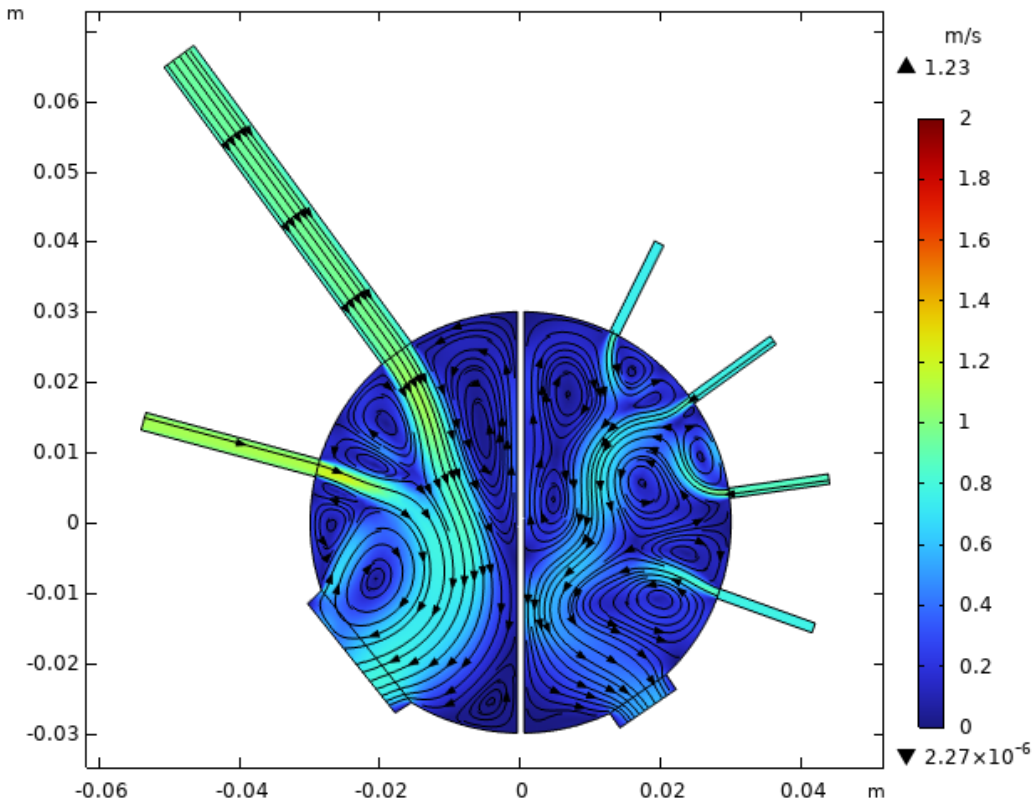

(b) Relative tolerance = 0.001

Figure C.1: Velocity field of the transient CFD simulation halfway through the diastole ($t = 0.35$ s) in absence of an 8 mm shunt for a relative tolerance of 0.005 (a) and 0.001 (b)

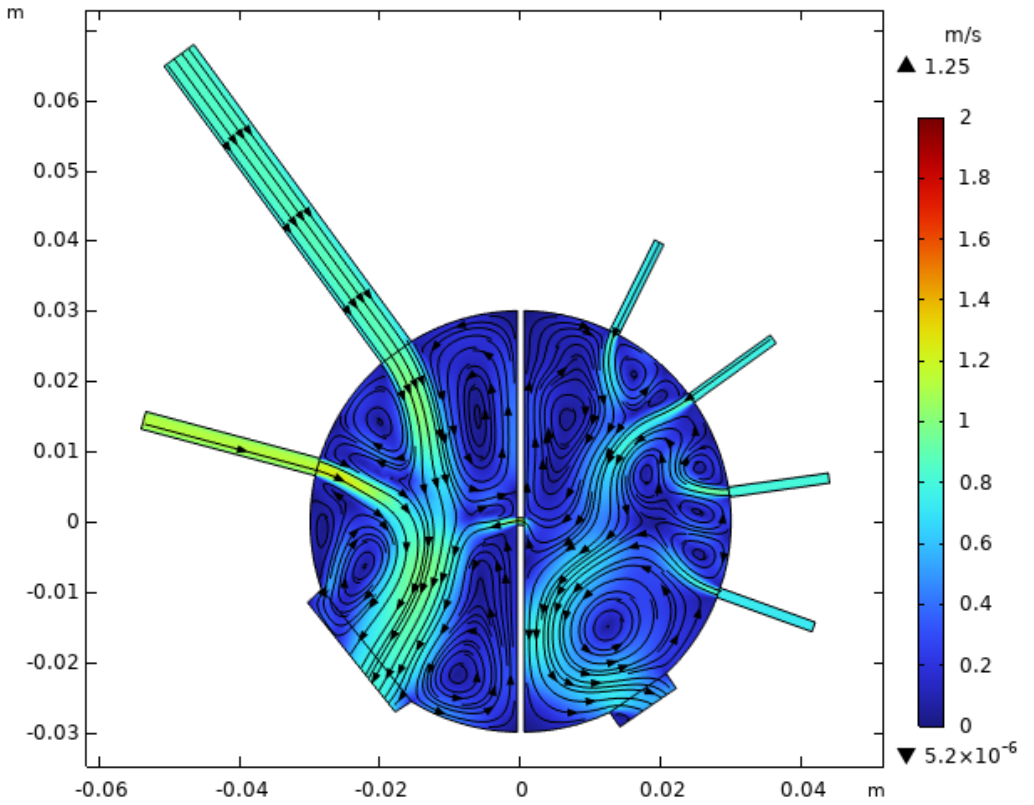

(a) Relative tolerance = 0.005

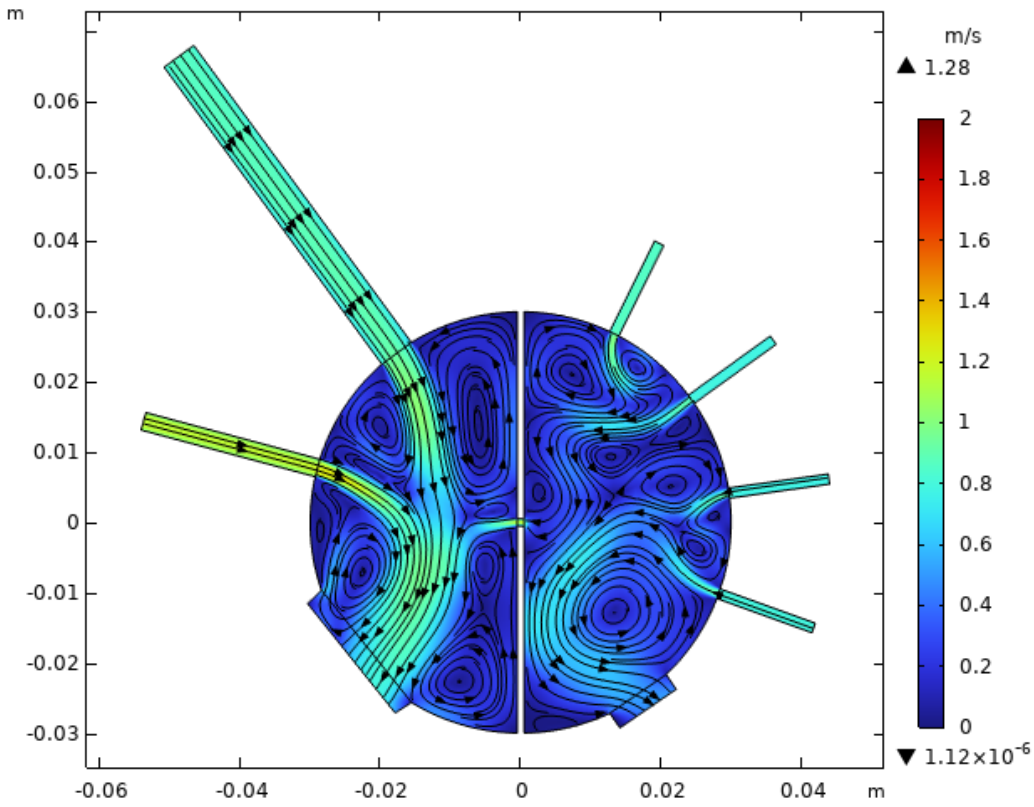

(b) Relative tolerance = 0.001

Figure C.2: Velocity field of the transient CFD simulation halfway through the diastole ($t = 0.35$ s) in presence of an 8 mm shunt for a relative tolerance of 0.005 (a) and 0.001 (b)

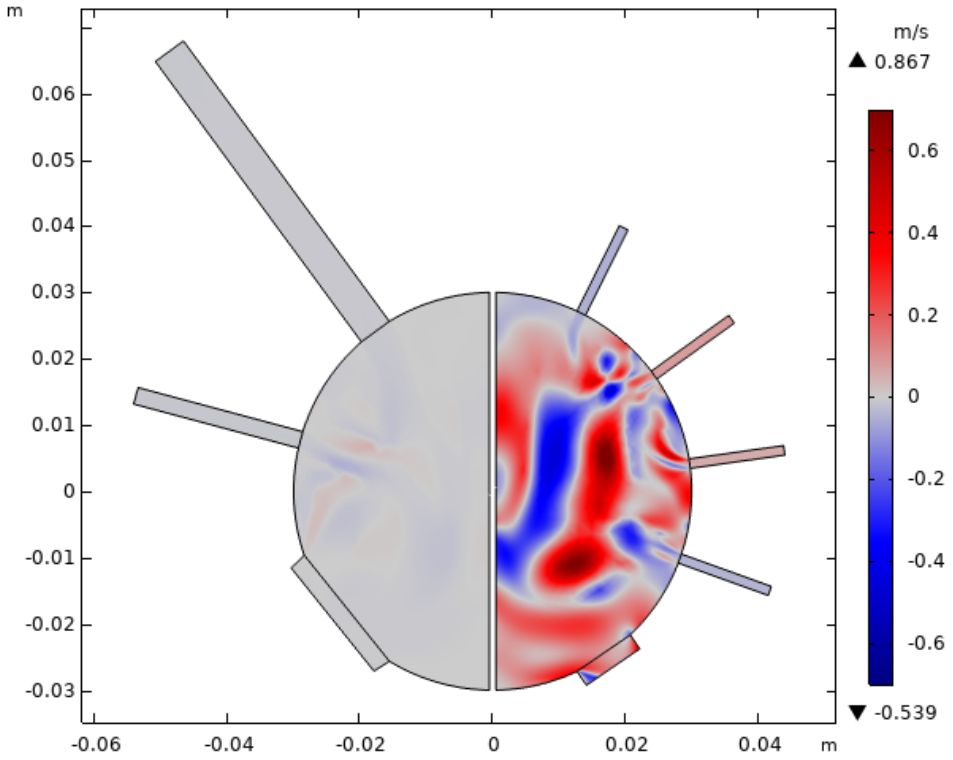

(a) Without shunt

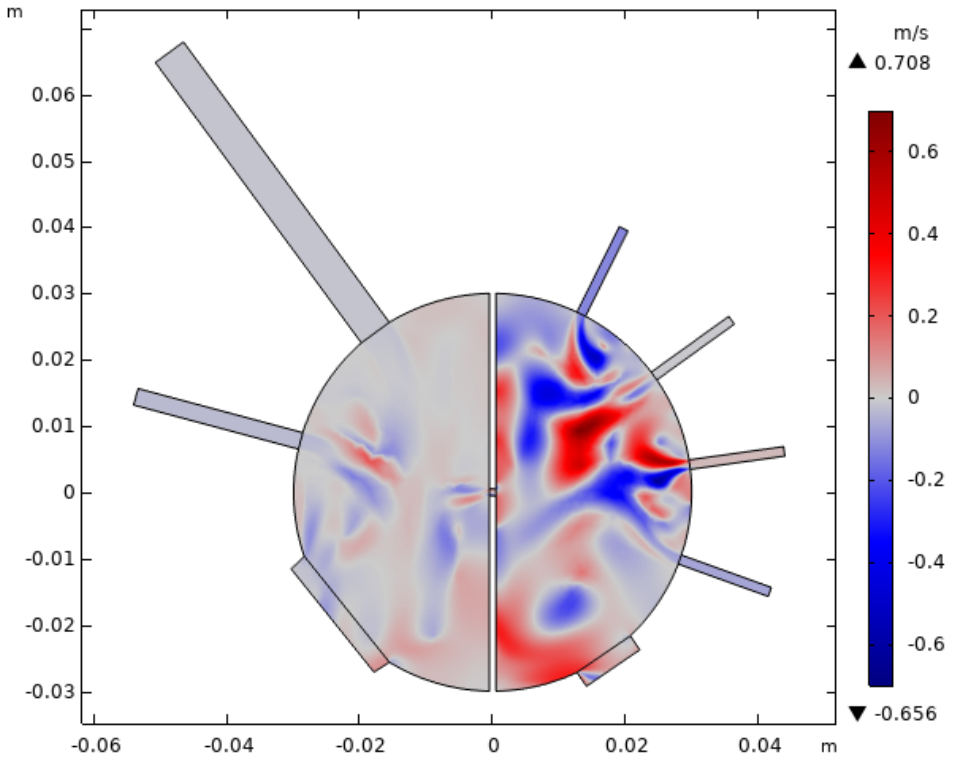

(b) 8 mm shunt

Figure C.3: Difference in velocity magnitude between the transient CFD simulation with a relative tolerance of 0.005 and a relative tolerance of 0.001, in absence (a) and presence (b) of an 8 mm shunt. A red color indicates a higher velocity magnitude for the simulation with a relative tolerance of 0.005, whereas a blue color indicates a higher velocity magnitude for the simulation with a relative tolerance of 0.001.

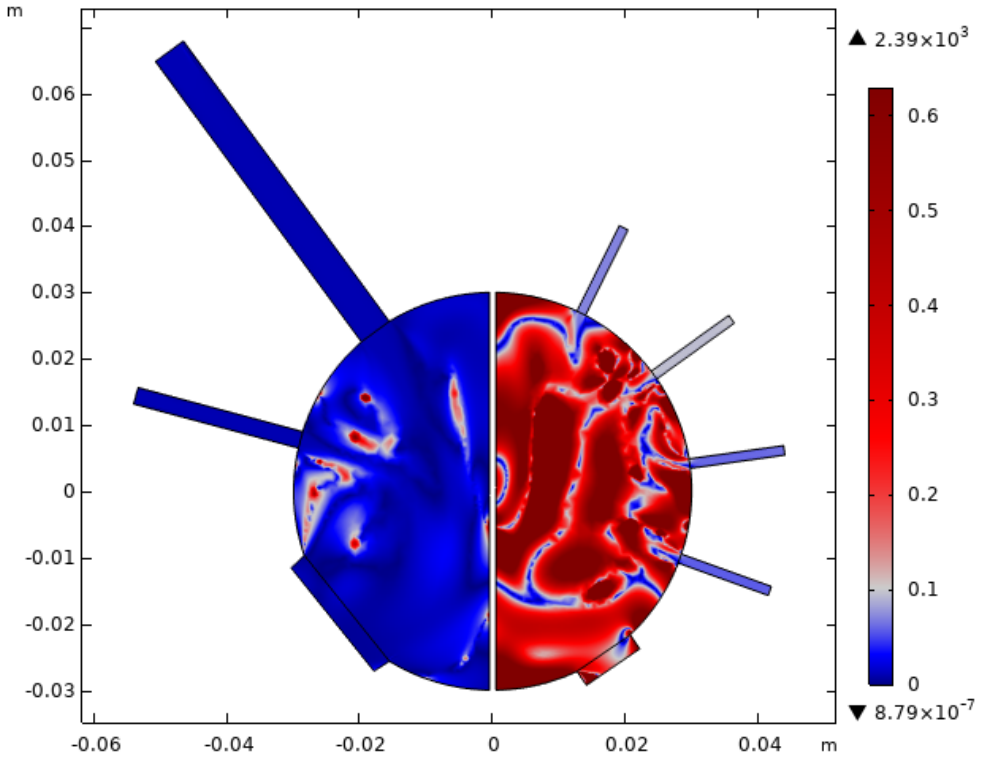

(a) Without shunt

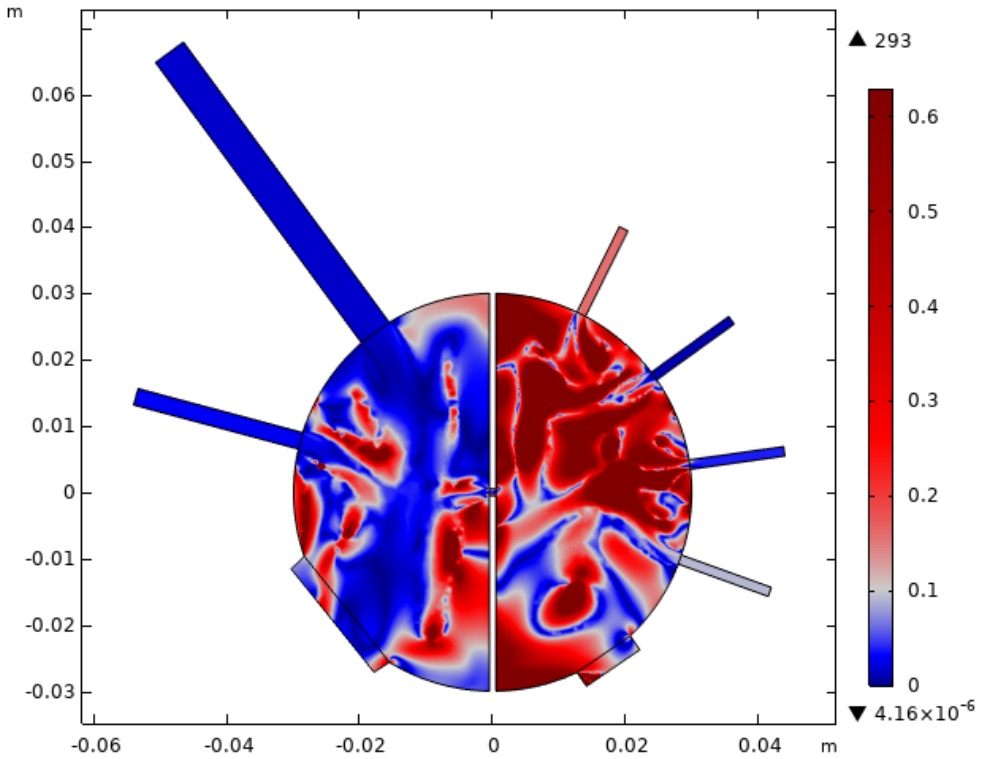

(b) 8 mm shunt

Figure C.4: Absolute value of the difference in velocity magnitude between the transient CFD simulation with a relative tolerance of 0.005 and a relative tolerance of 0.001, relative to the local velocity magnitude, in absence (a) and presence (b) of an 8 mm shunt. A red color indicates a relative difference greater than 10%, whereas a blue color indicates a relative difference smaller than 10%.

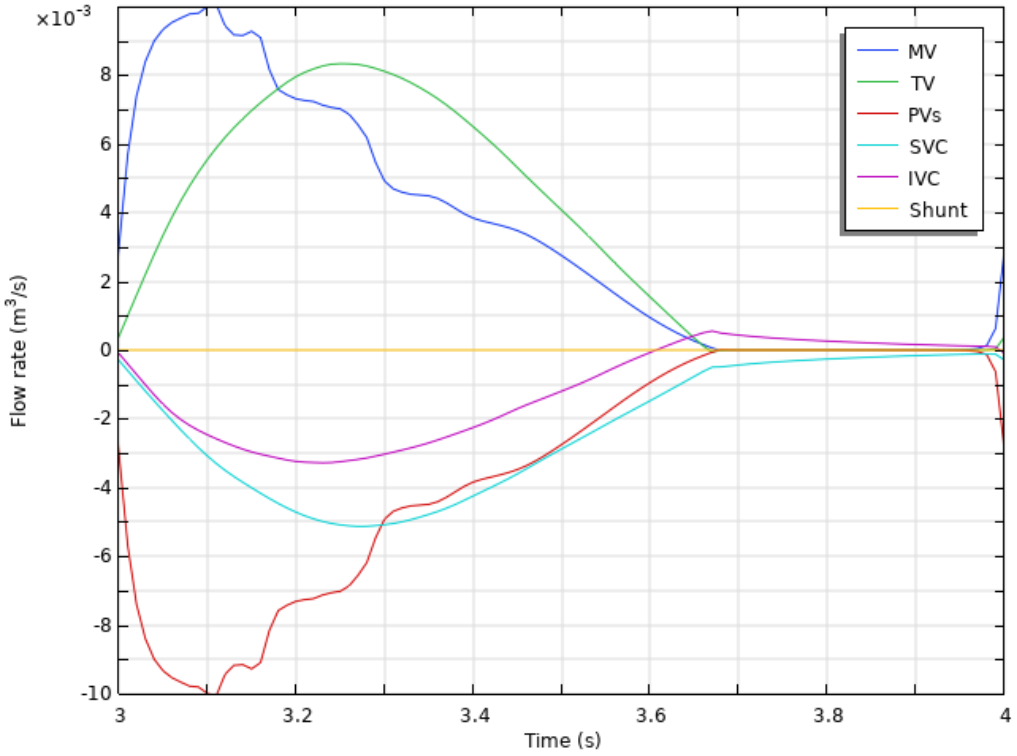

(a) Without shunt

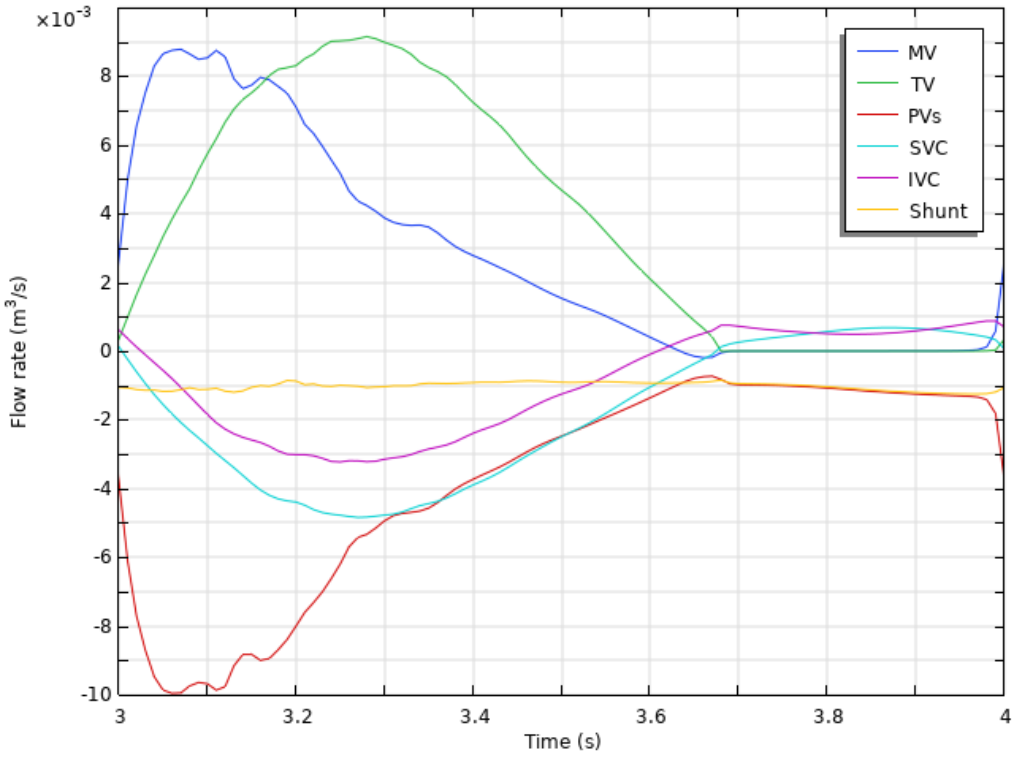

(b) 8 mm shunt

Figure C.5: Flow rates through the inlets, outlets and interatrial shunt of the transient CFD simulation with a relative tolerance of 0.001 over one cardiac cycle in absence (a) and presence (b) of an 8 mm shunt. Positive values indicate flow rate exiting the domain and negative values indicate flow rate entering the domain. For the shunt, a negative value indicates a flow from left to right.

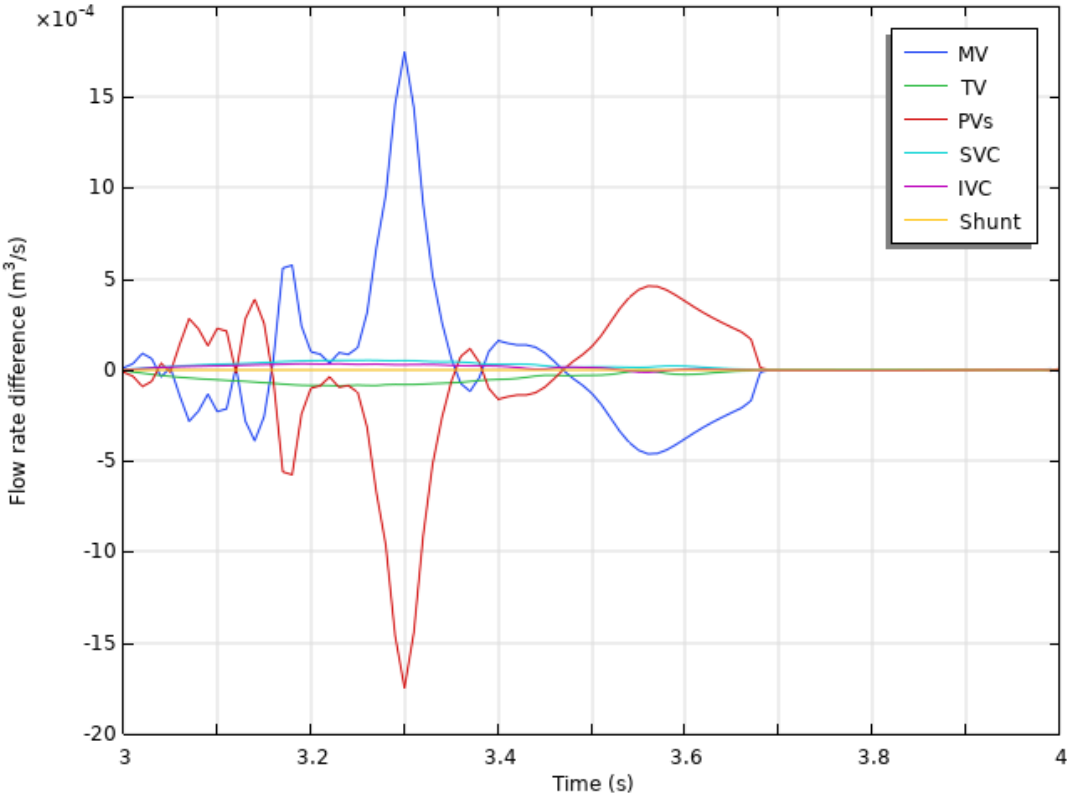

(a) Without shunt

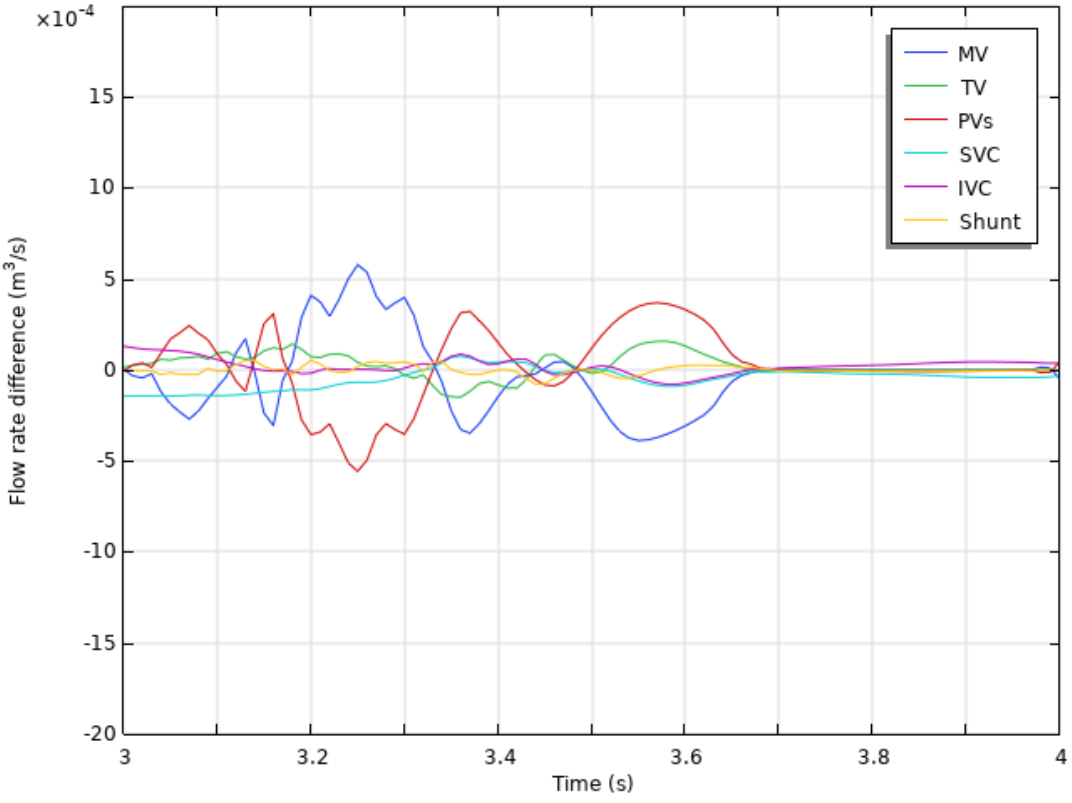

(b) 8 mm shunt

Figure C.6: Difference in flow rates between the transient CFD simulation with a relative tolerance of 0.005 and a relative tolerance of 0.001 over one cardiac cycle in absence (a) and presence (b) of an 8 mm shunt. Positive values indicate larger values for the simulation with a relative tolerance of 0.005.

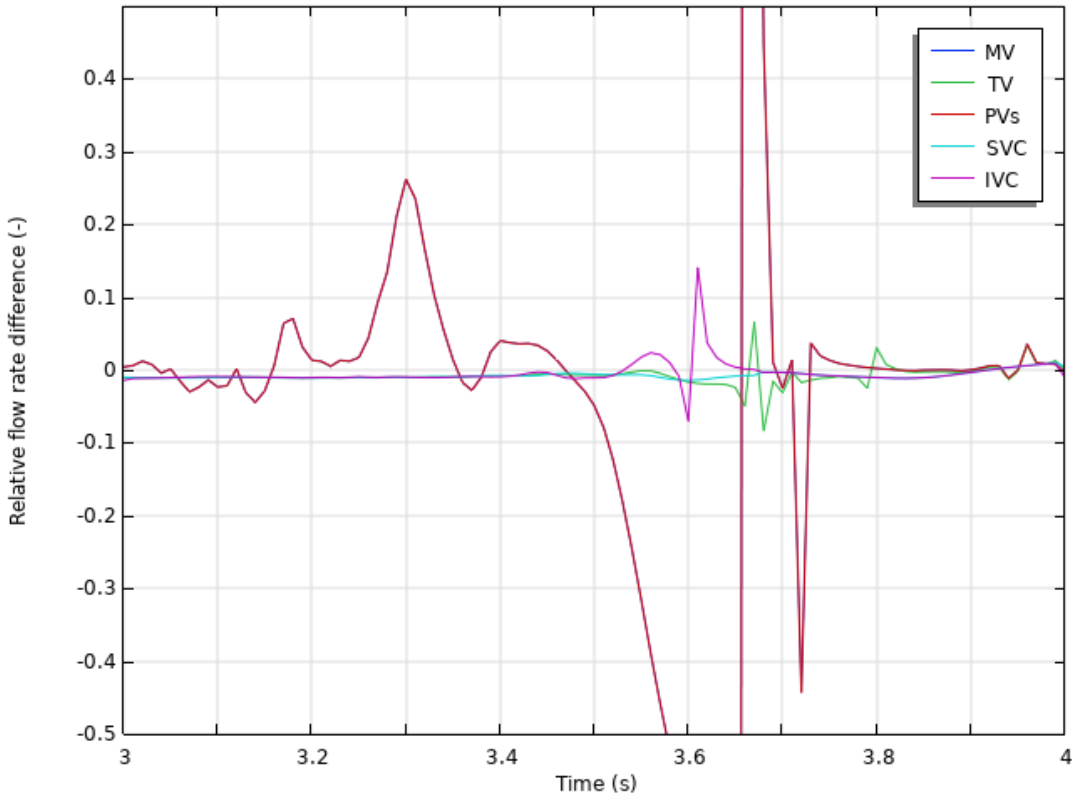

(a) Without shunt

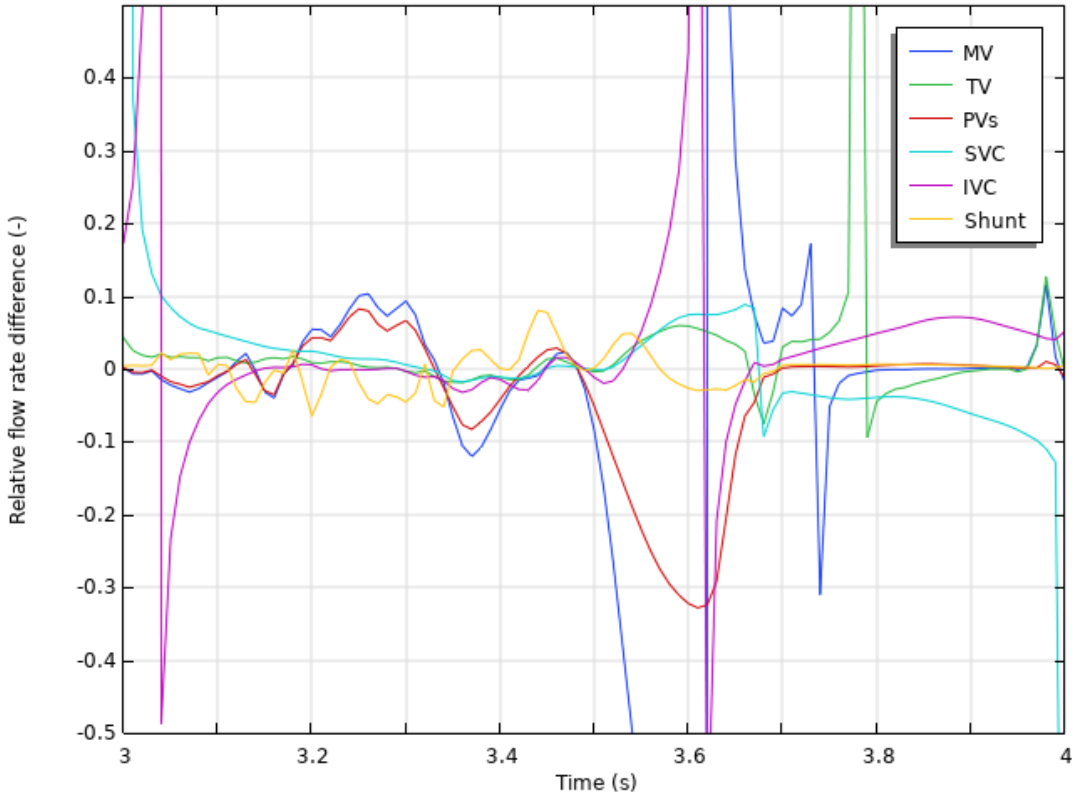

(b) 8 mm shunt

Figure C.7: Relative difference in flow rates between the transient CFD simulation with a relative tolerance of 0.005 and a relative tolerance of 0.001 over one cardiac cycle in absence (a) and presence (b) of an 8 mm shunt. Positive values indicate larger values for the simulation with a relative tolerance of 0.005.

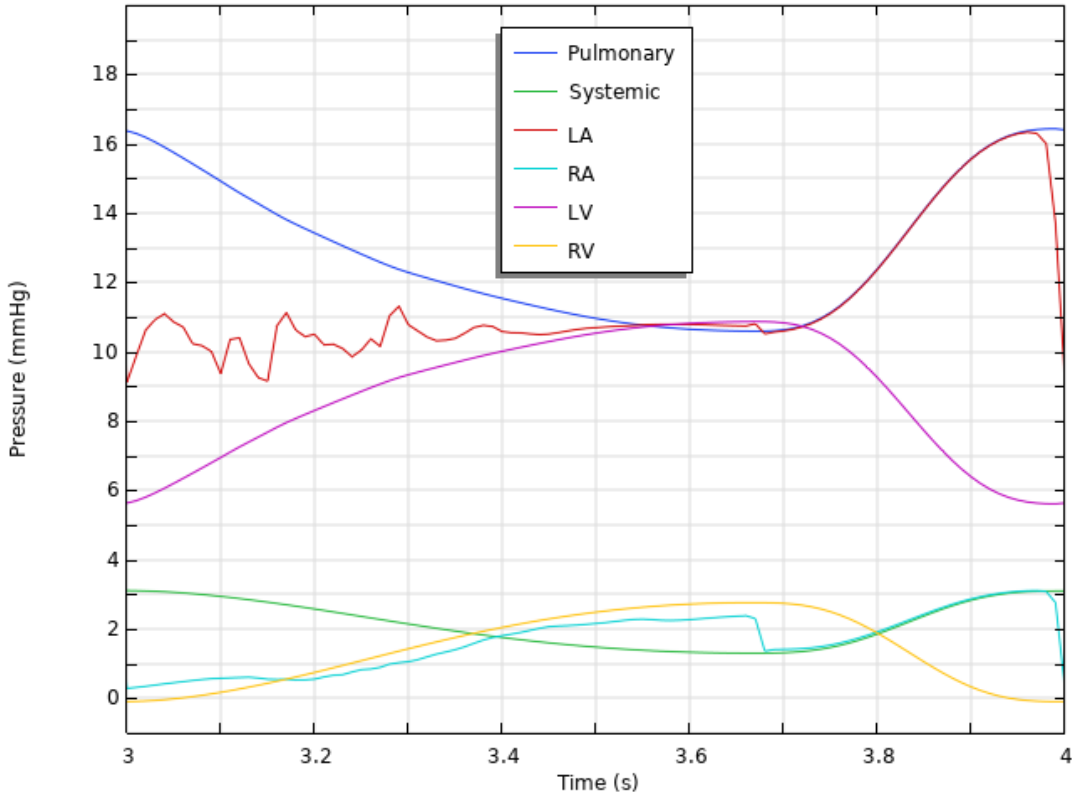

(a) Without shunt

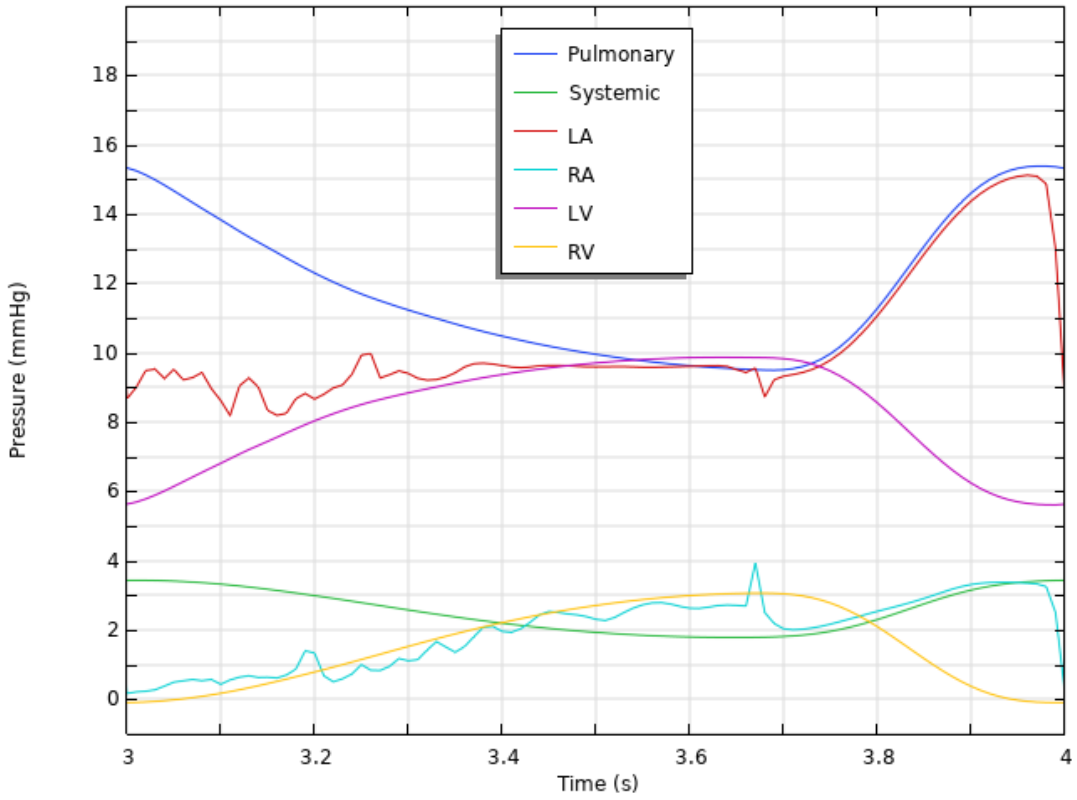

(b) 8 mm shunt

Figure C.8: Pulmonary, systemic, left (LA) and right (RA) atrial and left (LV) and right (RV) ventricular pressures of the transient CFD simulation with a relative tolerance of 0.001 over one cardiac cycle in absence (a) and presence (b) of an 8 mm shunt

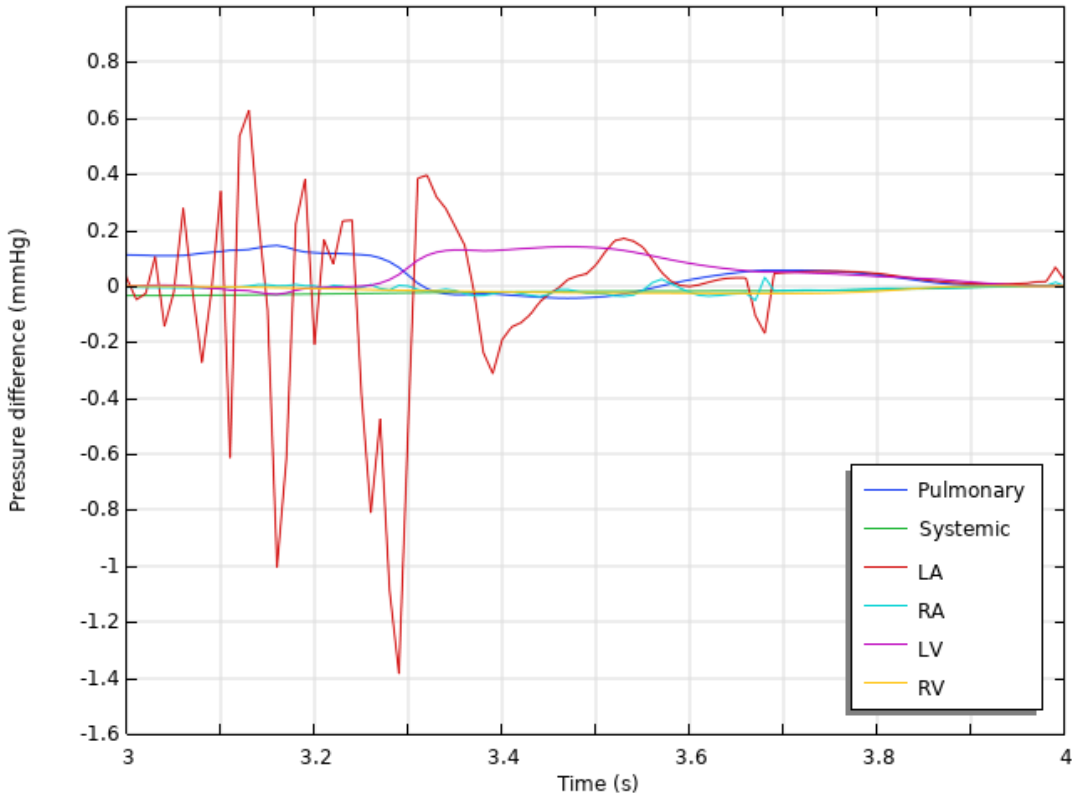

(a) Without shunt

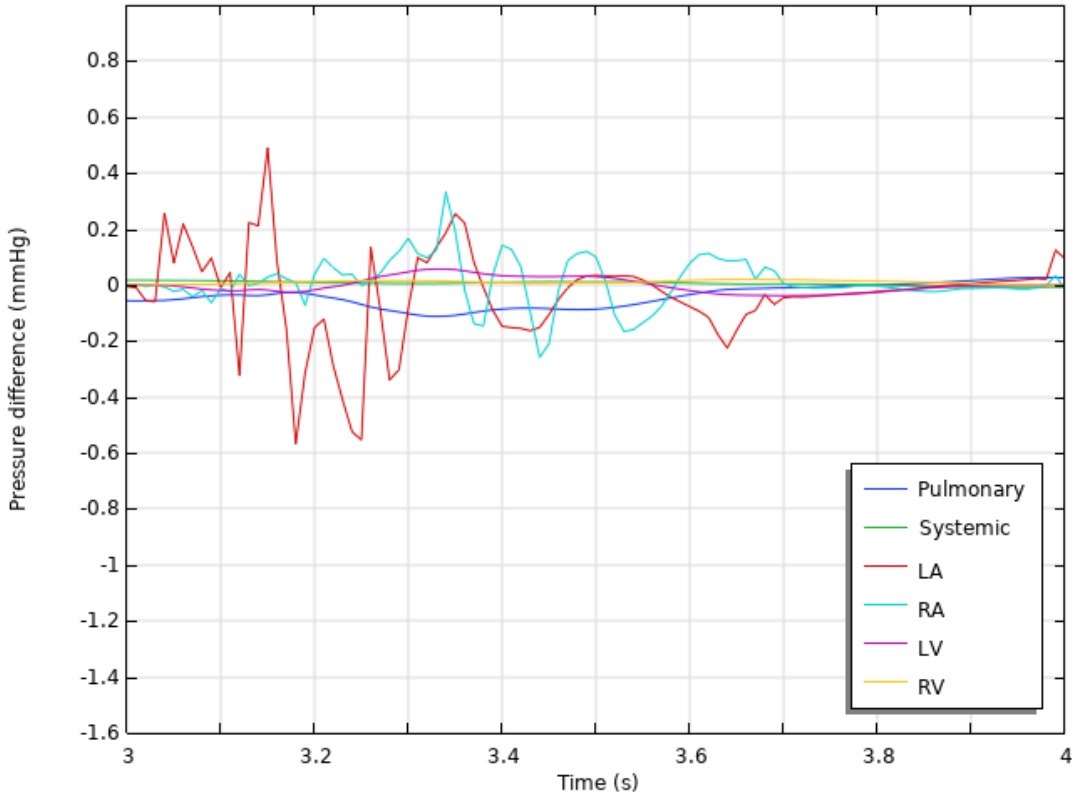

(b) 8 mm shunt

Figure C.9: Difference in pressures between the transient CFD simulation with a relative tolerance of 0.005 and a relative tolerance of 0.001 over one cardiac cycle in absence (a) and presence (b) of an 8 mm shunt. Positive values indicate higher pressures for the simulation with a relative tolerance of 0.005.

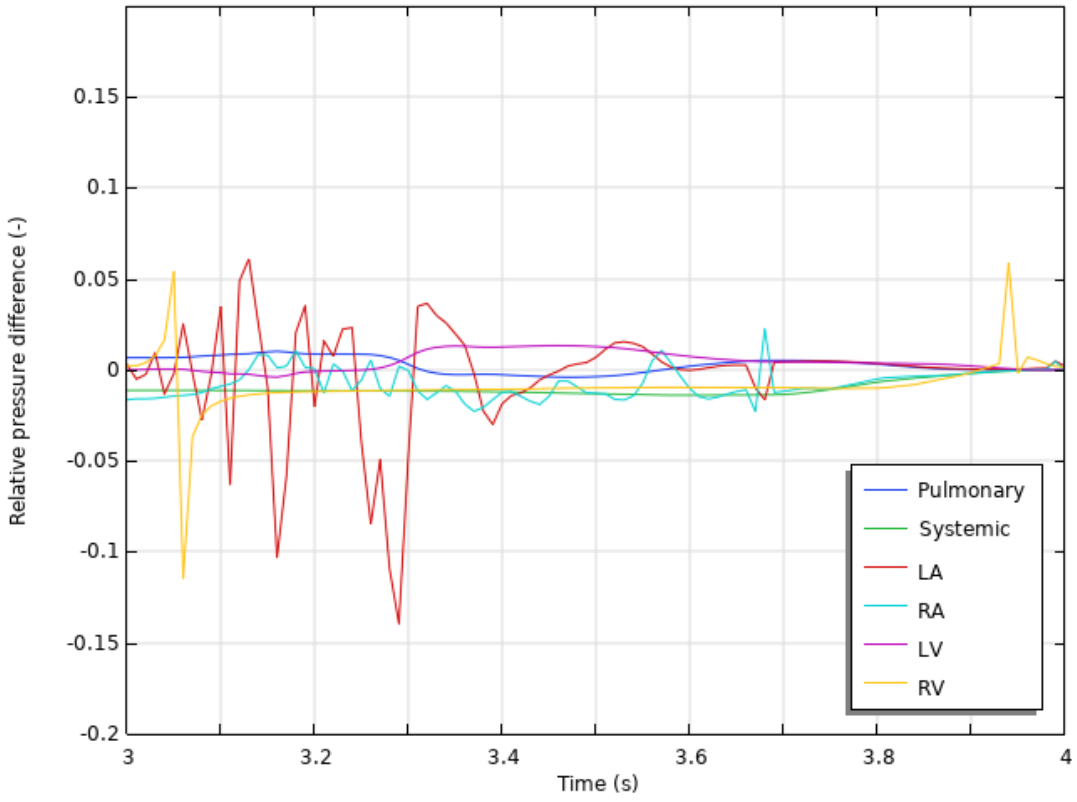

(a) Without shunt

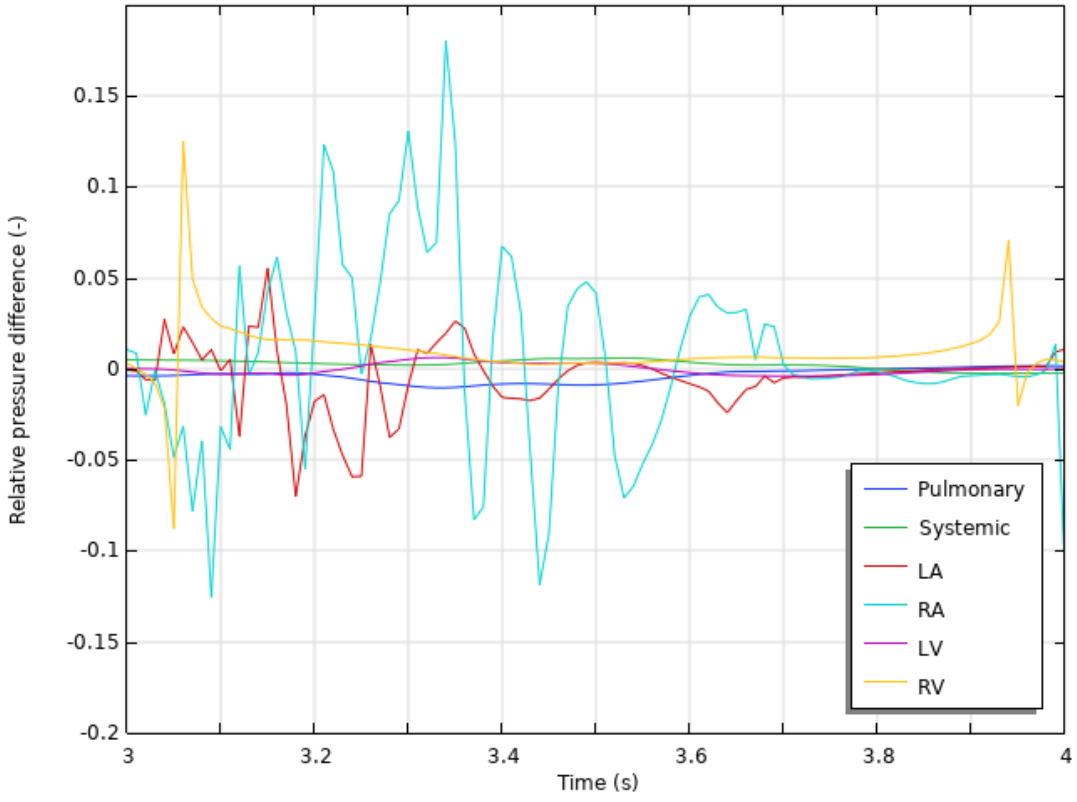

(b) 8 mm shunt

Figure C.10: Relative difference in pressures between the transient CFD simulation with a relative tolerance of 0.005 and a relative tolerance of 0.001 over one cardiac cycle in absence (a) and presence (b) of an 8 mm shunt. Positive values indicate higher pressures for the simulation with a relative tolerance of 0.005.

D

Physically unrealistic results

This appendix presents the results of the transient simulation including wall movement on the mesh presented in subsection 4.1.1. As discussed in section 4.4, this refined mesh applied to the moving mesh simulation produces physically unrealistic results. Therefore, the decision is made in section 4.4 to perform these simulations on a coarser mesh that does not show these results. For reference in future work, the physically unrealistic results are included in this report nevertheless.

The physically unrealistic results appear during the first cardiac cycle of the simulation. In this cycle, the initial conditions have not damped out, as shown in Figure 4.21 in section 4.4. Therefore, the results on any mesh are not physically realistic during this cycle. However, the simulation employing the coarse mesh as presented in section 4.4 leads to physically realistic results as the initial conditions damp out (see section 4.4), whereas this does not happen for the simulation employing the refined mesh as presented in subsection 4.1.1. Instead, the results from the simulation with the refined mesh start to highly deviate from those on the coarse mesh from the moment that the atrioventricular valves open at $t = 0.33$ s. Depending on the mesh density, the simulation either overcomes this deviation (if the mesh is coarse enough) or diverges and crashes around $t = 0.5$ s. For the refined mesh as presented in subsection 4.1.1, the simulation crashes just after $t = 0.55$ s.

Figures D.1 to D.6 show the progression of the velocity field between $t = 0.3$ s and $t = 0.55$ s on the coarse mesh as presented in section 4.4 (a) and on the refined mesh as presented in subsection 4.1.1 (b), both in presence of an 8 mm shunt. The results in this appendix only consider simulations in presence of a shunt, but the physically unrealistic results are also present in absence of a shunt. In Figure D.1, the velocity field is shown at $t = 0.3$ s, which is moments before the atrioventricular valves open. As mentioned, no significant difference is observed between the results on the different meshes at this point. At $t = 0.4$ s in Figure D.2, however, the outlet valves have just opened and a difference can already be seen between the two results. The maximum velocity in the computational domain is found in the Inferior Vena Cava (IVC) inlet, which is 1.06 m/s in Figure D.2b: 32% higher than the value of 0.804 m/s in Figure D.2a as the legends indicate. The results continue to diverge as time progresses, as Figure D.3 at $t = 0.45$ s shows a difference between the maximum velocities of 74%: 2.66 m/s for the refined mesh (Figure D.3b) versus 1.53 m/s for the coarse mesh (Figure D.3a). At $t = 0.5$ s, Figure D.4 shows that the simulation on the refined mesh further blows up, reaching velocities up to 7.23 m/s, 283% higher than the maximum velocity on the coarse mesh. Meanwhile, the velocity through the Superior Vena Cava (SVC) is clearly lower on the refined mesh compared to the coarse mesh. In Figure D.4b, it can also be seen that the Tricuspid Valve (TV) outlet partly shows reversed flow, whereas most of the jet from the IVC does flow out through the TV. Only 0.03 seconds later at $t = 0.53$ s, this reversed flow from the TV outlet has aggravated, as can be seen in Figure D.5. The IVC jet now reaches velocities up to 23.4 m/s, 1053% higher than the maximum velocity on the coarse mesh. Figure D.6b shows the velocity field at $t = 0.55$ s, moments before the simulation on the refined mesh crashes. Almost the entire right atrium now shows a velocity magnitude exceeding 2 m/s, with a maximum velocity of 77 m/s and reversed flow through the SVC. On the coarse mesh, the two jets from the vena cavae create a more realistic flow field in the right atrium, although these velocities are also higher than in reality due to the initial conditions as mentioned.

Figure D.7 shows the flow rates through the inlets, outlets and interatrial shunt during the first 0.6

seconds of the simulation on the coarse (a) and on the fine (b) mesh. As mentioned, the simulation starts with the systolic phase of the cardiac cycle, which is characterized by the closed atrioventricular valves. The outlet valves open around $t = 0.33$ s, as can be seen in Figure D.7 by the flow rates through the MV and TV becoming nonzero. In this figure, it can also be seen that the flow rates are fairly similar before $t = 0.33$ s, while the results from the two different meshes are very different after the outlet valves have opened. In Figure D.7a, the tricuspid valve flow rate can be seen to increase to about 0.016 m^3/s at $t = 0.6$ s, which is provided by the flow from the IVC (0.004 m^3/s), the SVC (0.01 m^3/s) and the decreasing atrial volume. Meanwhile, the mitral valve flow rate increases to about 0.0015 m^3/s, which is almost completely provided by the shrinking atrial volume. Remember that this is not physically realistic, but is an effect of the initial conditions. On the refined mesh in Figure D.7b, however, the tricuspid valve flow rate can also be seen to increase, but its flow rate goes beyond the limits of the figure to almost 0.11 m^3/s at $t = 0.55$ s. Until about $t = 0.45$ s, this flow rate is provided by the SVC and the IVC in approximately equal amounts. After this, the flow rate through the IVC increases rapidly to 0.15 m^3/s at $t = 0.55$ s and the flow rate through the SVC even reverses to 0.04 m^3/s at $t = 0.55$ s. The strong IVC jet is also responsible for the right-to-left shunt flow rate of 0.005 m^3/s at $t = 0.54$ s, contributing to the outflow through the mitral valve and the pulmonary veins. As can be seen in Figure D.7, the simulation crashes at $t = 0.55$ s, as there are no results after this.

Figures D.8 to D.13 show the progression of the pressure field at the same moments as the velocity field for both meshes. Similar to the velocity field discussed before, no significant difference is observed between the results at $t = 0.3$ s in Figure D.8. In Figure D.9, however, the outlet valves have opened and the the pressure fields at $t = 0.4$ s are shown. Here, pressure differences can be seen in the right atrium near the interatrial shunt and in the IVC inlet, as Figure D.9b shows much lower pressures in these regions. In Figure D.10b at $t = 0.45$ s, the lower pressure region near the interatrial shunt has faded, whereas the pressure in the IVC inlet has become even lower and has increased in size. Comparing this to the velocity field in Figure D.3, this is the moment when the IVC jet starts to reach unrealistically high velocities, causing a low pressure recirculation zone between the IVC inlet and the TV outlet as a result. As the IVC jet continues to accelerate, the pressure of this recirculation zone and the pressure in the IVC further decrease, as can be seen in Figure D.11b at $t = 0.5$ s. Meanwhile, the pressure in the rest of the right atrium is higher compared to the results on the coarse mesh in Figure D.11a. Between $t = 0.5$ s and $t = 0.53$ s, this has rapidly aggravated, as Figure D.12b shows a sharp contrast between a region with a pressure below -500 Pa (relative to 1 atm) and a region with a pressure exceeding 2500 Pa. Note that the entire TV outlet is now surrounded by the region of low pressure, indicating that the outlet pressure is far lower than the prescribed pressure, as will be shown later. Also note that the left atrium has now increased in pressure compared to Figure D.12a as a result of the high pressure in the right atrium. Figure D.13 shows the pressure fields at $t = 0.55$ s, moments before the simulation on the refined mesh crashes. Looking at the pressure field of the refined mesh in Figure D.13b, it can be seen that the region of low pressure has increased in size in the right atrium. At the same time, the region of high pressure has propagated further into the SVC inlet, whereas a region of low pressure is still present near the inlet of the computational domain. Furthermore, the left atrial pressure has now decreased, after having increased between $t = 0.5$ s and $t = 0.53$ s.

Figure D.14 shows the progression of the pulmonary, systemic, left (LA) and right (RA) atrial and left (LV) and right (RV) ventricular pressures during the first 0.6 seconds of simulation time. Figure D.14a shows this for the coarse mesh as presented in section 4.4 and Figure D.14b shows this for the refined mesh as presented in subsection 4.1.1. As discussed previously, the results between the two meshes are fairly similar during the systolic phase in the first 0.33 seconds of the simulation. Interestingly, however, a clear difference can be seen in the spatially averaged LA pressure at $t = 0$ s between the two simulations, as this is 1 mmHg in Figure D.14a and 2 mmHg in Figure D.14b. This difference can also clearly be seen in the pressure fields at $t = 0$ s in Figure D.15. Note that these pressures are on a much finer scale than the previously presented pressure fields. Meanwhile, there is no difference between the initial or boundary conditions that are set for the two simulations, which begs the question what causes this difference in initial LA pressure. As presented in Table 4.6 in section 4.4 and repeated here for convenience, both simulations use the initial pressures shown in Table D.1. Figure D.14 confirms that the inlet (pulmonary and systemic) and outlet (LV and RV) pressures are according to the set values, but the LA and RA pressures are different from the prescribed pressures on both meshes. The reason for this could be that COMSOL smooths the pressure field between the inlet and outlet pressures (see Figure D.15), therefore not being able to fully comply with this requirement. However,

this does not explain the difference in LA pressure between the two simulations. Even more concerning is the observation that the outlet pressures do not respect those in Table D.1, whereas the inlet pressures do seem to match. So, COMSOL recognizes the given inlet and outlet pressures at $t = 0$ s as apparent from Figure D.14, but does not end up respecting the outlet pressures in the pressure field in Figure D.15. Note that this is the case for both simulations, not just for the simulation in which the physically unrealistic results appear. However, this still does not explain the difference in the initial pressure field between the two simulations. Therefore, the reason behind the physically unrealistic results that become apparent during the diastole might lie in the initialization of the simulation.

Boundary	Reservoir/chamber	Pressure (mmHg)
Inlet	Pulmonary	0
	Systemic	2
Domain	LA	0
	RA	2
Outlet	LV	5.6
	RV	-0.1

Table D.1: Initial pressures of the transient simulation with a moving mesh from Table 4.6

In Figure D.14, it can be seen that the results start to significantly deviate from the moment that the atrioventricular valves open around $t = 0.33$ s. The pressure that is built up in the right atrium during the systole is now released by the opening of the outlets and the right atrial pressure drops. As blood flows from the pulmonary and systemic reservoirs through the atria into the ventricles, the pulmonary and systemic reservoir pressures decrease while the LV and RV pressures increase, as can be seen in the figure. Figure D.14b shows that the systemic pressure decreases quicker and the RV pressure rises quicker than in Figure D.14a, which is likely due to the higher velocity of the IVC jet. The most obvious difference between the two simulations is actually observed in the right atrial pressure, as this can be seen to rise significantly quicker between $t = 0.37$ s and $t = 0.46$ s on the refined mesh compared to the coarse mesh. After $t = 0.46$ s, however, the right atrial pressure can be seen to rapidly decrease until $t = 0.53$ s, but only on the refined mesh in Figure D.14b. This corresponds to the observation made previously that the region of low pressure increases in size between Figures D.10b at $t = 0.45$ s and D.12b at $t = 0.53$ s. Also the left atrial pressure can be seen to increase between $t = 0.5$ s and $t = 0.53$ s as previously observed. At $t = 0.54$ s, the right atrial pressure goes beyond the limits of the figure and peaks at 82 mmHg, before dropping to -258 mmHg at $t = 0.55$ s. As observed in Figure D.13b, also the left atrial pressure has decreased between $t = 0.53$ s and $t = 0.55$ s, which is -7.5 mmHg at $t = 0.55$ s.

In short, this appendix has discussed the physically unrealistic results that appear in the transient simulation including wall movement when the refined mesh as presented in subsection 4.1.1 is applied. These results include the jet from the IVC inlet reaching unrealistically high velocities and the right atrium reaching unrealistically high and low pressures before the simulation crashes. The results are compared to a simulation on a coarser mesh as presented in section 4.4 in which these physically unrealistic results do not appear. A possible cause is found in the initialization of the simulation, where the pressure distribution differs between the two simulations despite the application of the same initial and boundary conditions. Furthermore, it is found that the prescribed initial left and right atrial pressures are not recognized (see Figure D.14), nor respected (see Figure D.15) on both meshes. The initial inlet and outlet pressures are recognized by COMSOL as apparent from Figure D.14, but only the inlet pressures are respected according to the pressure fields at $t = 0$ s in Figure D.15 on both meshes. However, none of this explains the difference in initialization of the pressure fields between the two simulations, which has to be mesh-related.

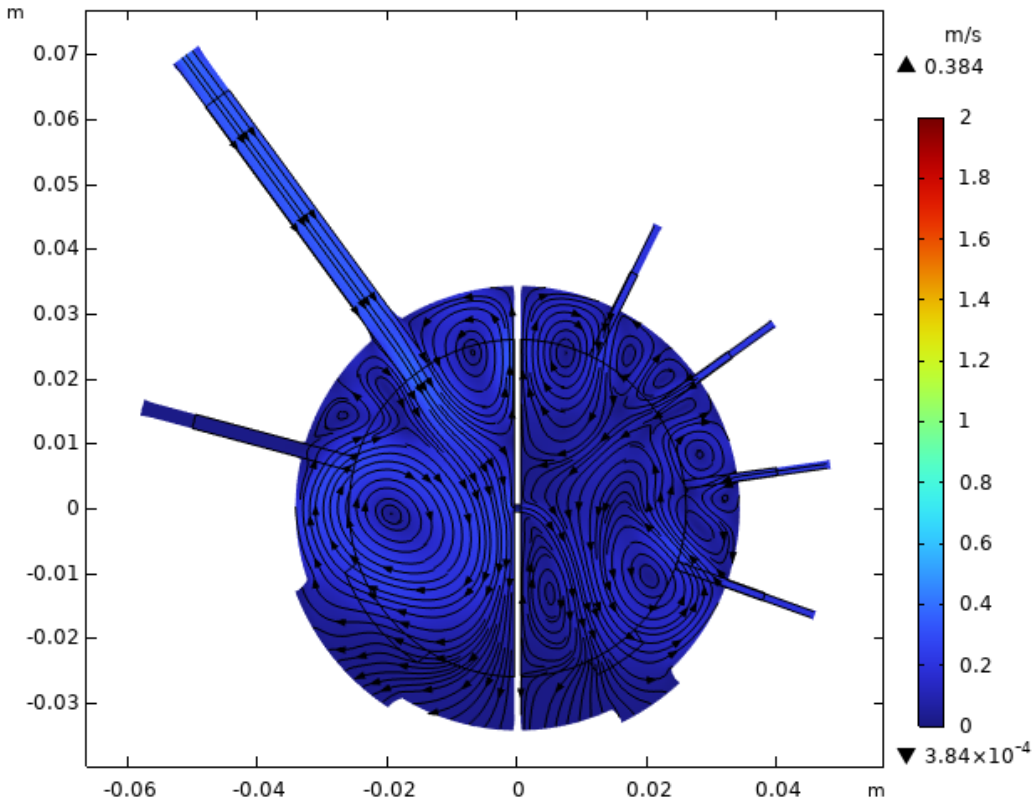

(a) Coarse

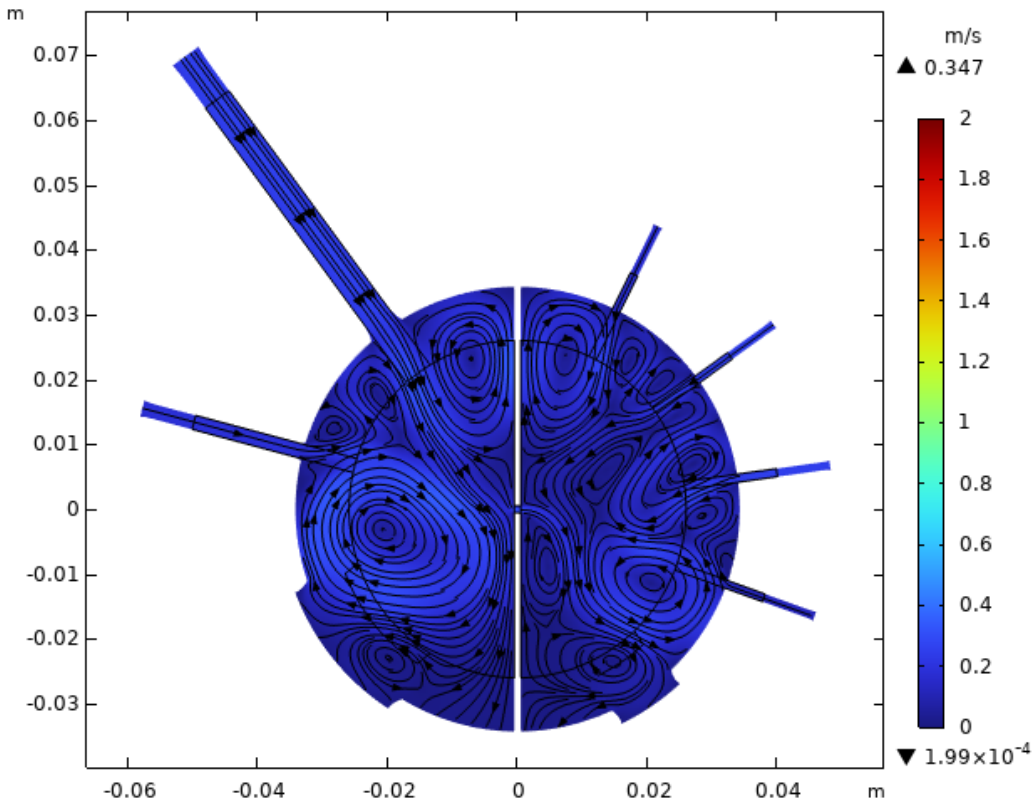

(b) Fine

Figure D.1: Velocity field of the transient CFD simulation at $t = 0.3$ s on the coarse mesh as presented in section 4.4 (a) and on the refined mesh as presented in subsection 4.1.1 (b), both in presence of an 8 mm shunt

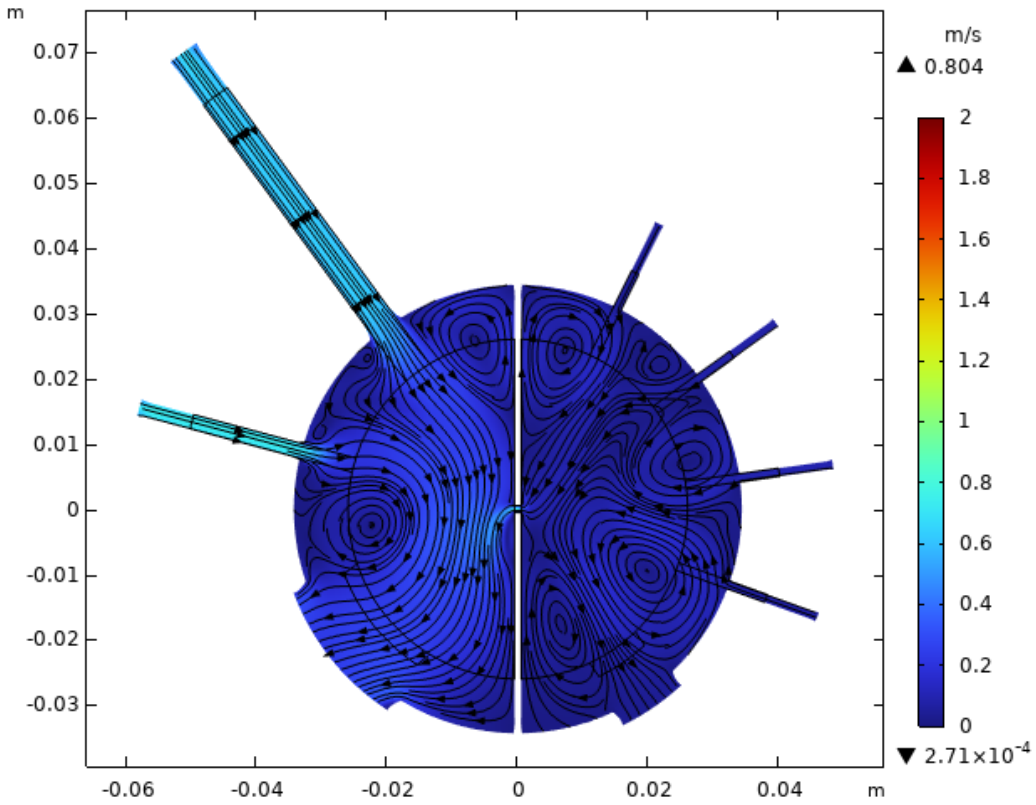

(a) Coarse

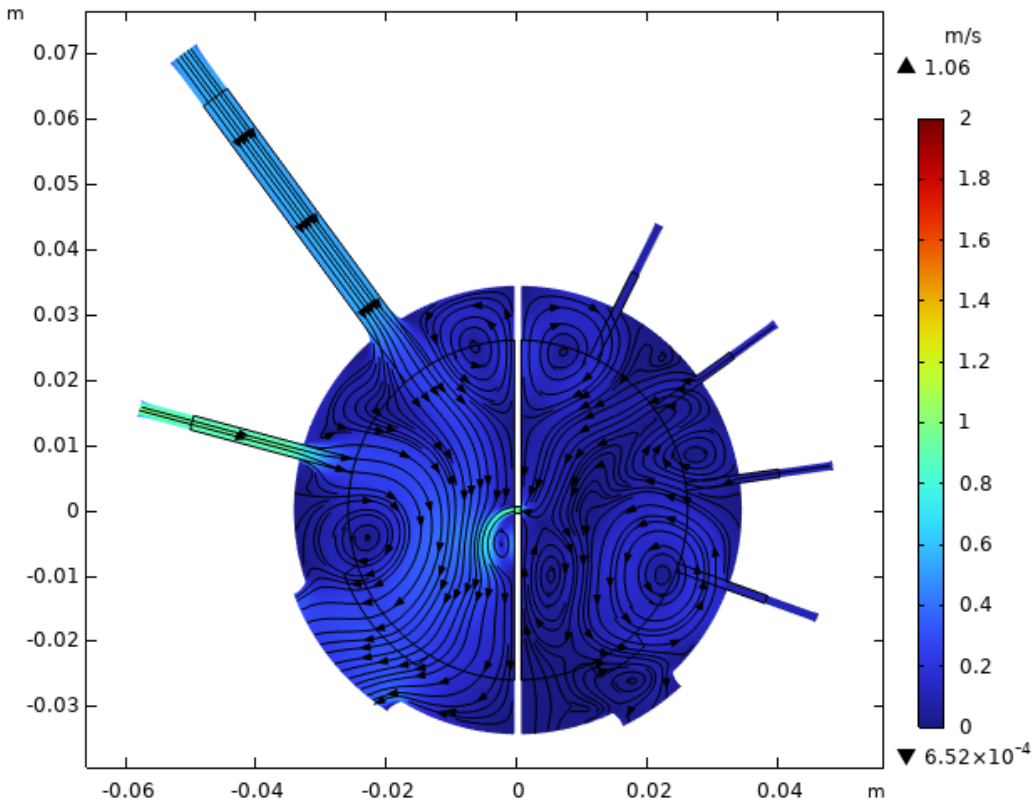

(b) Fine

Figure D.2: Velocity field of the transient CFD simulation at $t = 0.4$ s on the coarse mesh as presented in section 4.4 (a) and on the refined mesh as presented in subsection 4.1.1 (b), both in presence of an 8 mm shunt

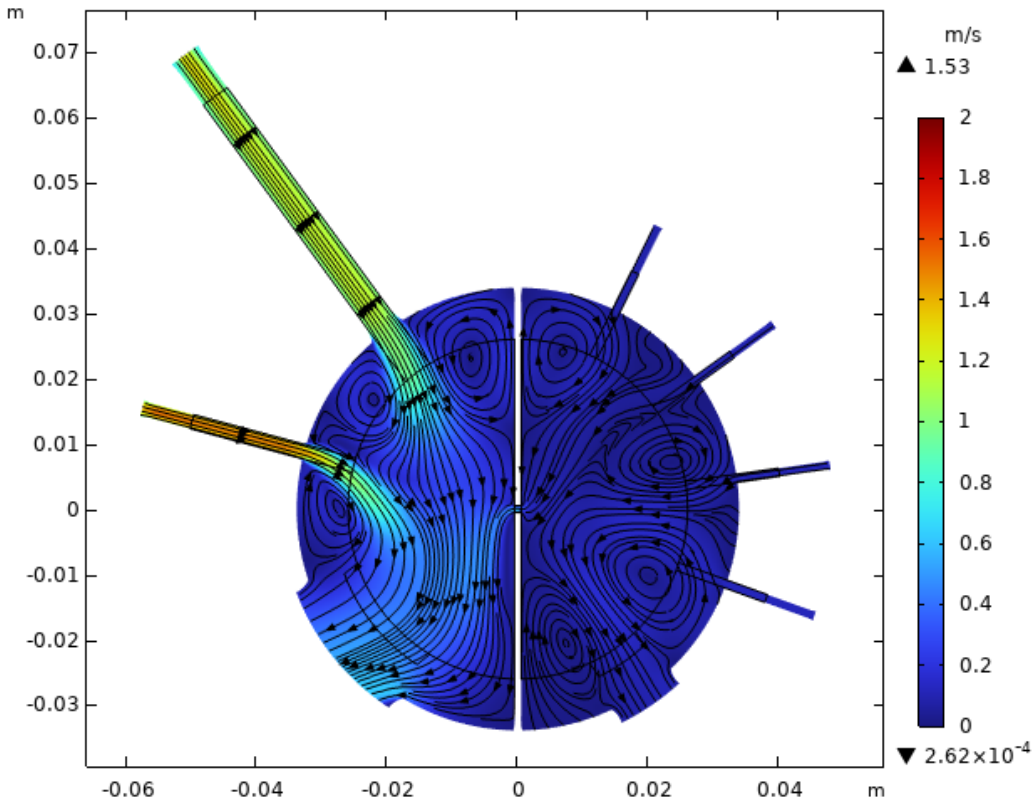

(a) Coarse

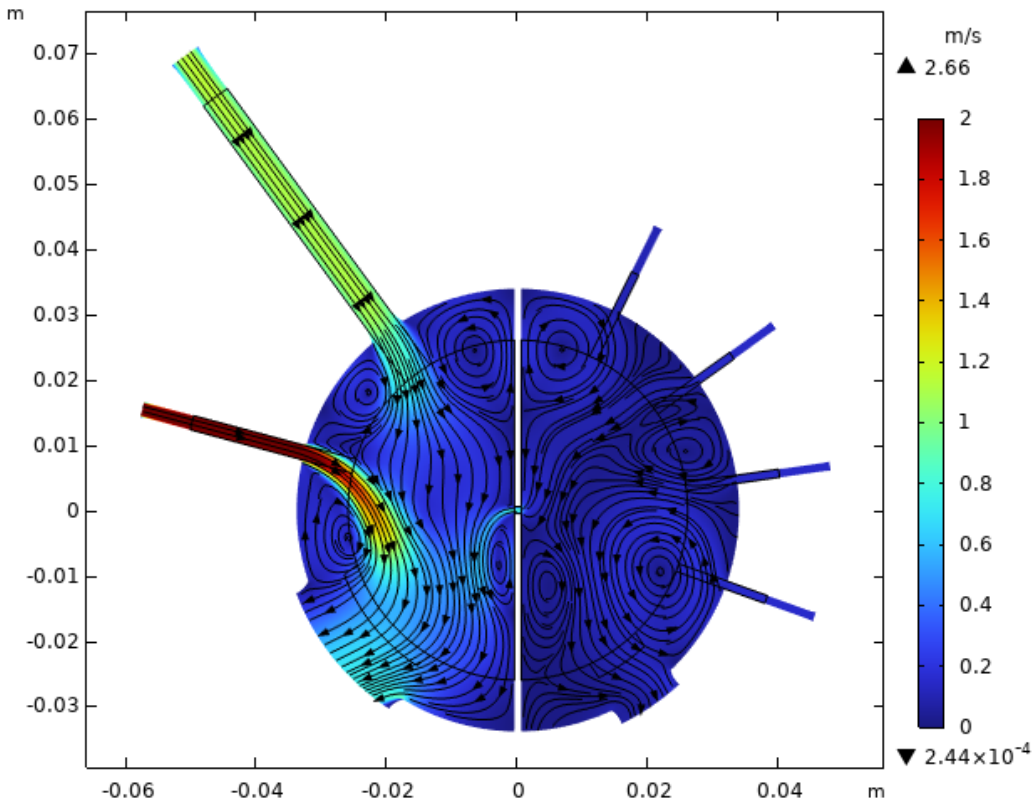

(b) Fine

Figure D.3: Velocity field of the transient CFD simulation at $t = 0.45$ s on the coarse mesh as presented in section 4.4 (a) and on the refined mesh as presented in subsection 4.1.1 (b), both in presence of an 8 mm shunt

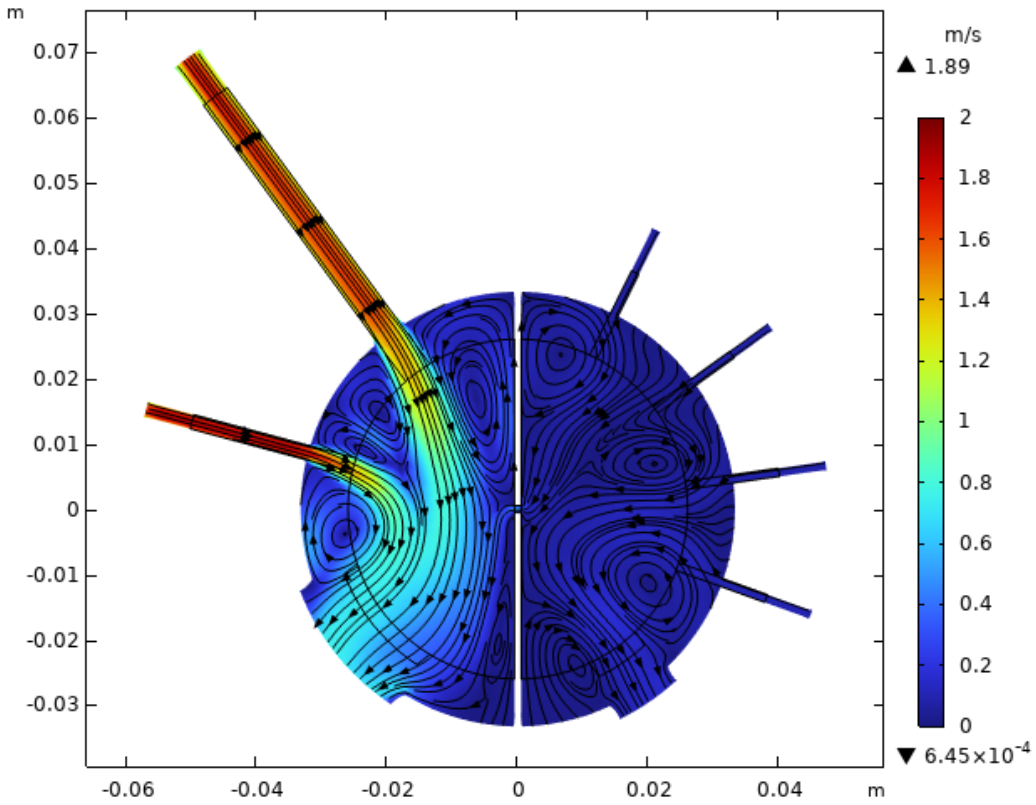

(a) Coarse

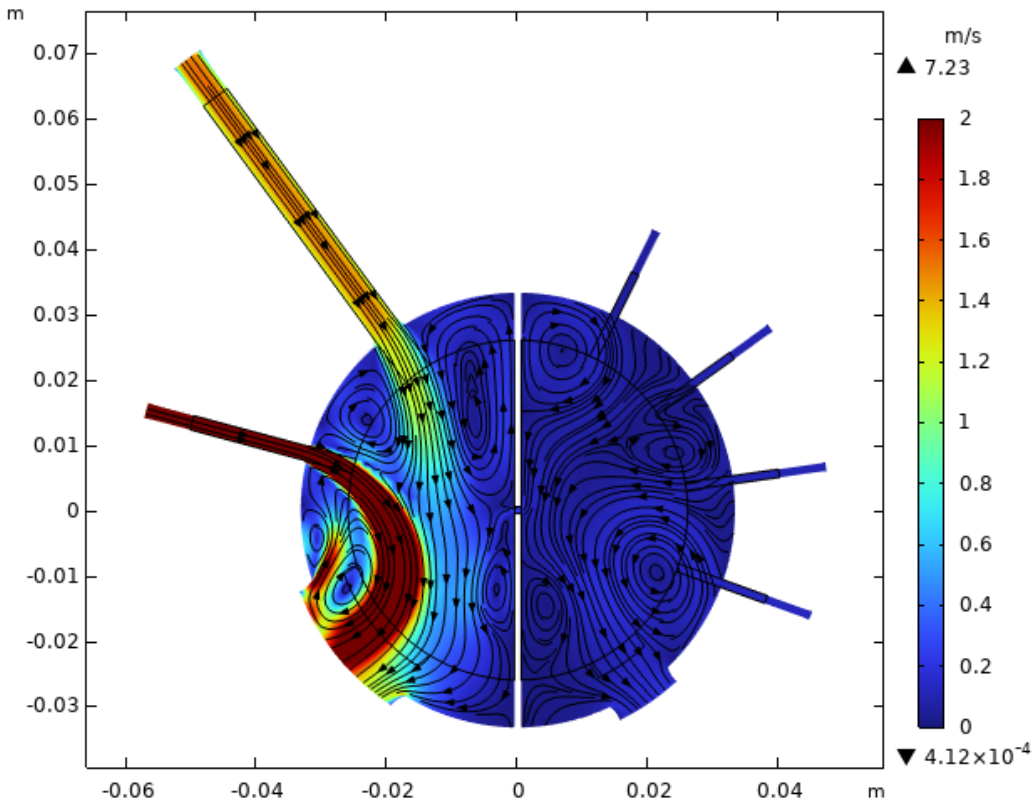

(b) Fine

Figure D.4: Velocity field of the transient CFD simulation at $t = 0.5$ s on the coarse mesh as presented in section 4.4 (a) and on the refined mesh as presented in subsection 4.1.1 (b), both in presence of an 8 mm shunt

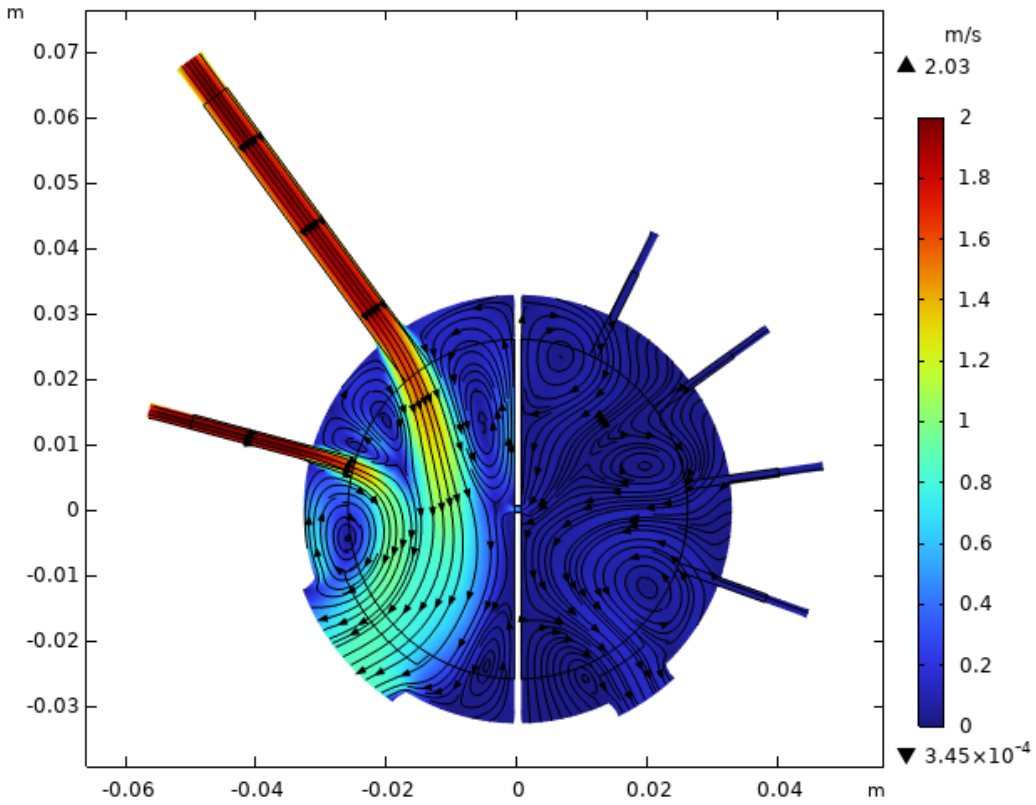

(a) Coarse

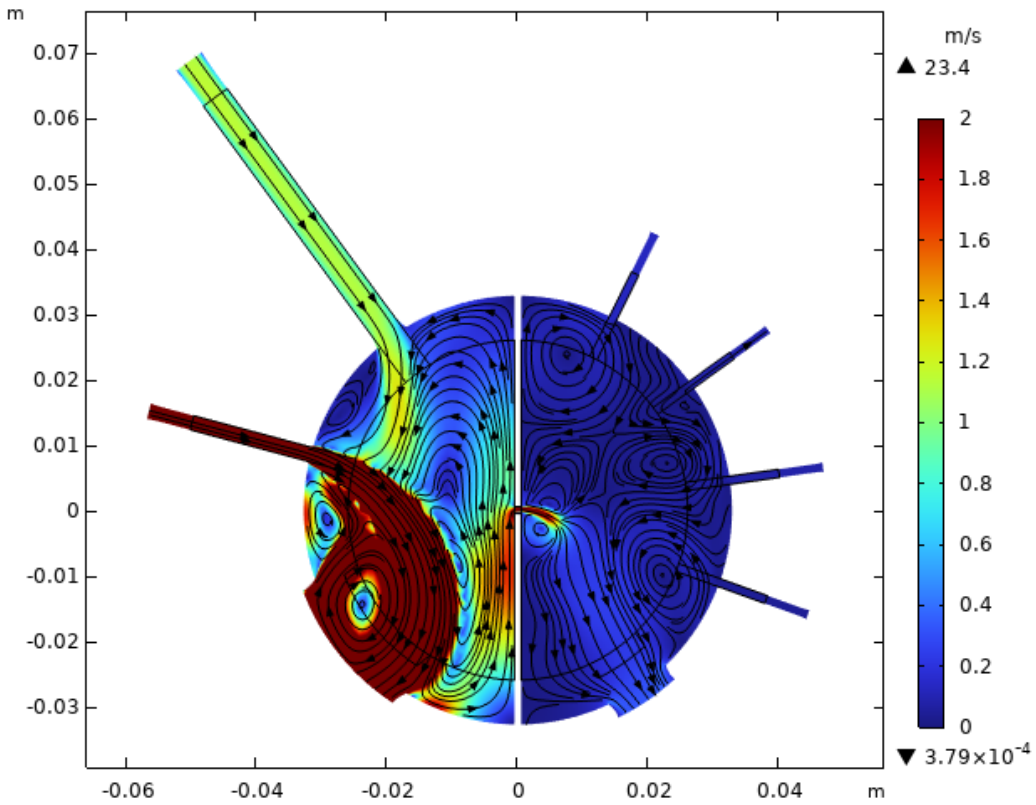

(b) Fine

Figure D.5: Velocity field of the transient CFD simulation at $t = 0.53$ s on the coarse mesh as presented in section 4.4 (a) and on the refined mesh as presented in subsection 4.1.1 (b), both in presence of an 8 mm shunt

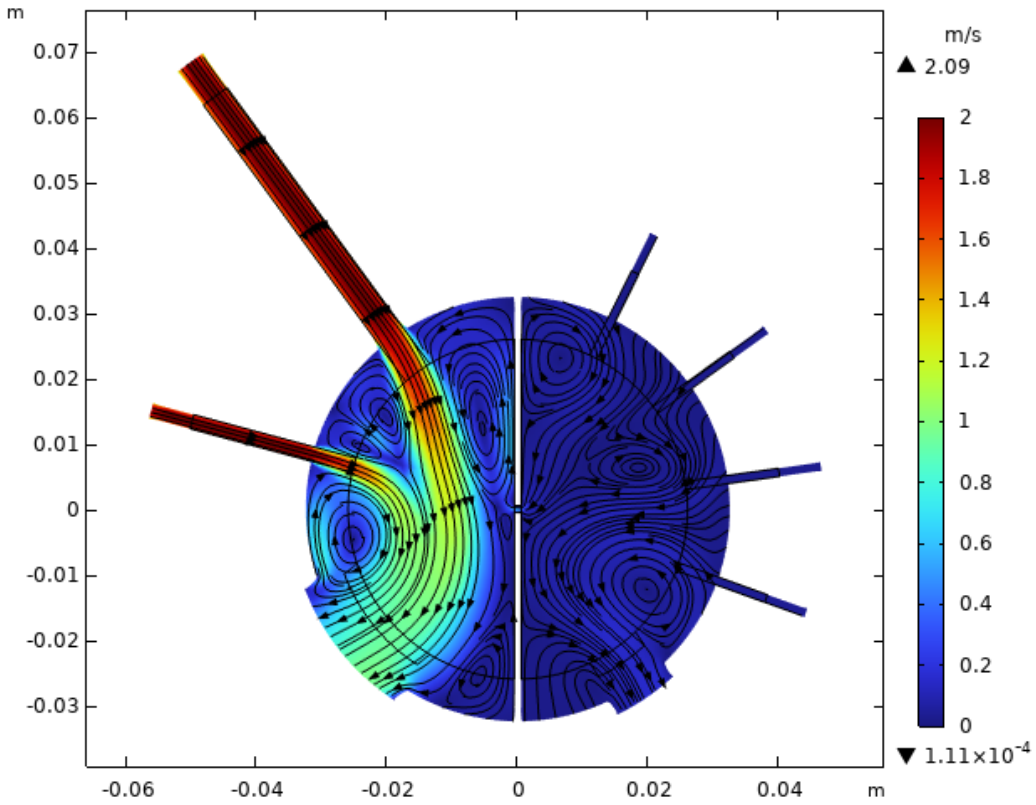

(a) Coarse

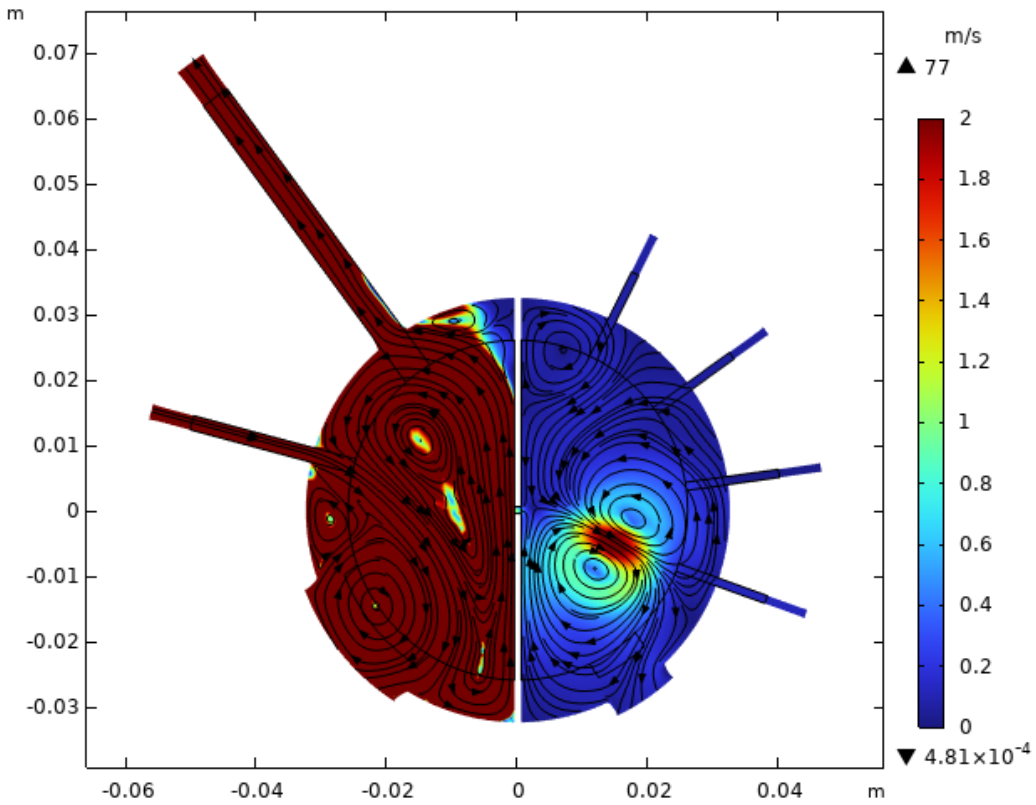

(b) Fine

Figure D.6: Velocity field of the transient CFD simulation at $t = 0.55$ s on the coarse mesh as presented in section 4.4 (a) and on the refined mesh as presented in subsection 4.1.1 (b), both in presence of an 8 mm shunt

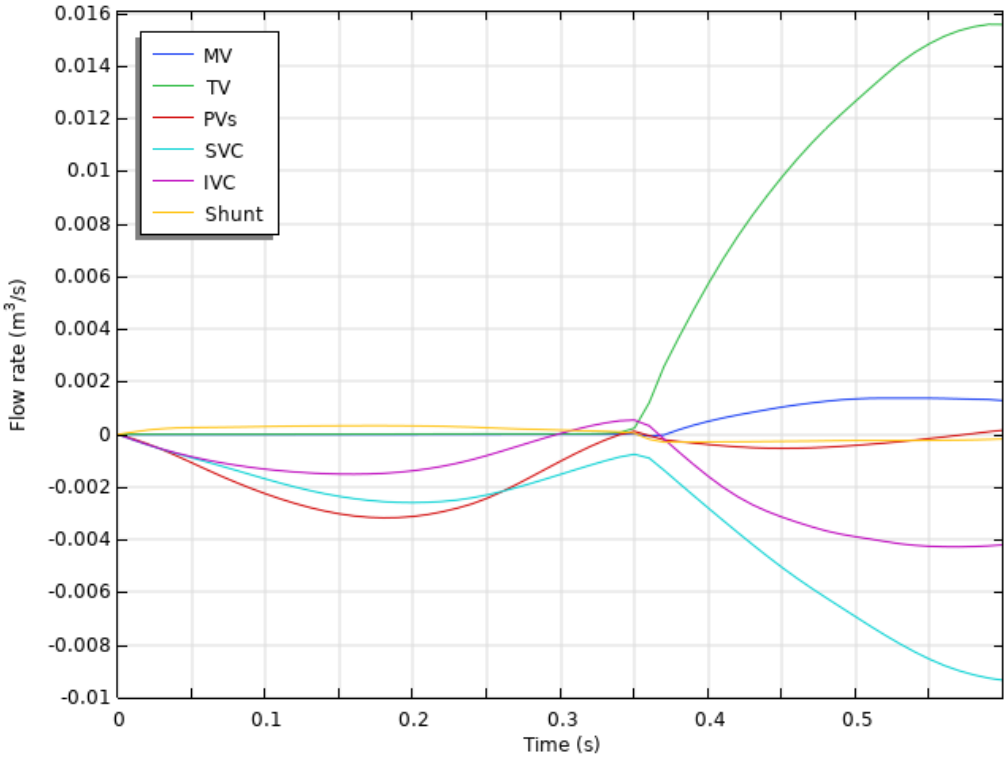

(a) Coarse

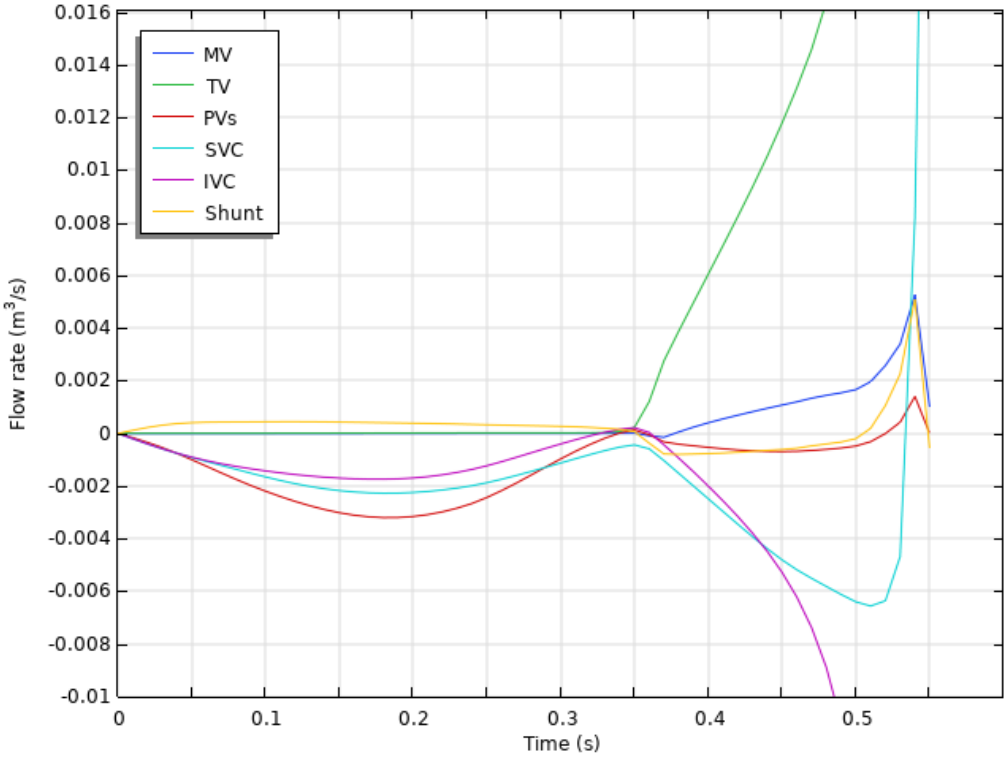

(b) Fine

Figure D.7: Flow rates through the inlets, outlets and interatrial shunt of the transient CFD simulation of the first 0.6 seconds of the simulation on the coarse mesh as presented in section 4.4 (a) and on the refined mesh as presented in subsection 4.1.1 (b), both in presence of an 8 mm shunt. Positive values indicate flow rate exiting the domain and negative values indicate flow rate entering the domain. For the shunt, a negative value indicates a flow from left to right.

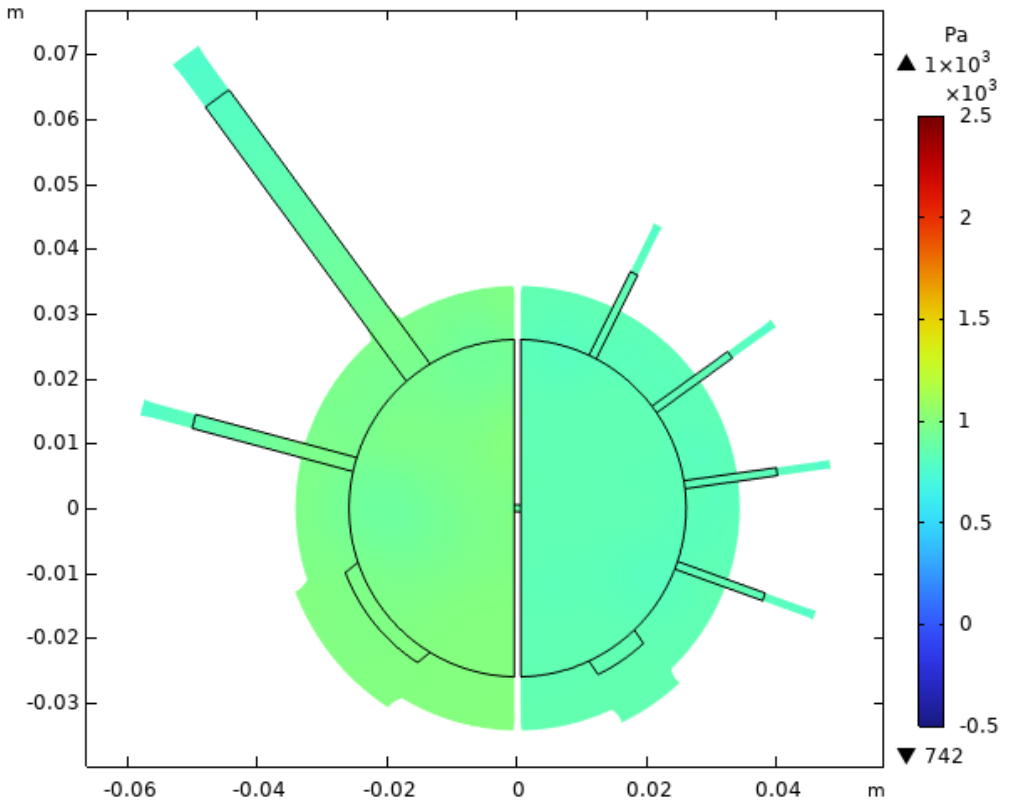

(a) Coarse

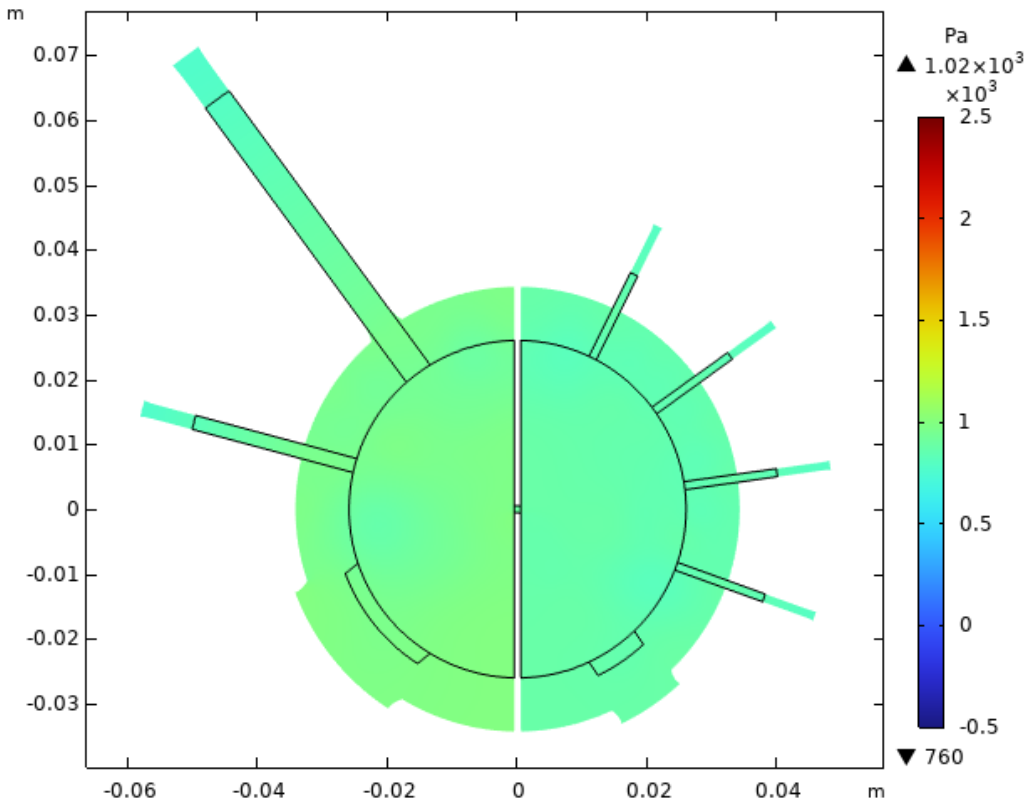

(b) Fine

Figure D.8: Pressure field of the transient CFD simulation at $t = 0.3$ s on the coarse mesh as presented in section 4.4 (a) and on the refined mesh as presented in subsection 4.1.1 (b), both in presence of an 8 mm shunt

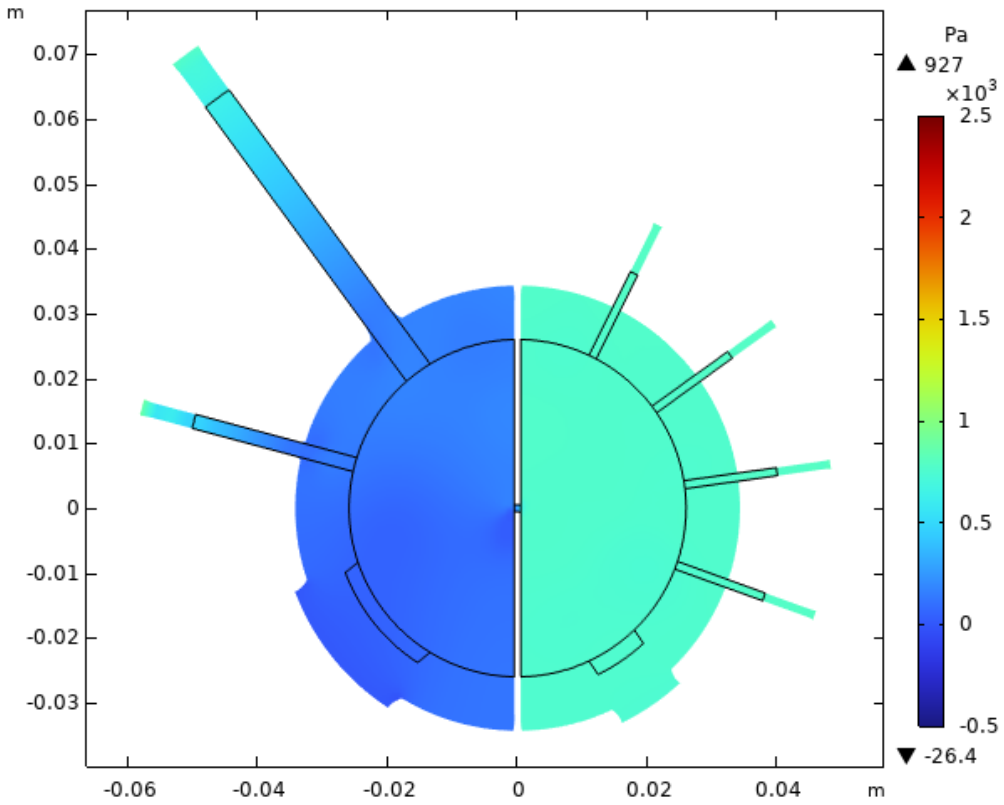

(a) Coarse

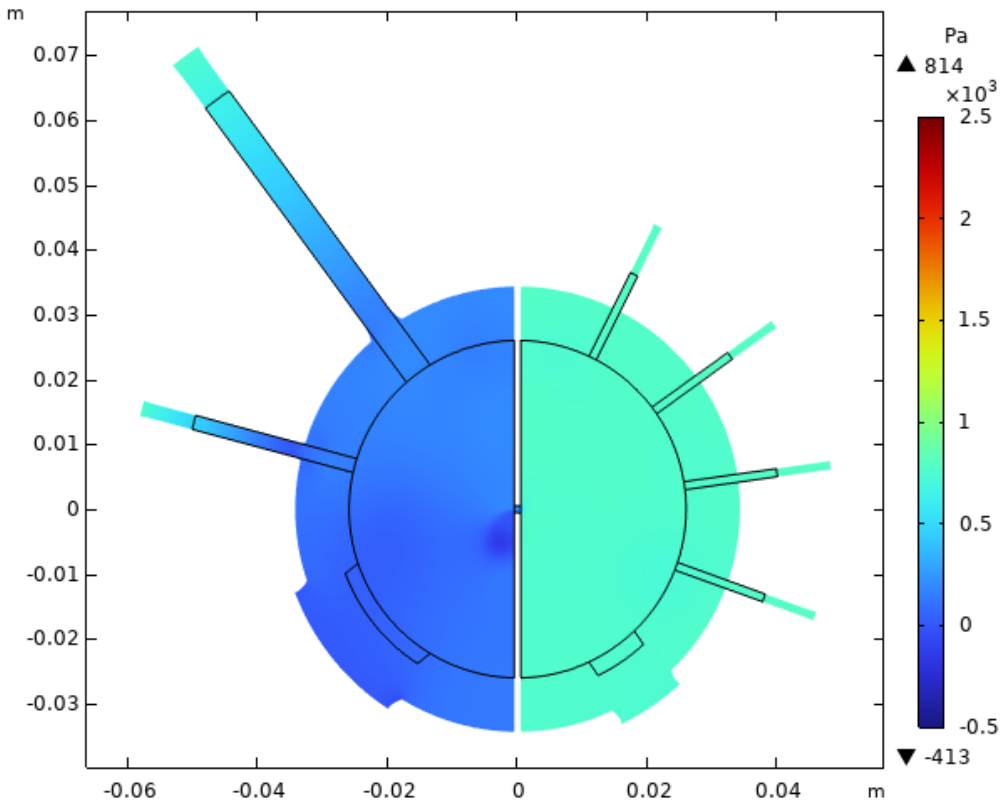

(b) Fine

Figure D.9: Pressure field of the transient CFD simulation at $t = 0.4$ s on the coarse mesh as presented in section 4.4 (a) and on the refined mesh as presented in subsection 4.1.1 (b), both in presence of an 8 mm shunt

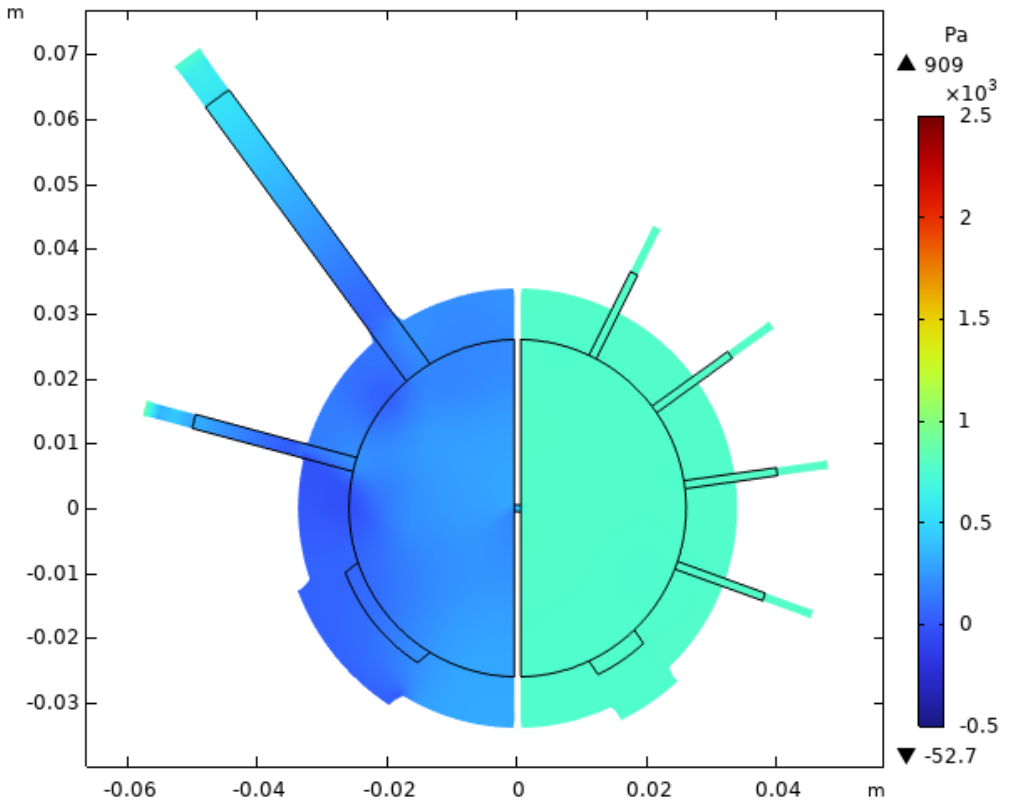

(a) Coarse

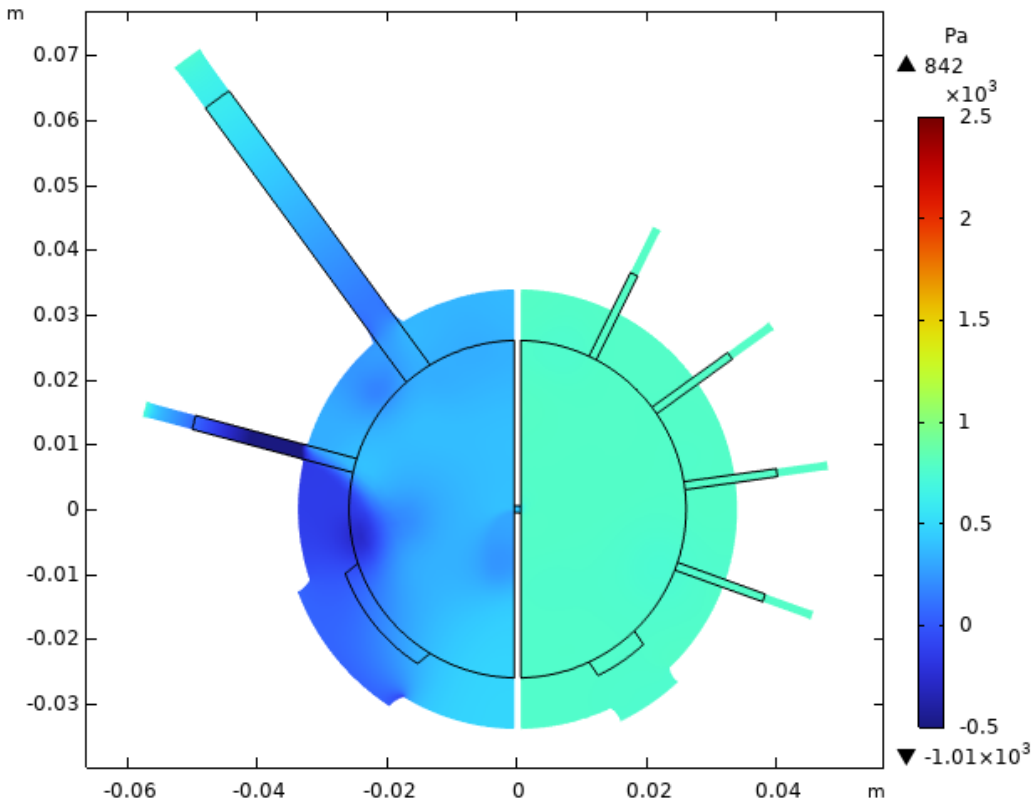

(b) Fine

Figure D.10: Pressure field of the transient CFD simulation at $t = 0.45$ s on the coarse mesh as presented in section 4.4 (a) and on the refined mesh as presented in subsection 4.1.1 (b), both in presence of an 8 mm shunt

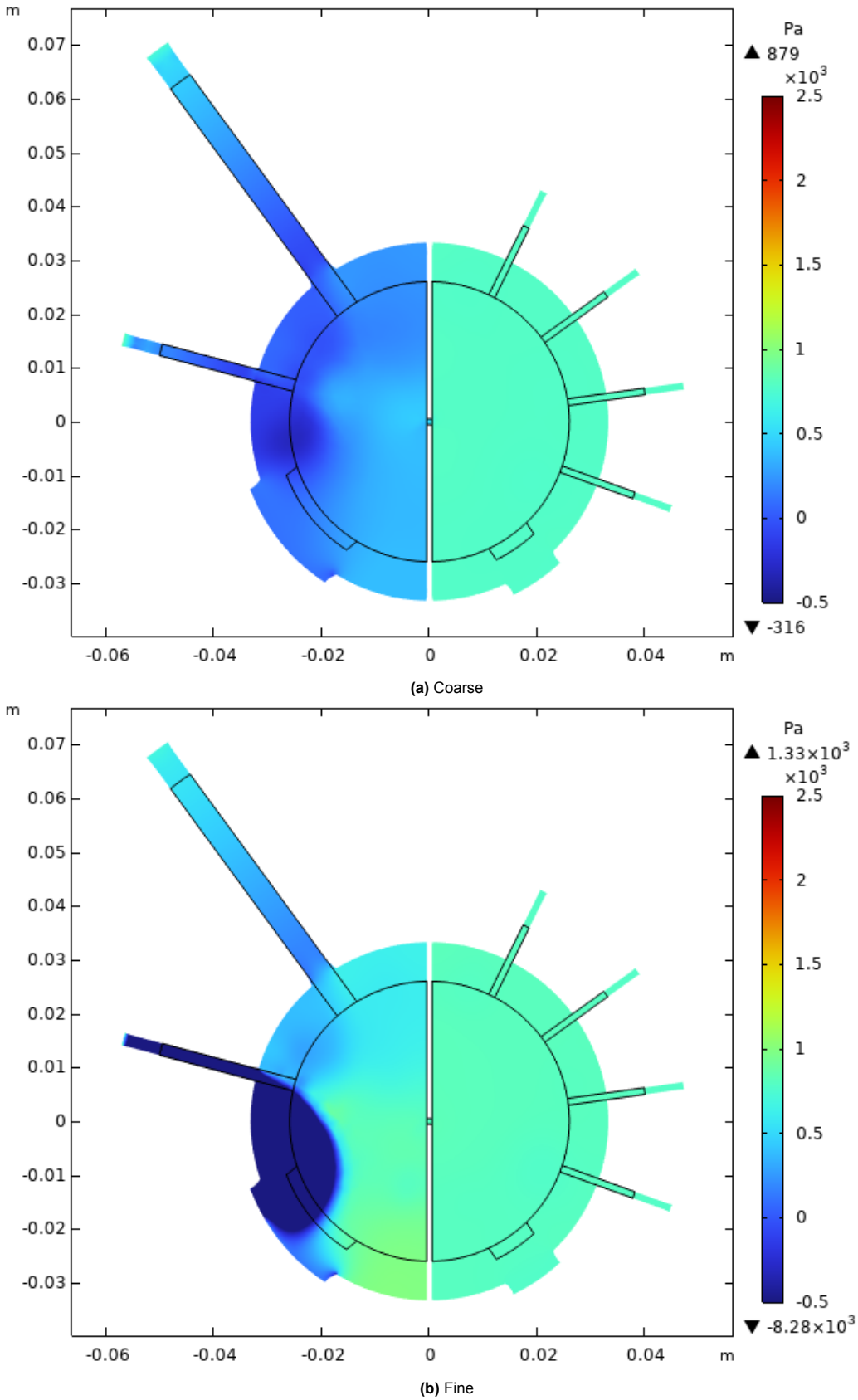

(a) Coarse

(b) Fine

Figure D.11: Pressure field of the transient CFD simulation at $t = 0.5$ s on the coarse mesh as presented in section 4.4 (a) and on the refined mesh as presented in subsection 4.1.1 (b), both in presence of an 8 mm shunt

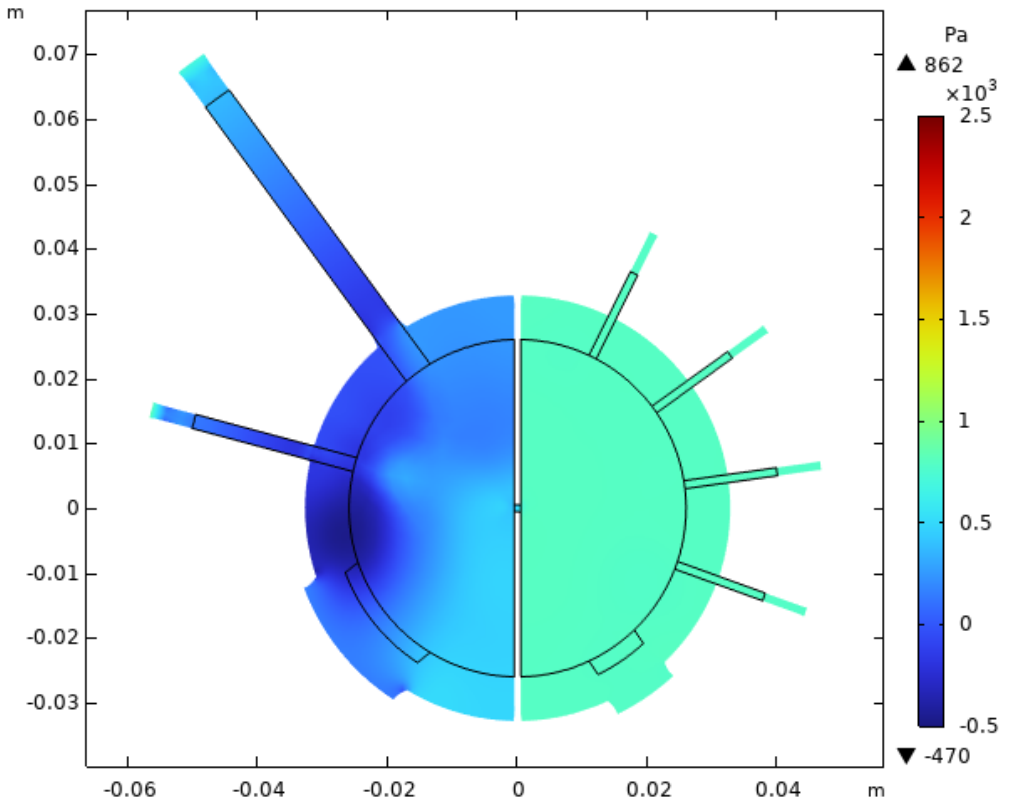

(a) Coarse

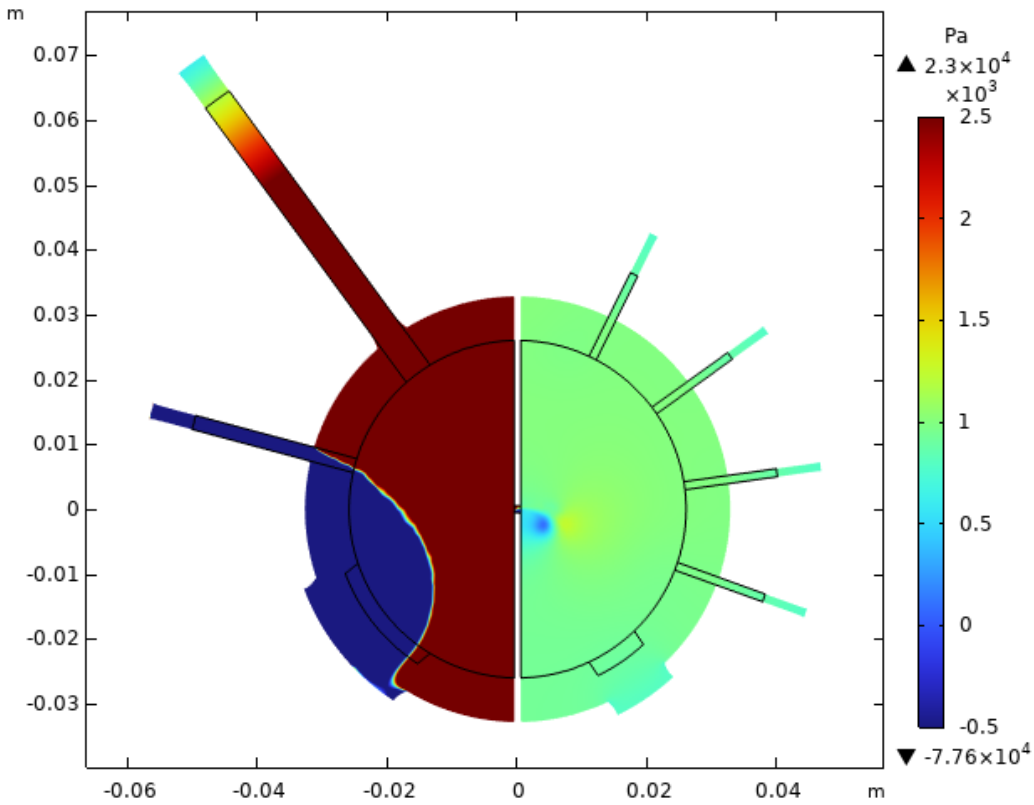

(b) Fine

Figure D.12: Pressure field of the transient CFD simulation at $t = 0.53$ s on the coarse mesh as presented in section 4.4 (a) and on the refined mesh as presented in subsection 4.1.1 (b), both in presence of an 8 mm shunt

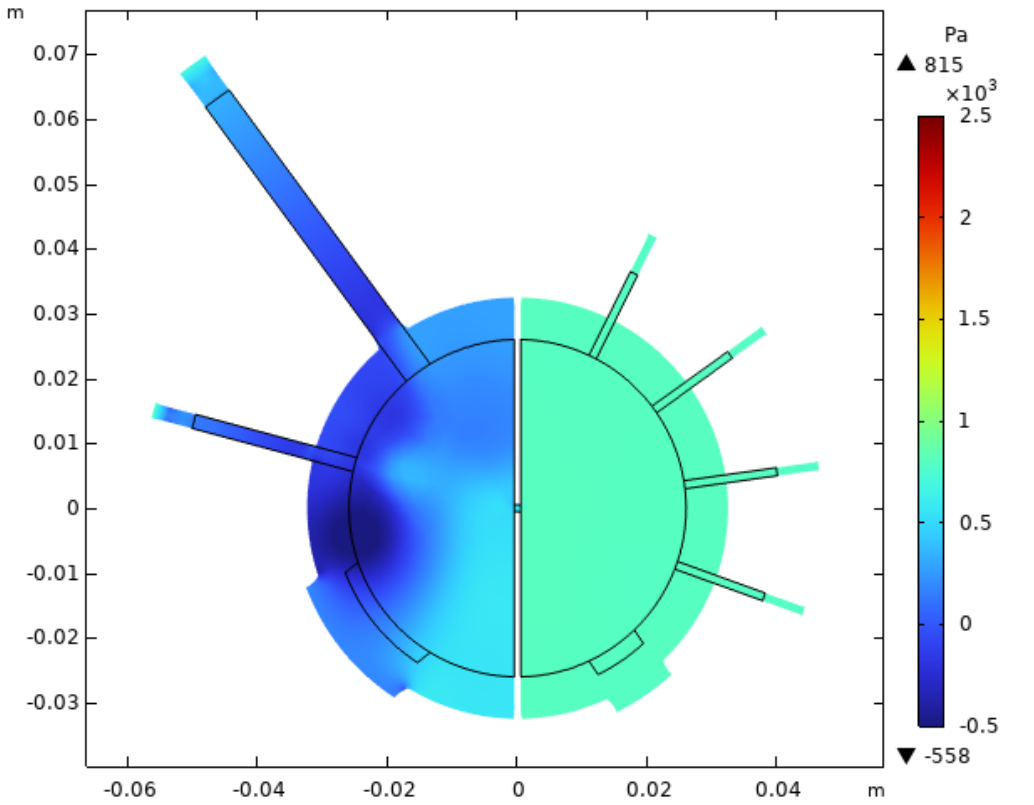

(a) Coarse

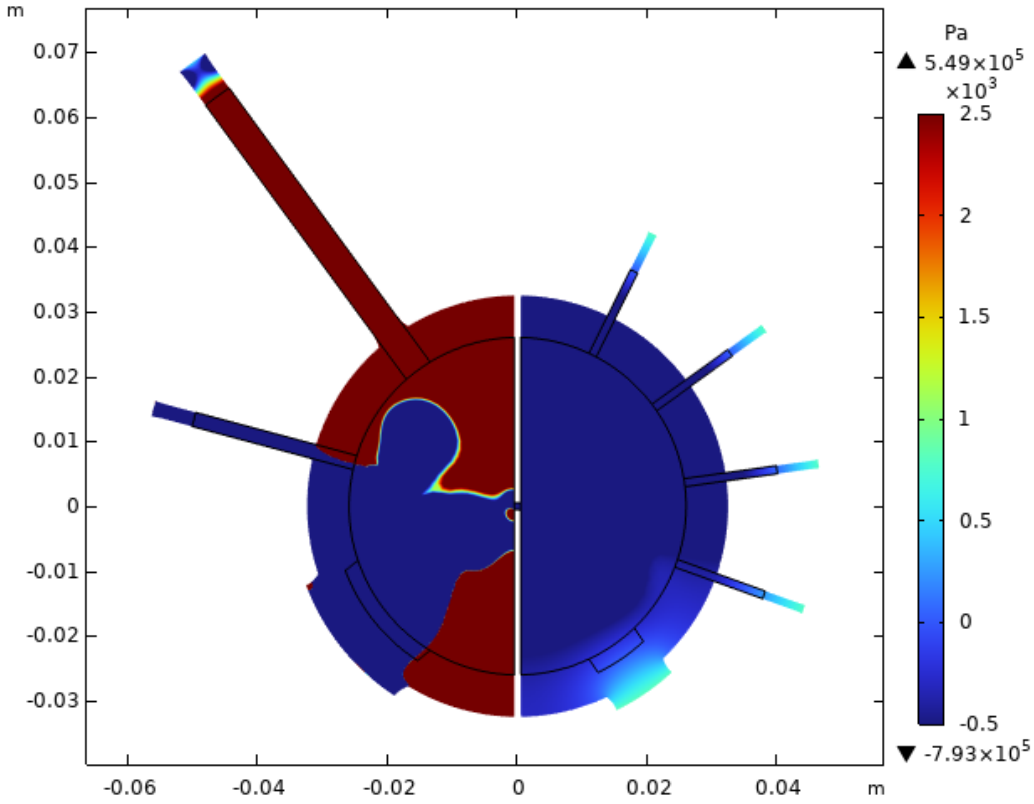

(b) Fine

Figure D.13: Pressure field of the transient CFD simulation at $t = 0.55$ s on the coarse mesh as presented in section 4.4 (a) and on the refined mesh as presented in subsection 4.1.1 (b), both in presence of an 8 mm shunt

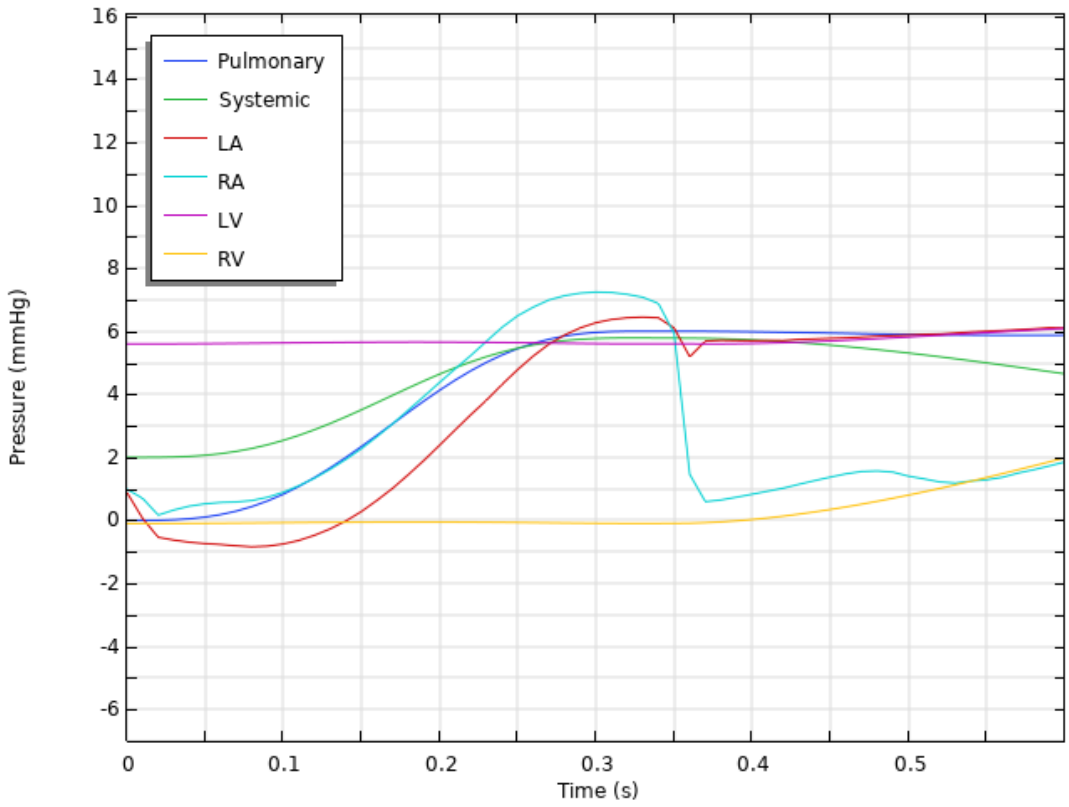

(a) Coarse

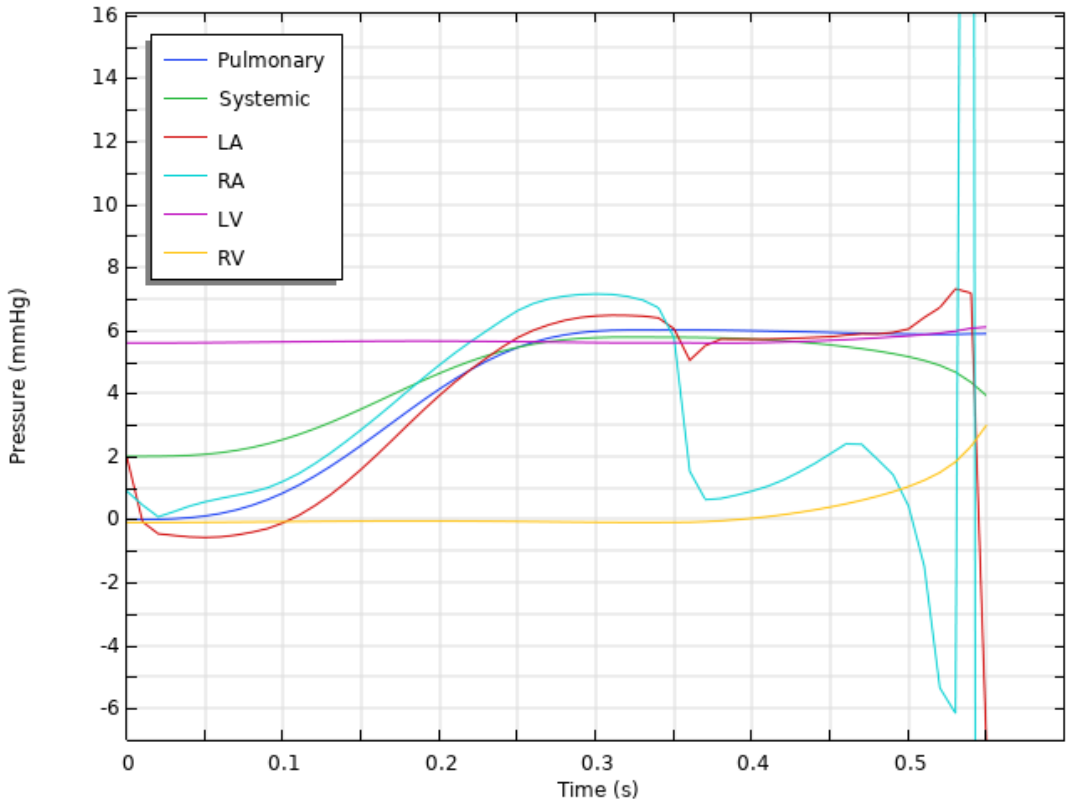

(b) Fine

Figure D.14: Pulmonary, systemic, left (LA) and right (RA) atrial and left (LV) and right (RV) ventricular pressures of the transient CFD simulation of the first 0.6 seconds of the simulation on the coarse mesh as presented in section 4.4 (a) and on the refined mesh as presented in subsection 4.1.1 (b), both in presence of an 8 mm shunt

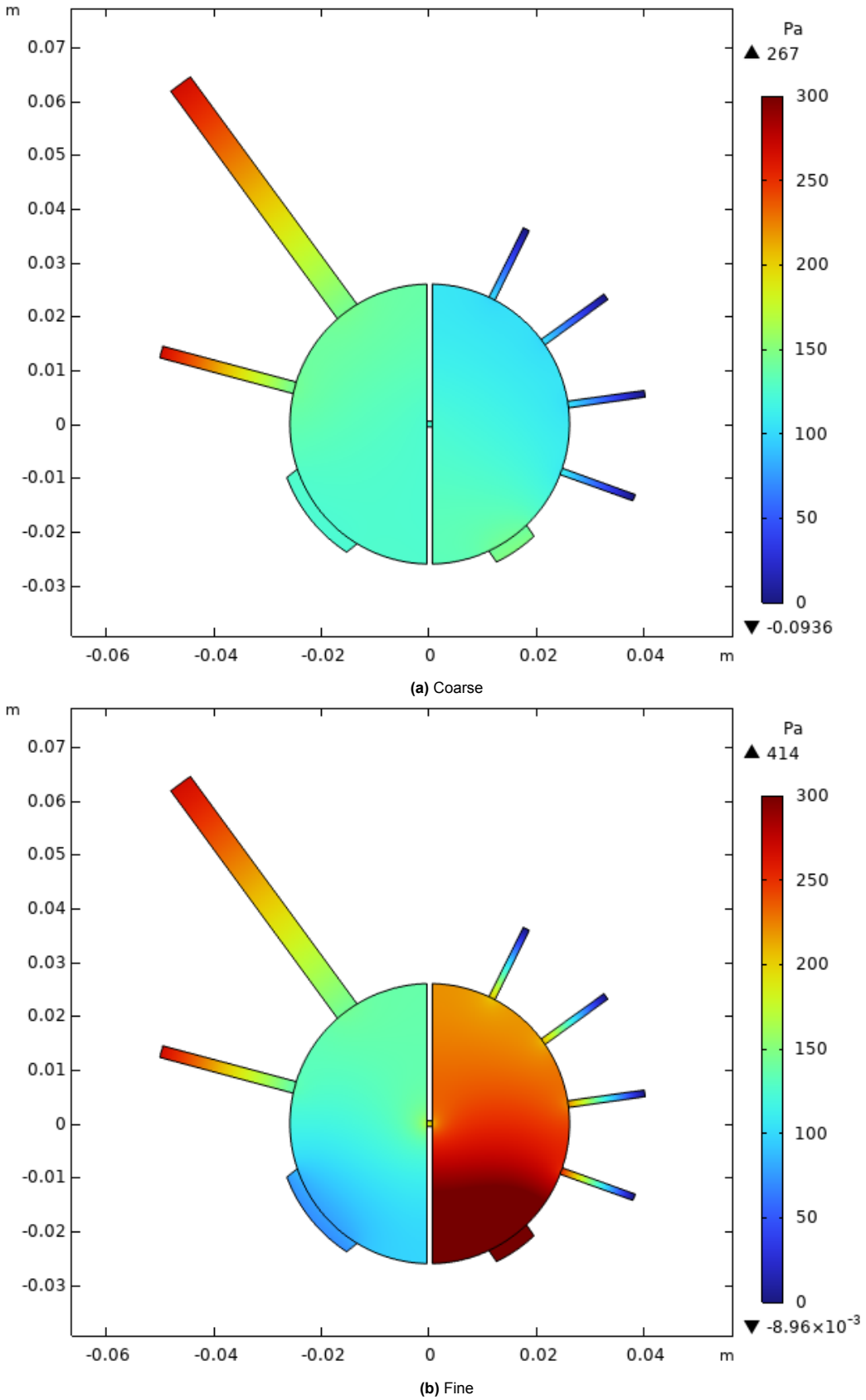

(a) Coarse

(b) Fine

Figure D.15: Pressure field of the transient CFD simulation at $t = 0$ s on the coarse mesh as presented in section 4.4 (a) and on the refined mesh as presented in subsection 4.1.1 (b), both in presence of an 8 mm shunt